

博士論文

**The Study of Martian Plasma Boundaries  
Based on Spacecraft Observations**

探査機による観測に基づく火星プラズマ境界層の研究

**Kazunari Matsunaga**  
松永 和成

名古屋大学大学院 理学研究科  
素粒子宇宙物理学専攻 宇宙地球物理系

博士 3 年  
学籍番号 461401145

指導教員：草野 完也

2017 年度



# Abstract

Mars does not possess an intrinsic global dynamo magnetic field [e.g. Acuña et al., 1998]. The solar wind can directly interact with the Martian upper atmosphere and energy, momentum, and material exchanges occur [e.g. Lundin, 2011]. The direct interaction between the solar wind and the Martian upper atmosphere forms a characteristic transition region, called the induced magnetosphere, between the shocked solar wind (magnetosheath) and the Martian ionosphere. In this transition region, the solar wind is decelerated due to mass loading by heavy ions, which are produced from the ionization of the extended Martian neutral atmosphere.

Since the interplanetary magnetic field (IMF) is frozen in the solar wind plasma, the solar wind deceleration causes the IMF to pile up and drape around the planet. After Mars Global Surveyor (MGS) observations, the outer boundary of the magnetic pile up region was referred to the magnetic pileup boundary (MPB) or the induced magnetosphere boundary (IMB) [e.g., Trotignon et al., 2006]. Observations by Phobos-2, and Mars Express (MEX) also showed the existence of a boundary that separates a region dominated by solar wind protons from a region dominated by planetary heavy ions dominant referred to as the ion composition boundary (ICB) [e.g., Breus et al. 1991]. Due to the lack of continuous simultaneous measurements of t magnetic field and ion composition prior to the recent arrival of the Mars Atmosphere and Volatile

## ABSTRACT

EvolutioN (MAVEN) mission at Mars, the relationship between the IMB and ICB remains far from understood.

In this thesis, we investigate the process of magnetosheath penetration and the relative locations of the IMB, ICB, and pressure balance boundaries as well as their dependence on solar wind parameters by using the data of the MGS and MAVEN spacecraft.

We use magnetic field and electron data from MGS from April 1999 to November 2006 to investigate magnetosheath penetration events. We identified 1,145 events and found that both solar wind dynamic pressure ( $P_{dyn}$ ) and the orientation of the interplanetary magnetic field (IMF) control the occurrence of the events. Magnetosheath penetration events during low  $P_{dyn}$  periods tend to occur at low latitudes of the northern hemisphere or where the crustal magnetic field is weak, while the event locations are widely distributed in latitude under high  $P_{dyn}$  conditions. During low  $P_{dyn}$  periods, a remarkable feature is that the observational probability is approximately 2.4 times larger during periods of the “away” IMF sector than during the “toward” sector. The northern hemisphere during the away sector corresponds to the upward electric field hemisphere due to the convection of draping solar wind origin magnetic flux tubes. These results thus indicate that the penetration of the magnetosheath into the Martian upper atmosphere more often occurs in the upward electric field hemisphere than the downward hemisphere during low  $P_{dyn}$  periods. Large-amplitude undulation of wavy structures excited by the Kelvin-Helmholtz instability in the upward electric field hemisphere is a candidate process to cause asymmetric penetration during low  $P_{dyn}$  periods.

Next, we use simultaneous ion, electron, and magnetic field observations from MAVEN to study the locations of the IMB, ICB, and pressure balance boundary ( $\beta^*$  boundary). The aim of this chapter is the understanding of differences and/or

## ABSTRACT

similarities between the IMB,  $\beta^*$  boundary, and ICB, including their characteristics and global structure. The effect of crustal magnetic fields and the upstream solar wind conditions on these boundaries is also investigated. We developed a method for automatically identifying each boundary based on the ion, electron, and magnetic field measurements from MAVEN. We identified the IMB using criteria combining the time derivative of electron flux, strength of the high frequency ( $>0.1\text{Hz}$ ) magnetic field fluctuation, and plasma beta. As for ICB identification, we used the density ratio between the planetary heavy ions and the solar wind protons. The  $\beta^*$  boundary was identified by the sum of the plasma pressure and the dynamic pressure, and the magnetic pressure.

The main results of the statistical study of MAVEN observations are summarized as follows. The IMB, ICB, and  $\beta^*$  boundary have a geographic asymmetry between the northern and southern hemispheres. The locations of all boundaries are affected by  $P_{dyn}$  as well as by the crustal magnetic fields. Since the IMB and the ICB tend to occur at similar positions on the dayside, the mass loading process controls the formation of these two boundaries on the dayside. The crustal magnetic fields seem to have a permanent effect to raise the boundary altitude in the nightside. Particularly, the combination of the crustal magnetic field and the downward electric field can raise the location of the ICB higher than usual and higher than the IMB on the nightside. A candidate physical mechanism is the enhanced cold ion outflow from the mini-magnetosphere regions via magnetic reconnection.



# Acknowledgement

This doctoral thesis would have not been written without the help of so many people in so many ways. Thus, the author would like to express his sincere gratitude to everyone who has helped throughout his study period.

First of all, the author would like to express the deepest appreciation to his supervisors, Professor Kanako Seki of University of Tokyo and Professor Kanya Kusano. The author cannot thank her and his enough for all the guidance, support and opportunities given to his during his study period. When the author was a 4th grade undergraduate student, he attended a space plasma class by Professor Kanako Seki. Thanks to her, he became interested in space plasma and planetary physics and got introduced to the Institute for Space-Earth Environmental Research (ISEE). She also gave him the opportunity to stay in the U.S.A. many times and to attend domestic and international science meetings. The author highly appreciates her guidance and support in everything.

The author would like to show his appreciation to Assistant Professor David A. Brain of Laboratory for Atmospheric and Space Physics (LASP), University of Colorado at Boulder, U.S.A., for his encouragement, insightful comments, and kind hospitality during the author's visit in Colorado.

## **ACKNOWLEDGEMENT**

The author sincere thanks also go to Professor Shinobu Machida, Associate Professor Satoshi Masuda, Associate Professor Yoshizumi Miyoshi, Assistant Professor Akimasa Ieda, and Assistant Professor Imada Shinsuke for their support on research and academic life.

Special thanks are extended to members at ISEE, members of Planetary Atmospheric Physics Group, Tohoku University, and members of Department of Earth and Planetary Science, University of Tokyo.

The author is indebted to Dr. Takuya Hara of Space Science Laboratory, University of California, Berkeley, U.S.A., for his genuine caring attitude and continuous support academic life. Without his help, it would have been difficult for the author to learn the data analysis of Mars with IDL.

This study could not be completed without the Mars Global Surveyor (MGS), Mars Atmosphere and Volatile EvolutioN (MAVEN), and Advanced Composition Explorer (ACE) data. The author expresses his great gratitude to all of the MAVEN, MGS, and ACE members.

The author gives thanks to the leadership development program for space exploration and research, Nagoya University program for leading graduate schools. The author was able to have a lot of valuable experience and to make many friends of PhD course students in this program.

Finally, the author would like to extend his indebtedness to his parents and his grandmother, who always encourage his with their gentle words, keeping his strong even in the hardest time.

# Table of Contents

<b>Abstract.....</b>	i
<b>Acknowledgment.....</b>	v
<b>Table of Contents.....</b>	vii
<b>List of Figures.....</b>	xi
<b>List of Tables.....</b>	xvii
<b>Chapter 1      Introduction.....</b>	1
1.1      General Characteristics of Mars.....	1
1.2      Plasma Environment around Mars.....	6
1.2.1      Solar Wind.....	7
1.2.2      Magnetosheath.....	8
1.2.3      Induced Magnetosphere.....	14
1.2.4      Ionosphere.....	15
1.2.5      The Crustal Magnetic Field.....	20
1.3      Plasma Boundaries.....	23
1.3.1      Bow shock.....	23
1.3.2      Induced Magnetosphere Boundary (IMB) and Magnetic Pile-up Boundary (MPB).....	26
1.3.3      Ion Composition Boundary (ICB).....	30

## TABLE OF CONTENTS

1.3.4	Pressure Balance Boundary.....	31
1.4.	Related Physical Mechanisms.....	35
1.4.1	Ion Pickup and Mass Loading Process.....	35
1.4.2	Kelvin-Helmholtz Instability.....	37
1.4.3	Magnetic Reconnection.....	39
1.4.4	Cold Ion Outflow.....	41
1.5	Objectives of This Thesis.....	43
<b>Chapter 2</b>	<b>Instrumentations and Data Sets.....</b>	<b>49</b>
2.1	Mars Global Surveyor (MGS).....	49
2.1.1	Overview.....	49
2.1.2	Magnetometer (MAG/MGS) and Electron Reflectometer (ER).....	51
2.1.3	Proxies of the Solar Wind Parameters.....	53
2.2	Advanced Composition Explorer (ACE).....	54
2.2.1	Overview.....	54
2.3	Mars Atmosphere and Volatile EvolutioN (MAVEN)...	56
2.3.1	Overview.....	56
2.3.2	Solar Wind Electron Analyzer (SWEA).....	59
2.3.3	Suprathermal and Thermal Ion Composition (STATIC).....	61
2.3.4	Solar Wind Ion Analyzer (SWIA).....	63
2.3.5	Magnetometer (MAG/MAVEN).....	65
2.3.6	Other Instruments.....	67
2.3.7	The Solar Wind Parameters.....	68
2.4	Data Sets.....	70

*TABLE OF CONTENTS*

<b>Chapter 3</b>	<b>Statistical Study Part I: MGS Observations</b>	
<b>Asymmetric Penetration of Shocked Solar Wind Down to</b>		
<b>400 km Altitudes at Mars.....</b>		<b>73</b>
3.1	Introduction.....	73
3.2.	Magnetosheath Penetration Event Selections.....	77
3.3	Determination of the Solar Wind Parameters.....	81
3.3.1	Determination of the Solar Wind Dynamic Pressure.....	82
3.3.2	Determination of the IMF Sector Polarity around Mars.....	82
3.4	Statistical Analysis.....	86
3.4.1	Dependence on the Solar Wind Dynamic Pressure.....	86
3.4.2	Dependence on the Mars Solar Orbital (MSO) Latitude.....	88
3.4.3	Dependence on the IMF Polarity.....	92
3.5	Summary and Discussion.....	94
<b>Chapter 4</b>	<b>Statistical Study Part II: MAVEN Observations</b>	
<b>Statistical Study of the Relation between the Plasma</b>		
<b>Boundaries around Mars.....</b>		<b>99</b>
4.1	Introduction.....	99
4.2.	Automatic Identification of the Martian Plasma Boundaries .....	104
4.2.1	Identification of the Induced Magnetosphere Boundary (IMB).....	104

## TABLE OF CONTENTS

4.2.2	Identification of the Ion Composition Boundary (ICB).....	106
4.2.3	Identification of the Pressure Balance Boundary.....	107
4.2.4	January 21, 2015 Event and September 16, 2015 Event.....	108
4.2.4.1	January 21, 2015 Event.....	108
4.2.4.2	September 16, 2015 Event.....	111
4.3	Statistical Analysis.....	114
4.3.1	Locations of the Martian Plasma Boundaries..	114
4.3.2	Effect of the Solar Wind Dynamic Pressure...	117
4.3.3	Effect of the Crustal Magnetic Fields.....	118
4.3.4	Relative Distances between the IMB, ICB, and $\beta^*$ Boundary.....	120
4.4	Summary and Discussion.....	125
<b>Chapter 5</b>	<b>Conclusion and Future Perspective.....</b>	<b>129</b>
<b>Appendix</b>	<b>A. Energy Dependence on Identification of the Induced Magnetosphere Boundary (IMB).....</b>	<b>137</b>
<b>References.....</b>		<b>139</b>
<b>Publications.....</b>		<b>155</b>

# List of Figures

1.1.	Image of the terrestrial planets (Courtesy of NASA).....	2
1.2.	Sketches of the Earth's magnetosphere and the plasma environment around unmagnetized planets (adapted from <i>Russell et al.</i> [1995] and <i>Luhmann</i> . [1990]).....	4
1.3.	O+ ion flux chart as observed by the MAVEN spacecraft (Courtesy of NASA).....	5
1.4.	Schematic illustration of plasma environment around Mars.....	7
1.5.	The image of the solar wind and the IMF parker spiral (Courtesy of NASA).....	8
1.6	Magnitude of the magnetic field and electron data recorded by MGS MAG/ER experiment (reproduced from <i>Nagy et al.</i> [2004]).....	10
1.7	The map of electron fluxes with the energy range of 80–100 eV in cylindrical coordinates was observed by MEX ASPERA-3(ELS) (adapted from <i>Dubinin et al.</i> [2006]).....	11
1.8	The maps of the H+ number density in cylindrical coordinates were observed by MEX ASPERA-3(IMA) (adapted from <i>Dubinin et al.</i> [2008]).....	11
1.9	Electron spectra were observed by ER/MGS (adapted from <i>Crider et al.</i> [2005]).....	12

## LIST OF FIGURES

1.10	The sheath-like electron spectra in dayside mapping (adapted from <i>Brain et al.</i> [2005]).....	14
1.11	Altitude profiles of neutral density measured by MAVEN NGIMS (adapted from <i>Mahaffy et al.</i> [2015]).....	16
1.12	Altitude profiles of the averaged density of ionospheric ions measured by NGIMS (adapted from <i>Benna et al.</i> [2015]).....	17
1.13	The electron plasma oscillations in the boundary region observed by MEX ASPERA-3(ELS) (adapted from <i>Gurnett et al.</i> [2010]).....	19
1.14	Ionopause-like signature of ion density profiles observed by MAVEN/NGIMS (adapted from <i>Vogt et al.</i> [2015]).....	20
1.15	Map of the magnetic field of Mars observed by the MGS (adapted from <i>Connerney et al.</i> [2005]).....	22
1.16	Time series plots of bow shock crossing observed by MAVEN.....	25
1.17	Martian bow shock boundary crossed by Phobos 2 and MGS (adapted from <i>Trotignon et al.</i> [2006]).....	26
1.18	Induced Magnetosphere Boundary (IMB) observed by MAG/ER onboard MGS (reproduced from <i>Trotignon et al.</i> [2006]).....	28
1.19	Positions of the induced magnetosphere boundary (IMB) of Mars crossed by Phobos 2 and MGS (adapted from <i>Trotignon et al.</i> [2006]).....	29
1.20	Ion Composition Boundary (ICB) observed by ASPERA and MAGMA experiment data (adapted from <i>Breus et al.</i> [1991]).....	31
1.21	Pressure profiles for the seven models (adapted from <i>Brain et al.</i> [2010c]).....	33
1.22	The simulation results of the magnetic pressure, the dynamic pressure, and the thermal pressure (adapted from <i>Xu et al.</i> [2016]).....	34

## LIST OF FIGURES

1.23	Cartoon of penetration of pickup ion to the solar wind (adapted from <i>Trotignon et al.</i> [2001]).....	36
1.24	Three-dimensional cutaway view of Earth's magnetosphere, showing signatures of Kelvin Helmholtz instability.....	38
1.25	Relations between ion density and velocity observed in the large-density gradient boundary by MAVEN and obtained in the MHD simulation with the entropy-based model (adapted from <i>Seki et al.</i> [submitted]).....	39
1.26	Boundary oscillations are observed by MAVEN (adapted from <i>Ruhunusiri et al.</i> [2016]).....	40
1.27	Sketch of possible magnetic reconnection and detached flux rope formation scenario (adapted from <i>Brain et al.</i> [2010b]).....	41
1.28	Cold (< 200 eV) planetary heavy ion (O+, O2+, CO2+) fluxes observed by MEX ASEPERA-3/IMA near Mars (adapted from <i>Lundin et al.</i> [2008a]).....	42
2.1	Summary of the MGS mission phases (adapted from <i>Albee et al.</i> [2001]).....	50
2.2	Overview of the MGS spacecraft (adapted from <i>Albee et al.</i> [2001]).....	51
2.3	Overview of the magnetometer (MAG/MGS), and the electron reflectometer (ER) (Courtesy of NASA).....	52
2.4	Two proxy datasets for Mars: the solar wind dynamic pressure and the IMF draping direction.....	54
2.5	Overview of the MAVEN spacecraft (Courtesy of NASA).....	57
2.6	Science instruments onboard MAVEN (Courtesy of NASA).....	57
2.7	The orbital trajectory of MAVEN (Courtesy of NASA).....	58

## LIST OF FIGURES

2.8	An example of time series plots of spacecraft potential (Courtesy of Dr. Dong).....	59
2.9.	Overview of the SWEA instrument (adapted from <i>Mitchell et al.</i> [2015])..	60
2.10	Overview of the STATIC instrument (adapted from <i>McFadden et al.</i> [2015] and Courtesy of NASA/GSFC and University of California Berkeley, SSL).....	62
2.11	The STATIC mass-energy spectra (adapted from <i>McFadden et al.</i> [2015]).....	64
2.12	Overview of the SWIA instrument (adapted from <i>Halekas et al.</i> [2015] and Courtesy of University of California Berkeley, SSL).....	65
2.13	Overview of the MAG instrument (Courtesy of NASA/GSFC).....	66
2.14	Time series plots of the solar wind parameters derived from SWIA and MAG (Courtesy of Dr. Halekas and Dr. Brain).....	69
3.1.	Overview of the time-series plots of the solar wind (magnetosheath) penetration event observed by MGS.....	80
3.2.	Time-series plots of the solar wind parameters estimated from ACE and MGS observations.....	83
3.3.	Histogram of the total duration and line plot of observational probability of the magnetosheath penetration events as a function of the solar wind dynamic pressure proxy.....	87
3.4.	Histograms of the total duration and line plots of observational probability of the magnetosheath penetration events as a function of the MSO latitude.....	90
3.5.	Histograms of the total duration and line plots of observational probability of the magnetosheath penetration events as a function of the estimated magnitude of crustal magnetic field from the Cain model.....	91

## LIST OF FIGURES

4.1	The MAVEN trajectories on January 21, 2015 event.....	109
4.2.	Overview time series plot of the plasma boundaries crossing event observed by MAVEN on January 21, 2015.....	110
4.3.	The MAVEN trajectories on September 16, 2015 event.....	112
4.4.	Overview time series plot of the plasma boundaries crossing event observed by MAVEN on September 16, 2015 event.....	113
4.5	The observed locations of the IMB, $\beta^*$ boundary and ICB.....	116
4.6.	The mean altitude for every $10^\circ$ of SZA of IMB, ICB, and $\beta^*$ boundary	117
4.7.	The observational locations of the IMB, $\beta^*$ boundary, and ICB colored by the solar wind dynamic pressure.....	118
4.8	The mean altitude of the IMB, $\beta^*$ boundary, and ICB.....	119
4.9.	The relative distance between the IMB and ICB, and between the $\beta^*$ boundary and ICB.....	121
4.10	The relative distances between the IMB and ICB on the nightside colored by the east longitude above the subsolar point.....	123
.		
5.1	A summary sketch of the Martian plasma boundaries.....	133
A	The observed locations of the IMB by the 80 eV electron selections and those of the 40 eV electron selections.....	137



# List of Tables

1.1	General physical characteristics about Mars, Earth, and Venus (ratio to Earth value).....	3
1.2	Summary of previous results about IMB locations.....	30
3.1.	Duration of each solar wind condition, ratio of each solar wind condition, number of events, ratio of events' duration, and ratio of observational probability (normalized by toward).....	92



# **Chapter 1**

## **Introduction**

### **1.1 General Characteristics of Mars**

There are three terrestrial planets that possess atmosphere in our solar system: Mars, Earth, and Venus (Figure 1.1). Mars has an elliptical orbit (eccentricity is about 0.09) outside of Earth's orbit and the average distance from the Sun is roughly 1.52 AU. Therefore, the energy input from the solar radiation and the solar wind parameters around Mars have lower values than those of Earth. The Martian axial tilt is 25.2 degrees, which is similar to the axial tilt of the Earth. As a result, Mars has seasons like the Earth. Since the Martian radius is about the half of Earth's and the Martian mass is about one tenth of Earth, the Martian strength of gravity on surface is about 40% of Earth. The solar day (sol) on Mars is remarkably similar to an Earth day: 24 hours, 39

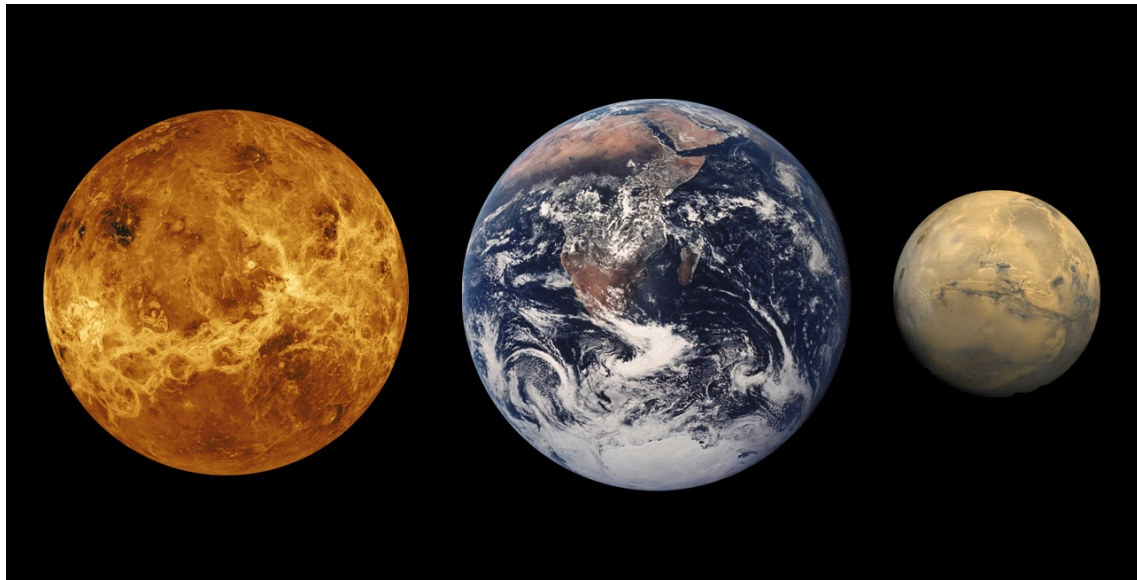


Figure 1.1: This diagram shows the approximate relative sizes of the terrestrial planets. Distances are not to scale. Courtesy of NASA

minutes, and 35.244 seconds [Allison, 1997].

Table 1.1 summarized general physical characteristics about Mars, Earth, and Venus.

As shown by Table 1.1., characteristics of Mars, Earth, and Venus are different from one another despite the fact of that Mars, Earth, and Venus are all classified as a terrestrial planet. There are a lot of reasons behind these differences. One important reason is the interaction between the solar wind and the upper atmosphere of the planets. Another crucial factor is the possessing an intrinsic global magnetic fields or not. The strong intrinsic global magnetic field of Earth forms a magnetosphere; however, Mars and Venus do not possess both of the intrinsic global magnetic field and a magnetosphere. Thus, these two planets are referred to as unmagnetized planets. Figure

Table 1.1: General physical characteristics about Mars, Earth, and Venus (ratio to Earth value). Negative numbers indicate retrograde (backwards relative to the Earth) rotation. Courtesy of NASA

Parameter	Venus	Earth	Mars
Distance from the Sun [AU]	0.723	1	1.52
Rotation period [hours]	-5832.5	23.9	24.6
Perihelion [AU]	0.731	1	1.41
Aphelion [AU]	0.716	1	1.64
Orbital Velocity [km/s]	35	29.8	24.1
Diameter [km]	12,104	12,756	6,792
Mass [ $10^{24}$ kg]	4.87	5.97	0.642
Density [kg/m <sup>3</sup> ]	5,243	5,514	3,933
Gravity [g/m <sup>2</sup> ]	8.9	9.8	3.7
Escape velocity [km/s]	10.4	11.2	5
Mean Temperature [°C]	464	15	-65
Axial Tilt [degrees]	177.4	23.4	25.2
Surface Pressure [bars]	92	1	0.01
Solar irradiance [W/m <sup>2</sup> ]	2,613.90	1,367.60	589.2
Global Magnetic Field ?	No	Yes	No
Atmospheric composition	CO <sub>2</sub> 96.5%, traces of N <sub>2</sub>	N <sub>2</sub> 78.1%, O <sub>2</sub> 21.0%, traces of Ar, CO <sub>2</sub> , H <sub>2</sub> O	CO <sub>2</sub> 95.3%, traces of N <sub>2</sub> , Ar

1.2 shows the magnetosphere of Earth and the plasma environment around unmagnetized planets.

The present Mars is cold and has a thin atmosphere that is dominated by carbon dioxide unlike in the case of Earth. This is the reason why Mars is not a habitable planet for mankind. However, in situ observation by a number of orbital spacecraft and Mars rovers provided the evidence that abundance of liquid water and thick atmosphere were

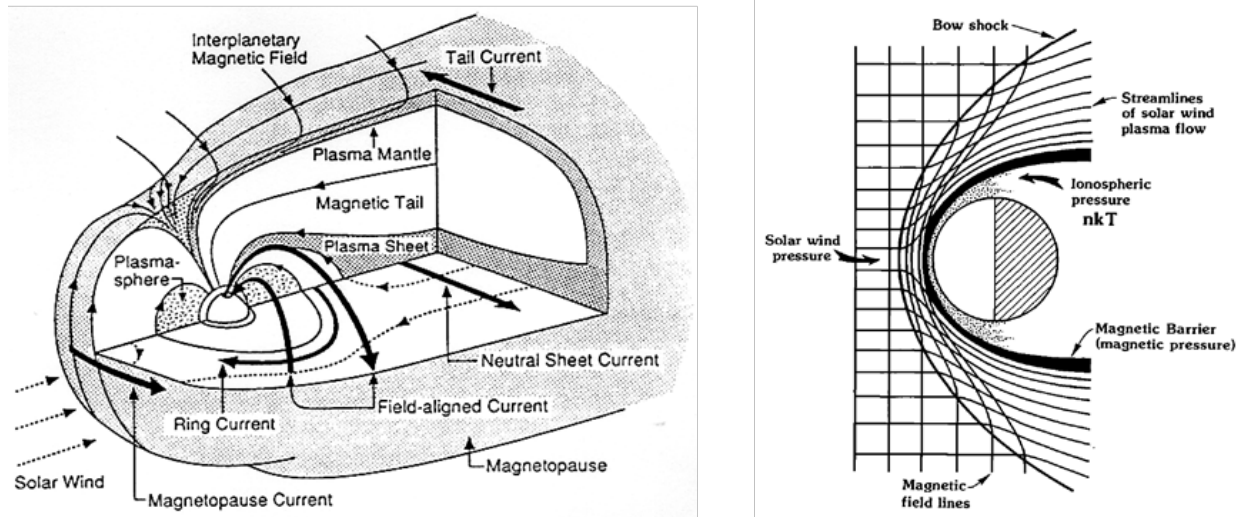


Figure 1.2: (Left) Cutaway sketch of the principal regions of the Earth's magnetosphere [Russell *et al.*, 1995], (right) schematic illustration of the plasma environment around unmagnetized planets [Luhmann., 1990]

once present on the Martian surface [e.g., Carr and Clow, 1981; Jakosky *et al.*, 1994;

Haberle, 1998; Smith *et al.*, 2009; Lundin, 2011; Ojha *et al.*, 2015]. Therefore, it is

suggested that the ancient Mars possessed a thicker atmosphere than present and a large

quantity of liquid water. It has been considered highly possible that the dramatic climate

change of Martian atmosphere and surface between past and present correlates well with

atmospheric escape to space from Mars [e.g., Jakosky and Phillips, 2001; Chassefière

and Leblanc, 2004; Jakosky *et al.*, 2015b, 2015c].

Since Mars is an unmagnetized planet, the Martian upper atmosphere directly interacts

with the solar wind [e.g., Luhmann, 1990; Luhmann *et al.*, 2004]. In consequence of this

interaction, the Martian atmosphere escapes to space from the Martian ionosphere. The

Phobos-2, Mars Express (MEX), and Mars Atmosphere and Volatile EvolutioN (MAVEN) spacecraft with onboard instruments of ion observation measured escape rates of oxygen ions. They also revealed that the escape rate has a large dependence on the solar activities and on the solar wind condition [Lundin *et al.*, 1989, 2008a; Nilsson *et al.*, 2011; Jakosky *et al.*, 2015b, 2015c; Brain *et al.*, 2015, Dong *et al.*, 2015]. Figure 1.3 shows an example of the flux of escaping oxygen ions observed by MAVEN.

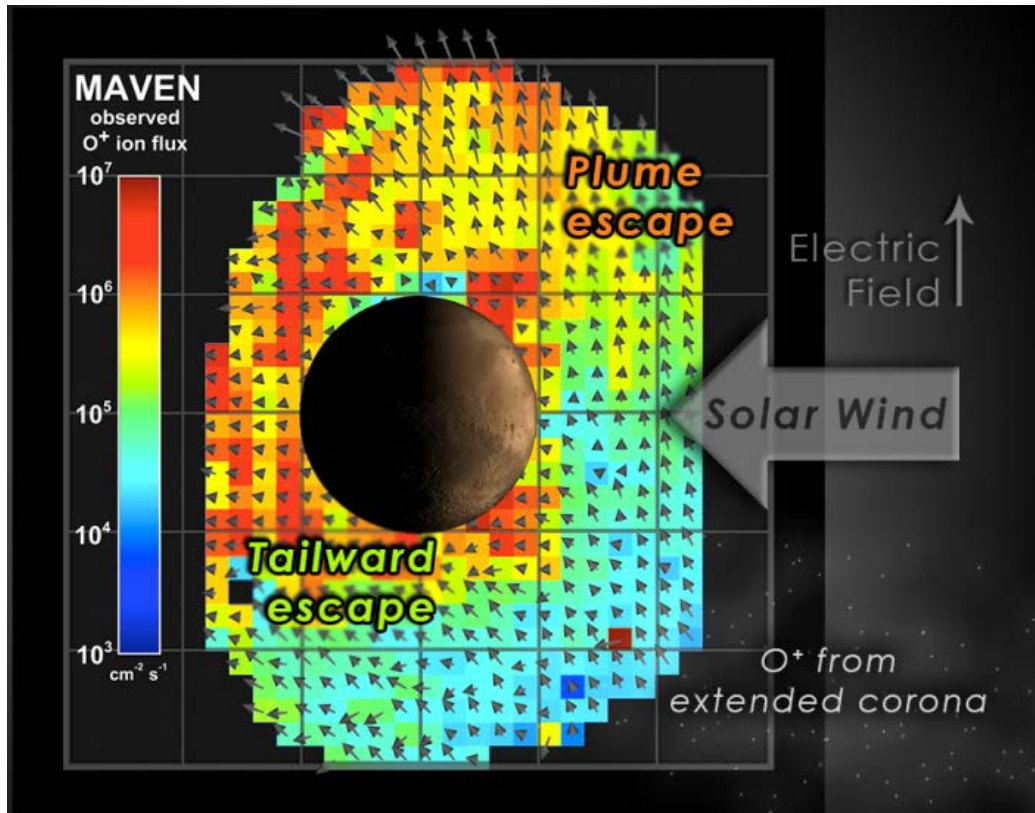


Figure 1.3: O<sup>+</sup> ion flux chart as observed by the MAVEN spacecraft. Courtesy of NASA

## 1.2 Plasma Environment around Mars

A lot of spacecraft have observed the space plasma around Mars [e.g., *Sagdeev and Zakharov, 1989; Barabash and Lundin, 2006; Albee et al., 2001; Jakosky et al., 2015a*].

However, Phobos-2, which has a magnetometer, an electron detector, and an ion mass analyzer, only operated for almost two months before it failed. Mars Global Surveyor (MGS), which has a magnetometer and an electron reflectometer, lacks an ion instrument [Albee et al., 2001]. MEX, which has an ion mass analyzer and an electron spectrometer, lacks a magnetometer [Barabash and Lundin, 2006]. Thus, before MAVEN was successfully inserted into the Martian areocentric elliptic orbit in September of 2014, we did not have a completed survey of particles, fields, and waves in the Mars near-space. Now instruments onboard MAVEN are observing the Martian upper atmosphere and the solar wind region with a higher temporal and spatial resolution to investigate plasma environment around Mars [Jakosky et al., 2015c].

In this section, the following domains of the Martian plasma environment are courtesy: the solar wind, the magnetosheath, the induced magnetosphere, the ionosphere and the crustal magnetic field. Figure 1.4 shows a schematic illustration of these plasma regions and boundaries.

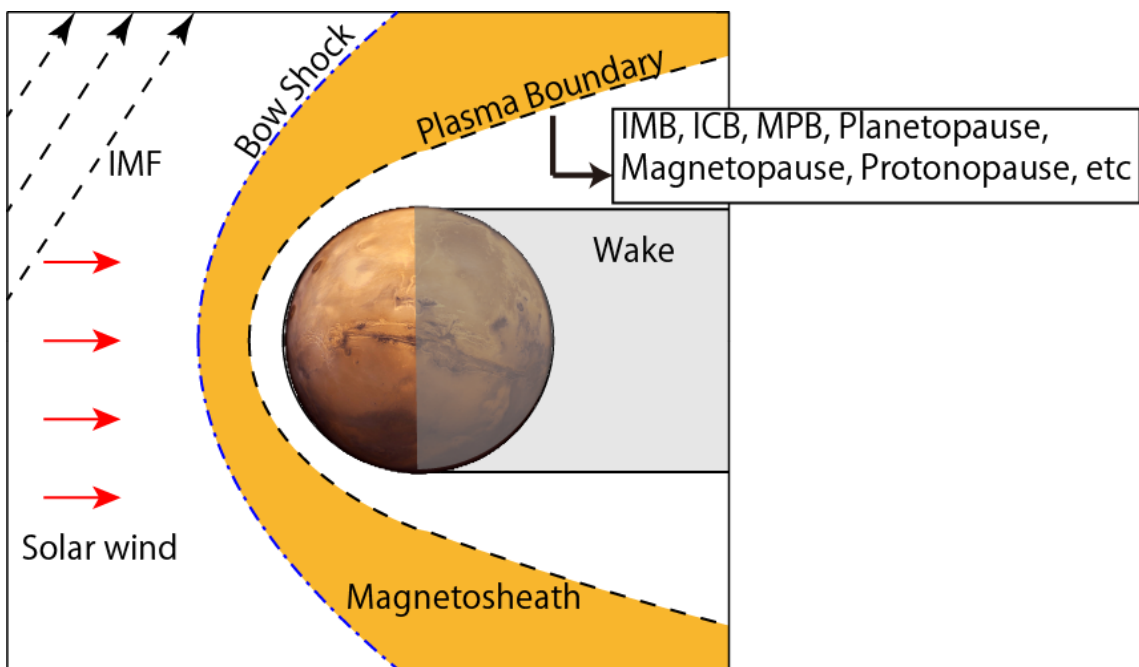


Figure 1.4: Schematic illustration of plasma environment around Mars. Left is sunward. Induced magnetosphere and ionosphere is above the magnetosheath.

### 1.2.1 Solar Wind

The solar wind is a plasma flow, which is emitted outward from the upper atmosphere of the Sun at supersonic speeds. The major ion in the solar wind is a proton ( $H^+$ ). The solar wind also contains alpha particles ( $He^+$ ). The velocity of the solar wind in the inner solar system typically varies from 300 to 800 km/s. The number density of the solar wind decreases with distance from the Sun and is typically  $2.5 \text{ cm}^{-3}$  at the Martian orbit [Dieval *et al.*, 2012]. This magnetic field of Sun is called as the interplanetary magnetic field (IMF), is frozen into the plasma flow and is carried with the solar wind. The rotation of Sun causes the magnetic field lines to bend into a spiral

called the Parker spiral (Figure 1.5). The magnetic field lines have a more radial orientation close to the Sun. The IMF Parker spiral angle at Mars is 57 degrees in average, 45 degrees at Earth, and 37 degrees at Venus [Zhang *et al.*, 2009]. The IMF strength also decreases with the distance from the Sun. Its strength is typically 3.3 nT at the Martian orbit [Blomberg *et al.*, 2003]. The solar wind sometimes has disturbances called corotating interaction regions (CIRs) and coronal mass ejections (CMEs).

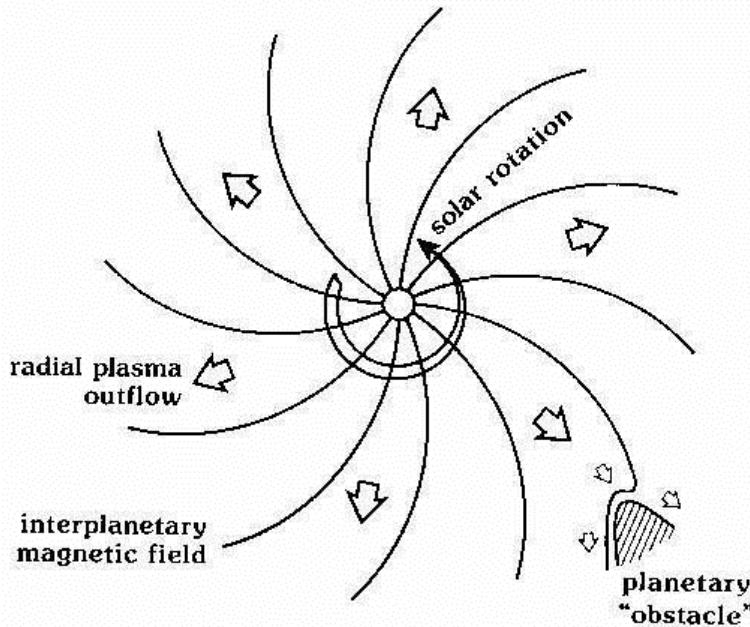


Figure 1.5: The image of the solar wind and the IMF Parker spiral. The Sun rotates anticlockwise and the view is from above the ecliptic plane. Courtesy of NASA

## 1.2.2 Magnetosheath

The solar wind becomes subsonic at the bow shock in front of Mars, or any planets, and the downstream region of the bow shock is called the magnetosheath. The flow

streamlines in the magnetosheath are almost entirely diverted around the obstacle. In the magnetosheath, there are the superthermal electron fluxes and the turbulent solar wind plasma and the magnetic field [e.g., Nagy *et al.*, 2004]. Figure 1.6 shows typical time series of the magnetic field strength and electron data observed by MGS. When the spacecraft passes through the magnetosheath region (Figure 1.6, 08:53-09:26 UT, 09:56-10:19 UT), fluctuations of the magnetic field and high-energy electron fluxes are known to be increased [e.g., Nagy *et al.*, 2004; Trotignon *et al.*, 2006].

Figure 1.7 and Figure 1.8 show the example of distribution maps of electron fluxes (80-100eV) and H<sup>+</sup> number density, observed by MEX ASPERA-3(IMA/ELS), respectively. It seems that the electron fluxes of 80-100 eV and H<sup>+</sup> number density are high in the magnetosheath. Since the solar wind energy and momentum transfer processes is likely to cause ionospheric plasma become energized, the planetary ion escape rate is changed by how far solar wind can penetrate [e.g., Crider *et al.*, 2005; Figure 1.7 and Figure 1.8 show the example of distribution maps of electron fluxes (80-100 eV) and H<sup>+</sup> number density, observed by ASPERA-3(IMA/ELS)/MEX, respectively. It seems that the electron fluxes of 80-100 eV and H<sup>+</sup> number density are high in the magnetosheath. Since the solar wind energy and momentum transfer processes is likely to cause ionospheric plasma become energized, the planetary ion escape rate is changed by how far solar wind can penetrate [e.g., Crider *et al.*, 2005;

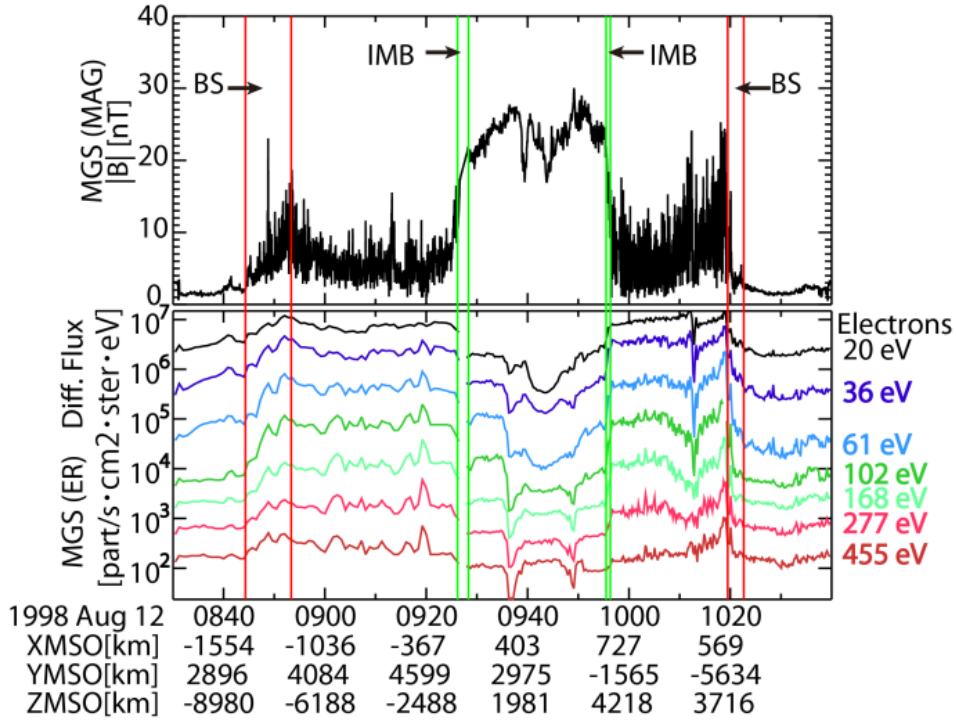


Figure 1.6: Magnitude of the magnetic field and electron data recorded by MAG/MGS and ER experiment during an early elliptical orbit (August 12, 1998) around the periapsis (09:43 UT, altitude 175.1 km). Bow shock (BS) and the induced magnetosphere boundary (IMB) crossing is indicated between two red and green vertical lines, respectively. The upper panels display the Magnitude of the magnetic field. The lower panel depicts electron fluxes for seven energy ranges. The horizontal axis shows both time and the spacecraft coordinates in the Mars-centered solar orbital (MSO) system. This figure is reproduced from *Nagy et al.* [2004].

*Lundin et al.*, 2008b; *Nilsson et al.*, 2010]. The boundary between magnetosheath and induced magnetosphere (induced magnetosphere boundary, IMB) can change significantly depending on the solar wind conditions. Previous studies indicate that the magnetosheath can penetrate into lower altitudes than usual when the solar wind pressure is high [e.g., *Crider et al.*, 2005; *Brain et al.*, 2005; *Matsunaga et al.*, 2015].

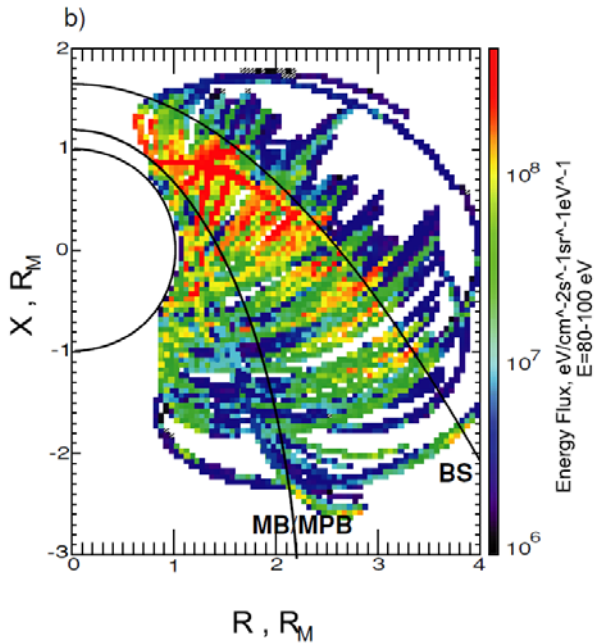


Figure 1.7: The map of electron fluxes with the energy range of 80–100 eV in cylindrical coordinates was observed by ASPERA-3(ELS) along the several orbits. The positions of the bow shock (BS) and the induced magnetospheric boundary (MB) respectively inferred from the MGS and MEX observations are also shown. This figure is adapted from *Dubinin et al.* [2006].

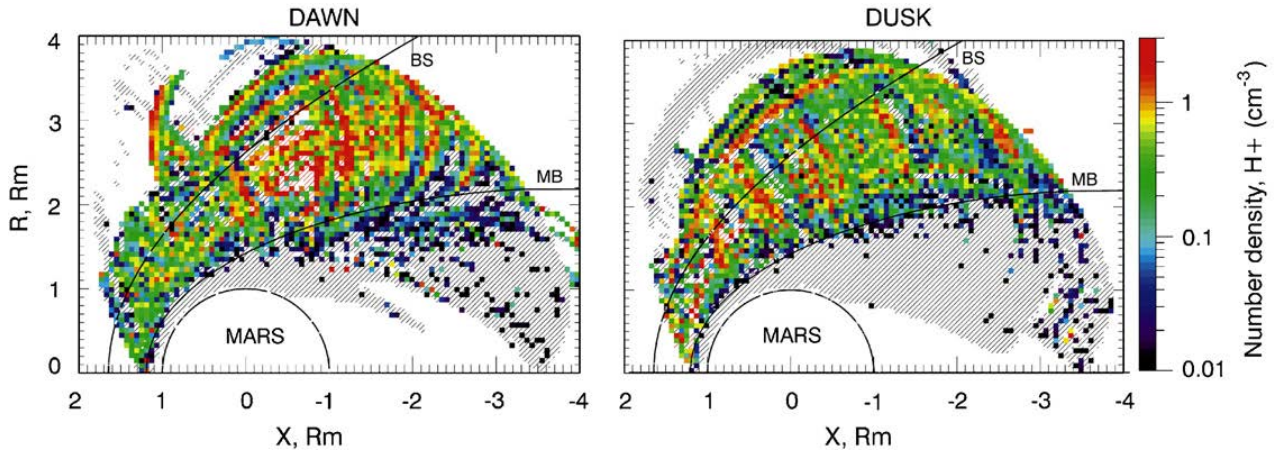


Figure 1.8: These maps of the  $H^+$  number density in cylindrical coordinates were observed by ASPERA-3(IMA) at the dawn and dusk sides from February 2004 to March 2006 (This is not the same time period as on Figure 1.7). The positions of the bow shock (BS) and the induced magnetospheric boundary (MB) respectively inferred from the MGS and MEX observations are also shown. This figure is adapted from *Dubinin et al.* [2008].

Figure 1.7 shows the electron energy spectra were observed by ER/MGS on April 10, 1998 (pre-mapping orbit), and October 30, 2003 (mapping orbit). During pre-mapping orbit (elliptical) periods, MGS was directly able to observe in the magnetosheath. Therefore, right panel of Figure 1.9 shows that the characteristics of electron energy spectra were identified for the various plasma regions. On the other hand, during mapping

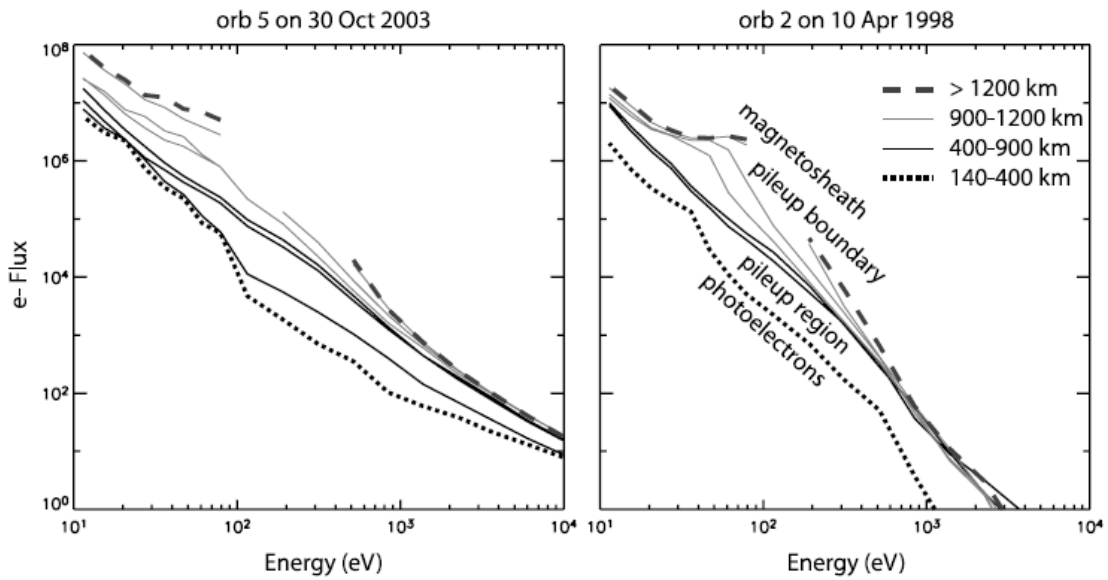


Figure 1.9: Electron spectra were observed by ER on October 30, 2003 (left), and April 10, 1998 (right). The altitude ranges in which the spectra were observed on April 10, 1998 are listed. All the spectra on October 30, 2003 were acquired around 400 km. The gaps in the spectra are from channels in which the dead time correction is too great to report the value. This figure is adapted from *Crider et al.* [2005].

orbit (circular) periods, MGS only observed around 400km altitude, which is usually below the magnetosheath. On October 28 2003, an x-class superflare occurred and released a Coronal Mass Ejection (CME). This CME arrived at Mars on October 30. Left panel of Figure 1.7 shows that the characteristics of electron energy spectra during the passage of CME. That electron energy spectra show MGS passes into the magnetosheath. In other word, the magnetosheath down to around 400 km altitude during the high pressure disturbance, such as CME. In addition, *Brain et al.* [2005] reported the Martian magnetosheath-like electrons were observed in dayside at about 400 km altitudes by MGS. Figure 1.10 shows the sheath-like electron spectra in dayside from MGS data (middle of 1999-February, 2005).

A number of investigators predicted IMB has an asymmetry in the shape [e.g., *Brech and Ferrante*, 1991; *Brech et al.*, 1993; *Harnett and Winglee*, 2003; *Brain et al.*, 2005, 2006a; *Matsunaga et al.*, 2015]. It has been also pointed out that the crustal magnetic fields can locally push the magnetosheath region upward and cause the asymmetric structure of IMB [e.g., *Brain et al.*, 2003, 2005, 2006a; *Matsunaga et al.*, 2015].

In Chapter 3, this thesis focuses on the penetration of magnetosheath plasma down to 400 km altitudes at Mars by using both magnetic field and electron data from MGS

(April, 1999–November, 2006). It shows that the magnetosheath penetration depends on the solar wind dynamic pressure, and the IMF orientation.

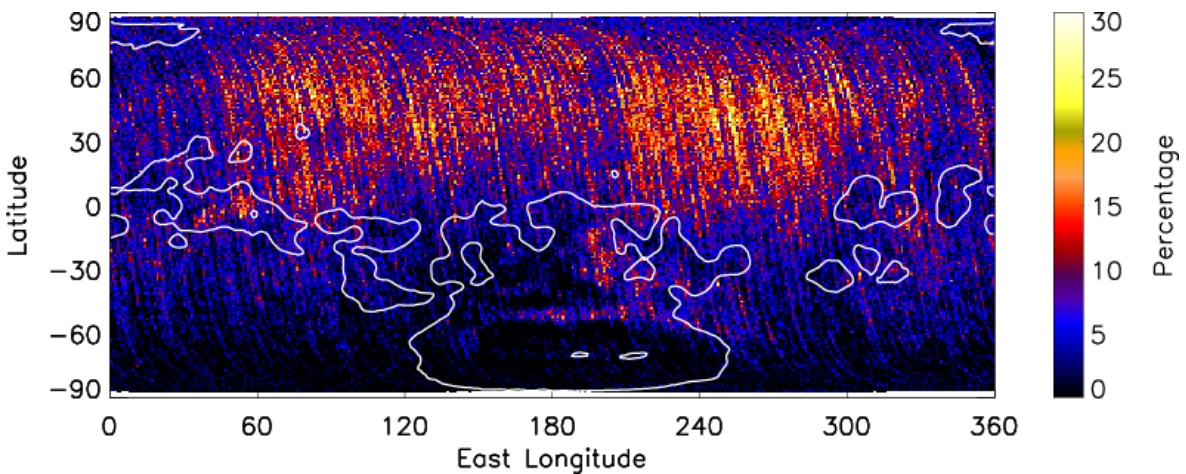


Figure 1.10: Percentage of sheath-like electron spectra in dayside mapping data as a function of geographic location. 20 nT field magnitude contours derived from nightside data are overlaid for reference. This figure is adapted from *Brain et al.* [2005].

### 1.2.3 Induced Magnetosphere

As a magnetosheath flux tube approaches Mars, it is decelerated by mass loading and draped around Mars. It thus forms the region of piled-up magnetic field. This region is referred as the induced magnetosphere, magnetic pile-up region, or magnetic barrier [e.g., *Vignes et al.*, 2000; *Luhmann et al.*, 2004]. In this thesis, the term induced magnetosphere is used. The boundary between the magnetosheath and the induced magnetosphere is called the induced magnetosphere boundary (IMB) as discussed in Subsection 1.3.2.

The magnetic field strength in the induced magnetosphere depends on the altitude and on the solar zenith angle (SZA). The SZA is the angle of the direction of Sun from the vertical direction. The magnetic field strength increases at altitudes at and below the MPB. The strength decreases when the SZA increases at a fixed altitude. The magnitude of induced magnetosphere is approximately 40 nT at a solar zenith angle of 20 degrees which decreases to approximately 25 nT around the terminator [Akalin *et al.*, 2010]. This result shows that the magnetic environment is sensitive to solar conditions [e.g., Vignes *et al.*, 2000].

## 1.2.4 Ionosphere

The Martian ionosphere is a layer of ionized gas. It is directly exposed to the solar wind. The first in situ measurements of the composition of the ionosphere were made by instruments onboard the Viking 1 and 2 entry probes in 1976 [Nier and McElroy, 1977]. These investigations measured altitude profiles from mass spectrometers mounted on the descent aeroshell of CO<sub>2</sub>, N<sub>2</sub>, Ar, O<sub>2</sub>, and NO and inferred the presence of CO. The Neutral Gas and Ion Mass Spectrometer (NGIMS) onboard MAVEN observed neutral gas and ion from its two sources (closed and open) from ~500km to ~125km during deep dip campaigns. Figure 1.11 and Figure 1.12 shows the altitude profile for 8 neutral

densities of CO<sub>2</sub>, Ar, N<sub>2</sub>, O, CO, O<sub>2</sub>, NO, N, and He, and for 22 averaged densities of H<sub>2</sub><sup>+</sup>, H<sub>3</sub><sup>+</sup>, He<sup>+</sup>, O<sup>2+</sup>, C<sup>+</sup>, CH<sup>+</sup>, N<sup>+</sup>, NH<sup>+</sup>, O<sup>+</sup>, OH<sup>+</sup>, H<sub>2</sub>O<sup>+</sup>, H<sub>3</sub>O<sup>+</sup>, N<sub>2</sub><sup>+</sup>/CO<sup>+</sup>, HCO<sup>+</sup>/HOC<sup>+</sup>/N<sub>2</sub>H<sup>+</sup>, NO<sup>+</sup>, HNO<sup>+</sup>, O<sub>2</sub><sup>+</sup>, HO<sub>2</sub><sup>+</sup>, Ar<sup>+</sup>, ArH<sup>+</sup>, CO<sub>2</sub><sup>+</sup>, and OCOH<sup>+</sup> in ionosphere, respectively. The most abundant ion species in the Martian ionosphere is O<sub>2</sub><sup>+</sup> formed by the following photochemical reactions driven in the Martian ionosphere (Equation 1.1-1.5) [e.g., Nagy *et al.*, 2004].

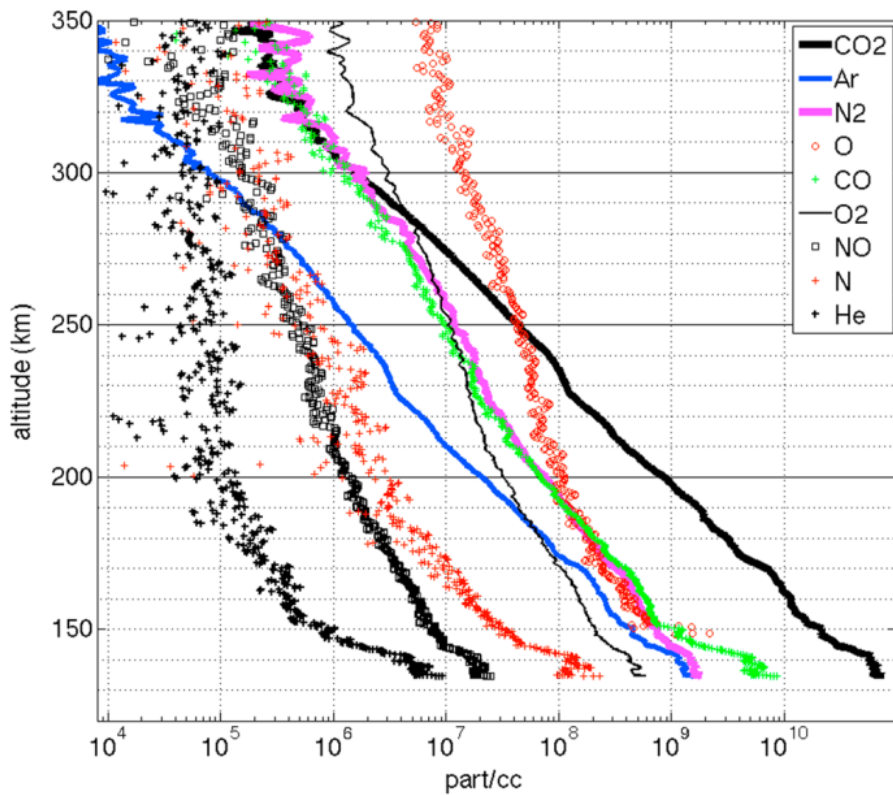


Figure 1.11: Altitude profiles of neutral density measured by NGIMS during a single deep dip pass on orbit No.1064, Ls (Solar Longitude) 256, LST (Local Solar Time) 11:50 A.M., and latitude 4.5°S at periapsis on this orbit. This figure is adapted from Mahaffy *et al.* [2015].

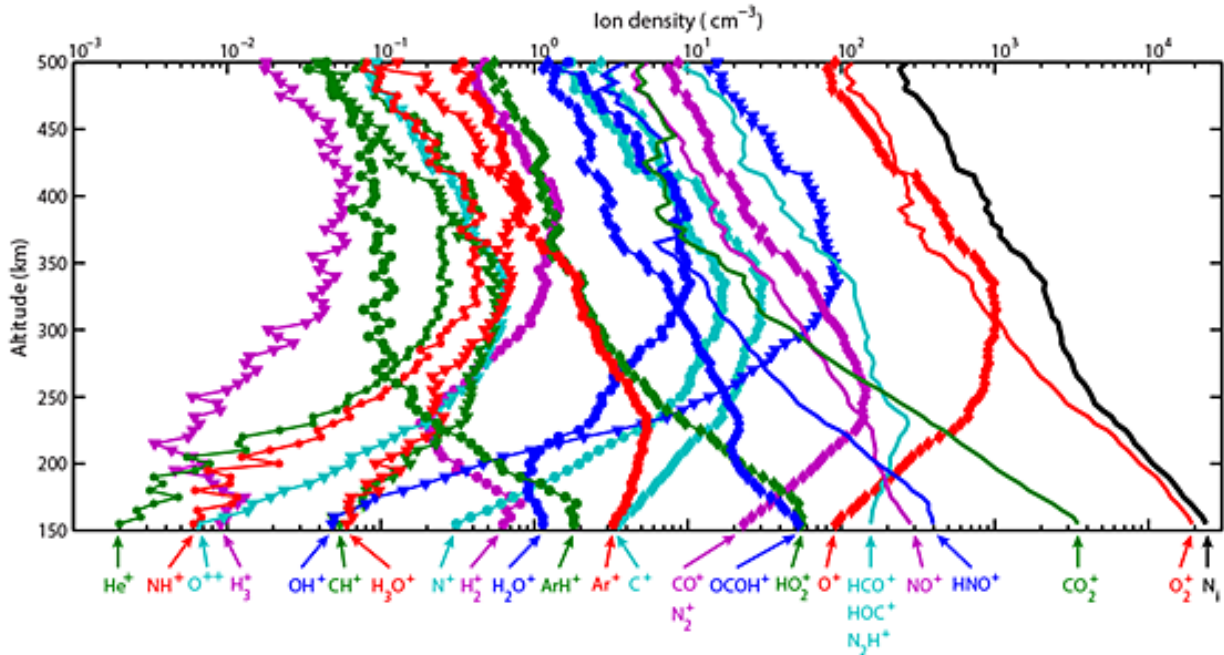
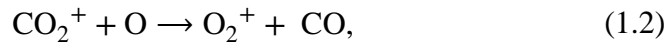
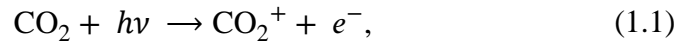


Figure 1.12: Altitude profiles of the averaged density of ionospheric ions measured by NGIMS at  $SZA = 60^\circ$  at altitudes between 150 and 500 km. The vertical profile of the total ion density  $N_i$  is plotted in black. This figure is adapted from *Benna et al.* [2015].



The dissociative recombination is expressed as Equation (1.5).

MEX carries the radar instrument, Mars Advanced Radar for Subsurface and Ionosphere Sounding (MARSIS), to determine local electron density and magnetic field intensity as well as top-side ionospheric electron density profiles [*Gurnett et al.*, 2005;

*Nielsen et al., 2006]. MARSIS observed large density fluctuations in the Martian ionosphere. From Figure 1.13, the electron density measurements observed by MARSIS (top panel) show a persistent level of large fluctuations (04:36-04:50 UT). Gurnett et al. [2010] suggested that candidates of the mechanism that could be generating this turbulence are solar wind pressure perturbations, instability in the magnetosheath plasma, or the Kelvin-Helmholtz instability.*

New results from MAVEN show that ionopause-like density gradients in the Martian ionosphere [Vogt et al., 2015]. Vogt et al. [2015] used NGIMS ion density as a proxy for the electron density and search for an ionopause-like density gradient are in the NGIMS total ion density. They found 84 MAVEN orbit segments (inbound or outbound pass) by using their automated criteria. Figure 1.14 shows some example of ion density profiles with ionopause-like density gradients (red lines). They also investigated the relations between locations of ion density gradients and the effect of crustal magnetic field (See Subsection 1.2.5), and the influence of solar wind drivers from Solar Wind Ion Analyzer (SWIA) (See Subsection 2.2.4). The available evidence does not suggest that the crustal magnetic fields strength or the solar wind dynamic pressure influences the altitude of the ionopause-like density gradients, though these factors both appear to influence the presence or absence of ionopause-like density gradients.

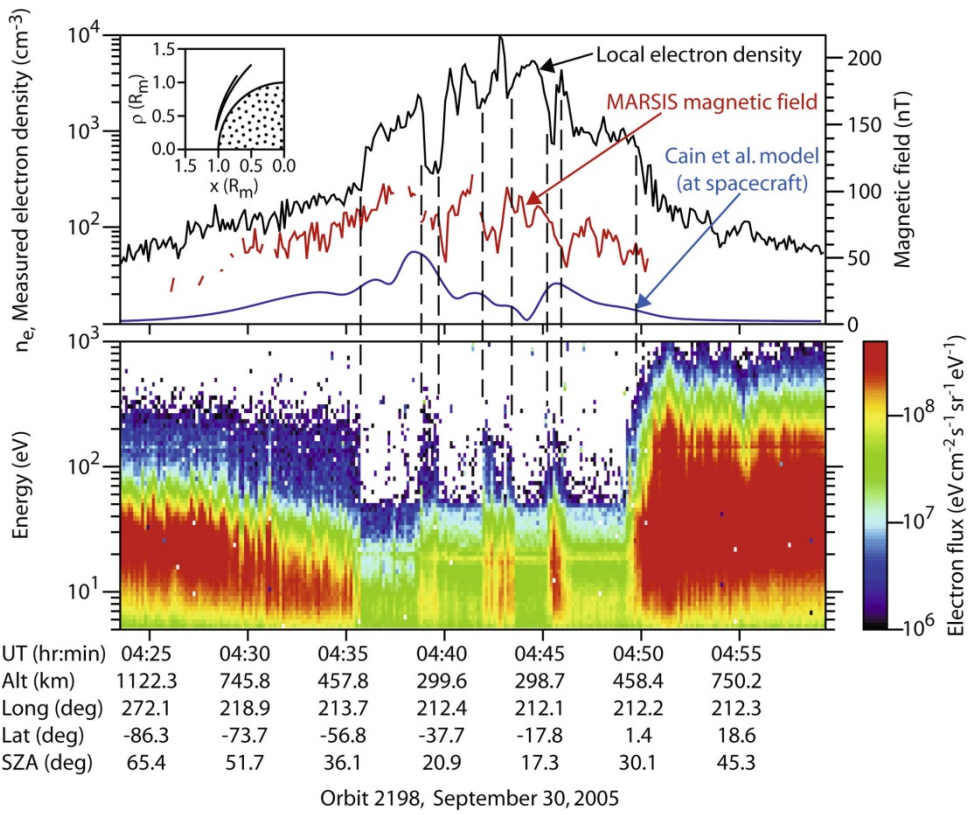


Figure 1.13: The black line in the top panel shows the local electron density obtained from the frequency of locally excited electron plasma oscillations during a typical dayside pass through the Martian ionosphere. The red line shows the local magnetic field strength determined from electron cyclotron echoes [Gurnett *et al.*, 2005], and the blue line shows the crustal magnetic field strength at the spacecraft computed from the model of Cain *et al.* [2003]. The bottom panel shows the corresponding color-coded electron intensity spectrums from the ASPERA-3 (ELS) spectrometer. This figure is adapted from Gurnett *et al.* [2010].

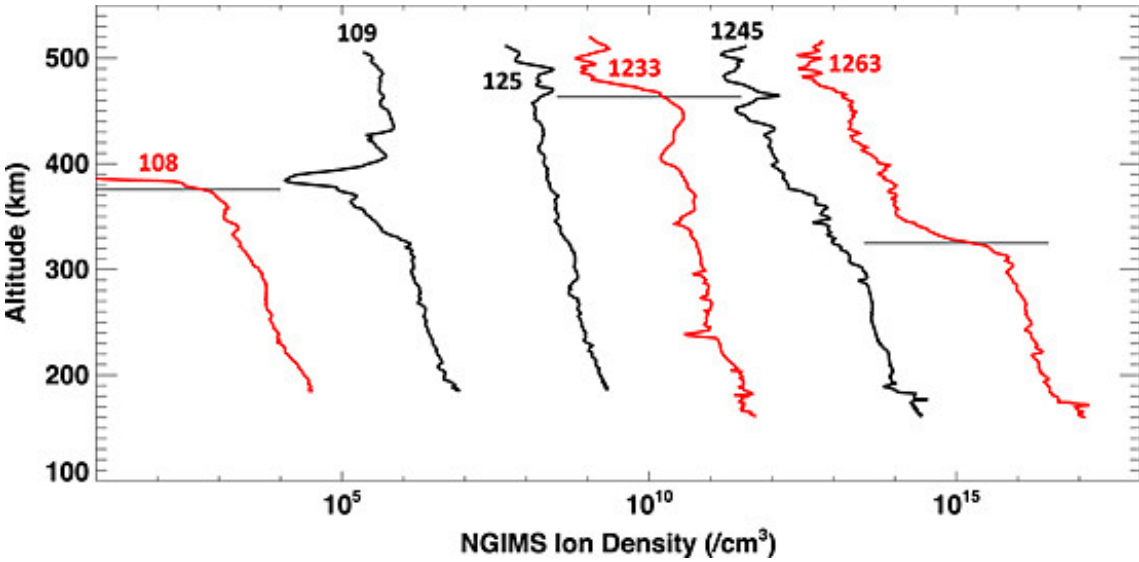


Figure 1.14: NGIMS ion density profiles for six MAVEN orbit segments. Each profile after the far left one has been multiplied by 102 per  $\text{cm}^3$  for clarity. Horizontal lines on the profiles from orbits 108, 1233, and 1263 show the ionopause-like altitude identified by the automated routine from *Vogt et al. [2015]*. Their automated criteria did not identify an ionopause-like in the other three orbits. This figure is adapted from *Vogt et al. [2015]*.

## 1.2.5 The Crustal Magnetic Field

The measurements observed by the magnetometer onboard MGS brought some new, fundamental elements for our understanding of the Mars system. The discovery of the crustal magnetic field [*Acuña et al., 1998, 1999*] shows that Mars has developed at the beginning of its history an intrinsic magnetic field, but that the primitive dynamo rapidly vanished (about 3.7 Gyr ago) [*Chassefière and Leblanc, 2004*]. *Connerney et al. [2005]* provided a new map of the magnetic field of Mars, compiled by using measurements acquired at 400 km mapping altitude by the MGS. Figure 1.15 is a global

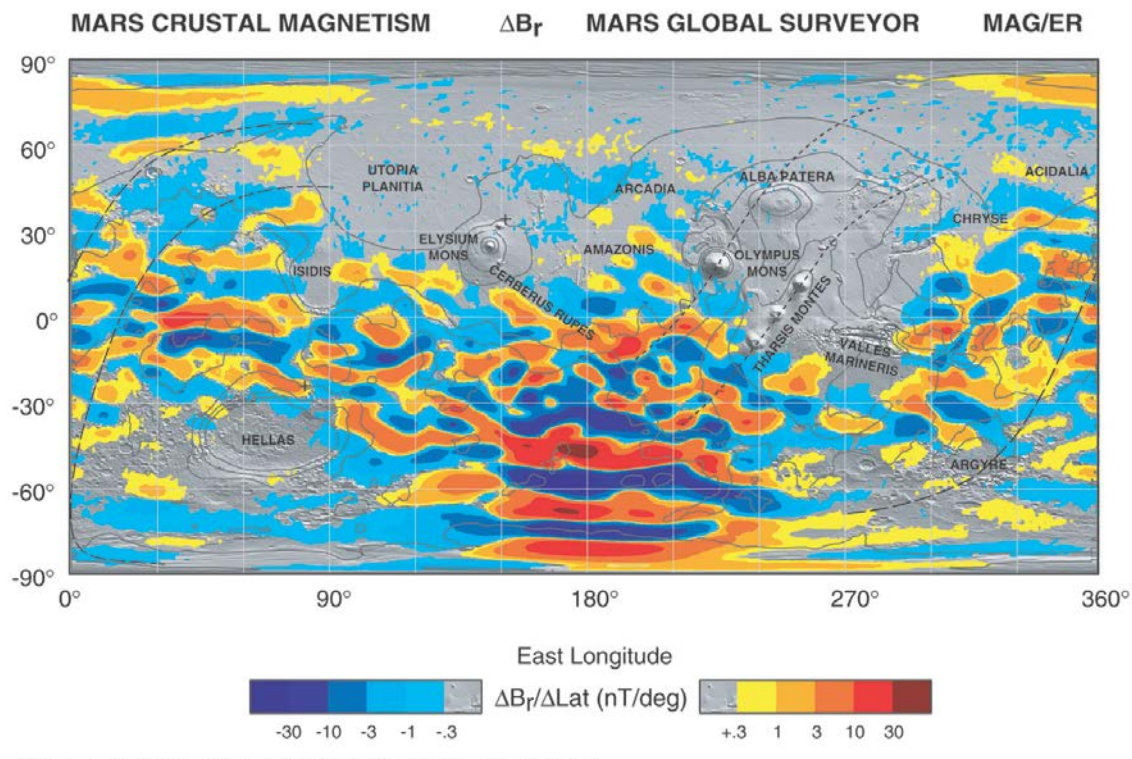
map of the magnetic field with color contoured over two orders of magnitude variation.

As you can see Figure 1.15, the Martian crustal magnetic field mainly exist the southern hemisphere. Especially, one strong magnetic anomaly is distributed from 90 to 240 degrees of east longitudes in the southern hemisphere. *Cain et al.* [2003] creates the global model of the Martian crustal magnetic field based on MGS pre-mapping and mapping orbit data. This model is called as “the Cain model”.

From previous studies, the magnetic anomalies affect the position of the Martian plasma boundaries [e.g., *Brain et al.*, 2005; *Matsunaga et al.*, 2015].

For example, the altitude of MPB was raised because the MPB was pushed by the crustal magnetic field. As a result of the interaction between the Martian crustal magnetic field and the IMF, the complex electromagnetic field structure was formed around Mars. *Lundin et al.* [2011] pointed out that the Martian crustal fields locally make “mini-magnetospheres” and it is suggested that it prevents the Martian atmospheric escape. On the other hand, it is also pointed out that significant amounts of the atmosphere are intermittently being carried away from Mars by flux rope: the top portions of crustal field loops are stretched through interaction with the solar wind and detach via magnetic reconnection [e.g., *Brain et al.*, 2010b]. Since there are conflicting allegations about the role of the Martian crustal magnetic field for the Martian

atmospheric escape, it is still an open question. MAVEN is the first spacecraft that carried all the magnetometer, the ion mass analyzer, and the electron detector to Mars. Therefore, the observation of MAVEN is invaluable in providing new clues to these questions [e.g., Connerney *et al.*, 2015; Brain *et al.*, 2015; Dong *et al.*, 2015; Hara *et al.*, 2015].



Connerney, J. E. P. et al., (2005) Proc. Natl. Acad. Sci. USA, 102, No. 42, 14970-14975.

R1599\_1pub

Figure 1.15: Map of the magnetic field of Mars observed by the MGS at a nominal 400 km altitude. This figure is adapted from Connerney *et al.* [2005].

## 1.3 Plasma Boundaries

As previously mentioned in Section 1.1, the Martian upper atmosphere directly interacts with the solar wind, since Mars does not possess an intrinsic global magnetic field. This interaction forms some plasma boundaries between the magnetosheath and the induced magnetosphere and ionosphere, in which characteristic boundary structures are embedded. It seems that the energy and momentum exchange between the solar wind dominant region and the Martian upper atmosphere occur via some physical mechanisms [e.g., *Luhmann.*, 1990; *Terada et al.*, 2002; *Dubinin et al.*, 2006; *Gurnett et al.*, 2010; *Lundin*, 2011; *Hara et al.*, 2014a, 2014b, 2015; *Matsunaga et al.*, 2015; *Ruhunusiri et al.*, 2016].

In this section, the following plasma boundaries caused by the interaction between the solar wind and the Martian upper atmosphere are described: the bow shock, the induced magnetosphere boundary (IMB), the ion composition boundary (ICB), and the pressure balance boundary.

### 1.3.1 Bow Shock

It is well known that the planetary bow shocks have established that their position, shape and jump conditions are functions of the upstream flow parameters and the nature

of the solar wind-planet interaction by previous studies [e.g., *Russel*, 1977; *Trotignon et al.*, 1993, 2006; *Mazelle et al.*, 2003]. Below the bow shock, the solar wind flow slows down from supersonic to subsonic speed by ion pickup. Ionized Martian neutral species, which by photoionization, by impact with solar wind electrons, or the charge exchange with solar wind ions, accelerate and escape into the solar wind along the solar wind motional electric field. We call this mechanism ion pickup. Figure 1.16 shows the example of bow shock crossing observed by MAVEN.

At the time of bow shock crossing, the kinetic energy of the solar wind is converted into thermal energy. Figure 1.16 shows the heated and turbulent solar wind plasma downstream of the bow shock. The decrease of the solar wind velocity is also shown here.

From many Martian bow shock crossings identified by the Phobos 2 and MGS data, *Trotignon et al.* [2006] investigated the positions and shapes of the bow shock by using curve-fitting techniques. They investigated that energized electrons were observed with a sudden increase in the magnetic field strength and its fluctuations to identify the bow shock crossings. As a result, the subsolar bow shock is typically located at a distance of 1.63 Martian radius ( $R_M = 3,397$  km) from the center of Mars, i.e. at an altitude of 2,140.1 km. On the other hand, the terminator bow shock is typically located at a

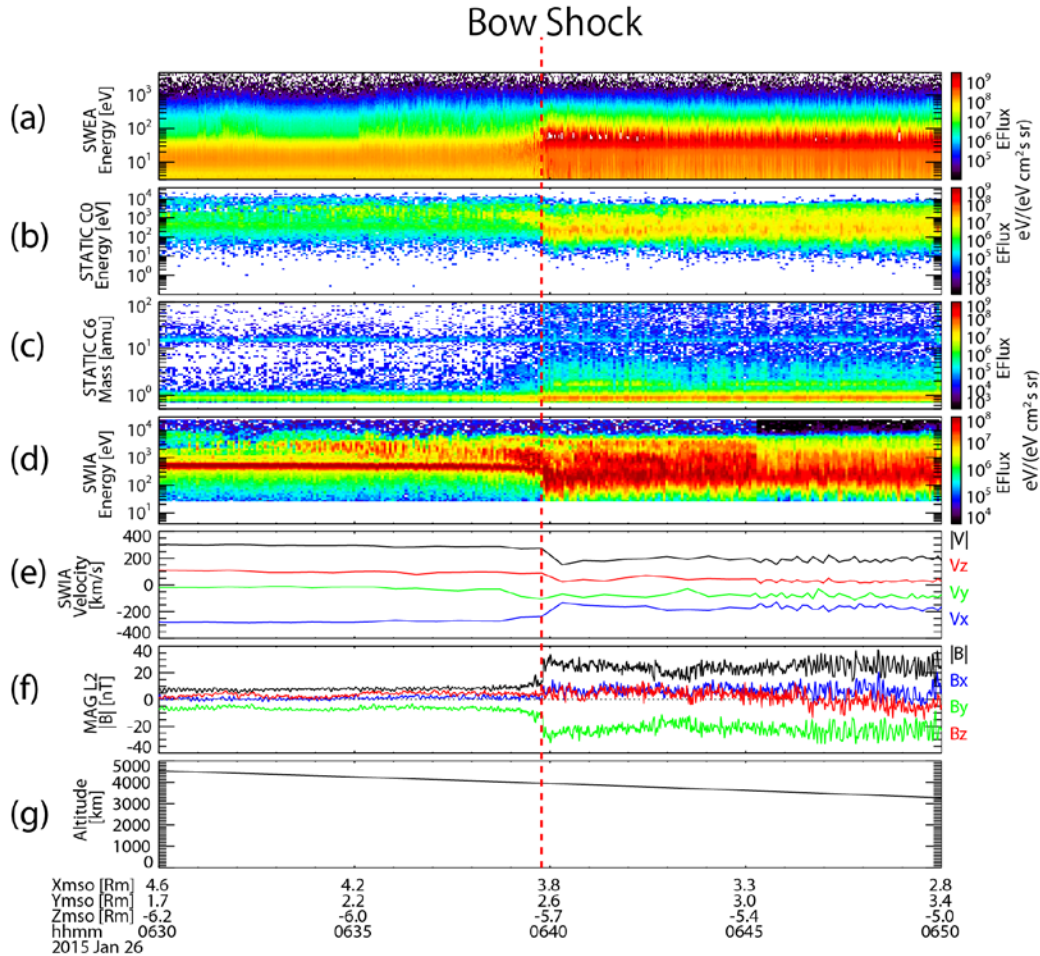


Figure 1.16: Time series plots of bow shock crossing observed by MAVEN. From top to bottom, the panels show (a) SWEA electron energy spectrum, (b) STATIC ion energy spectra, (c) STATIC ion mass spectrum, (d) SWIA ion energy spectrum and (e) SWIA proton velocity, (f) magnetic field observed by MAG, and (g) altitude.

distance of  $2.63 R_M$ , i.e. at an altitude of 5,537.1 km. This paper uses the results of

*Trotignon et al. [2006]* as a location of model bow shock in Chapter 4. Figure 1.17

shows the shape of bow shock from *Trotignon et al. [2006]*.

### 1.3.2 Induced Magnetosphere Boundary (IMB) and Magnetic Pile-up Boundary (MPB)

The boundary between the magnetosheath and the induced magnetosphere or the magnetic pile-up region has several observational characteristics by different

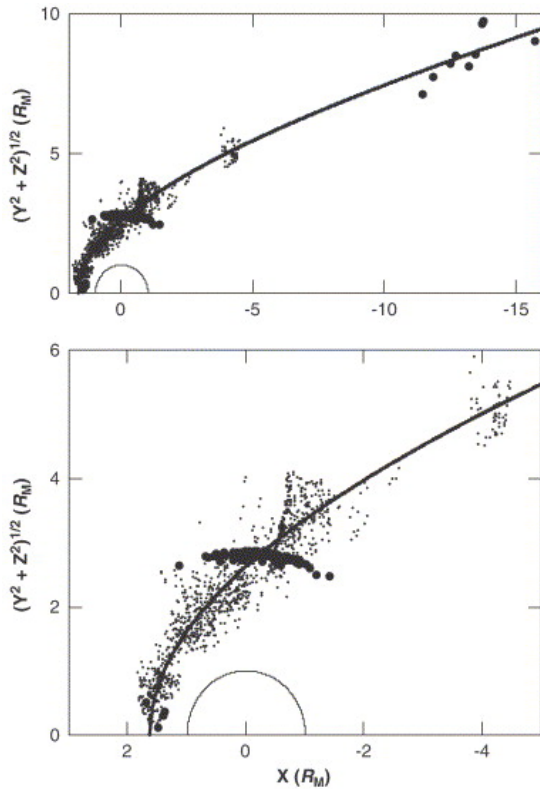


Fig. 1.17 Martian bow shock boundary crossed by Phobos 2 (127 large dots) and MGS (573 small dots) along with the inferred off-centre model (solid line) in cylindrical coordinates. The bottom panel zooms in on the closest part to the planet. This Figure is adapted from *Trotignon et al.* [2006].

instruments on various spacecraft. One feature is an enhancement of electron flux coincident with a sharp increase in magnetic field strength and a decrease in field

fluctuations, which was observed by Phobos-2 [e.g., *Riedler et al.*, 1989; *Trotignon et al.*, 1996, 2006], MGS [e.g., *Vignes et al.*, 2000; *Crider et al.*, 2002; *Bertucci et al.*, 2005; *Brain et al.*, 2005; *Trotignon et al.*, 2006; *Matsunaga et al.*, 2015], and also MAVEN [e.g., *Jakosky et al.*, 2015a, 2015b; *Connerney et al.*, 2015; *Halekas et al.*, 2015]. Based on these observations, this boundary has many names; the magnetopause [e.g. *Lundin et al.*, 1989], the planetopause [Riedler et al., 1989], the protonopause [Sauer et al., 1994], the magnetic pile-up boundary (MPB) [e.g. *Trotignon et al.*, 1996, 2006], and the induced magnetosphere boundary (IMB) [e.g. *Dubinin et al.*, 2006]. Another feature of this boundary is a change of ion composition from solar wind ions (mainly H<sup>+</sup>) to planetary heavy ions (ex. O<sup>+</sup>, O<sub>2</sub><sup>+</sup>, CO<sup>2+</sup>). It will be mentioned it in Subsection 1.3.3.

MPB is basically named by MGS observations. Therefore, this thesis uses MPB in Chapter 3, which is the study by using MGS data. On the other hand, this thesis uses IMB in other chapters because the identification method of IMB is different to Chapter 3. However, please note that MPB and IMB indicate the same boundary in this thesis.

Investigation of *Trotignon et al.* [2006] discussed the positions and shapes of IMB as well as the case of bow shock (See Subsection 1.3.1). The IMB crossings in *Trotignon et al.* [2006] are identified in the MGS data by three simultaneous signatures: a more or

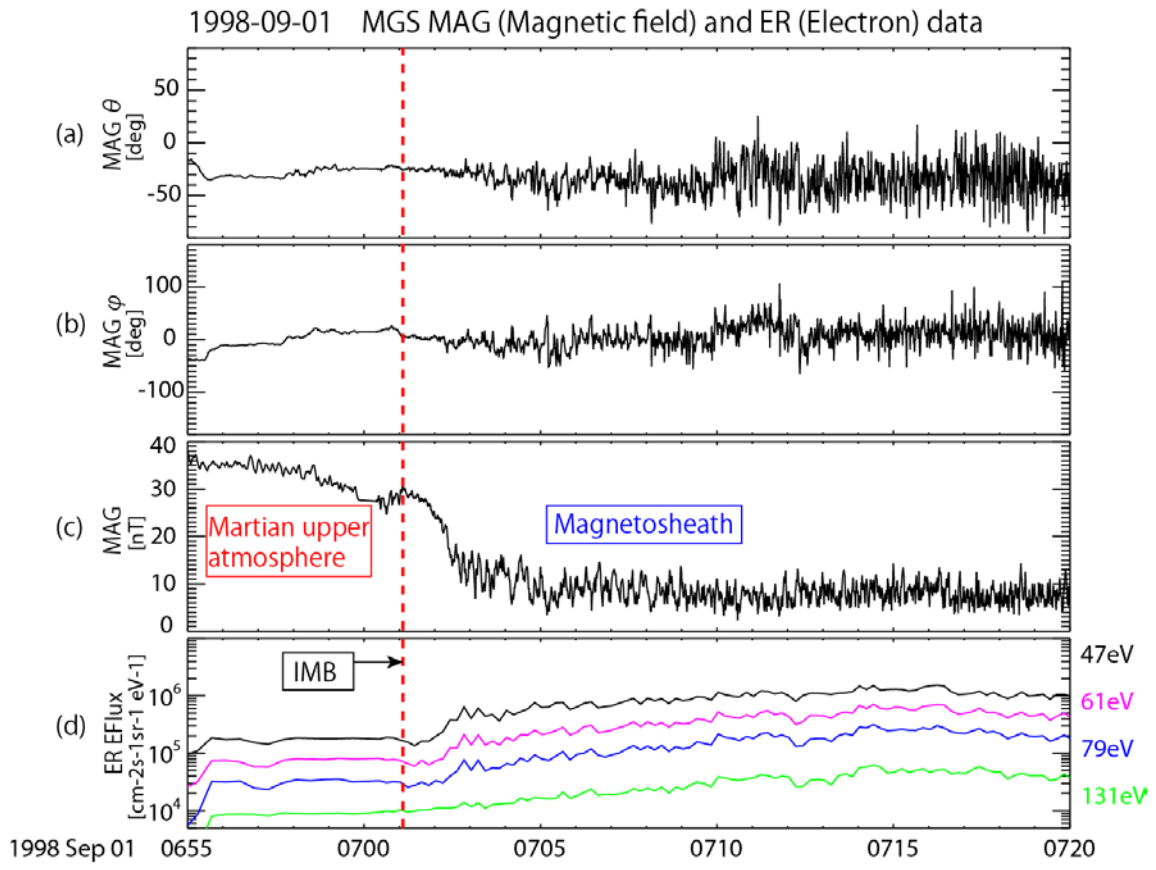


Figure 1.18: Induced Magnetosphere Boundary (IMB) observed by MAG/ER onboard MGS: (a) The elevation angle (b) the azimuth angle,(c) the magnitude of magnetic field, and (d) the electron fluxes for four energy ranges. The red lines show IMB crossing. This figure is reproduced from *Trotignon et al.* [2006].

less sharp increase of the magnetic field magnitude, a correlated reduction of the electron fluxes for energy greater than 10 eV, and a decrease in the fluctuations of the magnetic field (Figure 1.18). As a result, the subsolar IMB is typically located at a distance of  $1.25 R_M$  from the center of Mars, i.e., at an altitude of 849.3 km. On the other hand terminator IMB is typically located at a distance of  $1.44 R_M$ , i.e. at an altitude of 1,494.7 km. This paper uses the results of *Trotignon et al.* [2006] as a

location of model IMB location in Chapter 4. Figure 1.19 shows the shape of IMB from *Trotignon et al.* [2006] and Table 1.2 shows the previous results about IMB locations.

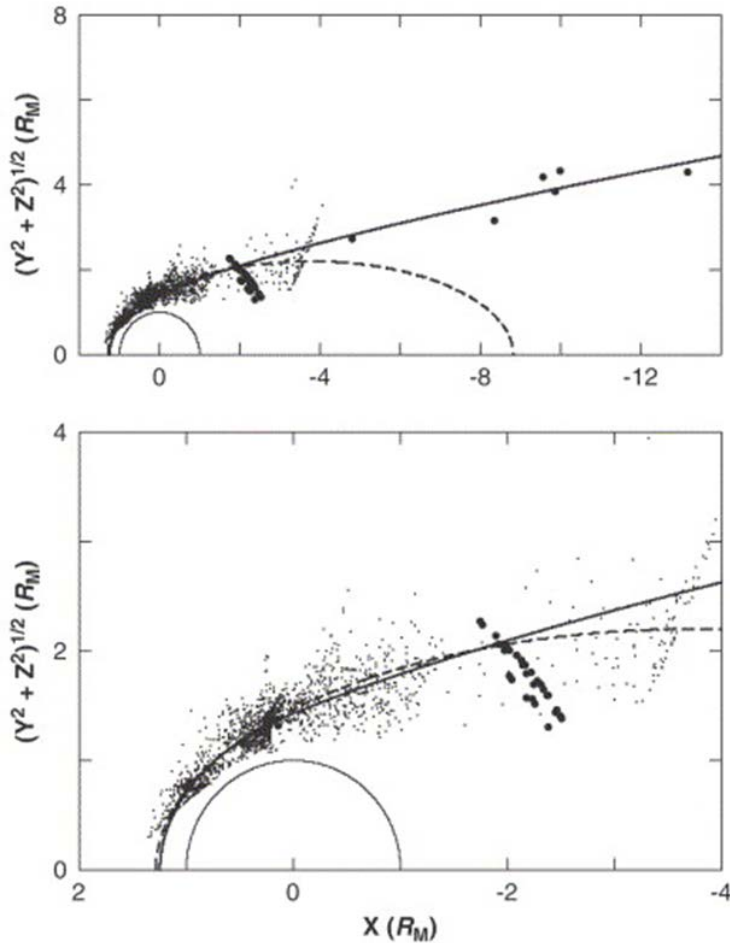


Figure 1.19: Positions of the induced magnetosphere boundary (IMB) of Mars crossed by Phobos 2 (41 large dots) and MGS (860 small dots) along with models derived from curve fitting techniques. Single conic sections are used for modelling the MPB boundary from the Phobos 2 measurements alone (dotted line), the MGS observations alone (dashed line), and the Phobos 2 and MGS combined data set (continuous line). The format is same as Figure 1.17. This Figure is adapted from *Trotignon et al.* [2006].

Table 1.2 Summary of previous results about IMB locations.

Study of IMB	Mission name	Number of crossings	Sub solar [Rm]	Terminator [Rm]
Vignes et al. [2000]	MGS	488	$1.29 \pm 0.04$	$1.47 \pm 0.08$
Trotignon et al. [1996]	Phobos-2	37	$1.19 \pm 0.07$	$1.38 \pm 0.09$
Trotignon et al. [2006]	Phobos-2 and MGS	901	$1.25 \pm 0.03$	$1.44 \pm 0.03$

### 1.3.3 Ion Composition Boundary (ICB)

As mentioned in Subsection 1.3.2, a signature of ion composition changing due to the mass loading process (See Subsection 1.4.1) in the boundary was observed by Phobos 2. We called this boundary the ion composition boundary (ICB). ICB forms in that spatial region where the number density of the heavy ions becomes comparable to the solar wind density (mainly  $H^+$ ) [Sauer et al., 1994].

Figure 1.20 shows the ratio of the  $O^+$  to  $H^+$  observed by Phobos-2 ASPERA. At the beginning of this figure, this ratio is about 10-50 %. Finally,  $O^+$  ions became the dominant component near the ICB (in Figure 1.20, it is represented by the word planetopause, PP) where the proton disappear. The relative locations of ICB by using the long term data, such as the study of Trotignon et al. [2006], have not known yet.

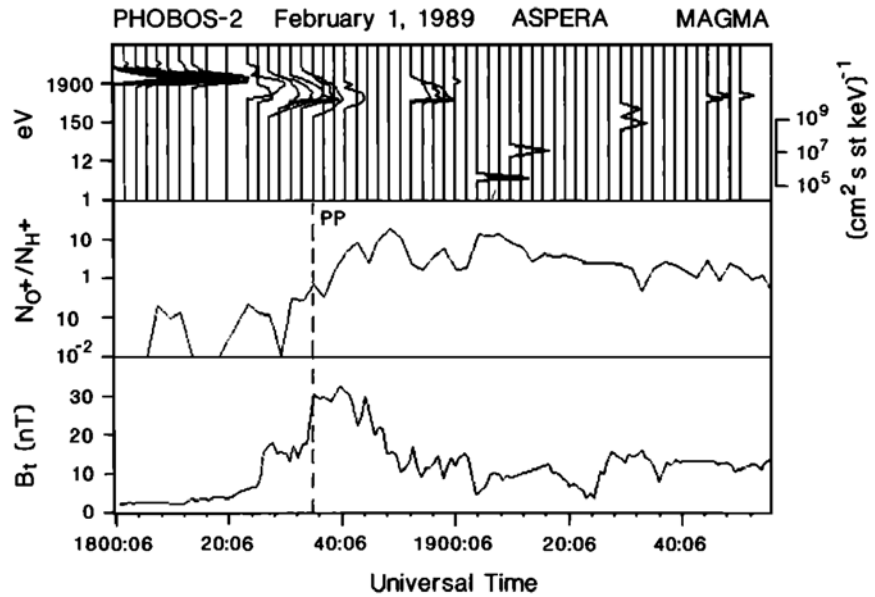


Figure 1.20: ASPERA and MAGMA experiment data from elliptical orbit of Phobos 2. The top panel shows the energy per charge spectra for the ions (the flux scale for the horizontal axis is given on the right), the center panel shows the ratio of the oxygen ion to hydrogen ion densities, and the bottom panel shows the time series of the magnetic field magnitude. The dashed vertical line marks the location defined as the ‘planetpause’ by *Lundin et al.* [1989], however, as the ion composition boundary (ICB) by *Breus et al.* [1991]. This figure is adapted from *Breus et al.* [1991].

### 1.3.4 Pressure Balance Boundary

Around the Martian plasma environment, the solar wind dynamic pressure, the thermal pressure and the magnetic pressure are the components of the total plasma pressure [Zhang *et al.*, 1991; Crider *et al.*, 2003]. However, due to the lack of continuous simultaneous observations of the ion, electron, and magnetic field near Mars, we have not understood the plasma pressure environment around Mars yet. Some MHD, multifluid MHD, and hybrid simulations have been developed to investigate the Martian

plasma environment, including the plasma pressure [e.g., *Simon et al.*, 2007; *Brain et al.*, 2010a; *Fang et al.*, 2015; *Xu et al.*, 2016]. Figure 1.21 shows the simulation model results from *Brain et al.* [2010a]. In Figure 1.21, the solar wind dynamic pressure is the dominant component in upstream from the shock, the thermal pressure is the dominant component in the magnetosheath, and the magnetic and thermal pressure are the dominant components near the planet. However, a current multifluid MHD simulation showed that the dynamic pressure is also important in the magnetosheath region (Figure 1.22) [*Xu et al.*, 2016]. *Xu et al.* [2016] investigated the parameter,  $\beta^*$  ( $\beta^* = (P_{th} + P_{dyn}) / P_B$ , the plasma thermal pressure ( $P_{th}$ ), the dynamic pressure ( $P_{dyn}$ ), and the magnetic pressure ( $P_B$ )) to understand the plasma pressure balance boundary, where  $\beta^* = 1$ . From the result of *Xu et al.* [2016], the plasma boundary has tail lobes signature and a larger extent.

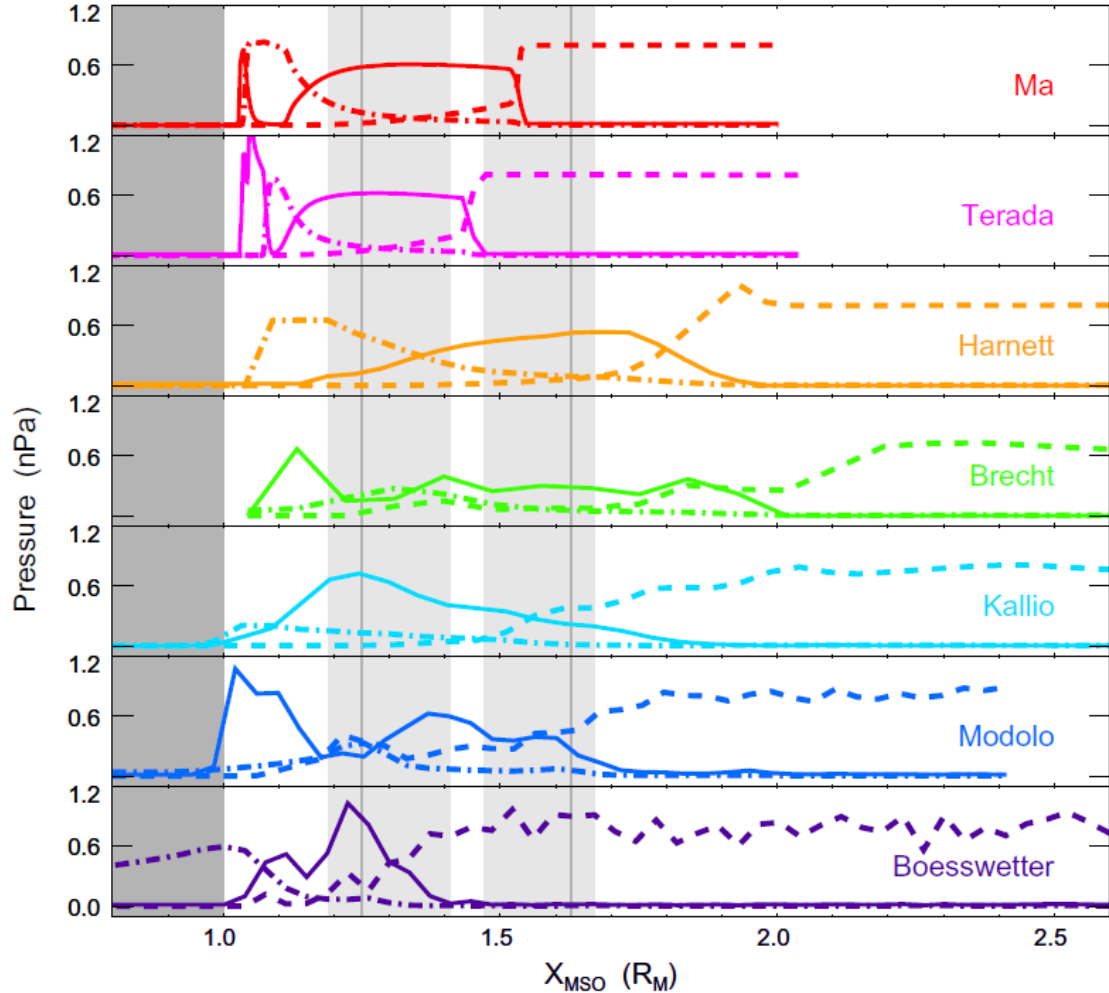


Figure 1.21: Pressure profiles for the seven models (MHD (Ma, Terada), multi-fluid (Harnett), hybrid (Brecht, Kallio, Modoro, Boesswetter)). Solid lines indicate plasma thermal pressure, dashed lines indicate dynamic pressure, and dot-dashed lines indicate magnetic pressure. The darker shaded area denotes regions interior to the planet. The best-fit MPB and bow shock derived in *Trotignon et al.* [2006] are indicated by vertical gray lines, and the ranges of best-fit boundary locations based on all previously published work are indicated by the light gray shaded areas. This figure is adapted from *Brain et al.* [2010a].

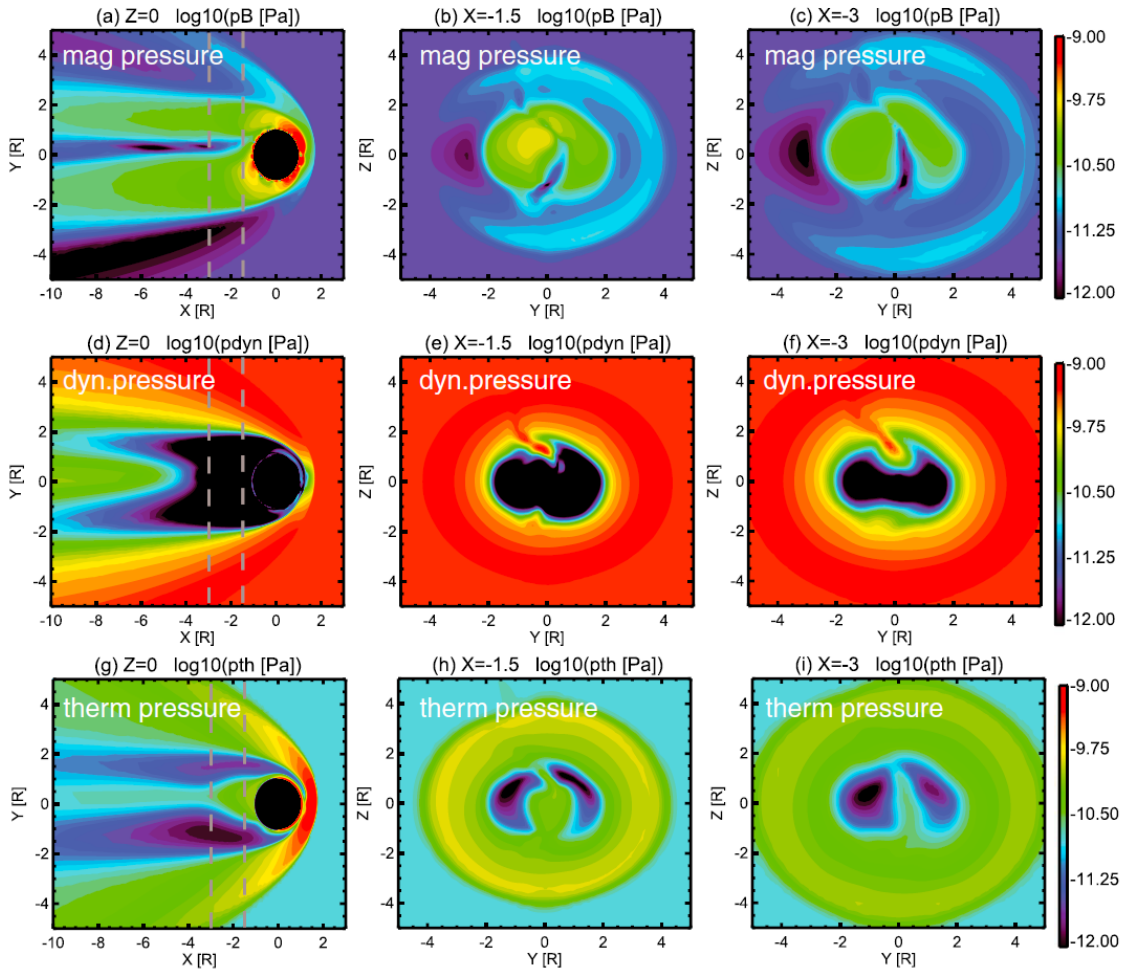


Figure 1.22: The simulation results of (a–c) the magnetic pressure, (d–f) the dynamic pressure, and (g–i) the thermal pressure. The planar cuts at (a, d, g)  $Z = 0$ , (b, e, h)  $X = -1.5R_M$ , and (c, f, i)  $X = -3R_M$  in MSO coordinates. The two vertical dashed lines in the first column mark the positions of the two X slices in the second and third columns. This figure is adapted from Xu *et al.* [2016].

## 1.4 Related Physical Mechanisms

As described above, the direct interaction between the solar wind and the Martian upper atmosphere causes some plasma boundaries. In and around the plasma boundary, there are many physical mechanisms occur. The following subsections describe some related physical mechanisms to the Martian plasma boundaries: the ion pickup, the mass loading process, the Kelvin-Helmholtz instability, the magnetic reconnection, and the cold ion outflow.

### 1.4.1 Ion Pickup and Mass Loading Process

Heavy ions generated by ionization from the Martian neutral atmosphere are accelerated by the solar wind motional electric field. These heavy ions can be captured in the IMF and get into the solar wind or magnetosheath. We call this process ion pickup. Ion pickup process is a very important atmospheric escape process on an unmagnetized planet, such as Mars and Venus. Phobos-2, MEX, and MAVEN have detected a large outflow of planetary heavy ions due to this process [e.g., *Lundin et al.*, 1989, 2004, 2008a; *Barabash et al.*, 2007; *Brain et al.*, 2015; *Dong et al.*, 2015]. Figure 1.23 shows the flow of the solar wind and the penetration of pickup ion into the solar wind.

The solar wind is mainly composed of hydrogen. When pickup heavy ions penetrate into the solar wind, velocity is decreased. We call it mass loading process. The effect of mass loading process makes the transition regions where the ion composition changes from solar wind proton dominant to planetary heavy ion dominant. A sudden drop of the magnitude of the magnetic field also appeared due to the deflection and piled up the IMF [e.g., Breus *et al.*, 1989; Dubinin and Lundin, 1995]. Therefore, it is assumed that some plasma boundaries (e.g., ICB, IMB) are formed by mass loading.

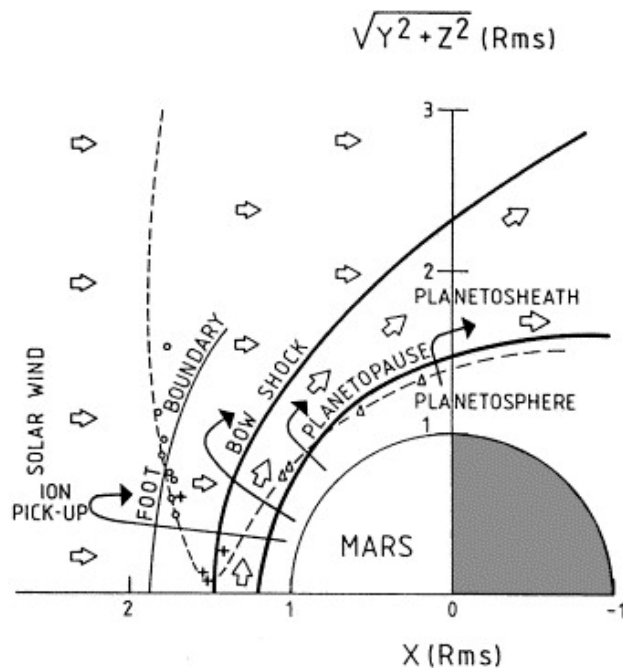


Figure 1.23: Cartoon of penetration of pickup ion to the solar wind is represented as black arrows. This figure is adapted from *Trotignon et al.* [2001].

### 1.4.2 Kelvin-Helmholtz Instability

When two flow or medium in motion adjoin with each other, the velocity shear layer is formed in the boundary region. It is well known that this velocity shear boundary becomes unstable with disturbances. This instability is called Kelvin-Helmholtz instability (KHI) [e.g., *Fujimoto and Terasawa*, 1994]. KHI is expected to play an important role of transporting energy, mass, and momentum exchange from the magnetosheath to the Martian upper atmosphere. Since the mixing layer has a finite thickness between them, this layer has a potential for the removal of a huge amount of ions from Mars through its history.

The velocity shear boundary with KHI exists and is observed at anyplace, for example astronomical phenomena, Earth's atmosphere and magnetopause, and plasma boundaries around planets [e.g., *Price and Rosswog*, 2006; *Hasegawa et al.*, 2006; *Berne et al.*, 2010; *Casanova et al.*, 2011; *Delamere, et al.*, 2013; *Ruhunusiri, et al.*, 2016; *Eriksson et al.*, 2016]. In case of the planetary plasma physics, some spacecraft recently observed KHI vortex or vortex-like signature [e.g., *Hasegawa et al.*, 2006; *Delamere, et al.*, 2013; *Ruhunusiri, et al.*, 2016; *Eriksson et al.*, 2016]. Figure 1.24 shows signatures of KHI at Earth's magnetopause. Some MHD or global hybrid simulation are successful in reproducing a variety of observed features and the

development of vortex-like flow perturbation which is occurred by the KHI [e.g., Fujimoto and Terasawa, 1995; Terada et al., 2002; Takagi et al., 2006; Seki et al., submitted]. Figure 1.25 shows the relations between ion density and velocity observed by MAVEN and obtained in the MHD simulation with our new model. Moreover, Figure 1.26 shows MAVEN observed KHI vortex-like signature at the induced magnetosphere.

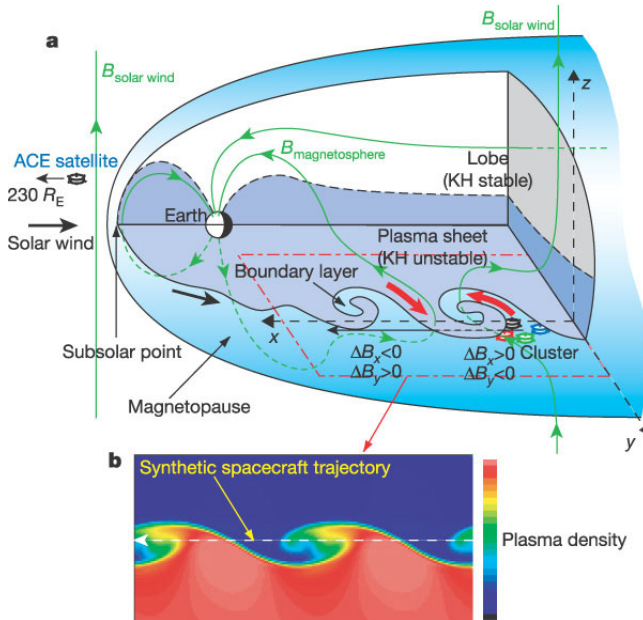


Figure 1.24: Three-dimensional (3D) cutaway view of Earth's magnetosphere, showing signatures of Kelvin Helmholtz instability (KHI). (a) View of the magnetosphere, showing the KHI vortices at the duskside of magnetopause. This figure is adapted from Hasegawa et al. [2004].

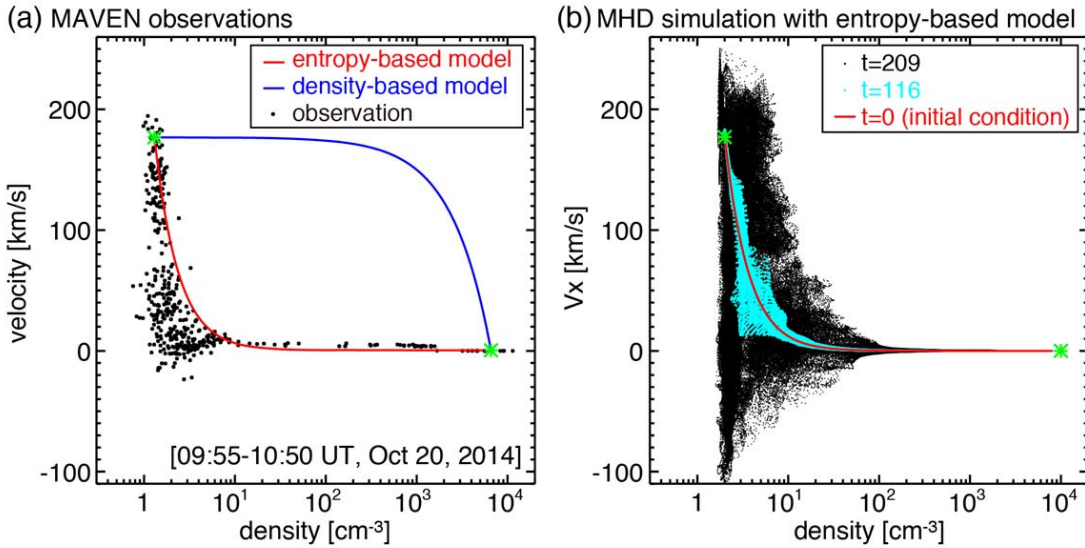


Figure 1.25: Relations between ion density and velocity (a) observed in the large-density gradient boundary by MAVEN and (b) obtained in the MHD simulation with the entropy-based model as the initial condition. In the panel (a), black dots show the MAVEN observation. In the panel (b), light blue and black dots indicate different time evolution stages, i.e.,  $t=116$  (linear stage of the KHI development) and  $209$  (non-linear stage), respectively. This figure is adapted from *Seki et al.* [submitted].

### 1.4.3 Magnetic Reconnection

Magnetic reconnection is one of the fundamental plasma phenomena in the universe.

It seems to occur in a lot of space plasma phenomena: magnetic merging at the dayside magnetopause of Earth [e.g., *Burch and Phan*, 2016] and other planets [e.g., *Brain et al.*, 2010b], magnetotails of the Earth [e.g., *Angelopoulos et al.*, 2008] and other planets [e.g., *Harada et al.*, 2016], and solar flares [e.g., *Tsuneta* 1996]. Magnetic reconnection rearranges the topology of magnetic field and converts magnetic energy into the particle energy. This energy conversion makes plasma particles be accelerated and heated. As a

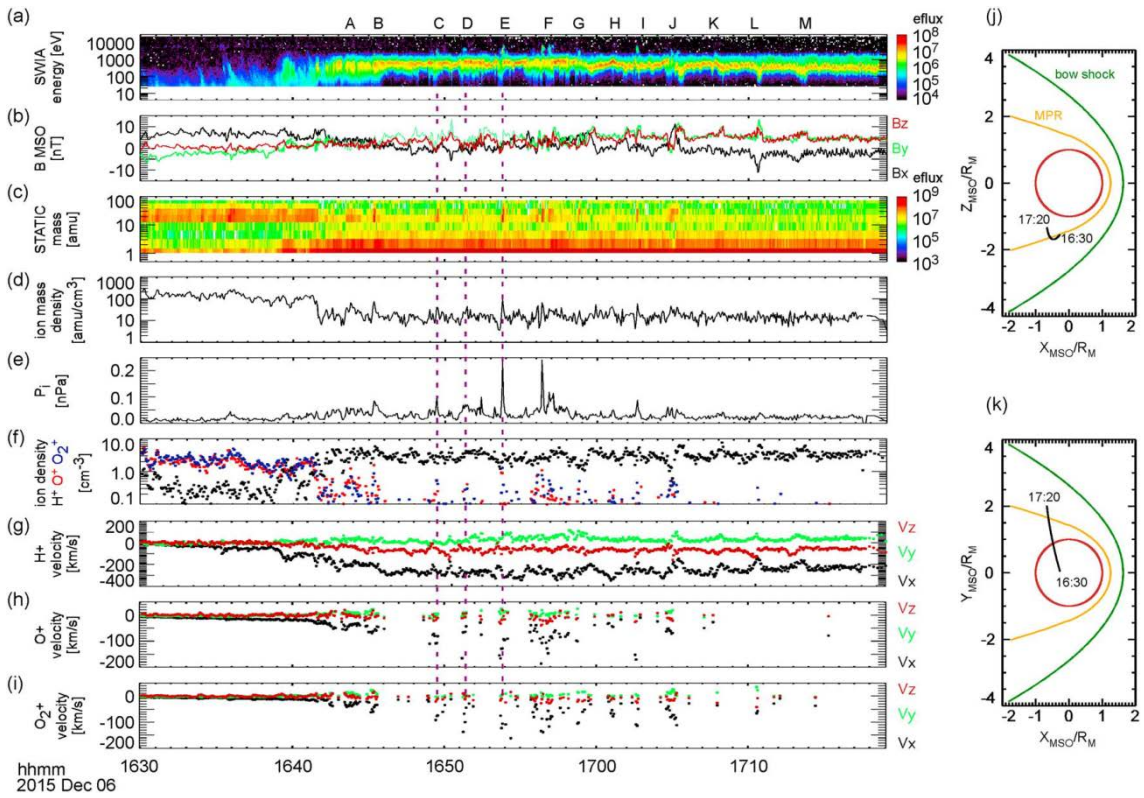


Figure 1.26: Boundary oscillations are observed by MAVEN. (a) SWIA energy spectrum displays periodic reductions in ion energy marked by A-M (b) Magnetometer observed magnetic field perturbations associated with these boundary oscillations. (c) STATIC mass spectrum shows that the boundary oscillations are characterized by periodic encounters of heavy ions. (d) Ion mass density from STATIC. (e) Ion pressure from STATIC  $P_i$  is the total pressure. (f) Ion densities for the dominant species, namely  $H^+$ ,  $O^+$ , and  $O_2^+$ . (g-i) Ion velocities for  $H^+$ ,  $O^+$ , and  $O_2^+$ , respectively, in MSO coordinates. (j and k) MAVEN orbit plots in MSO coordinates. This figure is adapted from Ruhunusiri *et al.* [2016].

result of the magnetic reconnection, magnetic flux rope can be formed [e.g., Russell and Elphic, 1979; Vignes *et al.*, 2004]. Magnetic flux rope is force-free (or almost force-free) and has twisted rope-like magnetic structures.

In the case of Mars, previous studies reported magnetic reconnection between the interplanetary magnetic field lines and/or crustal field lines and the magnetic flux ropes observed by MGS and MAVEN [e.g., *Halekas et al.*, 2009; *Brain et al.*, 2010b; *Hara et al.*, 2014a, 2014b, 2015, 2016; *Harada et al.*, 2015]. Magnetic flux rope around Mars interacts with planetary and interplanetary charged particles, and can transport large volumes of plasma. Thus, flux rope plays an important role in ion escape process at Mars. Figure 1.27 shows the sketch of detached flux rope from the crustal magnetic field.

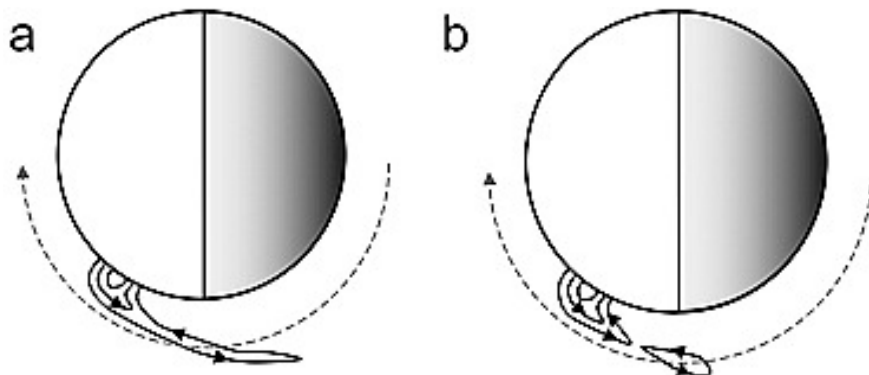


Figure 1.27: Sketch of possible magnetic reconnection and detached flux rope formation scenario between the Martian crustal magnetic fields. This figure is adapted from *Brain et al.* [2010b].

#### 1.4.4 Cold Ion Outflow

In May 2007, ASPERA-3 ion mass analyzer (IMA) changed its energy settings. The new energy range of IMA covered from ~10-100 eV in order to investigate the cold ion outflow from the Martian upper atmosphere [*Lundin et al.*, 2008a]. The observation of

MEX showed that the escape rate of cold ion outflow correlates with the distance from the Martian surface. The escape rate of cold ( $< 200$  eV) heavy ions ( $O^+$ ,  $O_2^+$ ,  $CO_2^+$ ) is about  $3.3 \times 10^{24} \text{ s}^{-1}$  in the solar minimum [Lundin *et al.*, 2008a]. Barabash *et al.* [2007] reported the escape rates of  $O^+$ ,  $O_2^+$ , and  $CO_2^+$  estimated to be  $1.6 \times 10^{23}$ ,  $1.5 \times 10^{23} \text{ s}^{-1}$ , and  $8.0 \times 10^{22} \text{ s}^{-1}$  by using MEX observations, respectively, and with energies from 30 eV to 30 keV. Brain *et al.* [2015] reported a lower bound estimate for the escape rate:  $\sim 3 \times 10^{24} \text{ s}^{-1}$  for energies  $> 25$  eV by using MAVEN observations. Therefore, cold ion outflow can significantly contribute to atmospheric escape from Mars. Figure 1.28 shows that the cold ion outflow is in the tail.

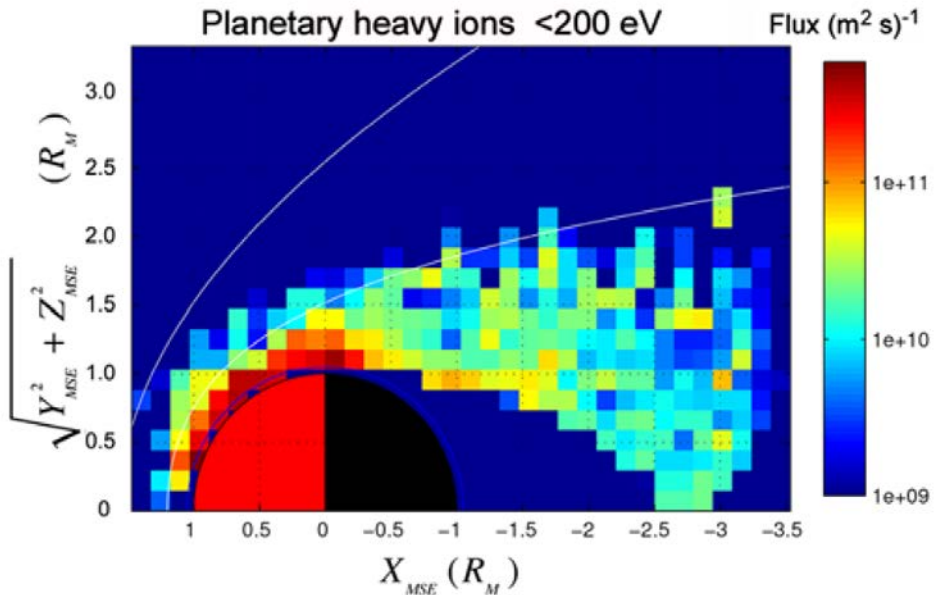


Figure 1.28: Cold ( $< 200$  eV) planetary heavy ion ( $O^+$ ,  $O_2^+$ ,  $CO_2^+$ ) fluxes observed by MEX ASEPERA-3/IMA near Mars. This figure is adapted from Lundin *et al.* [2008a].

## **1.5 Objectives of This Thesis**

Direct interaction between the solar wind and the Martian upper atmosphere forms a characteristic transition region. At surfaces of such region, energy, particle, and momentum transportation between the solar wind and the Martian upper atmosphere plasmas could occur through some physical processes, plasma instabilities, or perturbations. As previously mentioned in Section 1.2 and 1.3, the morphology of the Martian plasma boundary is still not known well due to the limitation of spacecraft's orbits and the lack of continuous simultaneous measurements of the ion composition, electron, and magnetic field before Mars Atmosphere and Volatile EvolutioN mission (MAVEN).

The main objectives of this thesis are to investigate the characteristics of plasma boundaries between the magnetosheath and the Martian upper atmosphere, as well as the dependences of plasma boundaries on solar wind parameters, and on the crustal magnetic field. In order to understand the differences and/or similarities of the plasma boundaries and to obtain insight into the physics and the morphology of them, this thesis is based on in-situ continuous and simultaneous observations of ion, electron, and magnetic field data acquired by the current and previous Martian spacecraft missions, including Mars Global Surveyor (MGS) from 1997–2006 for NASA, and MAVEN

mission from 2014-present for NASA. This thesis has primarily utilized ion (STATIC/MAVEN, SWIA/MAVEN), electron (ER/MGS and SWEA/MAVEN), and magnetic field (MAG/MGS and MAG/ MAVEN) data.

Chapter 2 provides overview of the instrumentation on board MGS, MAVEN, and Advanced Composition Explorer (ACE) data which were used in this thesis.

Chapter 3 focuses on the magnetic pile-up boundary (MPB, same as the induced magnetosphere boundary) and its dependence of the solar wind condition and the crustal magnetic field based on MGS and ACE observations. Time period is from April 1999 to November 2006. Chapter 3 statistically investigates MPB which is the penetration boundary of the magnetosheath into the Martian upper atmosphere. MPB typically locate above 800km, however the magnetosheath occasionally penetrates into low altitudes below 400 km. This thesis identified 1,145 magnetosheath penetration events and found that both the solar wind dynamic pressure ( $P_{dyn}$ ) and the orientation of the interplanetary magnetic field (IMF) control the occurrence of the magnetosheath penetration events. The magnetosheath penetration events during the relatively low  $P_{dyn}$  periods ( $P_{dyn} \leq 100$  nT  $\sim 4$  nPa) tend to be distributed in low latitudes of the northern hemisphere or where the crustal magnetic field is weak. While the event locations are widely distributed in terms of the latitude during the relatively high  $P_{dyn}$  periods ( $P_{dyn} >$

100 nT). During low  $P_{dyn}$  periods, a remarkable feature is that the observational probability is approximately 2.4 times larger during periods of the away IMF sector of the parker spiral structure in the solar wind than during the toward sector. The northern hemisphere during the away sector corresponds to the upward electric field hemisphere due to the convection of the draping solar wind originating from magnetic flux tubes. These results thus indicate that the magnetosheath penetrations into Martian upper atmosphere occur more often in the upward electric field hemisphere than the downward hemisphere during low  $P_{dyn}$  periods. Large-amplitude undulation excited by the Kelvin-Helmholtz instability in the upward electric field hemisphere is a candidate process to cause the asymmetric penetration during low  $P_{dyn}$  periods. Another possibility might be the mirror-mode instability by the asymmetric distribution of planetary pickup ions.

Chapter 4 focuses on the induced magnetosphere boundary (IMB), the ion composition boundary (ICB), and the pressure balance boundary and their dependences of the solar wind condition, and the crustal magnetic field based on MAVEN observation. Chapter 4 statistically investigates of IMB, ICB, and the pressure balance boundary based on  $\beta^*$  ( $\beta^* = (P_T + P_D) / P_B$ , the plasma thermal pressure ( $P_T$ ), the dynamic pressure ( $P_D$ ), and the magnetic pressure ( $P_B$ )) from November, 2014 to March, 2015 and from June, 2015

to October, 2015. In these two periods, MAVEN directly observed the upstream solar wind region and estimated the solar wind parameters. Chapter 4 also investigates relative locations of IMB, ICB, and  $\beta^*$  boundary (location of  $\beta^* = 1$ ) as well as their dependence on solar wind parameters by using the ions, electron, and magnetic field data from MAVEN. This thesis conducted a statistical analysis for two periods from November, 2014 to March, 2015 and from June, 2015 to October, 2015, when MAVEN orbital configuration allows direct measurements of the solar wind near its apoapsis. This thesis developed an automated algorithm to identify IMB, ICB, and  $\beta^*$  boundary. This thesis identified IMB with criteria combining the time derivative of electron flux, strength of the high frequency ( $> 0.1\text{Hz}$ ) magnetic field fluctuation. As for ICB identification, this thesis used the density ratio between the planetary heavy ions ( $\text{O}^+$  and  $\text{O}_2^+$ ) and the solar wind protons ( $\text{H}^+$ ). Results show there is a north-south asymmetry in locations of all boundaries in MSO coordinates. The locations of all boundaries are affected by  $P_{dyn}$  as well as by the crustal magnetic field. IMB and ICB tend to locate at the similar positions in the dayside. On the other hand, IMB tends to locate at higher altitude than ICB in the nightside. When the solar wind induced electric field is downward, IMB and ICB tend to locate at higher altitudes in the nightside of the southern hemisphere. Observations indicated that the crustal magnetic field seems to

have a permanent effect to raise the boundary altitude in the nightside. In addition, it is suggested that the mass loading process is dominant to form all boundaries in the dayside. Particularly, combination of the crustal magnetic field and the downward electric field can raise the location of ICB upward than usual and higher than IMB in the nightside. Candidate physical mechanism is enhanced cold ions outflow in the mini-magnetosphere via the magnetic reconnection.

In Chapter 5, the results are summarized with respect to the Martian plasma boundaries derived from MGS and MAVEN measurements. This chapter concludes with the Martian global plasma structures and their dependences of the solar wind conditions, and the crustal magnetic field.



# **Chapter 2**

## **Instrumentations and Data Sets**

This thesis uses the data of three spacecraft, Mars Global Surveyor (MGS), Advanced Composition Explorer (ACE), and Mars Atmosphere and Volatile EvolutioN (MAVEN) in order to investigate the Martian plasma boundaries.

### **2.1 Mars Global Surveyor (MGS)**

#### **2.1.1 Overview**

The Mars Global Surveyor (MGS) spacecraft was launched by NASA on November, 1996 and inserted into orbit around Mars on September, 1997. Firstly, MGS started to the elliptical orbit (periapsis altitude is 263km, apoapsis altitude is 54,026km) after orbit insertion. The mission team tried to start the aerobraking phase in order to decrease its speed and attain the low circular-mapping orbit (378 km) [Albee *et al.*, 2001]. However,

## CHAPTER 2. INSTRUMENTATIONS AND DATA SETS

damages to a solar panel were found during the elliptical orbit. Therefore, they repeated using aerobraking and stopping it in 1.5 Earth years (Pre-mapping orbit). During pre-mapping orbit, MGS observed the solar wind region and the Martian magnetosheath. Finally, on March 9, 1999, MGS had slowly circularized through aerobraking to a sunsynchronous, near-polar orbit with an average altitude of 378 km (Mapping orbit). Figure 2.1 shows the variation of MGS's orbit. The mapping orbit is fixed in the local time at 2 am/pm, and the spacecraft orbital period is roughly two hours [Albee *et al.*, 2001]. The MGS mission continued until the mission team lost its signal on November 2, 2006. Figure 2.2 is the overview of the MGS spacecraft.

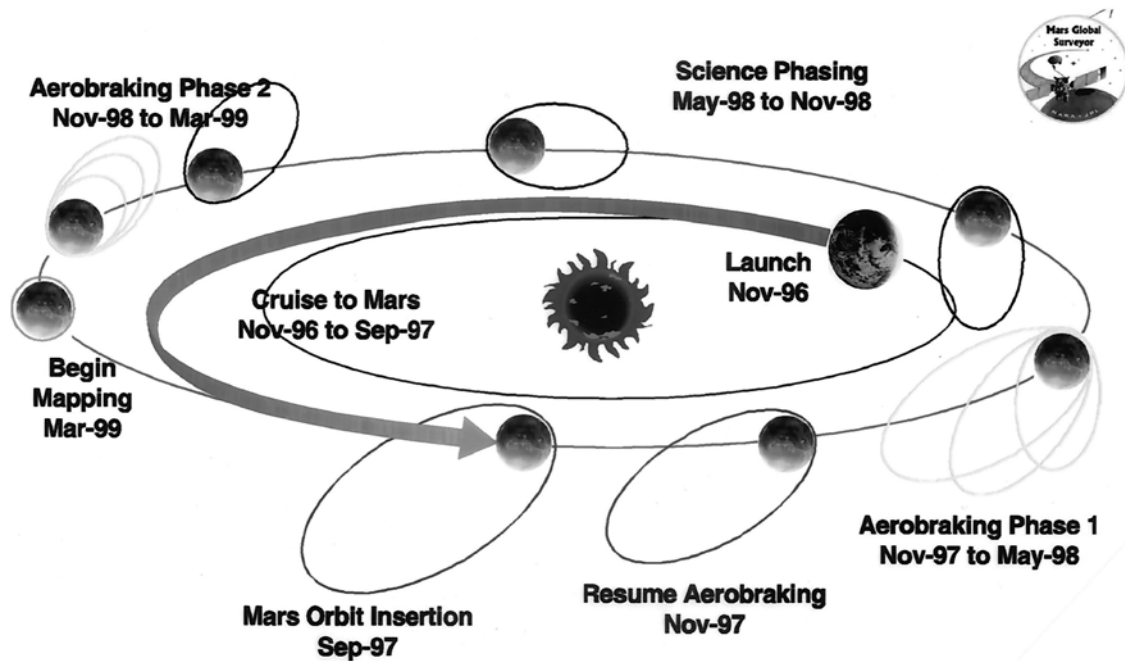


Figure 2.1: Summary of the MGS mission phases from launch to Mars orbit insertion in an elliptical orbit, initial aerobraking period, science-phasing period, aerobraking resumption, and mapping in the circular orbit. This figure is adapted from Albee *et al.* [2001].

## CHAPTER 2. INSTRUMENTAIONS AND DATA SETS

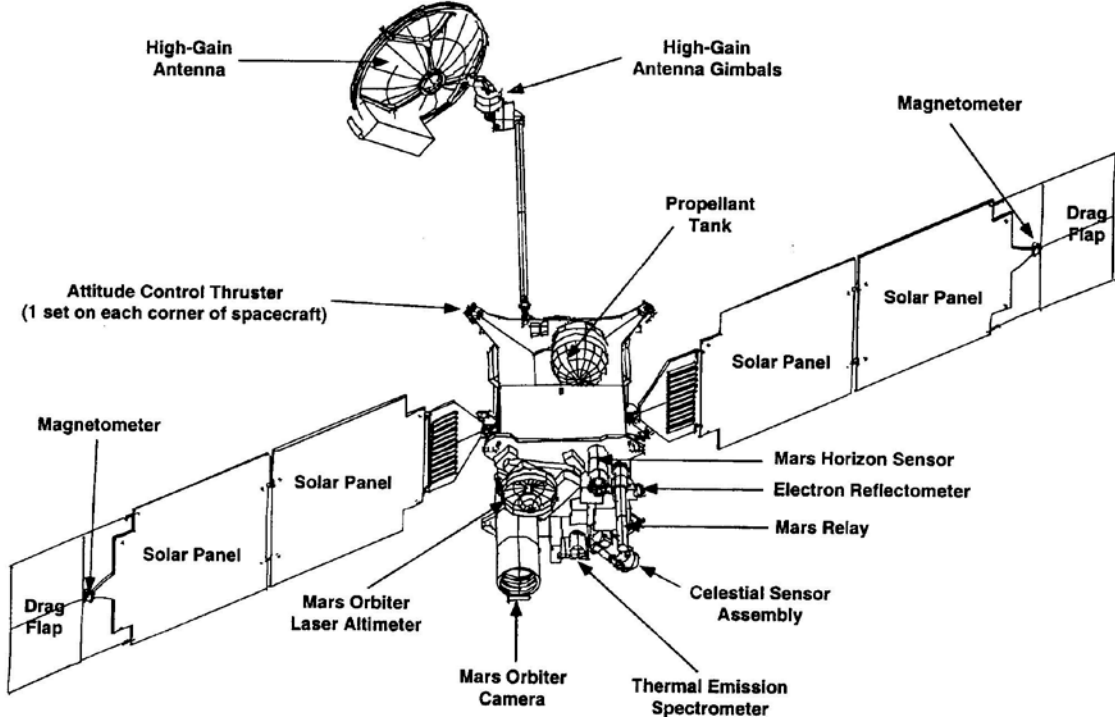


Figure 2.2: Overview of the MGS spacecraft showing major components and instruments. This figure is adapted from *Albee et al.* [2001].

### 2.1.2 Magnetometer (MAG/MGS) and Electron Reflectometer (ER)

MGS carried the magnetometer (MAG/MGS), and the electron reflectometer (ER) sensors in order to investigate the existence and characteristics of the global magnetic field, and to characterize surface magnetic features [*Acuña et al.*, 1992]. MAG/MGS consists of two redundant tri-axial fluxgate magnetometers. They provided 3 dimensional magnetic field data with the time resolution of 0.75-3 seconds, the range of 1-65,536 nT, and a digital resolution of 12 bits. Each magnetometer sensor is located at

## CHAPTER 2. INSTRUMENTATIONS AND DATA SETS

the outer edge of the articulated solar panels (5 m from the center of the spacecraft bus) in order to reduce interference by spacecraft-generated magnetic fields. The ER instrument measured electrons in the range of about 10 eV to 20 keV with time resolution of 12-48 seconds and energy resolution of  $\Delta E/E \sim 25\%$  [Mitchell *et al.*, 2001; Albee *et al.*, 2001]. The figure 2.3 is the overview of the MAG/ER instruments.

In order to determine if a spacecraft passes the magnetosheath region, it is necessary to compare the data of the magnetic field and the electrons. MGS is the first spacecraft which observed the Martian plasma environment with the help of a magnetometer and an electron reflectometer at the same time. Thus, firstly this thesis uses the MAG/MGS and ER data to investigate the magnetosheath penetration (See Chapter 3).

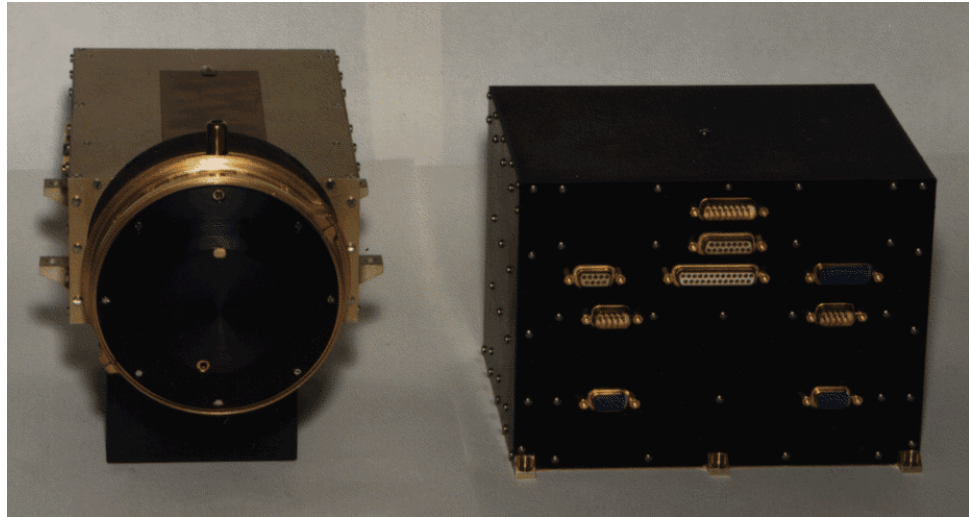


Figure 2.3: Overview of the magnetometer (MAG/MGS) (right), and the electron reflectometer (ER) (left). Courtesy of NASA

### 2.1.3 Proxies of the Solar Wind Parameters

As mentioned above, MGS did not observe in the solar wind region or the magnetosheath during its mapping orbit phase. However, from previous studies, we can get proxies of the upstream solar wind dynamic pressure ( $P_{dyn}$ ) and the orientation of the upstream IMF. *Crider et al.* [2003] developed a method to infer the upstream  $P_{dyn}$  at Mars using data from the MAG/MGS instrument. This method assumes that the magnetic field pressure in the induced magnetosphere balances the incident  $P_{dyn}$ . The direction of the upstream IMF has been estimated in a different way between the pre-mapping phase and mapping phase. For pre-mapping data, the IMF draping direction was determined from field vectors recorded at downstream from the bow shock [*Crider et al.*, 2003; *Brain et al.*, 2006a]. For mapping data, *Brain et al.* [2006a] used the configuration of the draped IMF on the dayside, far from crustal magnetic fields, as an indicative of the clock angle of the upstream IMF. Hereafter, this proxy is referred to as “the IMF draping direction” in this thesis. Both proxies of the  $P_{dyn}$  and the IMF draping direction were calculated on an orbit-by-orbit basis, and assuming that external conditions do not change during each orbit. Figure 2.4 shows these proxies from April, 1999 to November, 2006.

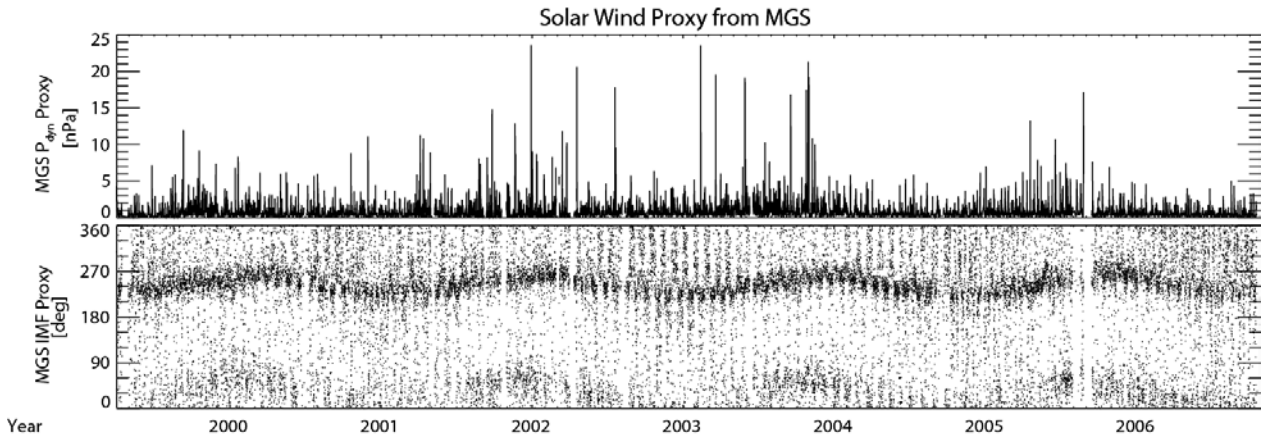


Figure 2.4: Two proxy datasets for Mars: (top) the solar wind dynamic pressure in units of nPa (converted from nT), and (bottom) the IMF draping direction.

## 2.2 Advanced Composition Explorer (ACE)

### 2.2.1 Overview

The Advanced Composition Explorer (ACE) is a solar wind monitor located upstream of Earth near the L1 Lagrange point ( $15 \times 10^5$  km from the Earth). ACE is dedicated to the observation of energetic particles within the interplanetary medium. This thesis used time-shifted data from the magnetometer (MAG/ACE) [Smith *et al.*, 1998] in order to estimate the IMF polarity around Mars more accurately (more discussions in Chapter 3).

The time-shifted data is determined by taking into account the radial distance and elongation between Earth and Mars (used the Equation 2.1 from Vennerstrom *et al.* [2003])

$$\Delta t = \frac{r_{mars} - r_{earth}}{v} + \frac{\phi_{mars} - \phi_{earth}}{\omega} \quad (2.1)$$

## *CHAPTER 2. INSTRUMENTATIONS AND DATA SETS*

where  $r$ ,  $\phi$ ,  $v$ , and  $\omega$  are the distance and the heliospheric longitude from the Sun to Mars, or Earth, the solar wind velocity measured by ACE, and the angular velocity of the Sun, respectively. Applying this equation the time-shift will be zero if the two planets are located at the same Parker field line.

## 2.3 Mars Atmosphere and Volatile EvolutioN (MAVEN)

### 2.3.1 Overview

The Mars Atmosphere and Volatile EvolutioN (MAVEN) spacecraft was launched by NASA on November 18, 2013, and inserted into orbit around Mars on September 21, 2014. Figure 2.5 shows the overview of the MAVEN spacecraft. The purpose of this mission is to explore the Martian upper atmosphere, ionosphere, and the interactions with the solar activity and the solar wind [Jakosky *et al.*, 2015a]. The science instruments onboard MAVEN enable simultaneous measurements of ions, electrons, neutrals and the magnetic field. Figure 2.6 shows the instruments onboard MAVEN. MAVEN has a 75° inclination science mapping orbit with periapsis altitude of about ~150 km, apoapsis altitude of about ~6,200 km. The orbital period is approximately 4.5 hours. During “deep-dip” campaigns, MAVEN goes down to periapsis altitudes ~125 km in order to investigate the altitude profile from the ionosphere to near the homopause [Bougher *et al.*, 2015]. Figure 2.7 shows the orbital trajectory of MAVEN. After starting the science observation, some issues of the instruments were revealed; the spacecraft potential issue and the straggling issue of Suprathermal and Thermal Ion Composition (STATIC) (See Section 2.3.3).

## CHAPTER 2. INSTRUMENTAIONS AND DATA SETS

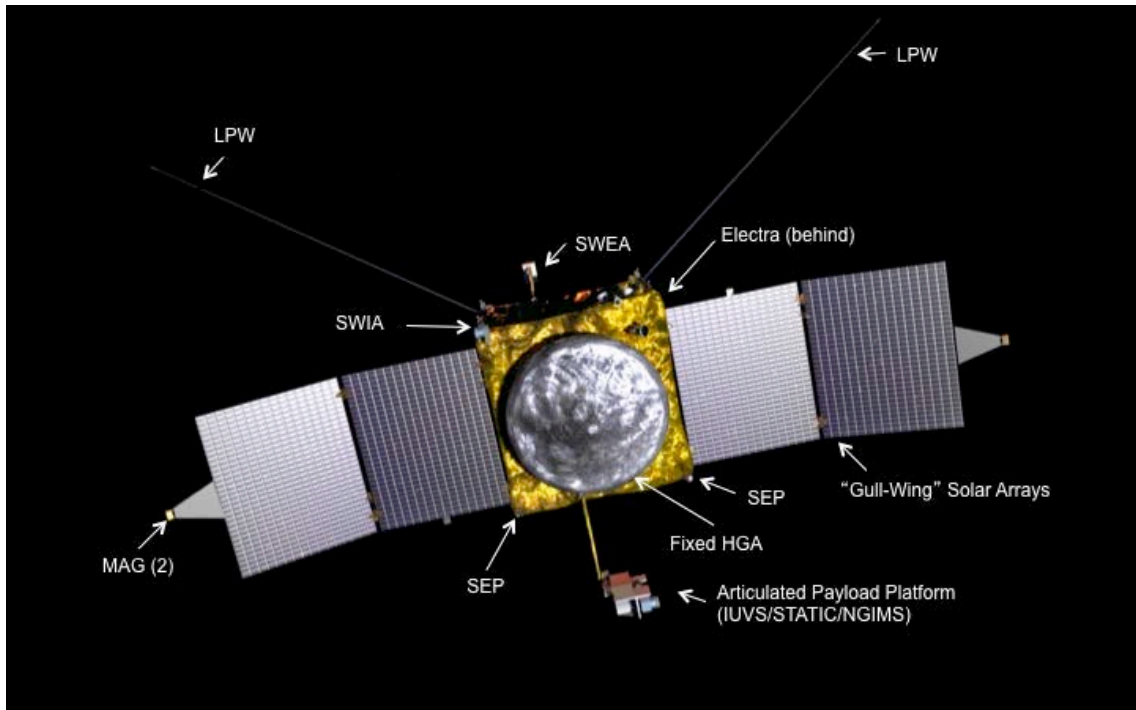


Figure2.5: Overview of the MAVEN spacecraft showing major instruments Courtesy of NASA

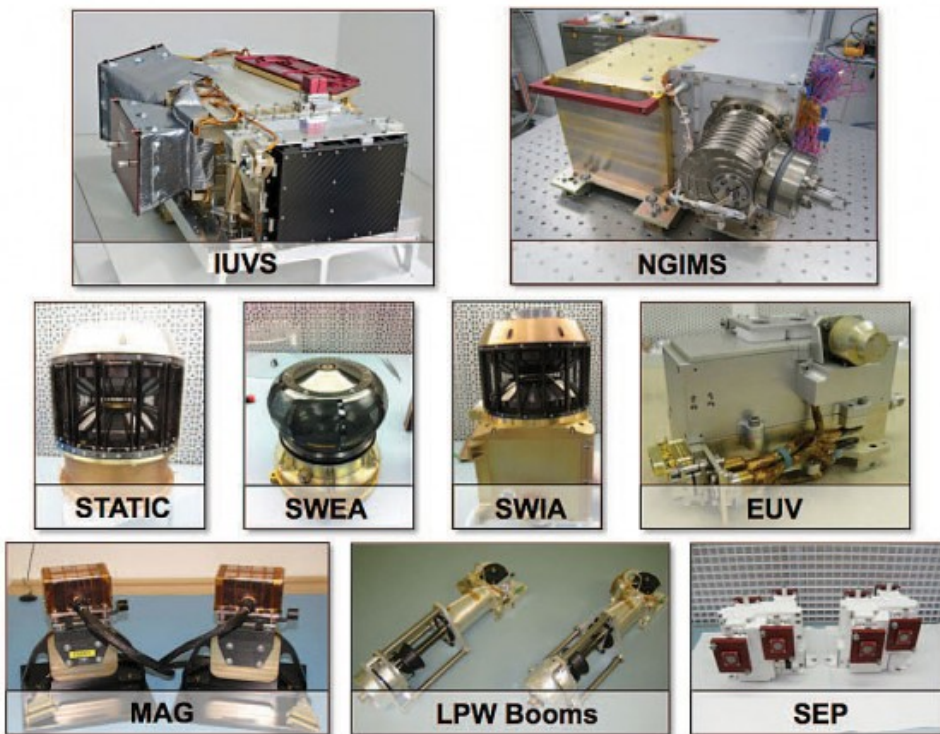


Figure2.6: Science instruments onboard MAVEN. Courtesy of NASA

## CHAPTER 2. INSTRUMENTAIONS AND DATA SETS

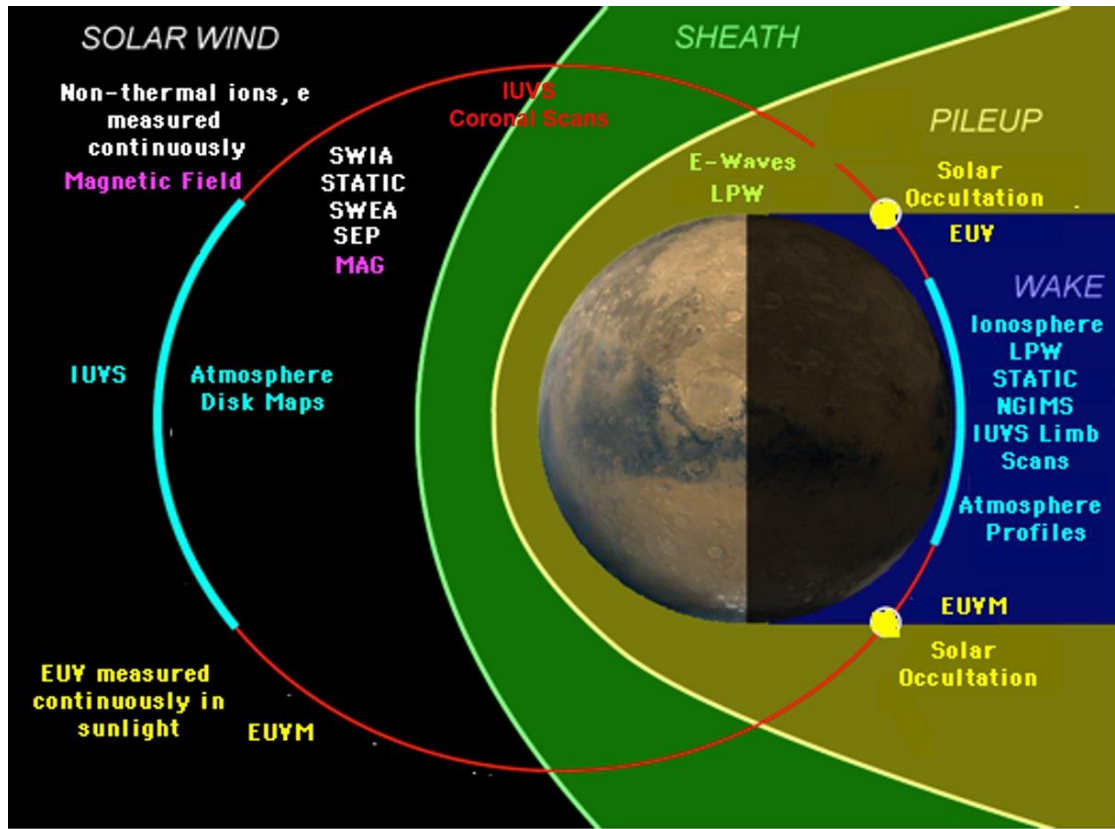


Figure 2.7: The orbital trajectory of MAVEN crosses different regions and boundaries around Mars. Instruments measure each region by different modes that are specific to each region. Courtesy of NASA

MAVEN team derived spacecraft potential of MAVEN from the STATIC d0 data (See Section 2.3.3), the Solar Wind Electron Analyzer (SWEA) data, the Langmuir Probe and Waves (LPW) data, and the SWEA-LPW fitted technique. Figure 2.8 shows an example of time series plots of spacecraft potential (up), and altitude of MAVEN (bottom). When the spacecraft was located in shadow, the negative spacecraft potential was estimated. On the other hand, when the spacecraft was located in solar wind region or magnetosheath, the positive spacecraft potential was estimated. This thesis took into

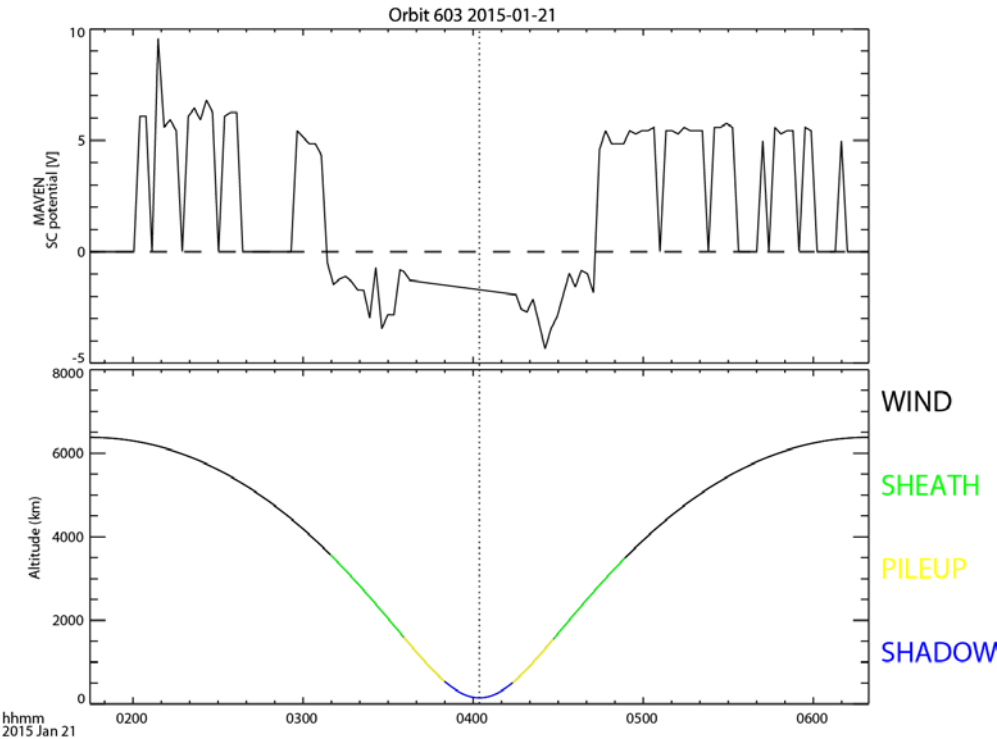


Figure 2.8: An example of time series plots of (up) spacecraft potential, and (down) altitude of MAVEN. Four color of altitude plot represents (black) the solar wind region, (green) the magnetosheath, (yellow) the magnetic pile-up region (induced magnetosphere), and (blue) the shadow (wake) region. Courtesy of Dr. Dong (a member of MAVEN team, University of Colorado Boulder, LASP)

account the simple solution of spacecraft potential to estimate the electron fluxes, and

the ion density.

### 2.3.2 Solar Wind Electron Analyzer (SWEA)

The Solar Wind Electron Analyzer (SWEA) is a symmetric hemispheric electrostatic analyzer with deflectors. It is designed to measure the energy and angular distributions of 5 eV to 4.6 keV electrons in the Martian environment with an energy resolution of

## CHAPTER 2. INSTRUMENTATIONS AND DATA SETS

$\Delta E/E = 17\%$ . The field of view (FOV) is  $360^\circ \times 120^\circ$  (azimuth  $\times$  elevation) for energies up to 1.6 keV (which represents 87 % of the sky). The angular resolution is  $22.5^\circ \times 20^\circ$  and the time resolution is 2 seconds. SWEA measures energy fluxes of electrons from  $10^3$  to  $10^9 \text{ eV} \cdot \text{cm}^{-2} \cdot \text{s}^{-1} \cdot \text{sr}^{-1} \cdot \text{eV}^{-1}$ . SWEA is mounted at the end of a 1.5-meter boom in order to prevent the interference with the spacecraft-generated magnetic fields, as well as spacecraft photoelectrons [Mitchell *et al.*, 2016]. Figure 2.9 shows the overview of SWEA instrument.

In Chapter 4, the SWEA measurements are used to identify the induced magnetosphere boundary (IMB).

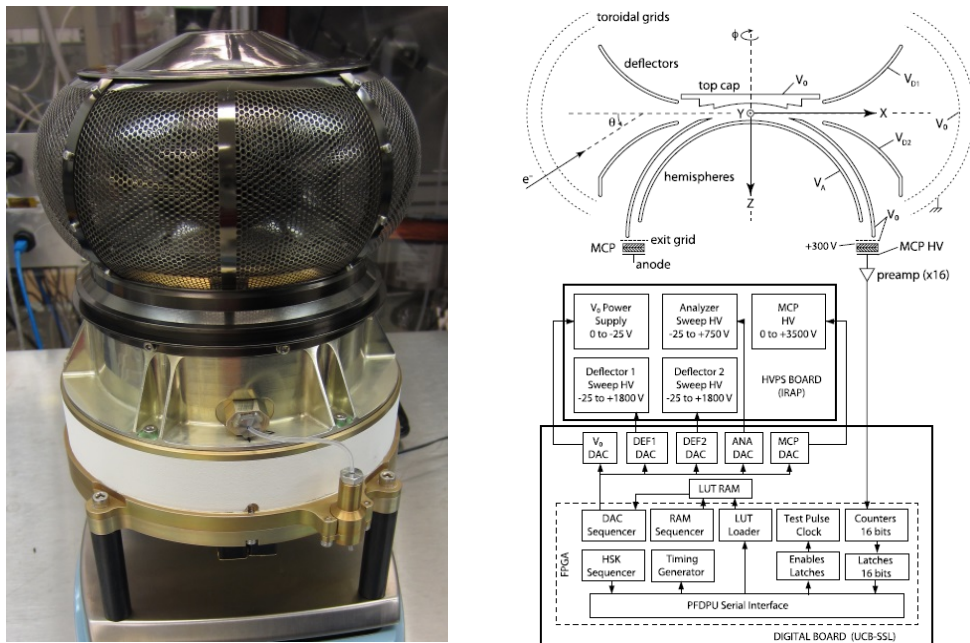


Figure 2.9: Overview of the SWEA instrument. This figure is adapted from Mitchell *et al.*, [2016].

### 2.3.3 Suprathermal and Thermal Ion Composition (STATIC)

The Suprathermal and Thermal Ion Composition (STATIC) instrument uses a toroidal top-hat electrostatic analyzer (ESA) and a time-of-flight (TOF) velocity analyzer to resolve ion energy per charge, direction, and velocity per charge. It is designed to measure the ion mass composition as well as the energy and angular distributions in every 4–128 seconds time resolutions. ESA has the energy range of 0.1 eV - 30 keV to detect thermal ionospheric ions, suprathermal ion tail, and pick-up ions with the energy resolution of  $\Delta E/E = 15\%$ . The FOV is  $360^\circ \times 90^\circ$  (which represents 70 % of the sky) with the angular resolution of  $22.5^\circ \times 6^\circ$ . TOF velocity analyzer resolves ion masses in the range of 1-70 amu (atomic mass unit) with the mass resolution of 25%. STATIC measures the energy flux of  $10^4$  to  $10^8 \text{ eV} \cdot \text{cm}^{-2} \cdot \text{s}^{-1} \cdot \text{sr}^{-1}$  when the attenuators turn off. STATIC has one mechanical attenuator and one electrostatic attenuator, they extend the energy flux dynamic range to  $10^{12} \text{ eV} \cdot \text{cm}^{-2} \cdot \text{s}^{-1} \cdot \text{sr}^{-1}$  [McFadden et al., 2015]. STATIC can produce 22 different data products, or Application Identifiers (APID) (See *McFadden et al.* [2015], for details of each APID). Figure 2.10 shows the overview of the STATIC instrument.

In Chapter 4, the STATIC measurements were used to identify the ion composition boundary (ICB). In this thesis, the STATIC APID of C6 mode (32 energy steps, 64

## CHAPTER 2. INSTRUMENTAIONS AND DATA SETS

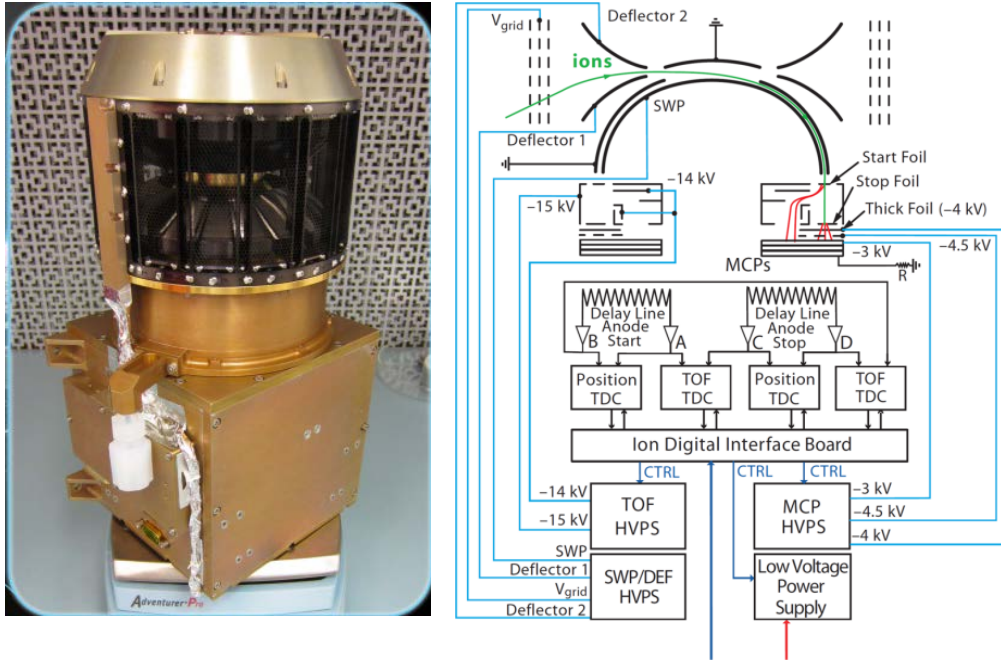


Figure 2.10: Overview of the STATIC instrument. This figure is adapted from *McFadden et al.* [2015] and Courtesy of NASA/GSFC and University of California Berkeley, SSL.

mass bins and time resolution of 128s) were mainly used. The STATIC APID of d0 mode (32 energy steps, 8 mass bins, and time resolution of 128s) was only used for the calculation of the spacecraft potential.

The STATIC measurement has some sources of error [*McFadden et al.*, 2015]. In this thesis, energy straggling issue was carefully treated (more discussions in Chapter 4).

Characterized proton and alpha straggling were observed after launching of MAVEN. Since tenuous pickup ions seems to be measured in the presence of intense solar wind fluxes both in the magnetosheath and in the solar wind, the effect of proton and alpha

straggling is a big issue. A background subtraction algorithm to remove proton and alpha straggling is illustrated in Figure 2.11. Upper panel in Figure 2.11, solar wind protons form the prominent peak centered at mass  $\sim$ 1 amu and energy  $\sim$ 500 eV. However, the vertical finger signature of counts that spans masses 2 amu to 60 amu at energy  $\sim$ 450 eV are due to proton straggling. After applying a background subtraction algorithm that assumes proton and alphas producing, lower panel in Figure 2.11 shows that the successful removal of proton and alpha straggling [McFadden *et al.*, 2015].

### **2.3.4 Solar Wind Ion Analyzer (SWIA)**

The Solar Wind Ion Analyzer (SWIA) is a cylindrically symmetric electrostatic analyzer. It is designed to measure the properties of solar wind and magnetosheath ions (primarily protons), including density, temperature, and velocity, in order to investigate the solar wind interaction with the Martian upper atmosphere [Halekas *et al.*, 2015]. SWIA has the energy range of 25 eV - 25 keV with the energy resolution of  $\Delta E/E = 15\%$ . The FOV is  $360^\circ \times 90^\circ$  with the angular resolution of  $22.5^\circ$ , and the time resolution of 4 seconds. In order to determine the solar wind proton and alpha particle angular distributions, it uses the FOV of  $3.75^\circ \times 4.5^\circ$  with the angular resolution of  $4.5^\circ$ . SWIA measures the energy flux of  $10^4$  to  $10^{11} \text{ cm}^{-2} \cdot \text{s}^{-1} \cdot \text{sr}^{-1} \cdot \text{eV}^{-1}$  and determines

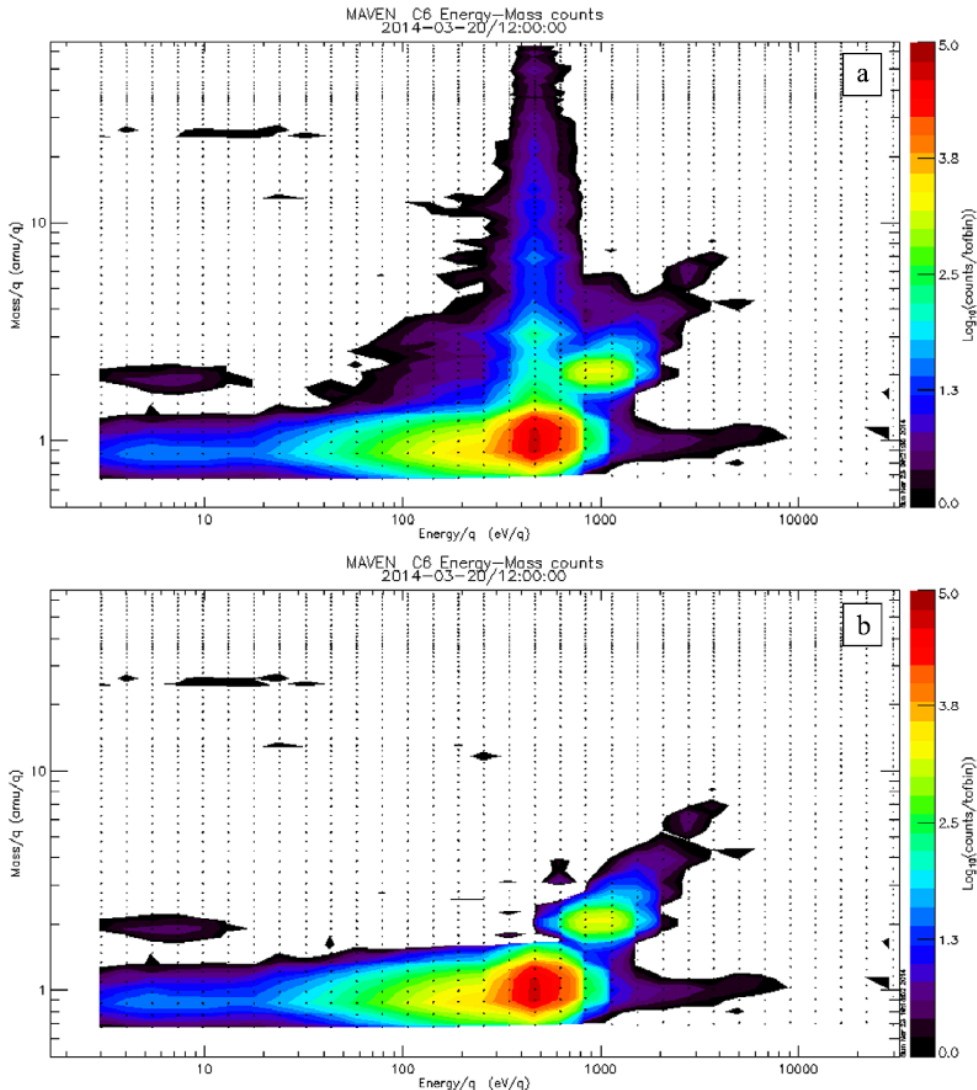


Figure 2.11: The STATIC mass-energy spectra (a) before and (b) after subtraction of background due to proton and alpha energy straggling. This figure is adapted from McFadden *et al.* [2015].

the bulk plasma flow from solar wind speeds ( $\sim 350$  to  $\sim 1000$  km/s), stagnating magnetosheath speeds (tens of km/s), and the solar wind density. The mechanical attenuator (a small stainless steel sheet with a slit) is attached on SWIA. That reduces the geometric factor by a factor of  $\sim 15$  when it closes [Halekas *et al.*, 2015]. Figure

2.12 shows the overview of the SWIA instrument.

In Chapter 4, the SWIA measurements were used to obtain the solar wind properties and to identify  $\beta^*$  boundary.

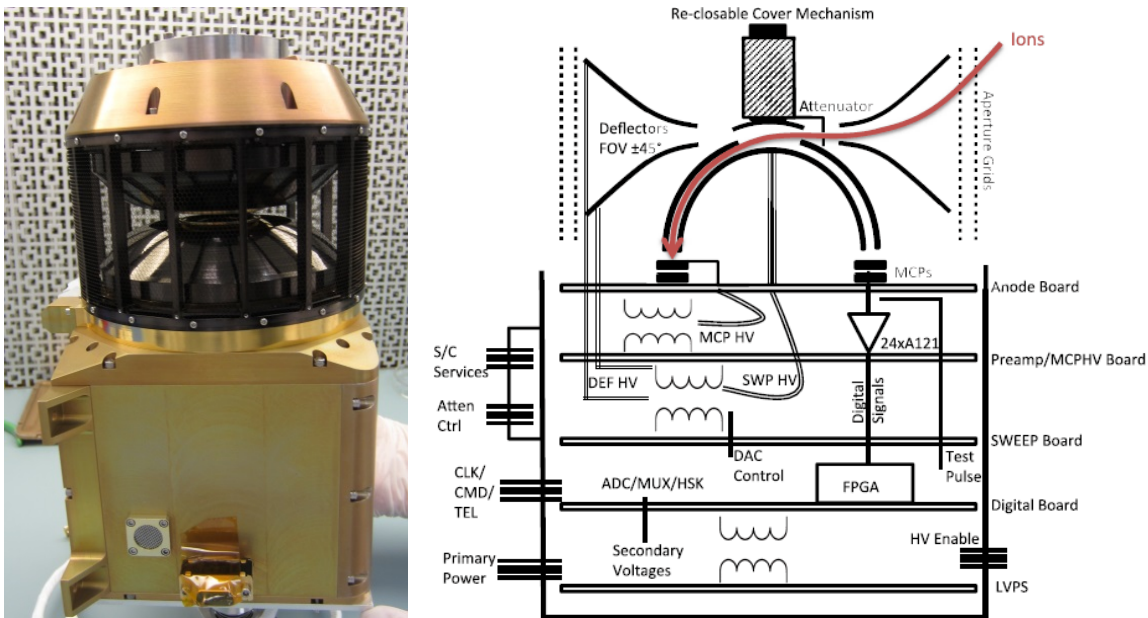


Figure 2.12: Overview of the SWIA instrument. This figure is adapted from *Halekas et al. [2015]* and Courtesy of University of California Berkeley, SSL.

### 2.3.5 Magnetometer (MAG/MAVEN)

The magnetic field investigation with other plasma investigation around Mars is important to understand the atmospheric escape from Mars. Magnetometer (MAG/MAVEN) onboard MAVEN consists of two independent tri-axial fluxgate magnetometer sensors in order to measures magnetic fields of the solar wind and the Martian upper atmosphere [*Connerney et al., 2015a*]. MAG/MAVEN sensors are

## CHAPTER 2. INSTRUMENTATIONS AND DATA SETS

attached to the ends of each solar panel (~5.6 m from the center of the spacecraft body) to minimize the relative contribution of spacecraft-generated magnetic fields. MAG/MAVEN measures the vector magnetic field in the unperturbed solar wind ( $B \sim 3$  nT), magnetosheath ( $B \sim 10\text{-}50$  nT), and crustal magnetospheres ( $B < 3000$  nT), with the ability to spatially resolve crustal magnetic cusps (horizontal length scales of ~100 km). The dynamic range of MAG/MAVEN is from 0.1 nT to 60,000 nT with a 32 vector samples/sec time resolution,  $1^\circ$  angular determination of vector magnetic field, and 5% precision on its scalar value [Connerney *et al.*, 2015a, b]. Figure 2.13 shows the overview of the MAG/MAVEN instrument.

In Chapter 4, the MAG/MAVEN measurements are used to identify IMB and  $\beta^*$  boundary.



Figure 2.13: Overview of the MAG/MAVEN instrument. Courtesy of NASA/GSFC

### 2.3.6 Other Instruments

Other instruments onboard MAVEN, which observational data were not used in this thesis, are described here: Extreme Ultraviolet (EUV) monitor, Solar Energetic Particle (SEP), Langmuir Probe and Waves (LPW), Imaging Ultraviolet Spectrograph (IUVS), and Neutral Gas and Ion Mass Spectrometer (NGIMS).

EUV monitor measures the solar extreme ultraviolet (wavelength: 0.1-7, 17-22, and 121.6 nm) input and variability to investigate ionization, dissociation, and heating of the Martian upper atmosphere [*Eparvier et al.*, 2015].

SEP measures the solar energetic particles (ions from 25 keV to 12 MeV and electrons from 25 keV to 1 MeV) to investigate its effect to the upper atmosphere and ionosphere of Mars through sputtering, heating, dissociation, excitation, and ionization [*Larson et al.*, 2015].

LPW measures the in situ electron density, electron temperature, and electric field wave power to investigate the ion recombination rates, the global structure and chemistry of the Martian ionosphere, and the effects of solar wind generated plasma waves and the auroral precipitation on ionosphere heating [*Andersson et al.*, 2015].

IUVS, which is a remote sensing instrument, acquires imaging spectroscopy in ultraviolet (wavelength: 110–190nm, 180-340 nm) to investigate vertical and horizontal

profiles of neutral atmosphere and ionosphere, global images, coronal scans for “Hot Oxygen”, and D/H ratio [McClintock *et al.*, 2015].

NGIMS measures the composition and isotopes of thermal neutrals and ions to investigate the basic structure of the upper atmosphere (major species He, N, O, CO, N<sub>2</sub>, NO, O<sub>2</sub>, Ar, and CO<sub>2</sub>) and ionosphere from the homopause to above the exobase, and stable isotope ratios [Mahaffy *et al.*, 2015].

### 2.3.7 The Solar Wind Parameters

Since the periapsis of MAVEN changes with time, MAVEN is not always able to measure the upstream solar wind. During November, 2014 to March, 2015 and June, 2015 to October, 2015, the apoapsis of MAVEN was continuously in the upstream solar wind. In this thesis, the upstream solar wind parameters, i.e. the solar wind velocity, density, and the magnetic field, as well as the solar wind dynamic pressure ( $P_{dyn}$ ), were derived from SWIA and MAG/MAVEN observations. In this thesis, these solar wind parameters were used in order to investigate the dependence of the plasma boundaries on the solar wind parameters. Figure 2.14 shows these parameters from November, 2014 to October, 2015. Moreover, the solar wind induced electric field was derived from the solar wind velocity and the local magnetic field,  $E_{sw} = -V_{sw} \times \mathbf{B}$  (the local

## CHAPTER 2. INSTRUMENTATIONS AND DATA SETS

magnetic field  $\mathbf{B}$  measured by MAG/MAVEN and the solar wind velocity  $\mathbf{V}_{sw}$  from SWIA data).

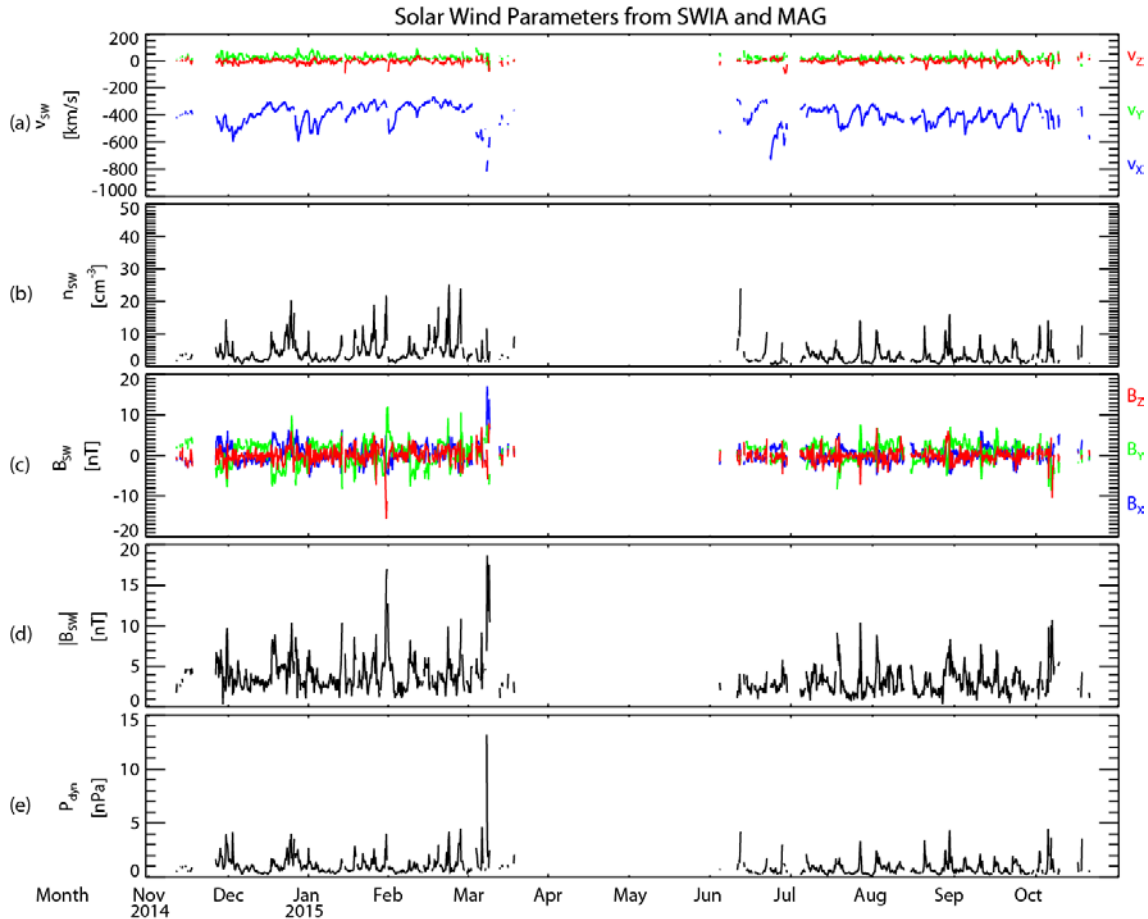


Figure 2.14: Time series plots of the solar wind parameters derived from SWIA and MAG/MAVEN: (a) the solar wind velocity, (b) the solar wind density, (c) the magnetic field, (d) the magnitude of magnetic field, and (e) the solar wind dynamic pressure. Courtesy of Dr. Halekas (a member of MAVEN team, University of Iowa) and Dr. Brain (a member of MAVEN team, University of Colorado Boulder, LASP)

## 2.4 Data Sets

Section 3 investigated the statistical study of magnetosheath penetration by using data from the MGS mapping orbits around 400 km altitudes from April 1999 to November 2006. In addition, the data from ACE were used to ensure the quality of the IMF polarity of the parker spiral (away/toward) estimation at Mars.

Section 4 investigated three plasma boundaries between the magnetosheath and the Martian upper atmosphere by using data from instruments onboard MAVEN during two time period: (1) from November 27, 2014 to March 16, 2015, and (2) from June 4, 2015 to October 24, 2015. Period (1) and period (2) correspond from autumn to winter in the Martian northern hemisphere ( $L_s = 224.9\text{--}318.1$ , the solar longitude ( $L_s$ ) is the Mars-Sun angle) and from winter to spring in the Martian northern hemisphere ( $L_s = 351.1\text{--}62.4$ ), respectively. During these periods, MAVEN directly observed in the solar wind region and obtained the solar wind parameters.

This thesis uses the two coordinate systems of Mars. One is the Mars Solar Orbital (MSO) Cartesian coordinate system and other is the Mars-Sun-Electric field (MSE) coordinate system. The MSO coordinate system is defined as follows: the  $X_{MSO}$  axis points from Mars to the Sun, the  $Y_{MSO}$  axis is opposite to the Mars orbital motion and the  $Z_{MSO}$  axis completes the right-handed system. In this thesis, the northern hemisphere

## CHAPTER 2. INSTRUMENTATIONS AND DATA SETS

represents the MSO latitude ( $\arctan(Z_{MSO}/\sqrt{X_{MSO}^2 + Y_{MSO}^2})$ ) is positive and the southern hemisphere represents the MSO latitude is negative.

The MSE coordinate system is defined as follows: the  $X_{MSE}$  axis points from Mars to the Sun, the  $Z_{MSE}$  axis along the direction of the solar wind induced electric field,  $\mathbf{E}_{sw} = -\mathbf{V}_{sw} \times \mathbf{B}$  (the local magnetic field  $\mathbf{B}$  and the solar wind velocity  $\mathbf{V}_{sw}$ ), and  $Y_{MSE}$  axis completes the right-handed system. It is assumed that the component of solar wind velocity is only  $X_{MSO}$  direction when the solar wind induced electric field calculations are made. Thus, when IMF By is negative and positive, the solar wind induced electric field is positive and negative, respectively.

*CHAPTER 2. INSRUMENTAIONS AND DATA SETS*

# **Chapter 3**

## **Statistical Study Part I: MGS Observations Asymmetric Penetration of Shocked Solar Wind Down to 400 km Altitudes at Mars**

### **3.1 Introduction**

As mentioned in Chapter 1, Mars has no intrinsic global magnetic field like Earth [Acuña et al., 1998]. However, Mars Global Surveyor (MGS) observed the magnetic field from remnant crustal magnetizations mainly in the southern hemisphere [e.g., Acuña et al., 1998, 1999]. Hence, Mars is not a simple unmagnetized planet, such as Venus. Interaction between the solar wind and the Martian ionosphere forms several varieties of plasma regime [e.g., Vignes et al., 2000; Luhmann et al., 2004]. The

magnetosheath region has shock-heated plasma and turbulent magnetic field signatures.

When the spacecraft passes through the magnetosheath region, fluctuations of the magnetic field and high-energy (from about 50 eV to  $\sim$ 1 keV) electron flux are known to increase [e.g., *Nagy et al.*, 2004; *Crider et al.*, 2005; *Guicking et al.*, 2010]. As a magnetosheath flux tube approaches Mars, it is decelerated by mass loading and draped around Mars. It thus forms the region of piled-up magnetic field. This region is referred to as the magnetic pile-up region or induced magnetosphere, and its outer boundary is called the magnetic pile-up boundary (MPB) or the induced magnetosphere boundary (IMB) [e.g., *Vignes et al.*, 2000; *Luhmann et al.*, 2004]. In this chapter, this boundary is referred to as “the magnetic pile-up boundary (MPB)”, whereas in chapter 4; it is referred to as “the induced magnetosphere boundary (IMB)”. The lower boundary of the magnetic pile-up region determines the upper boundary of ionosphere. MPB does not always have clearly structure. It sometimes has complicated structure.

Ionospheric ions and electrons, accelerated by the electric field induced by the flowing solar wind, produce a current in the planetary ionosphere, which reduces the compressed interplanetary magnetic field (IMF) with decreasing altitude. The IMF draping can be described as produced by this electric field [e.g., *Alfvén*, 1957; *Cloutier and Daniell*, 1973]. Hence, the flux tubes originated from the solar wind can directly

interact with the Martian ionosphere. The situation is very different from the case of Earth, where the global intrinsic magnetic field deflects the shocked solar wind at much higher altitudes. Since the direct interaction with the solar wind causes energy and momentum exchange between the solar wind and the Martian ionosphere [e.g., *Lundin*, 2011], atmospheric escape processes induced by such interaction are important subjects of study in unmagnetized planets like Mars [e.g., *Jakosky and Phillips*, 2001]. The escape rate of planetary ions is related to the condition and/or location of magnetosheath region. Therefore, it is important to know how often the magnetosheath plasma penetrates into lower altitudes than usual [e.g., *Brain et al.*, 2005; *Crider et al.*, 2005; *Nilsson et al.*, 2010; *Matsunaga et al.*, 2015] and to understand what is the physical mechanism to cause the penetration.

MGS observations showed that the MPB is typically located at about 650-990 km (at subsolar), about 1,300-1,600 km (at terminator) altitudes from the surface [*Trotignon et al.*, 1996, 2006; *Vignes et al.*, 2000]. However, this boundary location can change significantly depending on solar wind conditions [e.g., *Brain*, 2006]. Previous studies indicate that the magnetosheath can penetrate to lower altitudes than usual when the solar wind dynamic pressure ( $P_{dyn}$ ) is high [e.g., *Crider et al.*, 2005; *Brain*, 2006]. In addition, a number of investigators predicted the MPB has an asymmetry in the shape

[*Brech and Ferrante*, 1991; *Brech et al.*, 1993; *Harnett and Winglee*, 2003, *Brain et al.*, 2006a]. It has been also pointed out that the crustal magnetic fields can locally push the magnetosheath region upward and cause an asymmetric structure of MPB [e.g., *Brain et al.*, 2003, 2006a]. Moreover, *Brain et al.* [2005] shows that the detection of magnetosheath plasma at 400 km altitudes (hereafter, referred to as “magnetosheath penetration events”) depends on the  $P_{dyn}$ , the IMF draping direction, and season. However, the physical mechanisms causing the observed dependencies, especially effects of the IMF orientation, are not understood.

This chapter focuses on the penetration of magnetosheath plasma down to 400 km altitudes on the dayside of Mars, based on the magnetic field and electron observations of MGS. In order to statistically investigate the properties of penetration events, we implemented a semi-automatic event selection and identified 1,145 events from ~7.6 years of MGS data. This thesis used the solar wind proxy data derived from the MGS observations [*Crider et al.*, 2003; *Brain*, 2006] and time-shifted solar wind data recorded at Earth by the Advanced Composition Explorer (ACE) satellite, to ensure the quality of the IMF polarity estimation at Mars. A model of Martian crustal magnetic fields (the Cain model) is also used [*Cain et al.*, 2003]. Thus, the dependence on the solar wind parameters and the role of the crustal magnetic fields are investigated.

Section 3.2 explains a semi-automatic method to select the magnetosheath penetration.

Section 3.3 explains a method to determinate the IMF draping direction at Mars from the MGS and ACE data sets. Section 3.4 reports on the dependence of magnetosheath penetration events on the solar wind parameters. Section 3.5 reports on statistical analysis of magnetosheath penetration events, especially focused on when the  $P_{dyn}$  is low. Finally, section 3.5 summarized the statistical results and discussed candidate physical mechanisms to cause the penetration of magnetosheath plasma to low altitudes.

## 3.2 Magnetosheath Penetration Event Selections

The data used in this chapter are from the MGS mapping orbits around 400 km altitudes from April, 1999 to November, 2006. Here introduces the selection criteria for magnetosheath penetration events. Previous measurements have shown that the various plasma regions have different characteristic magnetic field fluctuations and electron energy spectra [e.g., *Nagy et al.*, 2004; *Brain*, 2006] (See Subsection 1.2.2). We use these signatures to identify the periods when magnetosheath plasma penetrated down to the 400 km altitude. According to previous studies [e.g., *Mitchell et al.*, 2001; *Bertucci et al.*, 2003; *Brain et al.*, 2003, 2006b; *Espley et al.*, 2004; *Nagy et al.*, 2004; *Crider et al.*, 2005; *Trotignon et al.*, 2006], when the spacecraft passes through the

magnetosheath region, fluctuations of the magnetic field are enhanced and the electron energy spectrograms show a characteristic change. Since the energy fluxes of high energy electrons (over 100 eV) observed in the magnetosheath and magnetic pile-up regions are higher than in the ionosphere [e.g., *Mitchell et al.*, 2001; *Crider et al.*, 2005], we can distinguish whether MGS is in or above the ionosphere. Since high-frequency fluctuations of the magnetic field in the magnetosheath are larger than in the magnetic pile-up region [e.g., *Nagy et al.*, 2004; *Trotignon et al.*, 2006], we can infer whether MGS is in the magnetosheath or the magnetic pile-up region based on the wave power.

First the time intervals when MGS is located on a dayside and the integrated differential electron flux above 400 eV was greater than  $5 \times 10^3 \text{ cm}^{-2} \cdot \text{s}^{-1} \cdot \text{sr}^{-1}$  were selected in order to eliminate the data when MGS was in the Martian ionosphere. The MGS electron reflectometer often saturates between about 100 eV and 400 eV in high electron flux regions [e.g., *Mitchell et al.*, 2001; *Crider et al.*, 2005] (See Figure 1.9).

Therefore, this thesis uses the electron flux above 400 eV for the selection criteria. Next, the time intervals when the power spectral density of the magnetic field fluctuation above 0.1 Hz was higher than  $1,000 \text{ nT}^2 \text{ Hz}^{-1}$  were selected in order to select the data when MGS was located in the Martian magnetosheath region by eliminating observations in the magnetic pile-up region. These threshold values are intentionally

conservative, to guard against false-positives in the list of magnetosheath penetration events. This thesis confirmed that the final conclusions are not sensitive to less stringent choices for these two threshold values. This thesis discusses the impact of the choice of threshold value on conclusions in section 3.5. After automatically selecting events, the current sheet crossings or solar energetic particles (SEPs) events were eliminated by inspection. In order to investigate the relation between the solar wind condition and the magnetosheath penetration and to understand the physical mechanisms of the magnetosheath penetration, these inappropriate events were eliminated. The current sheet crossings events and the SEPs events were eliminated from the signature of inverting of magnetic field direction and from the signature of suddenly enhanced high energy (10-20 keV) electrons, respectively. Finally, the events with duration less than 1 minute and the crustal field magnitude larger than 15 nT were excluded. These events are most likely to be observed when MGS passes through the Martian magnetic field cusps. Above cusp regions, the magnetosheath plasma can more easily access low altitudes, regardless of the solar wind conditions. This thesis focuses on magnetosheath penetration to ionospheric regions typically shielded by induced magnetic fields.

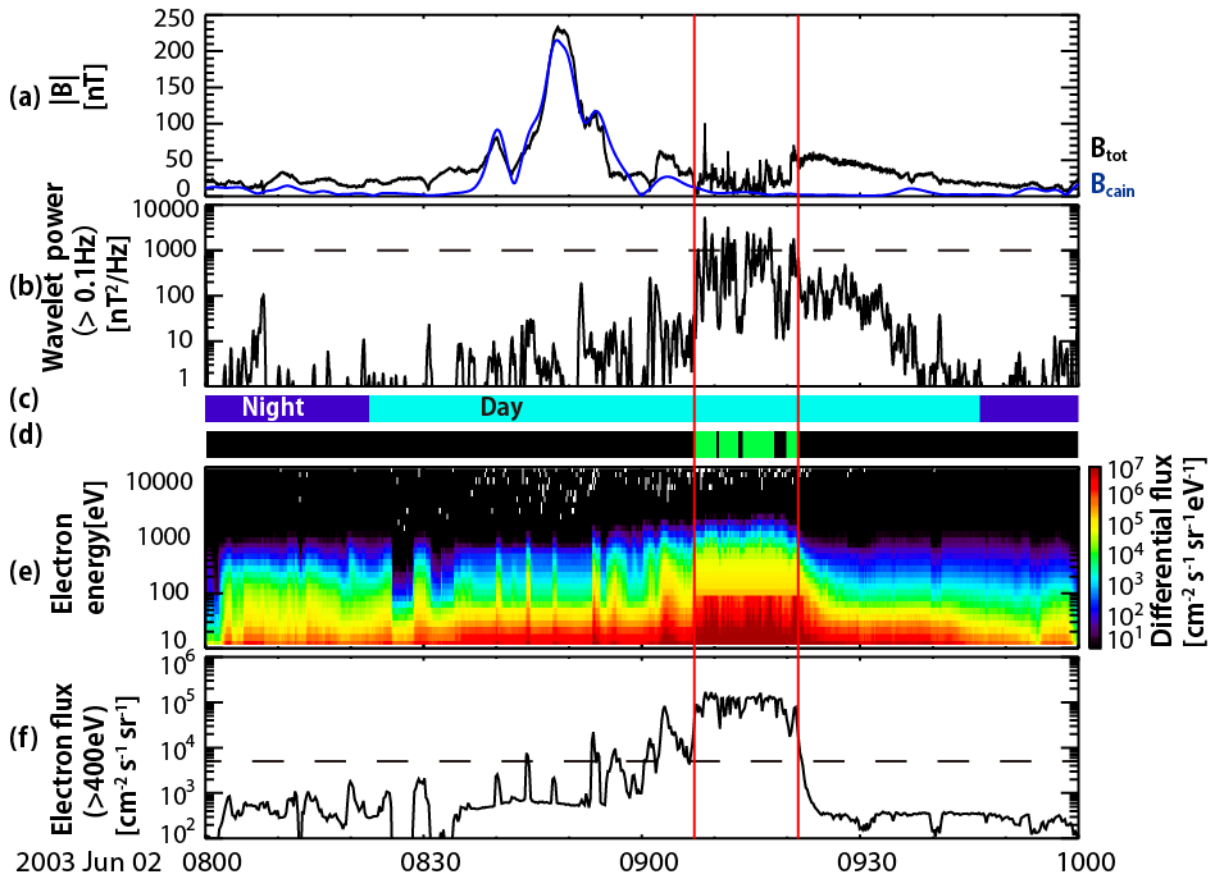


Figure 3.1: Overview of the time-series plots of the solar wind (magnetosheath) penetration event observed by MGS on 2 June, 2003: (a) the magnitude of magnetic field, (b) the power of magnetic field fluctuations above 0.1 Hz, (c) the day-night indices, (d) the indices of event time, (e) the differential electron flux, and (f) the integrated differential electron flux above 400 eV. The blue line in Figure 3.1a shows the crustal magnetic field model [Cain et al., 2003]. Missing data due to instrument saturation around 100 eV in the magnetosheath region are interpolated linearly. The time interval between two vertical red lines indicates the period of the magnetosheath penetration identified by the criteria described in the text. Black horizontal dash lines in Figures 3.1b and 3.1f mean our thresholds used in this study, respectively.

As a result, 1,145 events of the magnetosheath penetration were identified. Figure 3.1 shows a typical event on 2 June, 2003. Figure 3.1a shows the magnitude of magnetic field and Figure 3.1e shows the differential electron flux from the MGS observation.

The power of magnetic field fluctuations were calculated and integrated above 0.1 Hz (Figure 3.1b). Moreover, the differential electron flux above 400 eV (Figure 3.1f) was integrated. This thesis only surveyed the periods when the spacecraft was on dayside, colored as light blue in Figure 3.1c. During 14.2 minutes in Figure 3.1 (the period between two vertical red lines), MGS simultaneously observed highly fluctuating magnetic field and significant flux of high energy electrons. The green color in Figure 3.1d indicates the time intervals satisfying the criteria. Since the wavelet power shows high fluctuations, it assumes that the event is continuous when the time gaps between green color (Figure 3.1 d) intervals are smaller than 5 minutes and identified the time interval between two red vertical lines as one event.

### 3.3 Determination of the Solar Wind Parameters

The upstream solar wind seldom has an access to the 400 km altitude of the MGS mapping orbit. We thus cannot directly obtain the solar wind properties, such as the  $P_{dyn}$  and the IMF draping direction around Mars from MGS data. Therefore, this thesis uses proxies for the  $P_{dyn}$  and the IMF draping direction at Mars implemented by *Brain et al.* [2005, 2006a] and *Crider et al.* [2003]. Since the time resolution of these proxies is

about 2 hours due to the MGS orbit, this thesis uses the closest data in time available to represent solar wind conditions for an event.

### **3.3.1 Determination of the solar wind dynamic pressure**

The  $P_{dyn}$  proxy is derived from the measured intensity of the piled-up magnetic field on the Martian dayside [Crider *et al.*, 2003; Brain *et al.*, 2005]. As described in Brain *et al.* [2005], they exclude observations above crustal magnetic sources and with solar zenith angle (SZA) greater than 110°. Then, they fit the remaining field strengths to a  $\cos(\text{SZA})$  function to estimate the field strength at SZA = 0°.

### **3.3.2 Determination of the IMF Sector Polarity around Mars**

The IMF draping direction proxy is derived from the azimuth direction of the draped magnetic field based on all dayside MAG/MGS data recorded in the latitude range between 50° and 60° in the northern hemisphere [Brain *et al.*, 2005; 2006a]. Azimuth direction is defined with 0° in the local eastward direction and 90° in the local northward direction [Brain *et al.*, 2005; 2006a]. However, the IMF draping direction proxy is known to have an asymmetry. Brain *et al.* [2006a] pointed out that the crustal magnetic fields locally push the MPB upward, which may play a role in creating the observed asymmetry.

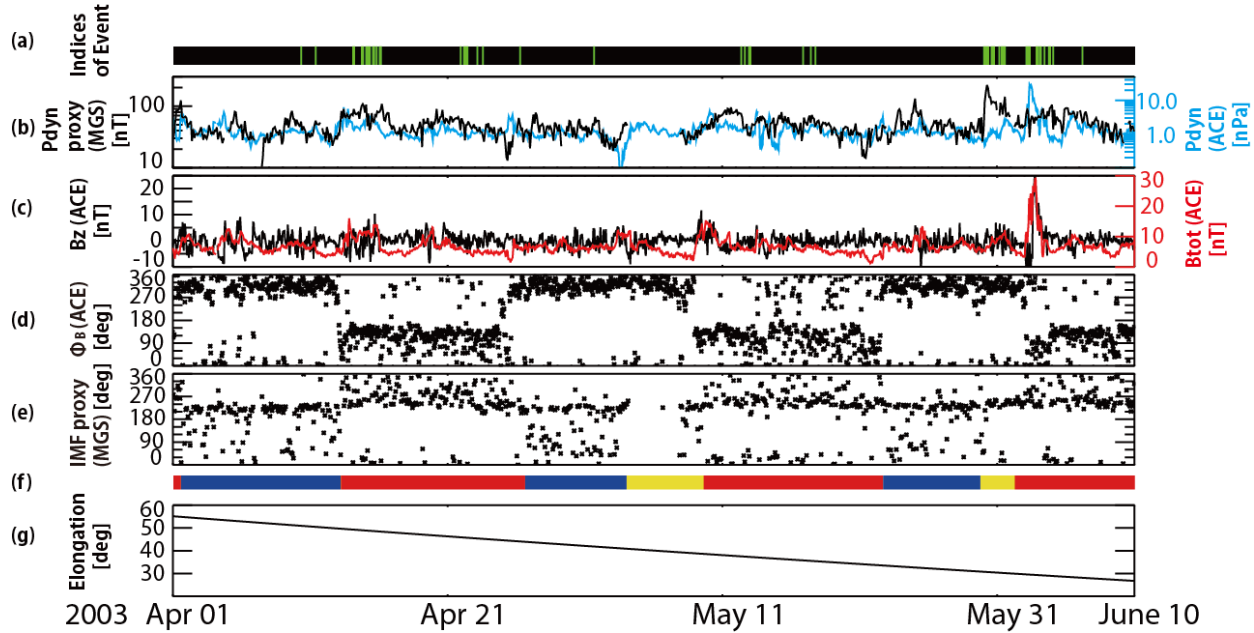


Figure 3.2: Time-series plots of the solar wind parameters estimated from ACE and MGS observations. (a) The indices of event time, (b) the magnitude of solar wind dynamic pressure (black line shows the MGS data and the blue corresponds to time-shifted ACE data), (c) the magnitude of magnetic field from time-shifted ACE data (black line shows z (north-south) component of B and the red indicates the total B), (d) the IMF polarity (GSE ( $\varphi_B$ )) from time-shifted ACE data, (e) the IMF polarity proxy from MGS data, (f) the estimated IMF polarity (red, blue and yellow correspond to the away polarity, toward polarity, and others, respectively), and (g) the elongation between Mars and Earth are shown. Noted that the unit of the solar wind dynamic pressure derived from MGS is nT and that of solar wind dynamic pressure derived from ACE is nPa in Figure 3.2b.

Figure 3.2 shows the time-series plots of the solar wind parameters estimated from ACE and MGS observations. The ACE solar wind data is time-shifted to the location of Mars in order to infer the IMF sector polarity at Mars. The shifted-time can be determined from a combination of propagation in the radial distance between Earth and Mars, and rotation of the angular distance between Earth and Mars [Vernerstrom *et al.*,

2003] (used the Equation 2.1 in Section 2.2). Green bars in Figure 3.2a correspond to the time of magnetosheath penetration events. The  $P_{dyn}$  (ACE) in Figure 3.2b is scaled to Mars heliocentric distances. In the scaling it was assumed that the density varies as  $1/r^2$  and that the solar wind speed is constant with heliocentric distance,  $r$ . Both the MGS and ACE pressure proxies could be used to sort the observations. Ideally, the two proxies would be highly correlated with each other, but this is not the case. The correlation coefficient for the two proxies is 0.25, and the mean absolute deviation is  $\sim 84\%$ , suggesting that there are non-negligible differences between the two. Some of the reasons for this are discussed in *Vennerstrom et al.* [2003]. In this study, the local proxy was chosen to be used, derived from MGS data, to sort the observations. Figure 3.2c shows the magnitude of magnetic field from time-shifted ACE data to see the variation of upstream condition around Mars. Comparing the IMF polarity from the time-shifted ACE data with the IMF draping direction proxy from MGS data (Figures 3.2d and 3.2e), the IMF polarity was derived from only the MGS IMF draping direction proxy data (Figure 3.2f). As pointed out by *Brain et al.* [2006a], the IMF draping direction proxy shows a clustering around  $210^\circ$ - $270^\circ$  regardless of the IMF sector polarity. Hence, it is sometimes difficult to determine the sector polarity only from an individual proxy value taken in isolation. However, it is often possible to determine

which solar wind sector polarities around Mars occupied for a given orbit based on the longer baseline time series of proxy values.

Firstly, the time-shifted ACE data with MGS data were compared, when elongation between Mars and Earth is small (within 90°), so as to investigate what characteristics of the IMF draping direction proxy from MGS correspond to the IMF sector polarity, i.e. “away” or “toward” sector of the Parker spiral structure in the solar wind. The azimuthal angle ( $\varphi_B$ ) of the IMF observed by ACE is defined by the Geocentric Solar Ecliptic (GSE) coordinate. As shown in Figure 3.2d, the time intervals when  $\varphi_B$  are distributed around 135° correspond to away polarity, and around 315° correspond to toward polarity. Therefore, this thesis found that the time intervals when the MGS IMF draping direction proxy is clustered from about 210° to 360° correspond to away sector, and 90° to 180° correspond to toward sector. Next, based on this correspondence, this thesis categorized the IMF sector polarity inferred from the MGS IMF draping direction proxy into three categories (away, toward, and other) for all MGS mapping phase data obtained during the surveyed 7 years and 7 months period regardless of the elongation between Earth and Mars. This way to determine IMF polarity makes it less sensitive to the time resolution of IMF proxy. All events including those occurring near sector boundaries or not clustering as described above were classified as “other”. “Other”

events include solar wind disturbances such as Corotating Interaction Regions (CIRs) or Coronal Mass Ejections (CMEs) and “unknown” events that we cannot categorize due to the lack of distinguishing clustering of the IMF proxy or sector boundary.

When this thesis categorized the 1,145 magnetosheath penetration events based on the inferred IMF conditions, it turned out that 442 events are identified as the away polarity events, 155 events as the toward polarity, and 548 events as other. Other events included 233 CMEs or CIRs events under the low  $P_{dyn}$  conditions. The CMEs or CIRs events were selected from the enhancement of  $P_{dyn}$  proxy data and rotation of IMF draping direction proxy.

## 3.4 Statistical Analysis

### 3.4.1 Dependence on the Solar Wind Dynamic Pressure

Firstly, this thesis investigates the dependence of the selected 1,145 magnetosheath penetration events on the  $P_{dyn}$  proxy. Figure 3.3 shows the total duration (histogram) and the observational probability (line plot) of the magnetosheath penetration events as a function of the MGS  $P_{dyn}$  proxy. The observational probability means the duration of events under each  $P_{dyn}$  condition divided by the total observation time under each  $P_{dyn}$  condition during about 7.6 years. Figure 3.3 shows that the observational probability

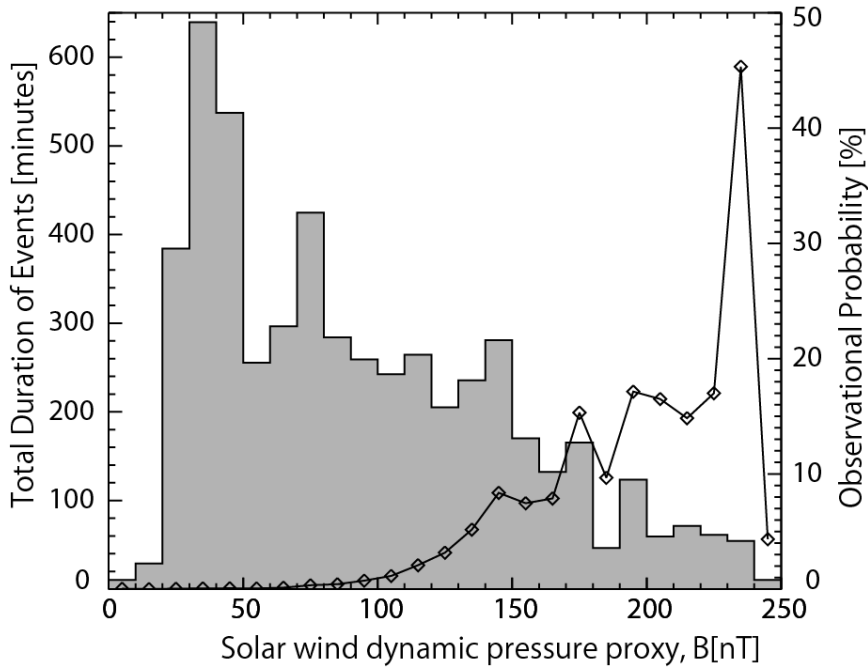


Figure 3.3: Histogram of the total duration and line plot of observational probability of the magnetosheath penetration events as a function of the solar wind dynamic pressure proxy obtained from the MAG/MGS observations.

(line plot) increases when the  $P_{dyn}$  proxy exceeds about 100 nT. This tendency is consistent with *Brain et al.* [2005]. Thus, henceforth the relatively lower  $P_{dyn}$  condition of  $\leq 100$  nT is defined as the “low”  $P_{dyn}$  periods, while the higher  $P_{dyn}$  periods of  $> 100$  nT are referred to as the “high”  $P_{dyn}$  periods. Assuming that the upstream dynamic pressure is balanced to the magnetic pressure on the dayside magnetic pile-up region, a dynamic pressure proxy of 100 nT can convert into a dynamic pressure of approximately 4 nPa. It can also be seen that there are a significant number of events even during the low  $P_{dyn}$  periods in Figure 3.3. Furthermore, the duration of the magnetosheath penetration events under the low and high  $P_{dyn}$  conditions accounts for

59.6 % and 40.4 % of the total duration, respectively. Therefore, more than the half of the magnetosheath penetration events was observed under the low  $P_{dyn}$  conditions. It should be noted that there is a rough tendency that short duration events are often seen under the low  $P_{dyn}$  conditions.

### 3.4.2 Dependence on the Mars Solar Orbital (MSO) Latitude

Next this thesis investigates the dependence on the observed event locations in terms of the Mars-centered Solar Orbital (MSO) latitude. MSO coordinate system is defined as follows: the  $X_{MSO}$  axis points from Mars to the Sun, the  $Y_{MSO}$  axis is opposite to the Mars orbital motion and the  $Z_{MSO}$  axis completes the right-handed system. The MSO latitude is computed via  $\arctan(Z_{MSO}/\sqrt{X_{MSO}^2 + Y_{MSO}^2})$ . Figure 3.4 shows the total duration (histogram) and the observational probability (line plot) of the magnetosheath penetration events as a function of the MSO latitude separately for the low (Figure 3.4a) and the high (Figure 3.4b)  $P_{dyn}$  periods. Both for the low and the high  $P_{dyn}$  cases, the observational probability is higher near  $0^\circ$  of the MSO latitude where the  $P_{dyn}$  is the highest. During the low  $P_{dyn}$  periods, the events tend to be observed in low latitudes of the northern hemisphere. On the other hand, during the high  $P_{dyn}$  periods, the events are distributed over a wide latitude range both in the southern and northern hemispheres.

The magnetosheath penetration peaking in the northern hemisphere is consistent with a previous study by *Brain et al.* [2005]. It is considered that the strong magnetic pressure of the localized crustal fields in the southern hemisphere pushes MPB to higher altitudes, preventing magnetosheath penetration. As the  $P_{dyn}$  increase, the shielding due to the crustal magnetic fields becomes less effective at the 400 km altitude and the magnetosheath penetration more frequently occurs in a wide latitude range.

As shown in Figure 3.5a, the events during low  $P_{dyn}$  periods are mostly observed in the region where the crustal magnetic field is relatively weak ( $< 25$  nT). This result is consistent with the concentration of magnetosheath penetration events in the northern hemisphere. On the other hand, the observation probability of the magnetosheath penetration during the high  $P_{dyn}$  periods is relatively constant regardless of the strength of the crustal magnetic fields (Figure 3.5b). It may indicate that such a high  $P_{dyn}$  condition is enough to overcome the magnetic pressure due to the crustal magnetic fields. Or the high  $P_{dyn}$  might make cusps due to the crustal magnetic fields wider than usual. Another possibility might be that the magnetic reconnection [e.g., *Halekas et al.*, 2009; *Brain et al.*, 2010b] plays an important role in eroding mini-magnetosphere. However, the observation probability during the high crustal magnetic field events (larger than 100 nT) is statistically less significant because of the small total duration of

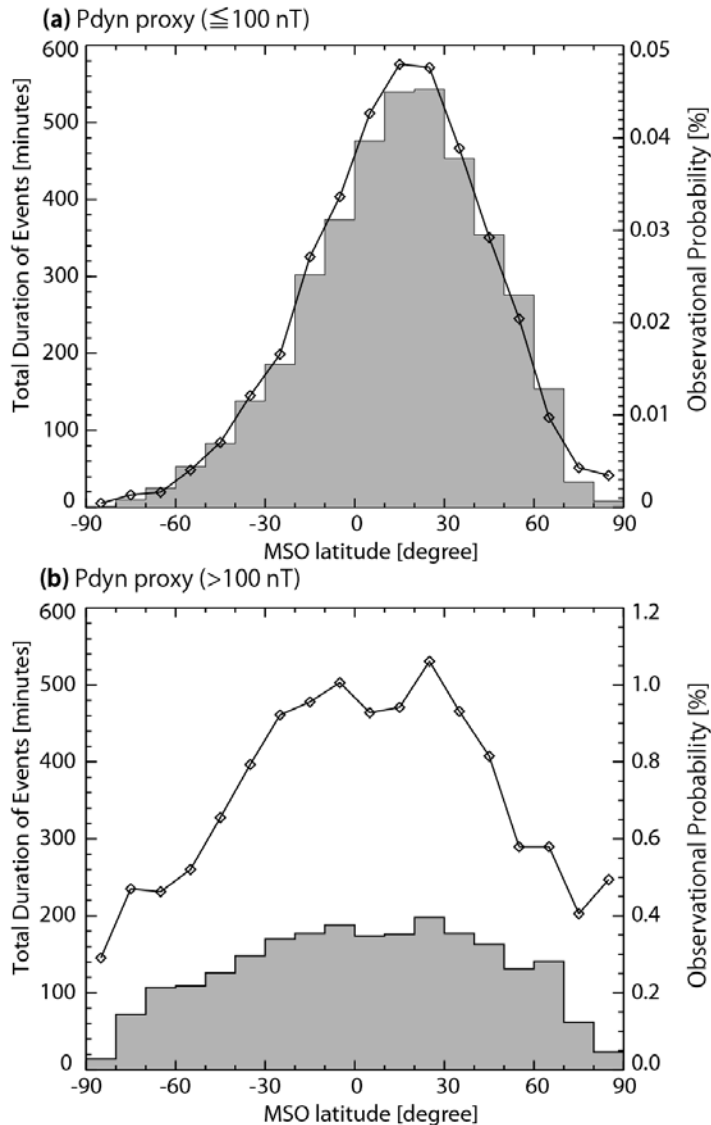


Figure 3.4: Histograms of the total duration and line plots of observational probability of the magnetosheath penetration events as a function of the MSO latitude, under (a) the low and (b) the high solar wind dynamic pressure ( $P_{dyn}$ ) conditions.

events (22.3 minutes or 1% of the histogram in Figure 3.5b). We shaded these less significant bins differently in Figure 3.5b.

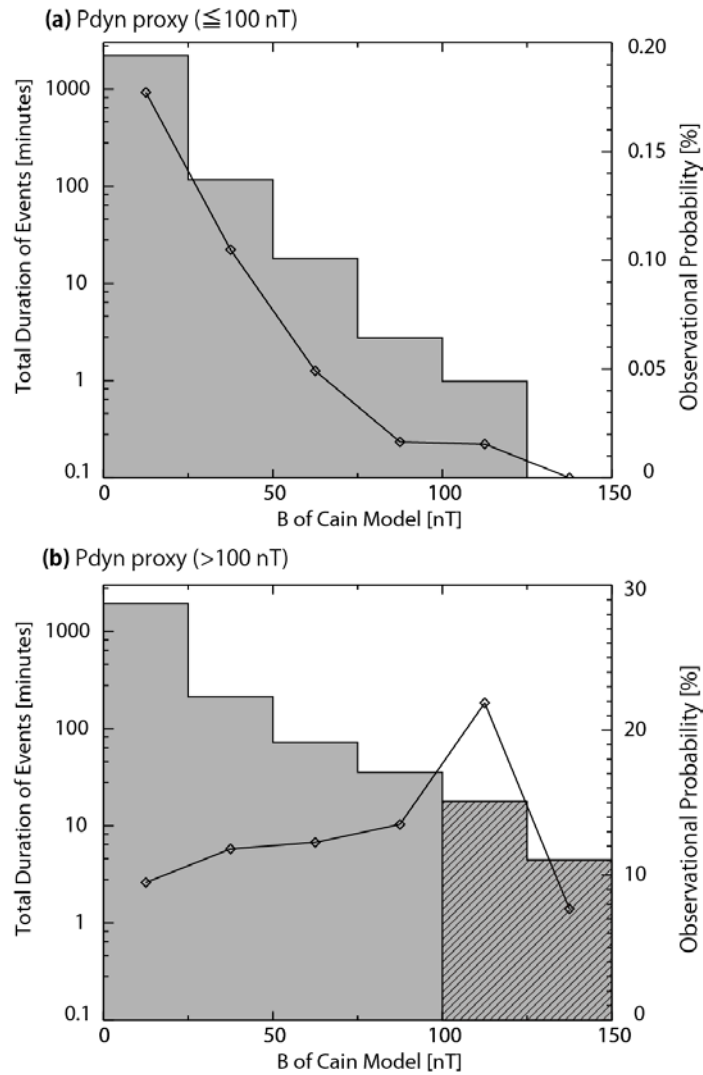


Figure 3.5: Histograms of the total duration and line plots of observational probability of the magnetosheath penetration events as a function of the estimated magnitude of crustal magnetic field from the Cain model [Cain et al., 2003], under (a) the low and (b) the high solar wind dynamic pressure ( $P_{dyn}$ ) conditions.

### 3.4.3 Dependence on the IMF Polarity

Table 3.1: Duration of each solar wind condition, ratio of each solar wind condition, number of events, ratio of events' duration, and ratio of observational probability (normalized by toward)

Solar wind condition	High P <sub>dyn</sub> ( $>100$ nT)			Low P <sub>dyn</sub> ( $\leq 100$ nT)		
	Away	Toward	Other			Total
Duration of each solar wind condition (days)	38.8	1,172.1	768.6	622.7		2,563.4
Ratio of each solar wind condition (%)	1.5	45.0	29.5	23.9		98.5
Events	High P <sub>dyn</sub> ( $>100$ nT)	Away	Toward	Low P <sub>dyn</sub> ( $\leq 100$ nT)		
Number of events(#)	248	416	150	CMEs or CIRs	Unknown	Total
Event total (hours)	35.2	20.9	5.6	19.9	5.4	51.8
Ratio of events' duration (%)	40.4	24.1	6.5	22.8	6.2	59.6
Ratio of observational probability (normalized by toward)	124.3	2.4	1	4.4	1.2	

In Subsection 3.3.2, 1,145 events were categorized into three categories (away, toward, other) in terms of the upstream IMF conditions. During the high  $P_{dyn}$  periods, it is natural to conclude that the  $P_{dyn}$  is strong enough to make the magnetosheath plasma to penetrate down to 400 km altitude. Most of the high  $P_{dyn}$  events are categorized as “other”, since high  $P_{dyn}$  is often caused by solar wind disturbances such as CIRs or CMEs. On the other hand, during the low  $P_{dyn}$  periods, other mechanisms are needed to cause the magnetosheath penetrations into 400 km altitude, especially when there are no CIRs or CMEs. Therefore, this thesis focuses on the 566 events (away and toward events) observed during the low  $P_{dyn}$  periods and further investigates their dependence on IMF polarity. Table 3.1 shows the summary of the magnetosheath penetration events with respect to the estimated solar wind conditions. The second row in Table 3.1 shows that the ratio of away to toward sector polarities during the low  $P_{dyn}$  periods was about 1.5 during the survey period. By contrast, the number of magnetosheath penetration events during the away polarity is significantly larger than that of during toward polarity. From Table 3.1, the observational probability of events during the away IMF sector periods is approximately 2.4 times higher than that of during the toward IMF sector periods.

## 3.5 Summary and Discussion

This chapter reported the results of a statistical investigation of the penetration of Martian magnetosheath plasma down to 400 km altitudes analyzing ~7.6 years of the MGS MAG and ER data (April 1999 - November 2006). The semi-automatic event selection criteria based on these measurements were used in order to identify 1,145 magnetosheath penetration events. A proxy for solar wind dynamic pressure ( $P_{dyn}$ ) was used. A developed method to determine the IMF sector polarities by comparing the IMF direction measured at Earth (time-shifted ACE data) with the IMF draping direction at Mars (MGS data) was also used.

This thesis investigated the dependence of these 1,145 events on the  $P_{dyn}$ , the MSO latitude, the local crustal magnetic field strength, and the IMF sector polarity. The events were frequently observed during the relatively high  $P_{dyn}$  periods ( $> 100$  nT). However, the number of events are larger for the relatively low  $P_{dyn}$  periods ( $\leq 100$  nT), which occur more often. Moreover, the magnetosheath tends to penetrate mostly into regions where the crustal magnetic field is weak. The observation probability of the magnetosheath penetration is approximately 2.4 times higher under the away IMF sector polarity conditions than under the toward IMF sector polarity conditions during low  $P_{dyn}$  periods (Table 3.1).

It was also investigated that the threshold for electron flux used to select events. When using a more restrictive threshold (electron flux of  $5 \times 10^4 \text{ cm}^{-2} \cdot \text{s}^{-1} \cdot \text{sr}^{-1}$ , 1 order of magnitude higher than the previous threshold), the total duration of magnetosheath penetration events decreases by a factor of about 6. The number of events (215 events) also decreases. Nevertheless the observation probability of the magnetosheath penetration is more than 7 times higher under the away IMF sector polarity conditions than under the toward IMF sector polarity conditions during low  $P_{dyn}$  periods. The qualitative trends with IMF sector polarity are not dependent upon the choice of threshold value, even though some of the quantitative results vary.

As mentioned in Section 3.1, *Brain et al.* [2005] also investigated the dependence of magnetosheath plasma penetration at 400 km altitudes on the  $P_{dyn}$ , the IMF draping direction, and season. The differences between this study and *Brain et al.* [2005] are the method and time range. *Brain et al.* [2005] used only the electron energy spectra to identify the magnetosheath region from mid-1999 to February 2005. In this study, the fluctuation of the magnetic field and the intensity of electron flux were used to identify whether MGS observed the magnetosheath region or not in all MGS mapping orbit phase (from April 1999 to November 2006). Using not only the magnetic field but also electron data, the detection of the magnetosheath plasma observation is more

conservative. Moreover, this thesis compared MGS data with time-shifted ACE solar wind data to estimate the IMF polarity. It thus allows us to more precisely investigate the solar wind dependence of the magnetosheath penetration at 400 km altitude.

The results indicate that during the low  $P_{dyn}$  periods, both northern hemisphere events and “away” IMF polarity events are favored. Further investigation reveals that these two conditions are usually met at the same time - that is the observed events often occur in the northern hemisphere during “away” IMF polarity. On the one hand, the frequent observation in the northern hemisphere compared to the southern hemisphere is consistent with the previous study by *Brain et al.* [2005]. The north-south asymmetry is most likely caused by the stronger crustal magnetic fields in the southern hemisphere than in the northern hemisphere. The northern hemisphere during the “away” IMF conditions corresponds to the upward electric field hemisphere, where the convective electric field is pointing away from Mars. It implies that the magnetosheath penetrations more often occur in the upward electric field hemisphere than in the downward electric field hemisphere. *Brain et al.* [2005] pointed out the sheath observations peak locally eastward, i.e. the IMF draping direction is around  $0^\circ$ . From these results, the magnetosheath penetration events tend to be observed during IMF away sector polarity which corresponds to the IMF draping direction clustering from  $210^\circ$  to  $0^\circ$ . Therefore,

this tendency is consistent with *Brain et al.* [2005].

This thesis suggests that one of the possible physical mechanisms is the Kelvin-Helmholtz instability (KHI). Previous two-dimensional global hybrid simulation to investigate the solar wind interaction with an unmagnetized planet pointed out that the upward electric field hemisphere enhances KHI [*Terada et al.*, 2002]. In the hemispheres of the upward electric field, the wavy structures generated by the KHI in the boundary of the simulation domain, which has shear of velocity and density, tend to be enhanced. This enhancement may make the magnetosheath plasma penetrate to lower altitudes than usual.

Another possibility might be the asymmetry in the magnetosheath caused by the solar wind electric field expected by the asymmetric distribution of planetary pickup ions [e.g., *Kallio et al.*, 2010]. If the pickup ions raise the temperature anisotropy, the resultant mirror-mode instability might cause the density fluctuations around the Martian ionopause [*Gurnett et al.*, 2010]. The enhanced density fluctuation is another candidate physical mechanism to explain the magnetosheath penetration.



# **Chapter 4**

## **Statistical Study Part II: MAVEN Observations Statistical Study of the Relation between the Plasma Boundaries around Mars**

### **4.1 Introduction**

The direct interaction between the solar wind and the Martian upper atmosphere forms a characteristic transition region between the shocked solar wind (magnetosheath) and the Martian ionosphere. In-situ spacecraft observations over the past several decades have led to the identification of several plasma boundaries in the transition region: the induced magnetosphere boundary (IMB) [e.g. *Vignes et al.*, 2000; *Dubinin et al.*, 2006], the magnetic pile-up boundary (MPB) [e.g., *Trotignon et al.*, 2006; *Matsunaga et al.*, 2015], the ion composition boundary (ICB) [e.g., *Sauer et al.*, 1994], the planetopause

[*Riedler et al.*, 1989], the protonopause [*Sauer et al.*, 1994], and the pressure balance boundary [e.g., *Brain et al.*, 2010a; *Xu et al.*, 2016]. The IMB regarded as same as MPB [*Vignes et al.*, 2000], and ICB regarded as same as protonopause and planetopause [e.g., *Breus et al.*, 1991]. Therefore, Chapter 4 will use the following boundary names in this study as the representative of the each category of the boundaries: IMB, ICB, and the pressure balance boundary.

When the spacecraft passes the IMB from the magnetosheath to the Martian induced magnetosphere, fluctuations of the magnetic field and the electron flux are known to decrease [e.g., *Nagy et al.*, 2004; *Trotignon et al.*, 2006; *Matsunaga et al.*, 2015]. On the other hand, when the spacecraft passes the ICB from the magnetosheath side to the Martian side, the main ion component changes from the solar wind protons to the planetary heavy ions [e.g., *Breus et al.*, 1991]. Previous simulation studies [e.g., *Brain et al.*, 2010a] pointed out that the magnetic pressure, the dynamic pressure, and the thermal pressure contributed to the pressure balance in the plasma environment around Mars. *Brain et al.* [2010a] reported that a transition from an upstream region dominated by plasma dynamic pressure to a magnetosheath region dominated by thermal pressure to a low altitude region dominated by magnetic pressure. However, recently, *Xu et al.* [2016] reported that the dynamic pressure is important in the flanks of Mars and showed

that  $\beta^*$  boundary, which is determined by the pressure ratio  $\beta^* = 1$  (where the  $\beta^*$  is defined as the ratio of the sum of plasma thermal and dynamic pressure to the magnetic pressure), matches reasonably well with ICBs.

A classical view of the induced magnetosphere formation is due to the mass loading process by pickup heavy ions originated from the neutral oxygen corona around Mars. From this view, IMBs and ICBs are expected to be observed at similar locations at least on the dayside. On one hand, a sudden increase of the magnitude of the magnetic field at the IMB is also appeared due to the deflection and piled up the IMF [e.g., *Breus et al.*, 1989; *Dubinin and Lundin*, 1995]. The magnetosheath can penetrate into  $\sim$ 400 km altitude [e.g., *Brain et al.*, 2005; *Matsunaga et al.*, 2015]. The Kelvin-Helmholtz instability (KHI) caused by a velocity shear across a boundary is also considered as the possible physical mechanism to characterize the Martian plasma boundary location [e.g., *Gurnett et al.*, 2011; *Matsunaga et al.*, 2015; *Ruhunusiri, et al.*, 2016].

Since Mars Global Surveyor (MGS) did not carry any ion detector and its mapping orbit was fixed around 400 km altitudes [*Albee et al.*, 2001], the ICB and the pressure balance boundary were not able to be investigated using the MGS data. Both, Phobos-2 and Mars Express (MEX) carried an ion mass analyzer, and observed the ICB [e.g., *Breus et al.*, 1991, *Dubinin et al.*, 2006]. Unfortunately, the observation period of

Phobos-2 was short until its signal lost and MEX lacked a magnetometer. Thus, the relations between IMBs, ICBs, and the pressure balance boundaries are still incompletely understood due to the lack of long-term simultaneous observations of the magnetic field, electrons, and ion composition near Mars. Some MHD, multifluid MHD, and hybrid simulations have been developed to investigate the Martian plasma environment, including the plasma balance boundaries [e.g., *Simon et al.*, 2007; *Brain et al.*, 2010a; *Fang et al.*, 2015; *Xu et al.*, 2016]. Utilizing simultaneous ion, electron, and magnetic field observations by MAVEN, this chapter conducted a statistical study of IMBs, ICBs, and pressure balance boundaries to investigate their relations and dependence on solar wind conditions and geographical configuration (location of strong crustal magnetic fields). The pressure balance boundary is based on  $\beta^*$  value proposed by Xu et al. [2016] ( $\beta^* = (P_{th} + P_{dyn}) / P_B$ , where  $P_{th}$ ,  $P_{dyn}$ , and  $P_B$  represent the plasma thermal pressure, the dynamic pressure, and the magnetic pressure, respectively). Hereafter, this boundary is referred to as “ $\beta^*$  boundary” in this study.

MAVEN entered into orbit around Mars on September 2014 and started simultaneous ion, electron, neutrals gas, and magnetic field measurements. MAVEN has a science mapping orbit with a periapsis and apoapsis altitude of ~150 km and ~6200 km, respectively. The data obtained from the Solar Wind Electron Analyzer

(SWEA) [Mitchell *et al.*, 2016], the Suprathermal and Thermal Ion Composition (STATIC) analyzer [McFadden *et al.*, 2015], Magnetometer (MAG/MAVEN) [Connerney *et al.*, 2015], and the Solar Wind Ion Analyzer (SWIA) [Halekas *et al.*, 2013] onboard MAVEN are used in this chapter. The SWEA electron data were utilized to identify IMBs. The STATIC ion mass composition data were utilized to identify the ICB. The MAG/MAVEN magnetic field data were utilized to identify the IMB and  $\beta^*$  boundarr. The SWIA ion data were utilized to identify the  $\beta^*$  boundary and to infer the solar wind parameters. The using data are recorded from 27 November 2014 to 17 March 2015 and from 4 June 2015 to 24 October, 2015, when the MAVEN orbital configuration allowed direct measurements of the solar wind conditions.

Section 4.2 explains an algorithm to automatically identify the Martian plasma boundaries, and show two example time events. Section 4.3 reports on results of the statistical analyses. Finally, Section 4.4 summarizes the results and discusses the global structure of the Martian plasma boundaries.

## 4.2 Automatic Identification of the Martian Plasma Boundaries

In order to identify the IMB, ICB, and  $\beta^*$  boundary, we developed a method for automatically identifying each boundary based on the ion, electron, magnetic field measurements from MAVEN. This chapter only focuses on the plasma boundaries in the sunlit region.

### 4.2.1 Identification of the Induced Magnetosphere Boundary (IMB)

From *Trotignon et al.* [2006], *Matsunaga et al.* [2015], and other previous studies [e.g., *Mitchell et al.*, 2001; *Brain et al.*, 2003, 2006b; *Nagy et al.*, 2004; *Crider et al.*, 2005; *Bertucci et al.*, 2005], when a spacecraft crosses the IMB, the fluctuations of the magnetic field and the electron energy flux characteristically change. Therefore, the fluctuation of magnetic field from MAG/MAVEN and the electron flux from SWEA are used in order to identify the IMB crossings.

First, the index of magnetic field fluctuation ( $B_{index}$ ) was calculated from the integrated power spectral density ( $PSD$ ) by the wavelet of magnetic field fluctuation above 0.1 Hz and the magnitude of the magnetic field ( $/B/$ ) using the Equation 4.1:

$$B_{index} = \text{the integrated PSD (above } 0.1\text{Hz) / } |B| \quad (4.1)$$

The use of *the integrated PSD (above 0.1Hz)* is similar to the method employed in *Matsunaga et al.* [2015] and a new practical criterion in order to identify the high fluctuations in the magnetosheath. We confirmed that this index enables to identify the magnetosheath region by inspection. Thus, we considered that observations for which  $B_{index}$  exceeded 0.5 were inferred to be in the magnetosheath region.

Next, the time derivative of electron flux of 80 eV above  $2 \times 10^6 \text{ cm}^{-2} \cdot \text{s}^{-1} \cdot \text{sr}^{-1}$  was calculated. In order to avoid selecting fluctuations of electron flux in the ionosphere, a lower limit was set. According to MEX observations [*Dubinin et al.*, 2006] (see Figure 1.7 in Subsection 1.2.2) and MGS observations [*Trotignon et al.*, 2006] (see Figure 1.18 in Subsection 1.3.2), the electron flux at 80 eV is relatively dominant in the magnetosheath region and characteristically changes after crossing the IMB. The observations were corrected for the spacecraft potential (see Subsection 2.3.1) before being used.

Finally, the peak of the time derivative of the 80 eV electron flux was chosen as the location of the IMB crossing, based on the inspection of many orbits of data. Using both the magnetic field and electron signatures described above, 1,097 IMB crossing events were identified in 1,294 orbits of MAVEN.

## 4.2.2 Identification of the Ion Composition Boundary (ICB)

From *Breus et al.* [1991], and other previous studies[e.g., *Lundin et al.*, 1989; *Sauer et al.*, 1994; *Dubinin et al.*, 2006], when a spacecraft crosses the ICB, the ion composition changes from predominantly solar wind protons ( $H^+$ ) to predominantly planetary heavy ions ( $O^+, O_2^+$ ). Therefore, ion number densities from STATIC are used in order to identify the ICB. The calculation of ion number densities took into account the spacecraft potential (see Subsection 2.3.1) and the straggling issue of STATIC (see Figure 1.18 in Subsection 2.3.4).

First, the density ratio of between the solar wind proton ( $H^+$ ) and the sum of planetary heavy ions ( $O^+, O_2^+$ ) was calculated (used the Equation 4.2).

$$\text{Density ratio} = (n_{O^+} + n_{O_2^+}) / n_{H^+} \quad (4.2)$$

Finally, the time that density ratio equaled 1 was chosen as the point of ICB crossings. After the identification of the time of ICB crossings, its validity was verified by inspection. Thus, the 1,709 ICB crossing events were identified in 1,294 orbits of MAVEN.

### 4.2.3 Identification of the Pressure Balance Boundary

The main components of the total pressure around the Martian plasma environment are the magnetic pressure, the dynamic pressure, and the thermal pressure. *Brain et al.* [2010a] reported that MHD, multi-fluid, and hybrid simulations showed a transition from an upstream region dominated by plasma dynamic pressure to a magnetosheath region dominated by thermal pressure to a low altitude region dominated by magnetic pressure. However, recently, *Xu et al.* [2016] reported that the dynamic pressure is important in the flanks of Mars. The observed values of the magnetic pressure, the dynamic pressure, and the thermal pressure obtained by using the ion density, ion velocity, and ion temperature derived from the SWIA data and the magnetic field data from the MAG/MAVEN data.

This chapter uses the  $\beta^*$  value proposed by *Xu et al.* [2016] identify the location of the pressure balance boundary according to Equation 4.3, which is the sum of the plasma thermal pressure ( $P_{th}$ ) and dynamic pressure ( $P_{dyn}$ ) divided by the magnetic pressure ( $P_B$ ),

$$\beta^* = (P_{th} + P_{dyn}) / P_B \quad (4.3)$$

The time when  $\beta^* = 1$  was chosen as the point of the  $\beta^*$  boundary crossing. After the identification of the time of  $\beta^*$  boundary crossings, its validity was verified by

inspection. Thus, 1,107  $\beta^*$  boundary crossing events were identified in 1,294 orbits of MAVEN.

#### 4.2.4 January 21, 2015 Event and September 16, 2015 Event

Here introduces two examples of MAVEN plasma boundaries crossing events on January 21, 2015 and September 16, 2015.

##### 4.2.4.1 January 21, 2015 Event

Figure 4.1 and Figure 4.2 show the MAVEN trajectories and the time series plots on January 21, 2015, respectively.

The inbound (trajectory toward to periapsis) crossings of this event are on the terminator in the southern hemisphere. At this time, the location of the ICB (left blue line in Figure 4.2) is higher than the other boundaries. The location of the IMB (left red line in Figure 4.2) is similar to that of the  $\beta^*$  boundary (left black dash line in Figure 4.2). The outbound (trajectory away from periapsis) crossings of this event are on the terminator in the northern hemisphere. At this time, the location of the IMB (right red line in Figure 4.2) is higher than other two boundaries. The location of the ICB (right blue line in Figure 4.2) is similar to that of the  $\beta^*$  boundary (right black line in Figure 4.2).

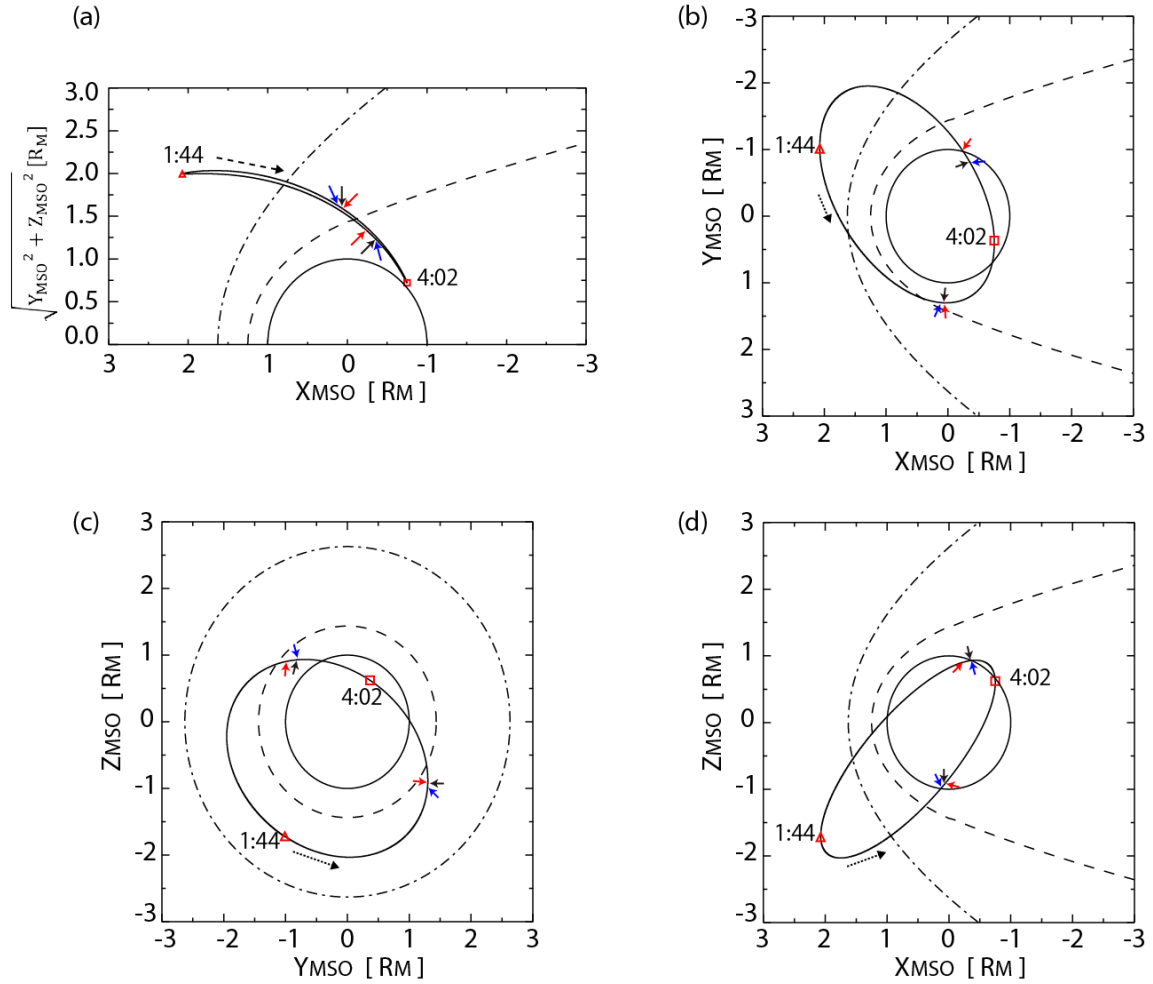


Figure 4.1: The MAVEN trajectories in the Mars-centered Solar Orbital (MSO) coordinates with units of Mars radii (3397km) on January 21, 2015 event: (a) a cylindrical ( $\sqrt{Y_{mso}^2 + Z_{mso}^2}$ ), (b)  $X_{mso}$ - $Y_{mso}$ , (c)  $Y_{mso}$ - $Z_{mso}$ , (d)  $X_{mso}$ - $Z_{mso}$  coordinates. Red, black, and blue arrows show the location of the IMB,  $\beta^*$  boundary, and ICB crossing, respectively. The models of the bow shock (BS) and the induced magnetosphere boundary (IMB) [Trotignon et al., 2006] are shown with the dash-dotted line and dashed line, respectively. The red square, the red triangle, and black dotted arrow show the periapsis, the apoapsis, the direction of MAVEN orbit, respectively.

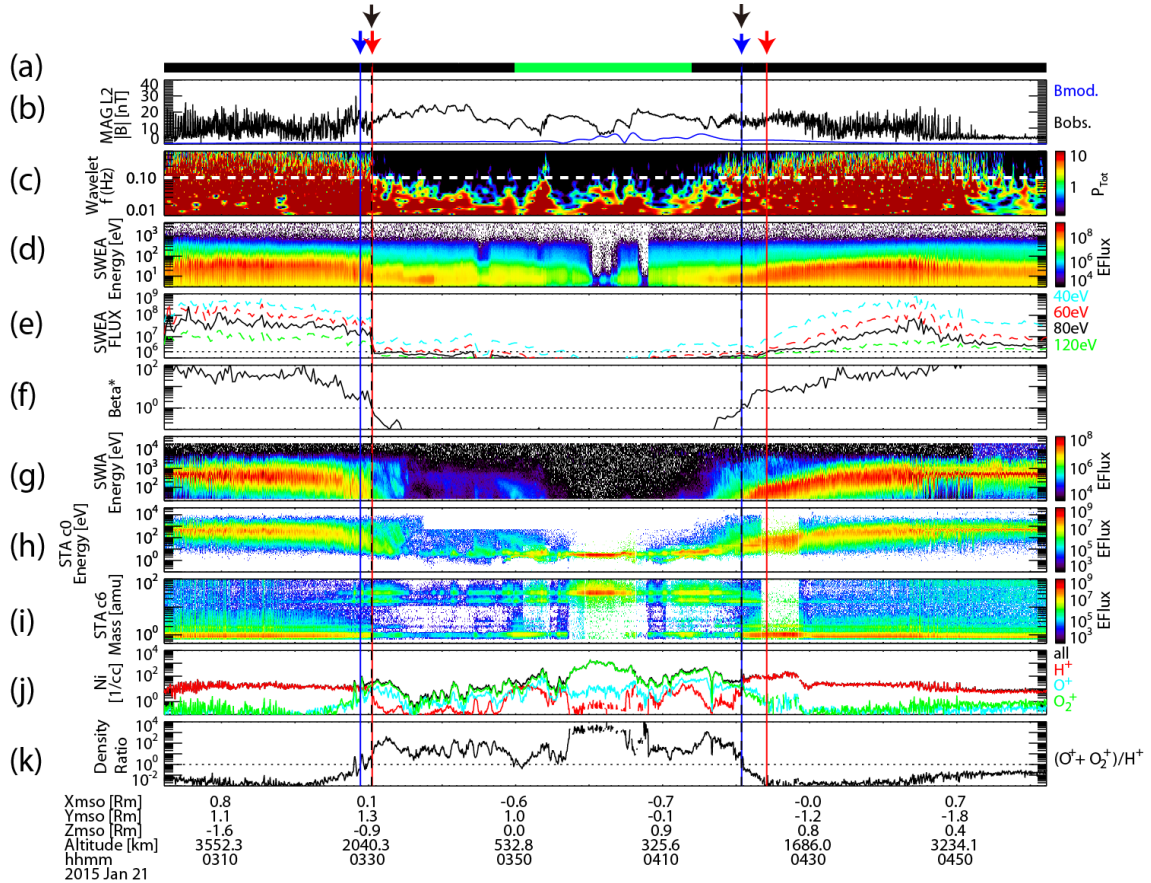


Figure 4.2: Overview time series plot of the plasma boundaries crossing event observed by MAVEN on January 21, 2015: (a) the wake indices (black is not-wake region), (b) the magnitude of magnetic field (black is the observational data and blue is the expected crustal magnetic field magnitude [Cain et al., 2003]), (c) the wavelet of magnetic field data (white line shows 0.1 Hz), (d) the electron energy flux, (e) the electron energy fluxes for four energy ranges (dash line shows  $2 \times 10^6 \text{ cm}^{-2} \cdot \text{s}^{-1} \cdot \text{sr}^{-1}$ ), (f)  $\beta^*$  value (dash line shows 1), (g) the ion flux from SWIA, (h) the ion energy flux from STATIC C0 mode, (i) the ion mass flux from STATIC C6 mode, (j) ion number densities from STATIC, (k) the ion number density ratio of  $(\text{O}^+ + \text{O}_2^+)/\text{H}^+$  (dash line shows 1). The vertical lines and arrows of red and blue indicate the time indices of IMB, and ICB crossing, respectively. The vertical dashed line and black arrow indicates the time index of the  $\beta^*$  boundary crossing. The periapsis is at 04:02:13.

#### 4.2.4.2 September 16, 2015 Event

Figure 4.3 and Figure 4.4 show the MAVEN trajectories and the time series plots on September 16, 2015, respectively.

The inbound crossings of this event are on the dayside in the southern hemisphere. At this time, the location of the ICB (left blue line in Figure 4.4) is similar to that of the IMB (left red line in Figure 4.4). The location of the  $\beta^*$  boundary (left black dash line in Figure 4.4) is higher than other two boundaries.

The outbound crossings of this event are on the nightside in the northern hemisphere. At this time, the location of the IMB (right red line in Figure 4.4) is higher than that of the ICB (right blue line in Figure 4.4). The location of the  $\beta^*$  boundary (right black dash line in Figure 4.4) is higher than the other two boundaries.

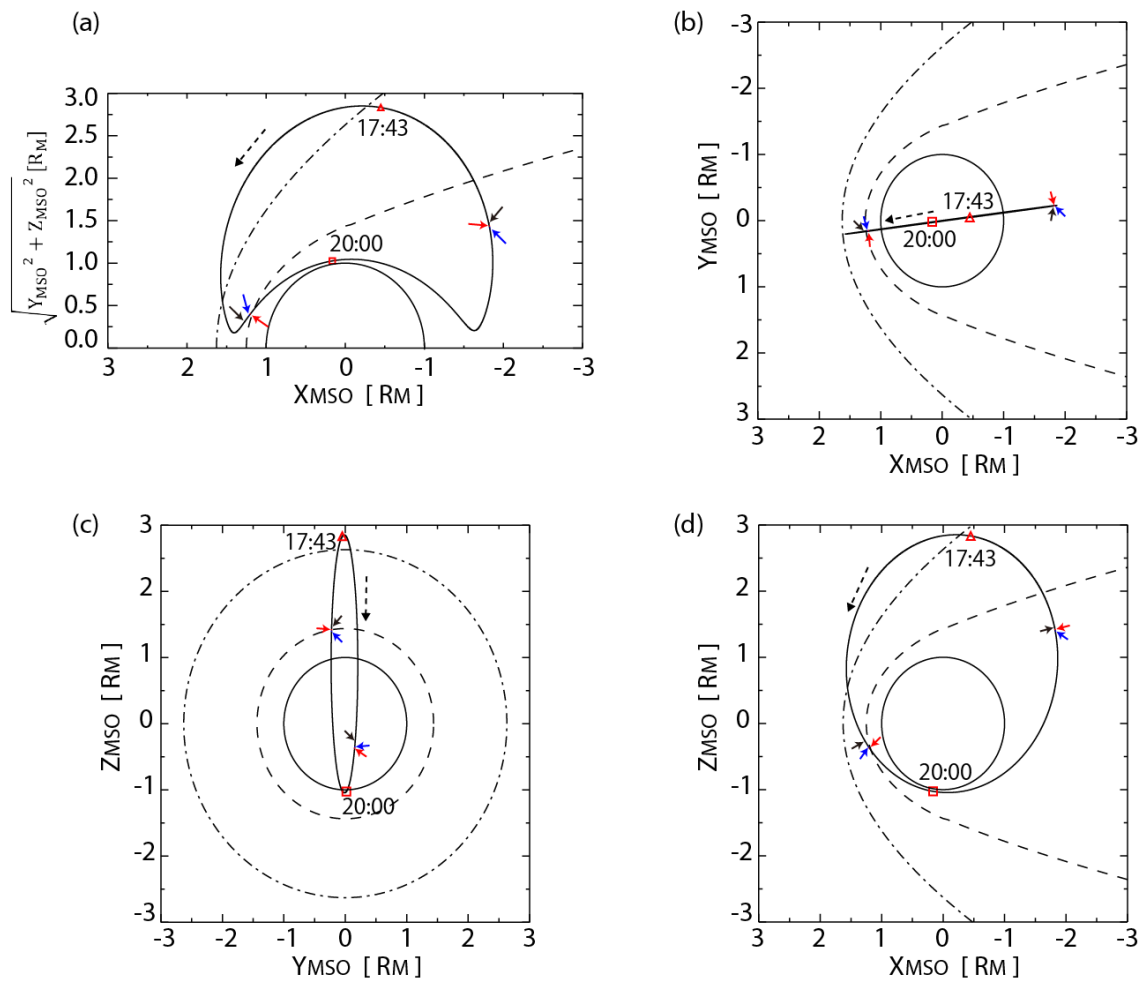


Figure 4.3: The MAVEN trajectories in the MSO coordinates on September 16, 2015 event. Red, black, and blue arrows show the location of the IMB,  $\beta^*$  boundary, and ICB crossing, respectively. The format is the same as Figure 4.1.

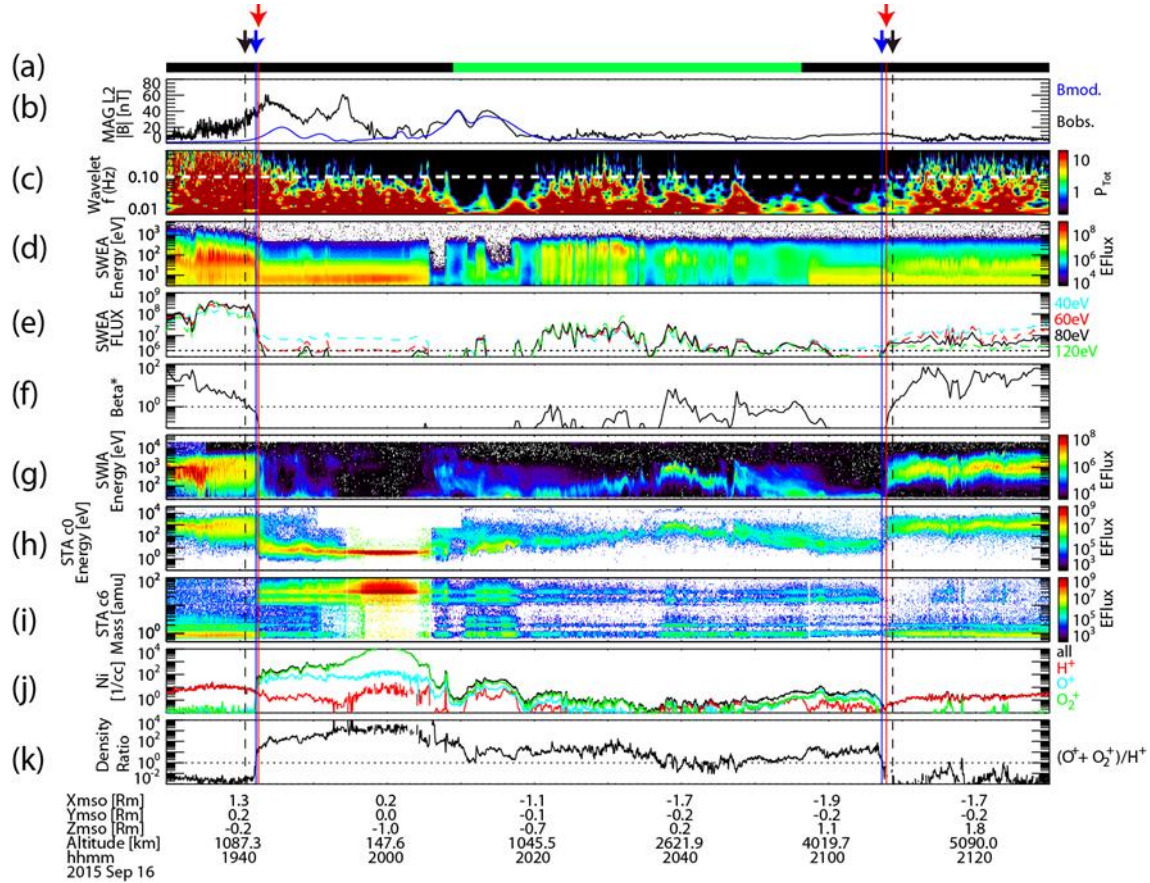


Figure 4.4: Overview time series plot of the plasma boundaries crossing event observed by MAVEN on September 16, 2015. The vertical line and arrow of red and blue indicate the time indices of the IMB, and ICB crossing, respectively. The vertical dashed line and black arrow of black indicates the time index of  $\beta^*$  boundary crossing. The format is the same as Figure 4.2. The periapsis is at 20:00:21.

## 4.3 Statistical Analysis

### 4.3.1 Locations of the Martian Plasma Boundaries

Firstly, this chapter reports the average locations of the three plasma boundaries. The locations of three plasma boundaries identified using the automatic identification described above are plotted in cylindrical coordinates.

Figure 4.5a, 4.5b, Figure 4.5d, 4.5e, and Figure 4.5g, 4.5h show the locations of the individual IMB,  $\beta^*$  boundary, and ICB crossings as plus signs, respectively. The figures also show the mean value of the radial distance ( $\sqrt{X_{MSO}^2 + Y_{MSO}^2 + Z_{MSO}^2}$ ) for every  $10^\circ$  of Solar Zenith Angle (SZA) as circles and the standard error as error bar. Figure 4.5a, 4.5d, 4.5g, Figure 4.5b, 4.5e, 4.5h, and Figure 4.5c, 4.5f, 4.5i show the events in the northern hemisphere, the southern hemisphere, and both hemisphere (solid line shows the northern hemisphere and the dash line shows the southern hemisphere), respectively. Figures 4.5c, 4.5f, and 4.5i show only the mean distance. Since the number of events in the southern hemisphere over SZA=140° is small, the mean value of the distance of the radial direction was calculated for SZA  $\leq 130^\circ$ .

These results show that all boundaries have a north-south asymmetry and the locations of all boundaries on the night side are higher in the southern hemisphere than the northern hemisphere.

Figure 4.6 shows only the mean distance of the IMB (red), ICB (blue), and  $\beta^*$  boundary (black). Figure 4.6a and Figure 4.6b show the events in the northern hemisphere and the southern hemisphere, respectively. From these results, the IMB and ICB tend to be located at the similar positions on the dayside. On the other hand, the IMB tends to be located higher than the ICB on the nightside. The  $\beta^*$  boundary tend to be located higher than other boundaries on the dayside.

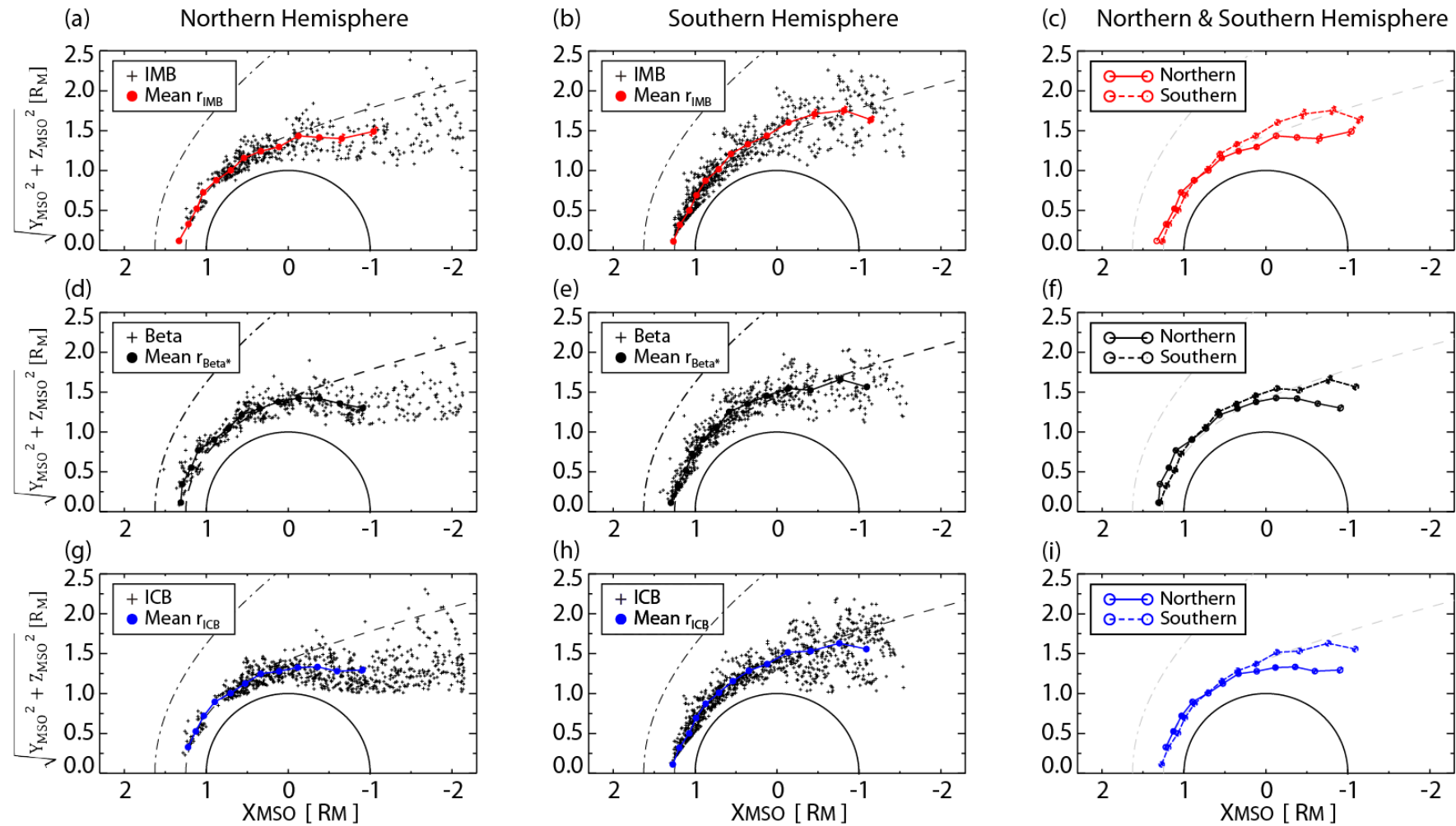


Figure 4.5: The observed locations of the IMB (a, b, c),  $\beta^*$  boundary (d, e, f), and ICB (g, h, i) in cylindrical coordinates (Left is sunward). The right panels, middle panels, and left panels show the crossing events in the northern hemisphere, the southern hemisphere, and both hemispheres, respectively. The mean values of radial distance for every  $10^\circ$  of Solar Zenith Angle (SZA) are plotted in all panels. Models for the BS and IMB are shown in all panels with the dash-dotted line and dashed line, respectively [Trotignon et al., 2006]. Error bars show the standard error

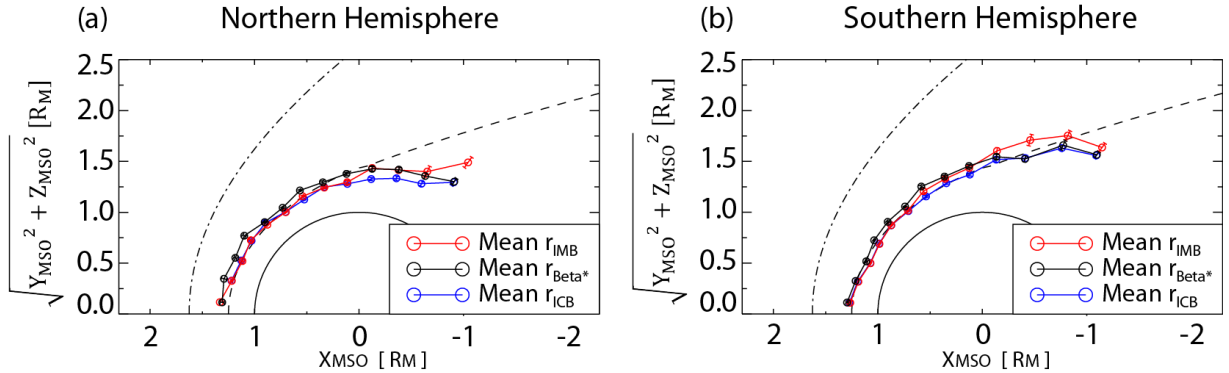


Figure 4.6: The mean altitude for every  $10^\circ$  of SZA: The red, blue, and black circle show the IMB, ICB, and  $\beta^*$  boundary, respectively. (a) and (b) use only events in the northern and the southern hemisphere, respectively. The format is the same as Figure 4.5.

### 4.3.2 Effect of the Solar Wind Dynamic Pressure

Secondly, this chapter investigates the effect of the solar wind dynamic pressure ( $P_{dyn}$ ) on the three plasma boundaries.

Figure 4.7a, 4.7b, Figure 4.7d, 4.7e, and Figure 4.7g, 4.7h show the locations of each IMB,  $\beta^*$  boundary, and ICB crossing, respectively, as plus signs. Colors indicate the value of  $P_{dyn}$ . Figure 4.7a, 4.7c, 4.7e, and Figure 4.7b, 4.7d, 4.7f show the events in the northern and the southern hemisphere, respectively.

The events of all boundaries during the high  $P_{dyn}$  period (red or orange color in Figure 4.7) tend to be located at lower altitudes. These results indicate the locations of all boundaries are affected by the  $P_{dyn}$ , corresponding with previous results [e.g., *Brain et al.*, 2003, 2006a; *Matsunaga et al.*, 2015].

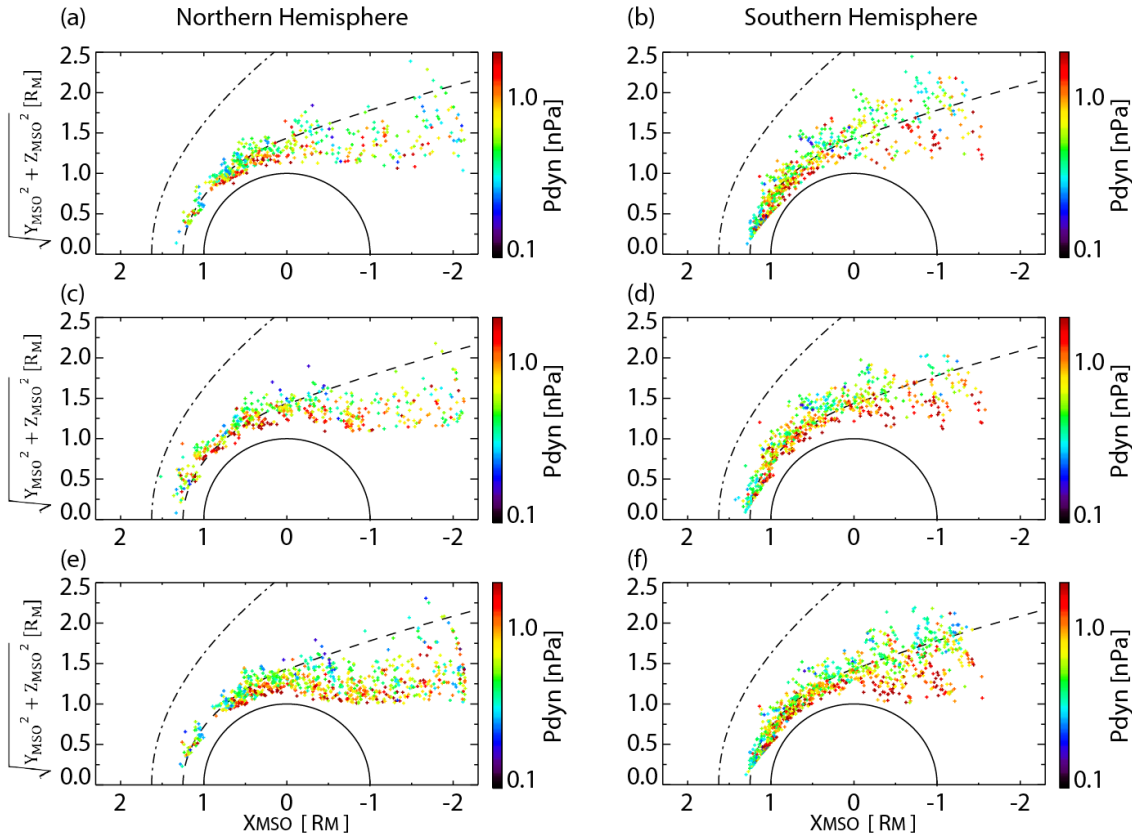


Figure 4.7: The observational locations of the IMB (a, b),  $\beta^*$  boundary (c, d), and ICB (e, f). (a, c, e) and (b, d, f) use only events in the northern and the southern hemisphere, respectively. The color code shows the solar wind dynamic pressure. The format is the same as Figure 4.5.

### 4.3.3 Effect of the Crustal Magnetic Fields

Thirdly, this chapter investigates the effect of the Martian crustal magnetic fields on the three plasma boundaries. Since MAVEN is a single speacecraft, it is difficult to quantitatively evaluate the effect of crustal magnetic fields when MAVEN crosses each of the boundaries. In order to investigate the location and qualitative effect of strong

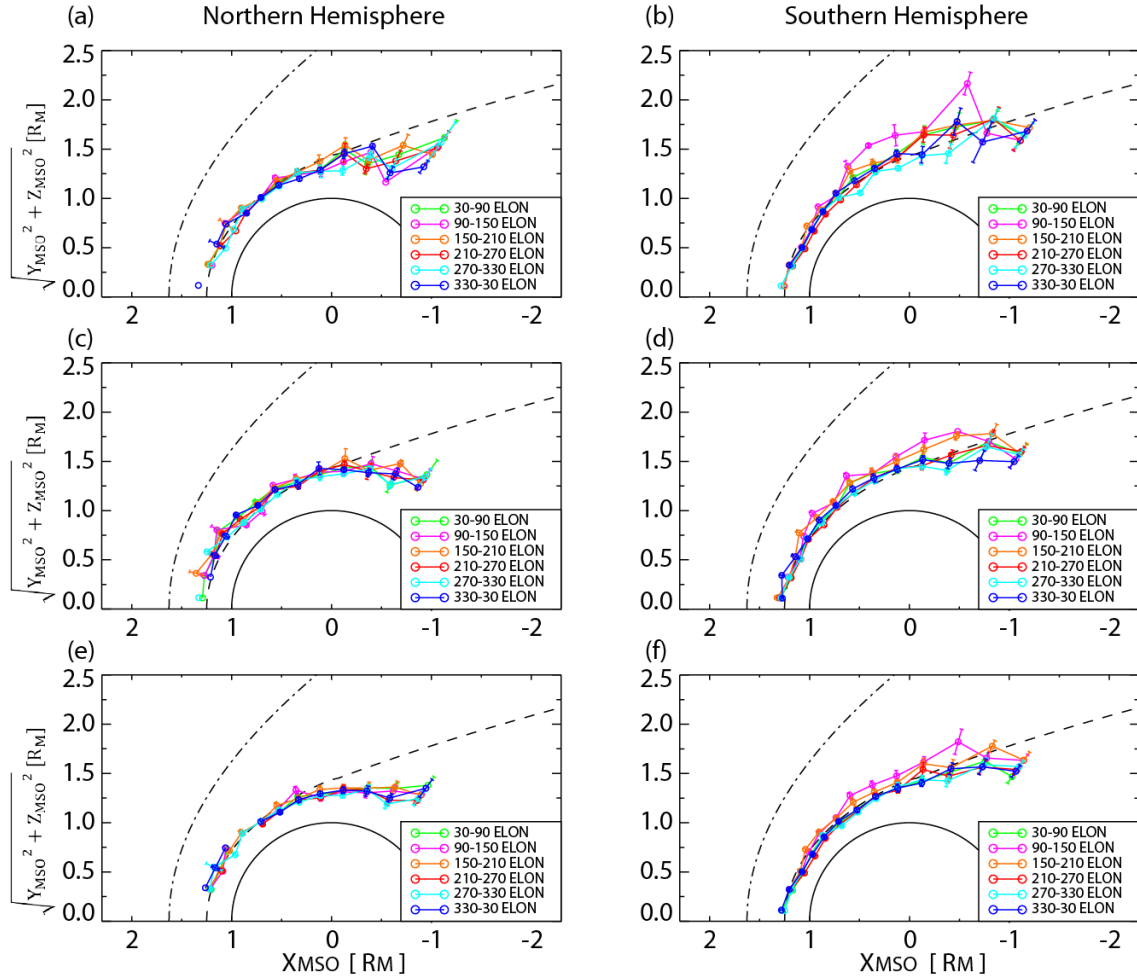


Figure 4.8: The mean altitude of the IMB (a, b),  $\beta^*$  boundary (c, d), and ICB (e, f). These values are calculated for every  $10^\circ$  of SZA and every  $60^\circ$  of the east longitude above the subsolar point. The format is the same as Figure 4.7.

crustal magnetic fields, this chapter used the east longitude above the subsolar point (hereafter, this east longitude is referred to as “subsolunar ELON”) at the time of each crossing event. From Figure 1.15 in Subsection 1.2.5, the strong crustal magnetic fields region ranges over  $90^\circ$  -  $210^\circ$  subsolar ELON [Connerney *et al.*, 2005]. Figure 4.8a, 4.8b, Figure 4.8c, 4.8d, and Figure 4.8e, 4.8f show the mean altitudes of the IMB,  $\beta^*$

boundary, and ICB crossing, respectively. These mean altitudes of the three boundaries are calculated for every  $10^\circ$  of SZA and every  $60^\circ$  of subsolar ELON. Figure 4.8a, 4.8c, 4.8e and Figure 4.8b, 4.8d, 4.8f show the events in the northern, and southern hemisphere, respectively.

In the northern hemisphere, it is difficult to recognize any variation related to the subsolar ELON. In the southern hemisphere, on the other hand, the mean altitudes of the three boundaries are higher when the crustal fields are near the subsolar point (magenta, orange, and red color in Figure 4.8) than at other times. These results show that all boundaries tend to be located at higher altitudes when the strong crustal magnetic fields region is near the subsolar point. However, on the nightside of the southern hemisphere, all boundaries tend to be located at higher altitudes than in the northern hemisphere regardless of the crustal magnetic fields locations.

#### **4.3.4 Relative Distances between IMB, ICB, and $\beta^*$ Boundary**

Fourthly, this chapter investigates the relative distance between the IMB, ICB, and  $\beta^*$  boundary based on the altitudes of the ICB by using crossing events of each boundary identified during the same orbit. Figure 4.9 shows the relative distances between the

IMB and ICB ( $r_{ICB} - r_{IMB}$ , red dots), and between the  $\beta^*$  boundary and ICB ( $r_{ICB} - r_{\beta^*}$ , black dots) and the mean value (red and black square) of them for every 0.1  $R_m$  of  $r_{ICB}$ .

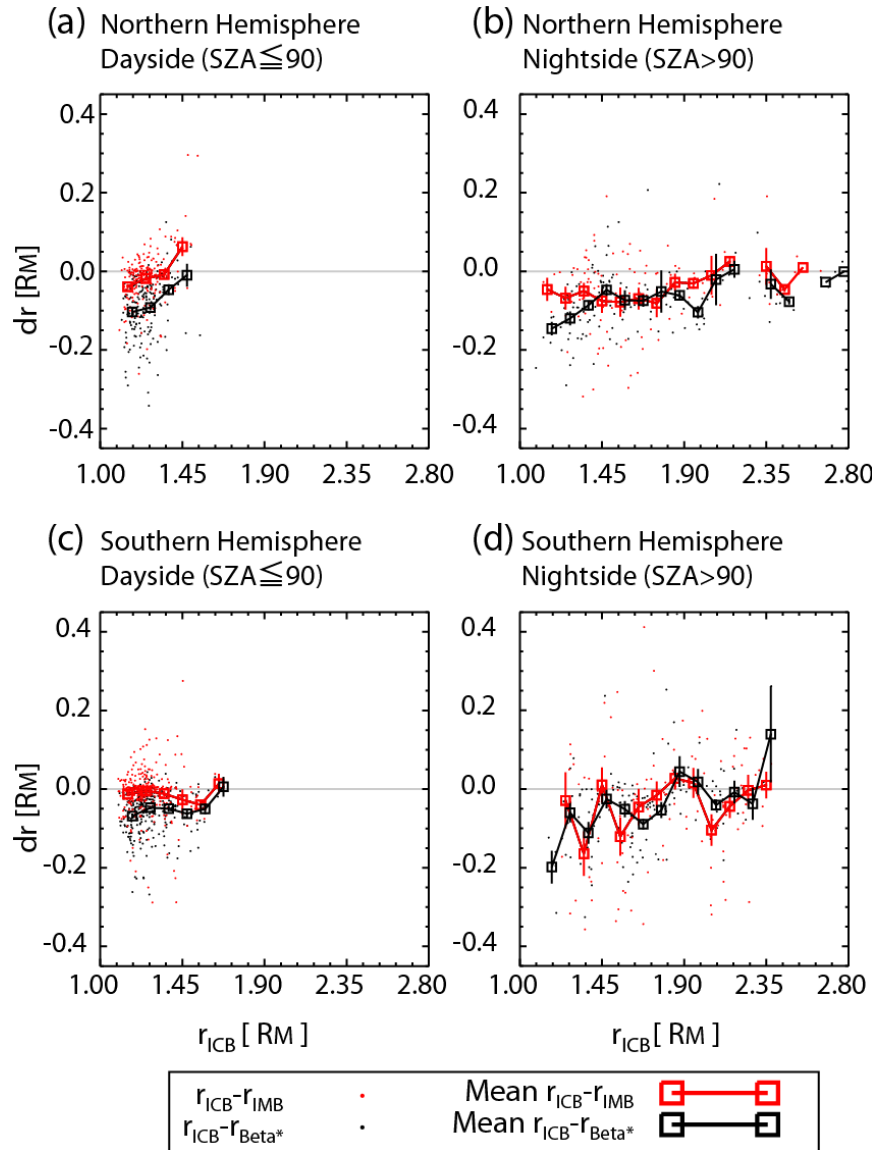


Figure 4.9: Red and black dots show the relative distance between the IMB and the ICB and between the  $\beta^*$  boundary and the ICB, respectively. The squares show the each mean value every 0.1  $R_m$  of  $r_{ICB}$ . (a, b) and (c, d) show in the northern and the southern hemisphere, respectively. (a, c) and (b, d) results for on the dayside and nightside, respectively. The gray solid line shows the relative distance is 0.

If  $r_{ICB} - r_{IMB} > 0$ , it means ICB is located higher than the IMB. Figure 4.9a, 4.9b and Figure 4.9c, 4.9d show the events in the northern and southern hemispheres, respectively. Figure 4.9a, 4.9c and Figure 4.9b, 4.9d show the events on the dayside ( $SZA \leq 90^\circ$ ) and the nightside ( $SZA > 90^\circ$ ), respectively. On the dayside, the IMB and ICB tend to be located at similar positions in both hemispheres and the  $\beta^*$  boundary tends to be located higher than other boundaries. On the nightside, the IMB tends to be located higher than the ICB in both hemispheres. The  $\beta^*$  boundary tends to be located higher than the ICB. However, when the ICB is located at high altitudes  $\beta^*$  boundary tends to be located at a similar or lower position than the ICB.

This chapter also investigates the relation between the relative distance of the crossing events on the nightside and the solar wind induced electric field. In order to investigate the effect of solar wind induced electric field, the latitude of the MAVEN spacecraft expressed in the Mars-Sun-Electric field (MSE) coordinate system is used. The MSE coordinate system is defined as follows: the  $X_{MSE}$  axis points from Mars to the Sun, the  $Z_{MSE}$  axis along the direction of the solar wind induced electric field,  $\mathbf{E}_{sw} = -\mathbf{V}_{sw} \times \mathbf{B}$  (the local magnetic field  $\mathbf{B}$  measured by MAG/MAVEN and the solar wind velocity  $\mathbf{V}_{sw}$  from SWIA data), and  $Y_{MSE}$  axis completes the right-handed system. Then, the MSE latitude ( $\theta_{MSE}$ ) is computed via  $\arctan(Z_{MSE} / \sqrt{X_{MSE}^2 + Y_{MSE}^2})$ .

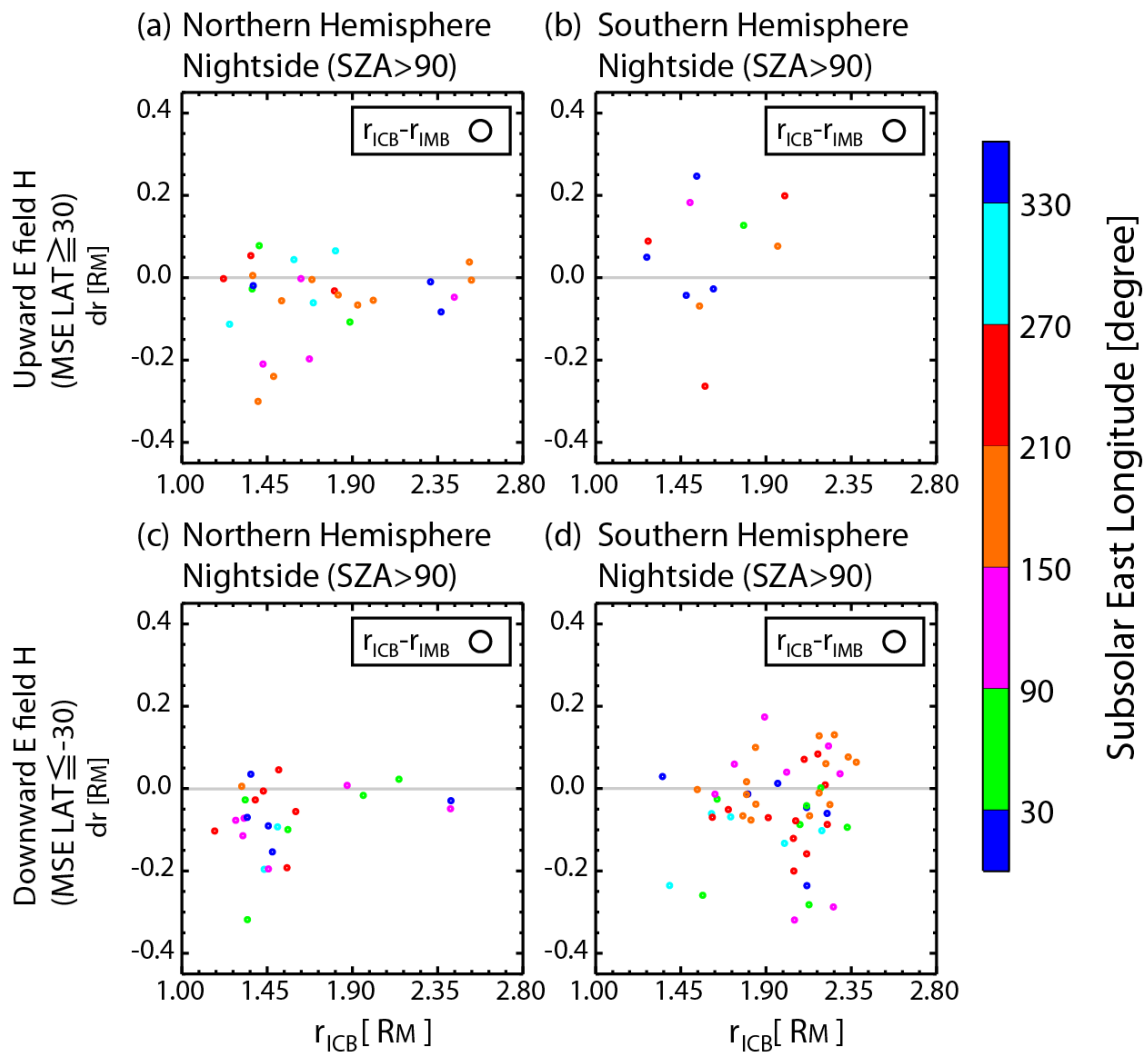


Figure 4.10: Circles show the relative distances between the IMB and ICB on the nightside colored by the east longitude above the subsolar point. (a, b) and (c, d) show results for the upward and downward electric field (E field) hemisphere, respectively. (a, c) and (b, d) show results for the northern and southern hemisphere, respectively. The gray solid line shows the relative distance is 0.

In order to exclude the time periods under the large disturbance condition of solar wind,

we set two criteria of selecting the time period under the steady solar wind condition.

One is the difference of IMF clock angle obtained from MAG between one orbit and

next orbit is less than  $30^\circ$ . Second is the difference of the  $P_{\text{dyn}}$  obtained from SWIA

between one orbit and next orbit is  $\pm 30\%$ . We use the ICB and IMB crossing events under the steady solar wind condition to investigate the effect of the solar wind induced electric field.

Figure 4.10a, 4.10b and Figure 4.10c, 4.10d show the events in the upward electric field hemisphere ( $\theta_{MSE} \geq 30^\circ$ ) and in the downward electric hemisphere ( $\theta_{MSE} \leq -30^\circ$ ), respectively. Figure 4.10a, 4.10c and Figure 4.10b, 4.10d show the events in the northern hemisphere and in the southern hemisphere, respectively. From Figure 4.10, the IMB tends to be located higher than the ICB. However, on the nightside, when the strong crustal magnetic fields region is near the subsolar point, the ICB tends to be located higher than the IMB in the downward electric field hemisphere (magenta, orange and red color points above the gray solid line in Figure 4.10d). Under these specific conditions, the mean value of relative distance between the ICB and IMB crossing events is  $0.08 R_M \sim 272$  km and the mean value of radial distance of ICB crossing events is  $2.11 R_M \sim 7200$  km.

## 4.4 Summary and Discussion

This chapter reported the results of a statistical investigation of the Martian plasma boundaries: the induced magnetosphere boundary (IMB), the ion composition boundary (ICB), and the pressure balance boundary based on  $\beta^*$ . In order to understand differences and/or similarities between the IMB, ICB, and  $\beta^*$  boundary and their dependence on the solar wind, this chapter used ion, electron, and magnetic field data recorded by MAVEN. Time period of using data is November, 2014 to March, 2015 and from June, 2015 to October, 2015.

This chapter developed a method for automatically identifying IMB, ICB, and  $\beta^*$  boundary crossings with criteria based on ion, electron, and magnetic field measurements in the sunlit region from MAVEN. Then, 1,097 IMB crossing events, 1,709 IMB crossing events, 1,107  $\beta^*$  boundary crossing events were identified in 1,294 orbits of MAVEN.

All boundaries show an asymmetry between the geographic northern and southern hemispheres. The locations of all boundaries are affected by the solar wind dynamic pressure ( $P_{dyn}$ ) as well as by the crustal magnetic fields. During high  $P_{dyn}$  period, all boundaries tend to be located at lower altitudes than usual. The effect of crustal magnetic fields makes all boundaries be located at high altitudes. These results are

consistent with previous observations [e.g., *Brain et al.*, 2003, 2006a, *Matsunaga et al.*, 2015]. However, on the nightside, all boundaries tend to be located at higher altitudes in the southern hemisphere than in the northern one regardless of the crustal magnetic field locations. It indicates that the crustal magnetic fields seem to have a permanent effect to raise the boundary altitude on the nightside. The results of MHD model from *Luhmann et al.* [2015] also showed that the induced magnetosphere can spread to high altitude at tail region regardless of the crustal magnetic field locations.

The IMB and ICB tend to be located at similar positions on the dayside. On the other hand, the IMB tends to be located at higher altitudes than the ICB on the nightside. These results suggest that the mass loading process is dominant to form the IMB and the ICB on the dayside. On the nightside, from the previous studies, the transition region has a mantle structure [e.g., *Dubinin et al.*, 1996]. It is assumed that the outside of mantle is the IMB, it seems that the density of solar wind protons gradually decreases by expansion waves in the mantle region. Thus, it is considered that the ion density balanced points between the solar wind protons ( $H^+$ ) and the planetary heavy ions ( $O^+$ ,  $O_2^+$ ) below the IMB. That is a hypothesis to make the difference between the locations of the IMB and the ICB on the nightside.

The  $\beta^*$  boundary tend to be located higher than other boundaries on the dayside. The

electron flux at 80 eV is used to identify the IMB. Since the IMB tends to located at lower than the  $\beta^*$  boundary, it is considered that high-energy electron flux may contribute to the plasma pressure. The results of MHD simulation model by *Xu et al.* [2016] also showed the  $\beta^*$  boundary tends to be located higher than the ICB.

In regions where the solar wind induced electric field is downward (toward the planet), the IMB and ICB tend to be located at higher altitudes than usual on the southern hemisphere nightside. The IMB usually locate at higher altitude than the ICB. However, on the nightside, the ICB locate at higher altitude than the IMB under the periods when the solar wind induced electric field is downward and the strong crustal fields locate on the dayside. These results show that the combinational effect of the crustal magnetic field and the downward electric field can raise the location of the ICB higher than the IMB on the nightside. A candidate physical mechanism is enhanced cold ions outflow in the mini-magnetospheres via process such as magnetic reconnection. The open field of crustal magnetic fields can reconnect with the IMF. The dense cold heavy ions can escape from the cusp region near the open field between the crustal magnetic fields. Thus, these heavy ions can move along the magnetic field which combined the open field and IMF. That escaped heavy ions may make the ion density balanced points between H<sup>+</sup> and heavy ions be higher than usual. This hypothesis suggests that the ICB

tend to be located higher than the IMB on the southern hemisphere under the downward solar wind induced electric field condition. The abundance of cold ion outflow flux above IMB is roughly estimated from our observational results under these specific conditions. It assumes that the solar wind velocity is 300 km/s and the cold ion escape from the surface area of half of spherical shell. From the Subsection 4.3.4, under these specific conditions, the mean value of relative distance between the ICB and IMB crossing events is  $0.08 R_M \sim 272$  km and the mean value of radial distance of ICB crossing events is  $2.11 R_M \sim 7200$  km. The calculated cold ion outflow escape flux is  $\sim 10^{24} \text{ cm}^{-3} \cdot \text{s}^{-1}$ . The observation of MEX showed that the escape rate of cold heavy ions is about  $3.3 \times 10^{24} \text{ s}^{-1}$  in the solar minimum [Lundin *et al.*, 2008a]. Brain *et al.* [2015] reported a lower bound estimate for the escape rate:  $\sim 3 \times 10^{24} \text{ s}^{-1}$  for energies  $> 25$  eV by using MAVEN observations. Our result suggests the cold ion outflow seems to play an important role of the Martian atmospheric escape.

# **Chapter 5**

## **Conclusion and Future Perspective**

As previously mentioned in Chapter 1, the Martian upper atmosphere directly interacts with the solar wind, since Mars does not possess an intrinsic global magnetic field. As a result of this interaction, several plasma boundaries between the magnetosheath and the induced magnetosphere are formed. These Martian plasma boundaries have been observed by Phobos-2, Mars Global Surveyor (MGS), Mars Express (MEX), and the Mars Atmosphere and Volatile EvolutioN (MAVEN) spacecraft. Until recently there has been a lack of continuous simultaneous spacecraft measurements of ions, electrons, and magnetic fields, and different boundaries have been identified and named based on observations from the available instruments on each spacecraft. The relationship between the different named Martian plasma boundaries is far from understood.

This thesis focused on the induced magnetosphere boundary (IMB) (also called the magnetic pile-up boundary (MPB)), the ion composition boundary (ICB), and the

pressure balance boundary based on  $\beta^*$  ( $\beta^* = (P_{th} + P_{dyn}) / P_B$ ). We used spacecraft data from MGS (electrons and magnetic field) and MAVEN (ions, electrons, and magnetic field) to address the characteristics of these boundaries, the differences and/or similarities between them, and their dependence on solar wind parameters and locations of the Martian crustal magnetic fields.

### **Results of MGS Observations**

The main results of the statistical study of MGS data are summarized as follows:

1. During relatively low solar wind dynamic pressure ( $P_{dyn}$ ) periods, both northern hemisphere events and “away” IMF polarity events are favored. Further investigation reveals that these two conditions are usually met at the same time that is, the observed events often occur in the northern hemisphere during “away” IMF polarity.
2. The frequent observation in the northern hemisphere compared to that in the southern hemisphere is consistent with a previous study by *Brain et al.* [2005]. The north-south asymmetry is most likely caused by the stronger crustal magnetic fields in the southern hemisphere than in the northern hemisphere.
3. The northern hemisphere during the “away” IMF conditions corresponds to the upward electric field hemisphere, where the solar wind convective electric field is

pointing away from Mars. It implies that the solar wind penetrations more often occur in the upward electric field hemisphere than in the downward electric field hemisphere.

4. It suggests that one possible physical mechanism occurs in the boundary region between the magnetosheath and the induced magnetosphere is the Kelvin-Helmholtz instability (KHI). Previous two-dimensional global hybrid simulations of the solar wind interaction with an unmagnetized planet revealed out that the upward electric field hemisphere enhances KHI [*Terada et al.*, 2002]. In the hemisphere of upward electric field, the wavy structures generated by the KHI in the boundary of the simulation domain, which has shear of velocity and density, tend to be enhanced.

### **Results of MAVEN Observations**

The main results of the statistical study of MAVEN observation are summarized as follows:

1. A remarkable feature is that all boundaries tend to locate at higher altitudes in the southern hemisphere than in the northern hemisphere on the nightside.
2. The locations of all boundaries are affected by  $P_{dyn}$  as well as by the crustal magnetic fields. The crustal magnetic fields seem to have a permanent effect to raise the boundary altitude on the nightside.

3. Since the IMB and the ICB tend to occur at the similar positions on the dayside, it suggests that the mass loading process is dominant to form the IMB and the ICB on the dayside. On the other hand, the IMB tends to be located at higher altitudes than the ICB on the nightside.

4. The  $\beta^*$  boundary tends to be located at higher altitudes than other boundaries on the dayside. We used 80 eV electron fluxes to identify the IMB. Since the IMB tends to be located at lower altitudes than the  $\beta^*$  boundary, high-energy electron flux may contribute to the plasma pressure.

5. In regions where the solar wind induced electric field is downward, the IMB and ICB tend to be located at higher altitudes than usual in the southern hemisphere on the nightside.

6. Under these specific conditions, the calculated cold ion outflow escape flux is roughly  $\sim 10^{24} \text{ cm}^{-3} \cdot \text{s}^{-1}$ . The previous studies show the escape rate of cold heavy ions is about  $3.3 \times 10^{24} \text{ s}^{-1}$  (MEX observations) [Lundin *et al.*, 2008a] and  $\sim 3 \times 10^{24} \text{ s}^{-1}$  (MAVEN observations) [Brain *et al.*, 2015]. Our result suggests the cold ion outflow seems to play an important role of the Martian atmospheric escape.

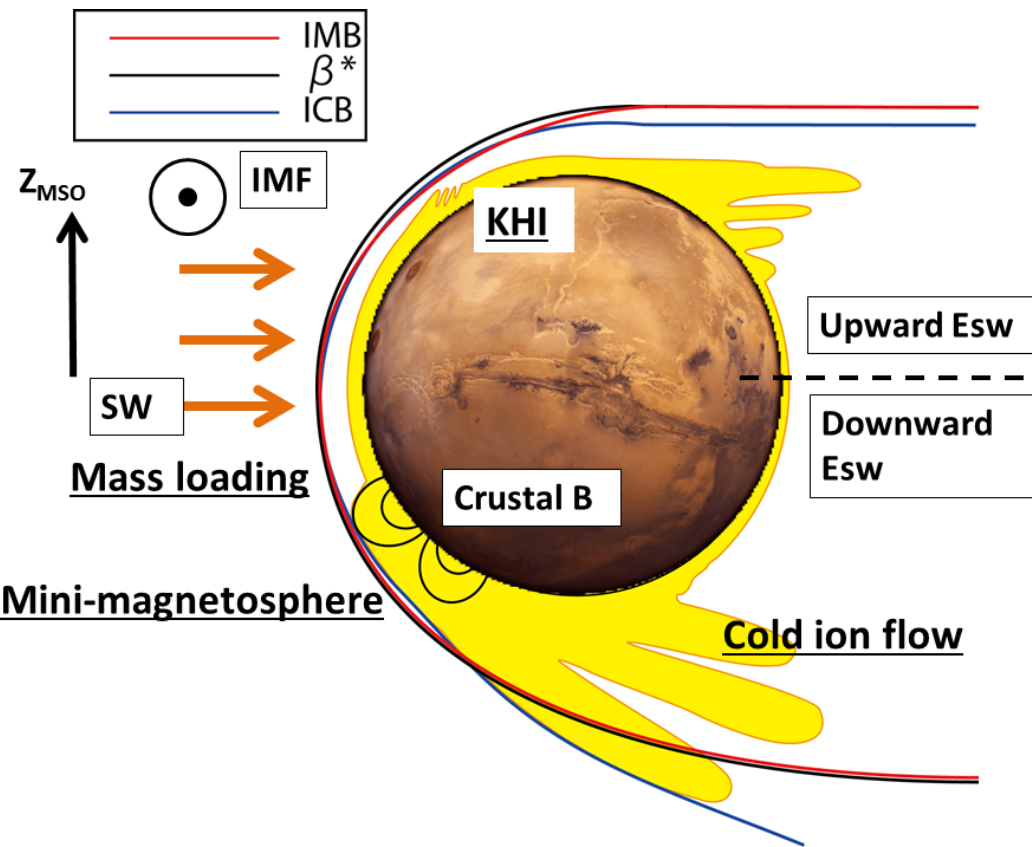


Figure 5.1: A summary sketch of the Martian plasma boundaries. The IMB, ICB,  $\beta^*$  boundary is the red, blue, black solid line, respectively. SW, KHI, and  $E_{sw}$  mean the solar wind, Kelvin-Helmholtz instability, and the solar wind induced electric field. The  $+Z_{MSO}$  direction corresponds to the direction of the northern hemisphere. The direction of the IMF makes the northern hemisphere correspond to the hemisphere of upward convection electric field.

Figure 5.1 shows a summary sketch of the Martian plasma boundaries from the observational results of this thesis.

On the dayside, the mass loading process forms the IMB and the ICB at similar locations. The IMB, ICB, and  $\beta^*$  boundary are cylindrical shape in the northern hemisphere. This structure is consistent with simulation studies [e.g., *Fang et al.*, 2015; *Xu et al.*, 2016]. The IMB tends to be located at higher altitudes than the ICB on the

nightside.

The crustal magnetic fields make all boundaries tend to be located higher altitudes in the southern hemisphere than the northern hemisphere. It corresponds to the previous studies [e.g., *Brain et al.*, 2006a]. In addition, this thesis reveals the crustal magnetic fields seem to have a permanent effect to raise the boundary altitude on the nightside from the MAVEN observation for the first time.

In the upward electric field hemisphere, KHI is one possible physical mechanism in IMB. Previous studies suggested the magnetosheath plasma and the Martian planetary plasma are mixed by the wave structure of KHI [e.g., *Terada et al.*, 2002; *Ruhunusiri et al.*, 2016] at the velocity shear region. Thus the magnetosheath plasma is enhanced to penetrate into the Martian upper atmosphere region by this effect. This magnetosheath plasma penetration makes the IMB tend to be located lower altitude than usual.

On the other hand, when the solar wind induced electric field is downward and the strong crustal fields locate on the dayside, the ICB is located above the IMB on the nightside. A candidate physical mechanism is enhanced cold ions outflow in the mini-magnetospheres [e.g., *Lundin et al.*, 2011] via process such as the magnetic reconnection between the crustal magnetic fields and IMF or the enhanced cold ion outflow from the cusp regions. The open field of crustal magnetic fields can reconnect

with the IMF [e.g., *Brain et al.*, 2010b, *Hara et al.*, 2016]. The reconnection can make the magnetic flux rope structure and it can contain the planetary heavy ions. *Hara et al.* [2015] reported the ion densities measured by MAVEN in the flux rope are  $4.2 \text{ cm}^{-3}$  for  $\text{O}^+$  and  $4.4 \text{ cm}^{-3}$  for  $\text{O}_2^+$ . The dense cold ions also can escape from the cusp region [*Lundin et al.*, 2006] along the magnetic field which combined the open field and IMF. The escaping heavy ions may make the ion density balanced points between  $\text{H}^+$  and heavy ions locate higher than usual and form the heavy ion rich layer in the magnetosheath above IMB. Thus the combination effect of the crustal magnetic fields and the downward solar wind induced electric field can raise the location of the ICB higher than the IMB on the nightside.

Future work will be a superposed epoch analysis of the electron flux, magnetic field, and ion number density data when MAVEN crosses boundaries. It will show that the physical phenomena inside of the Martian plasma boundaries in more detail.



# **Appendix**

## **A. Energy Dependence on Identification of the Induced Magnetosphere Boundary (IMB)**

In Subsection 4.2.1, this thesis used the electron flux at 80 eV obtained from SWEA in order to identify the IMB crossings of MAVEN. In addition, this thesis checked the energy dependence on identification of the IMB.

1,097 IMB crossing events were identified by using the electron flux at 80 eV and 1,534 IMB crossing events were identified by using the electron flux at 40 eV. The time period of data sets is from November, 2014 to March, 2015 and from June, 2015 to October, 2015 (1,294 orbits of MAVEN). In order to investigate the difference between the location of ICB crossing by 80 eV electron selections and those by 40 eV electron selections, 869 IMB crossing events which were identified by both 80 eV and 40 eV electron selections during the same MAVEN orbit were selected.

## APPENDIX

Figure A shows the comparison of the results of the 80 eV electron selections (black triangles) and those of the 40 eV electron selections (magenta diamonds). These results show that the locations of the 40 eV electron selections are a little bit lower than those of the 80 eV electron selections in both hemispheres. Moreover, the locations of both electron selections show an asymmetry between the geographic northern and southern hemispheres. Thus, the trends with the locations of IMB crossing are not dependent upon the choice of electron flux of 40 eV and 80 eV.

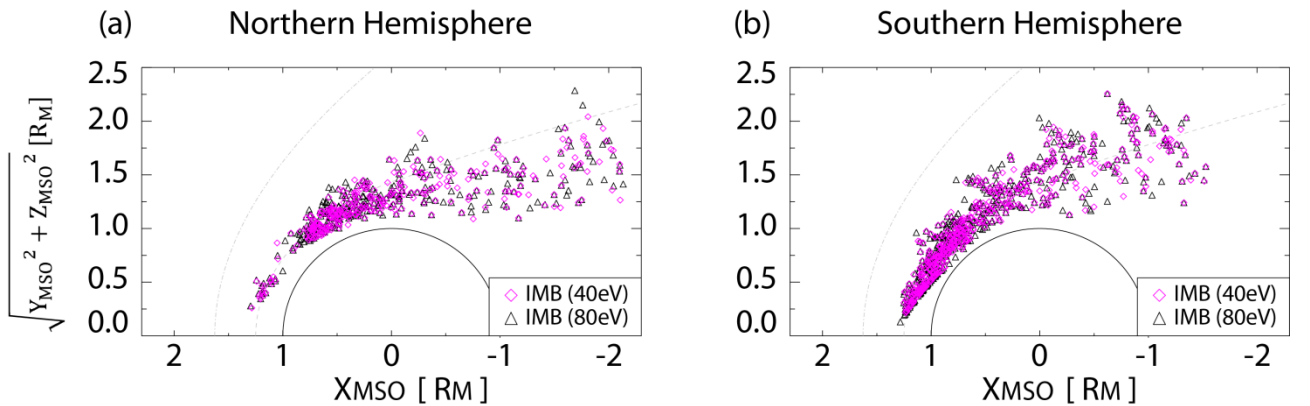


Figure A: The observed locations of the IMB by the 80 eV electron selections and those of the 40 eV electron selections. In panels (a, b), the black triangles and magenta diamonds show the 80 eV electron selections events and the 40 eV electron selections events, respectively. The right panels and left panels show the crossing events in the northern hemisphere and the southern hemisphere, respectively. Models for the BS and IMB are shown in all panels with the dash-dotted line and dashed line, respectively [Trotignon et al., 2006].

# References

- Acuña, M. H., et al. (1992), Mars Observer magnetic fields investigation, *J. Geophys. Res.*, 97 (E5), 7799–7814, doi:10.1029/92JE00344.
- Acuña, M. H., et al. (1998), Magnetic field and plasma observations at Mars: Initial results of the Mars Global Surveyor mission, *Science*, 279, 1676–1680, doi: 10.1126/science.279.5357.1676.
- Acuña, M. H., et al. (1999), Global Distribution of Crustal Magnetization Discovered by the Mars Global Surveyor MAG/ER Experiment, *Science*, 284, 790–793, doi: 10.1126/science.284.5415.790.
- Akalin, F., D. D. Morgan, D. A. Gurnett, D. L. Kirchner, D. A. Brain, R. Modolo, M. H. Acuña, and J. R. Espley (2010), Dayside induced magnetic field in the ionosphere of Mars, *Icarus*, 206, 104–111, doi:10.1016/j.icarus.2009.03.021.
- Albee, A. L., R. E. Arvidson, F. Palluconi, and T. Thorpe (2001), Overview of the Mars Global Surveyor mission, *J. Geophys. Res.*, 106(E12), 23,291–23,316, doi:10.1029/2000JE001306.
- Allison, M. (1997), Accurate analytic representations of solar time and seasons on Mars with applications to the Pathfinder/Surveyor missions, *Geophys. Res. Lett.* 24, 1967-1970, doi:10.1029/97GL01950.

## REFERENCES

- Andersson, L., et al. (2015), The Langmuir probe and waves (LPW) instrument for MAVEN, *Space Sci. Rev.*, 195, 173, doi:10.1007/s11214-015-0194-3.
- Angelopoulos et al., (2008), Tail reconnection triggering substorm onset, *Science*, 321, 931-935, doi: <https://doi.org/10.1126/science.1160495>.
- Barabash, S., and R. Lundin (2006), ASPERA-3 on Mars Express, *Icarus*, 182, 301–307, doi:10.1016/j.icarus.2006.02.015.
- Barabash, S., et al. (2006), The Analyzer of Space Plasmas and Energetic Atoms (ASPERA-3) for the Mars Express Mission, *Space Sci. Rev.*, 126, 113–164, doi: 10.1007/s11214-006-9124-8.
- Benna, M., P. R. Mahaffy, J.M. Grebowsky, J. L. Fox, R. V. Yelle, and B. M. Jakosky (2015), First measurements of composition and dynamics of the Martian ionosphere by MAVEN's Neutral Gas and Ion Mass Spectrometer, *Geophys. Res. Lett.*, 42, doi:10.1002/2015GL066146.
- Berne, O., N. Marcelino, and J. Cernicharo (2010), Waves on the surface of the Orion molecular cloud, *Nature*, 466, 947-949, doi:10.1038/nature09289.
- Bertucci, C., C. Mazelle, M. Acuna, C. Russell, and J. Slavin (2005), Structure of the magnetic pileup boundary at Mars and Venus, *J. Geophys. Res.*, 110, A01209, doi:10.1029/2004JA010592.
- Blomberg, L. G., J. A. Cumnock, and A. I. Eriksson (2003), The martian plasma environment: electric field and Langmuir probe diagnostics, *IEEE Transactions on Plasma Science*, 31, 1232–1236, doi:10.1109/TPS.2003.821353.
- Bougher, S. W., S. Engel, D. P. Hinson, and J. M. Forbes (2001), Mars Global Surveyor radio science electron density profiles: Neutral atmosphere implications, *Geophys. Res. Lett.*, 28, 3091–3094, doi:10.1029/2001GL012884.

## REFERENCES

- Bougher, S. W., et al. (2015), Early MAVEN Deep Dip campaign reveals thermosphere and ionosphere variability, *Science*, 350(6261), doi:10.1126/science.aad0459.
- Barabash, S., A. Fedorov, R. Lundin, and J.-A. Sauvaud (2007), Martian atmospheric erosion rates, *Science*, 315, 501–503, doi:10.1126/science.1134358.
- Brain, D. A. (2006), Mars Global Surveyor Measurements of the Martian Solar Wind Interaction, *Space Sci. Rev.*, 126, 77–112, doi:10.1007/s11214-006-9122-x.
- Brain, D. A., F. Bagenal, M. H. Acuña, and J. E. P. Connerney (2003), Martian magnetic morphology: Contributions from the solar wind and crust, *J. Geophys. Res.*, 108 (A12), 1424, doi:10.1029/2002JA009482.
- Brain, D. A., J. S. Halekas, R. Lillis, D. L. Mitchell, R. P. Lin, and D. H. Crider (2005), Variability of the altitude of the Martian sheath, *Geophys. Res. Lett.*, 32, L18203, doi:10.1029/2005GL023126.
- Brain, D. A., D. L. Mitchell, and J. S. Halekas (2006a), The magnetic field draping direction at Mars from April 1999 through August 2004, *Icarus*, 182, 464–473, doi:10.1016/j.icarus.2005.09.023.
- Brain, D. A., et al. (2006b), On the origin of aurorae on Mars, *Geophys. Res. Lett.*, 33, L01201, doi:10.1029/2005GL024782.
- Brain, D. A., et al. (2010a), A comparison of global models for the solar wind interaction with Mars, *Icarus*, 206, 139–151, doi:10.1016/j.icarus.2009.06.030.
- Brain, D. A., A. H. Baker, J. Briggs, J. P. Eastwood, J. S. Halekas, and T.-D. Phan (2010b), Episodic detachment of Martian crustal magnetic fields leading to bulk atmospheric plasma escape, *Geophys. Res. Lett.*, 37, L14108, doi:10.1029/2010GL043916.

## REFERENCES

- Brain, D. A., J. P. McFadden, J. S. Halekas, J. E. P. Connerney, S. W. Bougher, S. Curry, C. F. Dong, Y. Dong, F. Eparvier, X. Fang, et al. (2015), The spatial distribution of planetary ion fluxes near Mars observed by MAVEN, *Geophys. Res. Lett.*, 42, 9142-9148, doi:10.1002/2015GL065293.
- Brecht, S. H., and J. R. Ferrante (1991), Global hybrid simulation of unmagnetized planets - Comparison of Venus and Mars, *J. Geophys. Res.*, 96, 11,209, doi: 10.1029/91JA00671.
- Brecht, S. H., J. R. Ferrante, and J. G. Luhmann (1993), Three-dimensional simulations of the solar wind interaction with Mars, *J. Geophys. Res.*, 98, 1345–1357,doi:10.1029/92JA02198.
- Breus, T. K., S. J. Bauer, A. M. Krymskii, V. Ya. Mitnitskii (1989), Mass loading in the solar wind interaction with Venus and Mars, *J. Geophys. Res.* 94, 2375-2382, doi:10.1029/JA094iA03p02375.
- Breus, T. K., A. M. Krymskii, R. Lundin, E. M. Dubinin, J. G. Luhmann, Ye G. Yeroshenko, S. V. Barabash, V. Ya. Mitnitskii, N. F. Pissarenko, V. A. Styashkin (1991), The solar wind interaction with Mars: consideration of Phobos 2 mission observations of an ion composition boundary on the dayside, *J. Geophys. Res.* 96, 11,165-11,174, doi:10.1029/91JA01131.
- Burch, J. L., and T. D. Phan (2016), Magnetic reconnection at the dayside magnetopause: Advances with MMS, *Geophys. Res. Lett.*, 43, 8327–8338, doi:10.1002/2016GL069787.
- Cain, J. C., B. B. Ferguson, and D. Mozzoni (2003), An  $n = 90$  internal potential function of the Martian crustal magnetic field, *J. Geophys. Res. (Planets)*, 108, 5008, doi:10.1029/2000JE001487.

## REFERENCES

- Casanova, J., J. José, E. García-Berro, S. N. Shore, and A. C. Calder (2011), Kelvin–Helmholtz instabilities as the source of inhomogeneous mixing in nova explosions, *Nature*, 478, 490–492, doi:10.1038/nature10520.
- Carr, M. H., and G. D. Clow (1981), Martian channels and valleys: Their characteristics, distribution, and age, *Icarus*, 48, 91–117, doi:10.1016/0019-1035(81)90156-1.
- Chassefière, E., and F. Leblanc (2004), Mars atmospheric escape and evolution; interaction with the solar wind, *Planet. Space Sci.*, 52, 1039–1058, doi:10.1016/j.pss.2004.07.002.
- Chicarro, A. F. (2004), The Mars Express Mission-Initial Scientific Results from Orbit, in *Lunar and Planetary Institute Science Conference Abstracts, Lunar and Planetary Institute Science Conference Abstracts*, vol. 35, edited by S. Mackwell and E. Stansbery, p. 2174.
- Connerney, J. E. P., M. H. Acuña, N. F. Ness, G. Kletetschka, D. L. Mitchell, R. P. Lin, and H. Rème (2005), Tectonic implications of Mars crustal magnetism, *Proc. Nat. Acad. Sci.*, 102, 14,970–14,975, doi:10.1073/pnas.0507469102.
- Connerney, J. E. P., J. Espley, P. Lawton, et al. (2015a), The MAVEN Magnetic Field Investigation, *Space Sci. Rev.*, 195, 257, doi:10.1007/s11214-015-0169-4.
- Connerney, J. E. P., J. R. Espley, G. A. DiBraccio, J. R. Gruesbeck, R. J. Oliversen, D. L. Mitchell, J. Halekas, C. Mazelle, D. Brain, and B. M. Jakosky (2015b), First results of the MAVEN magnetic field investigation, *Geophys. Res. Lett.*, 42, doi:10.1002/2015GL065366.
- Crider, D. H., et al. (2002), Observations of the latitude dependence of the location of the Martian magnetic pileup boundary, *Geophys. Res. Lett.*, 29(8), 1170, doi:10.1029/2001GL013860.

## REFERENCES

- Crider, D. H., D. Vignes, A. M. Krymskii, T. K. Breus, N. F. Ness, D. L. Mitchell, J. A. Slavin, M. H. Acuña (2003), A proxy for determining solar wind pressure at Mars using Mars Global Surveyor data, *J. Geophys. Res.* *108(A12)*, 1461, doi:10.1029/2003JA009875.
- Crider, D. H., J. Espley, D. A. Brain, D. L. Mitchell, J. E. P. Connerney, and M. H. Acuña (2005), Mars Global Surveyor observations of the Halloween 2003 solar superstorm's encounter with Mars, *J. Geophys. Res. (Space Physics)*, *110*, A09S21, doi:10.1029/2004JA010881.
- Delamere, P. A., R. J. Wilson, S. Eriksson, and F. Bagenal (2013), Magnetic signatures of Kelvin-Helmholtz vortices on Saturn's magnetopause: Global survey, *J. Geophys. Res.*, *118*, 393–404, doi:10.1029/2012JA018197.
- Diéval, C., (2012), Solar Wind Ions Inside the Induced Magnetosphere of Mars, PhD thesis, Luleå University of Technology, Kiruna, Sweden.
- Dong, Y., X. Fang, D. A. Brain, J. P. McFadden, J. S. Halekas, J. E. Connerney, S. M. Curry, Y. Harada, J. G. Luhmann, and B. M. Jakosky (2015), Strong plume fluxes at Mars observed by MAVEN: An important planetary ion escape channel, *Geophys. Res. Lett.*, *42*, 8942–8950, doi:10.1002/2015GL065346.
- Dubinin, E., and R. Lundin (1995), Mass-loading near Mars, *Adv. Space Res.*, *16*, 75-79, doi:10.1016/0273-1177(95)00211-V.
- Dubinin, E., K. Sauer, R. Lundin, K. Baumgärtel, and A. Bogdanov (1996), Structuring of the transition region (plasma mantle) of the Martian magnetosphere, *Geophys. Res. Lett.*, *23*, 785-788, doi: 10.1029/96GL00701.
- Dubinin, E., M. Fränz, J. Woch, E. Roussos, S. Barabash, R. Lundin, J. D. Winnigham, R. A. Frahm, and M. Acuña (2006), Plasma Morphology at Mars. Aspera-3 Observations, *Space Sci. Rev.*, *126*, 209–238, doi:10.1007/s11214-006-9039-4.

## REFERENCES

- Dubinin, E., G. Chanteur, M. Fraenz, R. Modolo, J. Woch, E. Roussos, S. Barabash, R. Lundin, J. D. Winningham (2008), Asymmetry of plasma fluxes at Mars. ASPERA-3 observations and hybrid simulations, *Planet. Space Sci.*, **56**, 832-835, doi:10.1016/j.pss.2007.12.006.
- Edberg, N. J. T., M. Lester, S. W. H. Cowley, and A. I. Eriksson (2008), Statistical analysis of the location of the Martian magnetic pileup boundary and bow shock and the influence of crustal magnetic fields, *J. Geophys. Res. (Space Physics)*, **113**, A08206, doi:10.1029/2008JA013096.
- Eparvier, F. G., P. C. Chamberlin, T. N. Woods, et al. (2015), The Solar Extreme Ultraviolet Monitor for MAVEN, *Space Sci. Rev.*, **195**, 293 ,doi:10.1007/s11214-015-0195-2.
- Eriksson, S., et al. (2016), Magnetospheric Multiscale observations of magnetic reconnection associated with Kelvin-Helmholtz waves, *Geophys. Res. Lett.*, **43**, 5606–5615, doi:10.1002/2016GL068783.
- Fang, X., Y. Ma, D. Brain, Y. Dong, and R. Lillis (2015), Control of Mars global atmospheric loss by the continuous rotation of the crustal magnetic field: A time-dependent MHD study, *J. Geophys. Res. (Space Physics)*, **120**,doi:10.1002/2015JA021605.
- Fairfield, D. H., A. Otto, T. Mukai, S. Kokubun, R. P. Lepping, J. T. Steinberg,A. J. Lazarus, and T. Yamamoto (2000), Geotail observations of the Kelvin-Helmholtz instability at the equatorial magnetotail boundary for parallel northward fields, *J. Geophys. Res.*, **105**, 21,159, doi:10.1029/1999JA000316.
- Fillingim, M. O., et al. (2007), Model calculations of electron precipitation induced ionization patches on the nightside of Mars, *Geophys. Res. Lett.*, **34**, L12101, doi:10.1029/2007GL029986.

## REFERENCES

- Fränz, M., et al. (2006), Plasma Moments in the Environment of Mars. Mars Express ASPERA-3 Observations, *Space Sci. Rev.*, 126, 165–207, doi:10.1007/s11214-006-9115-9.
- Fränz, M., E. Dubinin, E. Nielsen, J. Woch, S. Barabash, R. Lundin, and A. Fedorov (2010), Transterminator ion flow in the Martian ionosphere, *Planet. Space Sci.*, 58, 1442–1454, doi:10.1016/j.pss.2010.06.009.
- Fujimoto, M. and T. Terasawa (1994), Anomalous ion mixing within an MHD scale Kelvin-Helmholtz vortex: 2. Effects of inhomogeneity, *J. Geophys. Res.*, 100(A7), 12025-12033, doi:10.1029/94JA02219
- Gurnett, D. A., et al. (2005), Radar Soundings of the Ionosphere of Mars, *Science*, 310, 1929–1933, doi:10.1126/science.1121868.
- Gurnett, D. A., D. D. Morgan, F. Duru, F. Akalin, J. D. Winningham, R. A. Frahm, E. Dubinin, and S. Barabash (2010), Large density fluctuations in the martian ionosphere as observed by the Mars Express radar sounder, *Icarus*, 206, 83–94, doi:10.1016/j.icarus.2009.02.019.
- Haberle, R. M. (1998), Early Mars climate models, *J. Geophys. Res.*, 103(E12), 28467–28479, doi:10.1029/98JE01396
- Halekas, J. S., J. P. Eastwood, D. A. Brain, T. D. Phan, M. Øieroset, and R. P. Lin (2009), In situ observations of reconnection Hall magnetic fields at Mars: Evidence for ion diffusion region encounters, *J. Geophys. Res.*, 114 (A13), A11204, doi:10.1029/2009JA014544.
- Halekas, J. S., E. R. Taylor, G. Dalton, et al. (2015), The Solar Wind Ion Analyzer for MAVEN, *Space Sci. Rev.*, 195, 125, doi:10.1007/s11214-013-0029-z.

## REFERENCES

- Halekas, J., et al. (2015), Time-dispersed ion signatures observed in the Martian magnetosphere by maven, *Geophys. Res. Lett.*, *42*, 8910–8916, doi:10.1002/2015GL064781.
- Hanson, W. B., and G. P. Mantas (1988), Viking electron temperature measurements—Evidence for a magnetic field in the Martian ionosphere, *J. Geophys. Res.*, *93*, 7538–7544, doi:10.1029/JA093iA07p07538.
- Hanson, W. B., S. Sanatani, and D. R. Zuccaro (1977), The Martian ionosphere as observed by the Viking retarding potential analyzers, *J. Geophys. Res.*, *82*, 4351–4363, doi:10.1029/JS082i028p04351.
- Hara, T., K. Seki, Y. Futaana, M. Yamauchi, M. Yagi, Y. Matsumoto, M. Tokumaru, A. Fedorov, and S. Barabash (2011), Heavy-ion flux enhancement in the vicinity of the Martian ionosphere during CIR passage: Mars Express ASPERA-3 observations, *J. Geophys. Res. (Space Physics)*, *116*, A02309, doi:10.1029/2010JA015778.
- Hara, T., K. Seki, H. Hasegawa, D. A. Brain, K. Matsunaga, and M. H. Saito (2014a), The spatial structure of Martian magnetic flux ropes recovered by the Grad-Shafranov reconstruction technique, *J. Geophys. Res. (Space Physics)*, doi: 10.1002/2013JA019414.
- Hara, T., K. Seki, H. Hasegawa, D. A. Brain, K. Matsunaga, M. H. Saito, and D. Shiota (2014b), Formation processes of flux ropes downstream from Martian crustal magnetic fields inferred from Grad-Shafranov reconstruction, *J. Geophys. Res. Space Physics*, *119*, 7947–7962, doi:10.1002/2014JA019943.
- Hara, T., et al. (2015), Estimation of the spatial structure of a detached magnetic flux rope at Mars based on simultaneous MAVEN plasma and magnetic field observations, *Geophys. Res. Lett.*, *42*, doi:10.1002/2015GL065720.

## REFERENCES

- Hara, T., et al. (2016), MAVEN observations of a giant ionospheric flux rope near Mars resulting from interaction between the crustal and interplanetary draped magnetic fields, *J. Geophys. Res. (Space Physics)*, 121, doi:10.1002/2016JA023347.
- Harada, Y., et al. (2015), Marsward and tailward ions in the near-Mars magnetotail: MAVEN observations, *Geophys. Res. Lett.*, 42, doi:10.1002/2015GL065005.
- Harnett, E. M., and R. M. Winglee (2003), The influence of a mini-magnetopause on the magnetic pileup boundary at Mars, *Geophys. Res. Lett.*, 30, 2074, doi:10.1029/2003GL017852.
- Hasegawa, H., M. Fujimoto, T.-D. Phan, H. Rème, A. Balogh, M. W. Dunlop, C. Hashimoto, and R. TanDokoro (2004), Transport of solar wind into Earth's magnetosphere through rolled-up Kelvin-Helmholtz vortices, *Nature*, 430, 755–758, doi:10.1038/nature02799.
- Hasegawa, H., B. U. Ö. Sonnerup, C. J. Owen, B. Klecker, G. Paschmann, A. Balogh, and H. Rème (2006), The structure of flux transfer events recovered from Cluster data, *Annales Geophysicae*, 24, 603–618, doi:10.5194/angeo-24-603-2006.
- Hu, Q., C. W. Smith, N. F. Ness, and R. M. Skoug (2004), Multiple flux rope magnetic ejecta in the solar wind, *J. Geophys. Res. (Space Physics)*, 109, A03102, doi:10.1029/2003JA010101.
- Jakosky, B. M., R. O. Pepin, R. E. Johnson, and J. L. Fox (1994), Mars atmospheric loss and isotopic fractionation by solar-wind-induced sputtering and photochemical escape, *Icarus*, 111(2), 271-288, doi:10.1006/icar.1994.1145.
- Jakosky, B. M., and R. J. Phillips (2001), Mars' volatile and climate history, *Nature*, 412, 237–244, doi:10.1038/35084184.
- Jakosky, B. M., et al. (2015a), The Mars Atmosphere and Volatile Evolution (MAVEN) Mission, *Space Sci. Rev.*, 195, 3 doi:10.1007/s11214-015-0139-x.

## REFERENCES

- Jakosky, B. M., J. M. Grebowsky, J. G. Luhmann, and D. A. Brain (2015b), Initial results from the MAVEN mission to Mars, *Geophys. Res. Lett.*, 42, 8791–8802, doi:10.1002/2015GL065271.
- Jakosky, B. M., et al. (2015c), MAVEN observations of the response of Mars to an interplanetary coronal mass ejection, *Science*, 350(6261), doi:10.1126/science.aad0210.
- Larson, D. E., R. J. Lillis, C. O. Lee, et al. (2015), The MAVEN Solar Energetic Particle Investigation, *Space Sci. Rev.*, 195, 153, doi:10.1007/s11214-015-0218-z.
- Luhmann, J. G., (1990) The Solar Wind Interaction with Unmagnetized Planets: A Tutorial, in *Physics of Magnetic Flux Ropes*, edited by C. T. Russell, E. R. Priest and L. C. Lee, doi: 10.1029/GM058p0401
- Luhmann, J. G., S. A. Ledvina, and C. T. Russell (2004), Induced magnetospheres, *Adv. Space Res.*, 33, 1905–1912, doi:10.1016/j.asr.2003.03.031.
- Luhmann, J. G., C. Dong, Y. Ma, S. M. Curry, D. Mitchell, J. Espley, J. Connerney, J. Halekas, D. A. Brain, B. M. Jakosky, et al. (2015), Implications of MAVEN Mars near-wake measurements and models, *Geophys. Res. Lett.*, 42, 9087–9094, doi:10.1002/2015GL066122.
- Lundin, R. (2011), Ion Acceleration and Outflow from Mars and Venus: An Overview, *Space Sci. Rev.*, 162, 309–334, doi:10.1007/s11214-011-9811-y.
- Lundin, R., H. Borg, B. Hultqvist, A. Zakharov, and R. Pellinen (1989), First measurements of the ionospheric plasma escape from Mars, *Nature*, 341, 609–612, doi:10.1038/341609a0
- Lundin, R., and S. Barabash (2004), Evolution of the Martian atmosphere and hydrosphere: Solar wind, *Planet. Space Sci.*, 52, 1059–1071, doi:10.1016/j.pss.2004.07.020

## REFERENCES

- Lundin, R., S. Barabash, M. Holmström, H. Nilsson, M. Yamauchi, M. Fränz, and E. M. Dubinin (2008a), A comet-like escape of ionospheric plasma from Mars, *Geophys. Res. Lett.*, 35, L18203, doi:10.1029/2008GL034811.
- Lundin, R., S. Barabash, A. Fedorov, M. Holmström, H. Nilsson, J.-A. Sauvaud, and M. Yamauchi (2008b), Solar forcing and planetary ion escape from Mars, *Geophys. Res. Lett.*, 35, L09203, doi:10.1029/2007GL032884.
- Lundin, R., S. Barabash, E. Dubinin, D. Winningham, and M. Yamauchi (2011), Low-altitude acceleration of ionospheric ions at Mars, *Geophys. Res. Lett.*, 38, L08108, doi:10.1029/2011GL047064.
- McFadden, J. P., O. Kortmann, D. Curtis, et al. (2015), MAVEN SupraThermal and Thermal Ion Composition (STATIC) Instrument, *Space Sci. Rev.*, 195, 199, doi:10.1007/s11214-015-0175-6.
- Mahaffy, P. R., M. Benna, M. Elrod, R. V. Yelle, S. W. Bougher, S. W. Stone, and B. M. Jakosky (2015), Structure and composition of the neutral upper atmosphere of Mars from the MAVEN NGIMS investigation, *Geophys. Res. Lett.*, 42, doi:10.1002/2015GL065329.
- Matsunaga, K., K. Seki, T. Hara, and D. A. Brain (2015), Asymmetric Penetration of Shocked Solar Wind Down to 400-km Altitudes at Mars, *J. Geophys. Res., (Space Physics)*, 120, 6874-6883, 2015, doi:10.1002/2014JA020757
- Mazelle, C., D. Winterhalter, K. Sauer, et al. (2004), Bow shock and upstream phenomena at Mars, *Space Sci. Rev.*, 111, 115-181, doi:10.1023/B:SPAC.0000032717.98679.d0
- McClintock, W. E., N. M. Schneider, G. M. Holsclaw, et al. (2015), The Imaging Ultraviolet Spectrograph (IUVS) for the MAVEN Mission, *Space Sci. Rev.*, 195, 75, doi:10.1007/s11214-014-0098-7

## REFERENCES

- Mitchell, D. L., R. P. Lin, C. Mazelle, H. Rème, P. A. Cloutier, J. E. P. Connerney, M. H. Acuña, and N. F. Ness (2001), Probing Mars' crustal magnetic field and ionosphere with the MGS Electron Reflectometer, *J. Geophys. Res.*, *106* (E10), 23,419–23,428, doi:10.1029/2000JE001435.
- Mitchell, D. L., C. Mazelle, JA. Sauvaud, et al. (2016), The MAVEN Solar Wind Electron Analyzer, *Space Sci. Rev.*, *200*: 495, doi:10.1007/s11214-015-0232-1.
- Nagy, A. F., et al. (2004), The plasma Environment of Mars, *Space Sci. Rev.*, *111*, 33–114, doi:10.1023/B:SPAC.0000032718.47512.92.
- Najib, D., A. F. Nagy, G. Tóth, and Y. Ma (2011), Three-dimensional, multifluid, high spatial resolution MHD model studies of the solar wind interaction with Mars, *J. Geophys. Res. (Space Physics)*, *116*, A05204, doi:10.1029/2010JA016272.
- Nielsen, E., et al. (2006), Observations of Vertical Reflections from the Topside Martian Ionosphere, *Space Sci. Rev.*, *126*, 373–388, doi:10.1007/s11214-006-9113-y.
- Nier, A. O., and M. B. McElroy (1977), Composition and structure of Mars' upper atmosphere - Results from the neutral mass spectrometers on Viking 1 and 2, *J. Geophys. Res.*, *82*, 4341–4349, doi:10.1029/JS082i028p04341.
- Nilsson, H., E. Carlsson, D. A. Brain, M. Yamauchi, M. Holmström, S. Barabash, R. Lundin, and Y. Futaana (2010), Ion escape from Mars as a function of solar wind conditions: A statistical study, *Icarus*, *206*, 40–49, doi:10.1016/j.icarus.2009.03.006.
- Nishino, M. N., et al. (2011), A case study of Kelvin-Helmholtz vortices on both flanks of the Earth's magnetotail, *Planet. Space Sci.*, *59*, 502–509, doi:10.1016/j.pss.2010.03.011.

## REFERENCES

- Nilsson, H., N. J. T. Edberg, G. Stenberg, S. Barabash, M. Holmström, Y. Futaana, R. Lundin, and A. Fedorov (2011), Heavy ion escape from Mars, influence from solar wind conditions and crustal magnetic fields, *Icarus*, 215, 475–484, doi:10.1016/j.icarus.2011.08.003.
- Ojha, L., M. B. Wilhelm, S. L. Murchie, A. S. McEwen, J. J. Wray, J. Hanley, M. Massé, and M. Chojnacki (2015), Spectral evidence for hydrated salts in recurring slope lineae on Mars, *Nature Geoscience*, 8, 829–832, doi:10.1038/ngeo2546.
- Price, D. J., and S. Rosswog, (2006), Producing ultrastrong magnetic fields in neutron star mergers, *Science*, 312, 719-722, doi:10.1126/science.1125201.
- Qiu, J., Q. Hu, T. A. Howard, and V. B. Yurchyshyn (2007), On the Magnetic Flux Budget in Low-Corona Magnetic Reconnection and Interplanetary Coronal Mass Ejections, *Astrophysical Journal*, 659, 758-772, doi:10.1086/512060.
- Riedler, W., et al. (1989), Magnetic fields near Mars: First results, *Nature*, 341(6243), 604–607, doi: 10.1038/341604a0.
- Ruhunusiri, S., et al. (2016), MAVEN observations of partially developed Kelvin-Helmholtz vortices at Mars, *Geophys. Res. Lett.*, 43, 4763–4773, doi:10.1002/2016GL068926.
- Russell, C. T. (1977), On the relative locations of the bow shocks of the terrestrial planets, *Geophys. Res. Lett.*, 4, 387–390, doi: 10.1029/GL004i010p00387.
- Russell, C. T., and R. C. Elphic (1979), Observation of magnetic flux ropes in the Venus ionosphere, *Nature*, 279, 616–618, doi:10.1038/279616a0.
- Russell, C. T., R. C. Snare, J. D. Means, D. Pierce, D. Dearborn, M. Larson, G. Barr, and G. Le (1995), The GGS/POLAR magnetic fields investigation, *Space Sci. Rev.*, 71, 563–582, doi:10.1007/BF00751341.

## REFERENCES

- Sauer, K., A. Bogdanov, and K. Baumgärtel (1994), Evidence of an ion composition boundary (protonopause) in bi-ion fluid simulations of solar wind mass loading, *Geophys. Res. Lett.*, 21(20), 2255–2258, doi:10.1029/94GL01691
- Sckopke, N., G. Paschmann, G. Haerendel, B. U. O. Sonnerup, S. J. Bame, T. G. Forbes, E. W. Hones, Jr., and C. T. Russell (1981), Structure of the low-latitude boundary layer, *J. Geophys. Res.*, 86, 2099–2110, doi:10.1029/JA086iA04p02099.
- Slavin, J. A., K. Schwingenschuh, W. Riedler, and E. Eroshenko (1991), The solar wind interaction with Mars - Mariner 4, Mars 2, Mars 3, Mars 5, and PHOBOS 2 observations of bow shock position and shape, *J. Geophys. Res.*, 96, 11,235, doi:10.1029/91JA00439.
- Simon, S., A. Boesswetter, T. Bagdonat, and U. Motschmann (2007), Physics of the Ion Composition Boundary: a comparative 3-D hybrid simulation study of Mars and Titan, *Ann. Geophys.*, 25, 99-115, doi:10.5194/angeo-25-99-2007
- Smith, C. W., J. L'Heureux, N. F. Ness, M. H. Acuña, L. F. Burlaga, and J. Scheifele (1998), The ACE Magnetic Fields Experiment, *Space Sci. Rev.*, 86, 613–632, doi:10.1023/A:1005092216668.
- Smith, P. H., L. K., Tamppari, R. E. Arvidson, D. Bass, D. Blaney, W. V. Boynton, et al., (2009). H<sub>2</sub>O at the phoenix landing site, *Science* 325, 58–61, DOI: 10.1126/science.1172339.
- Sonnerup, B. U. Ö., H. Hasegawa, and G. Paschmann (2004), Anatomy of a flux transfer event seen by Cluster, *Geophys. Res. Lett.*, 31, L11803, doi:10.1029/2004GL020134.
- Takagi, K., C. Hashimoto, H. Hasegawa, M. Fujimoto, R. TanDokoro (2006), Kelvin-Helmholtz instability in a magnetotail flank-like geometry: Three-dimensional

## REFERENCES

- MHD simulations, *J. Geophys. Res. (Space Physics)*, 111, A08202, doi:10.1029/2006JA011631.
- Terada, N., S. Machida, and H. Shinagawa (2002), Global hybrid simulation of the Kelvin-Helmholtz instability at the Venus ionopause, *J. Geophys. Res. (Space Physics)*, 107, 1471, doi:10.1029/2001JA009224.
- Trotignon, J. G., R. Grard, and A. Skalsky (1993), Position and shape of the Martian bow shock - The PHOBOS 2 plasma wave system observations, *Planet. Space Sci.*, 41, 189–198, doi:10.1016/0032-0633(93)90058-A.
- Trotignon, J. G., E. Dubinin, R. Grard, S. Barabash, R. Lundin, (1996), Martian planetopause as seen by the plasma wave system onboard Phobos 2, *J. Geophys. Res.* 96, 11, doi: 10.1029/96JA01898.
- Trotignon, J. G., H.-C. Seran, C. Beghin, N. Meyer-Vernet, R. Manning, R. Grard, and H. Laakso (2001), In situ observations of the ionized environment of Mars: the antenna impedance measurements experiment, AIM, proposed as part of the Mars advanced radar for subsurface and ionospheric sounding, MARSIS, *Planet. Space Sci.*, 49, 155–164, doi:10.1016/S0032-0633(00)00134-3.
- Trotignon, J. G., C. Mazelle, C. Bertucci, M. H. Acuña (2006), Martian shock and magnetic pile-up boundary positions and shapes determined from the Phobos 2 and Mars Global Surveyor data sets, *Planet. Space Sci.*, 54, 357–369, doi:10.1016/j.pss.2006.01.003.
- Tsuneta, S., (1996), Structure and dynamics of magnetic reconnection in a solar flare, *Astrophysical Journal*, 456, 840, doi:10.1086/176701
- Vennerstrom, S., N. Olsen, M. Purucker, M. H. Acuña, and J. C. Cain (2003), The magnetic field in the pile-up region at Mars, and its variation with the solar wind, *Geophys. Res. Lett.*, 30 (7), 1369, doi:10.1029/2003GL016883.

## REFERENCES

- Vignes, D., et al. (2000), The solar wind interaction with Mars: Locations and shapes of the Bow Shock and the magnetic pile-up boundary from the observations of the MAG/ER experiment onboard Mars Global Surveyor, *Geophys. Res. Lett.*, 27 (1), 49–52, doi:10.1029/1999GL010703.
- Vignes, D., M. H. Acuña, J. E. P. Connerney, D. H. Crider, H. Reme, and C. Mazelle (2004), Magnetic Flux Ropes in the Martian Atmosphere: Global Characteristics, *Space Sci. Rev.*, 111, 223–231, doi:10.1023/B:SPAC. 0000032716.21619.f2.
- Vogt, M. F., et al. (2015), Ionopause-like density gradients in the Martian ionosphere: A first look with MAVEN, *Geophys. Res. Lett.*, 42, doi:10.1002/2015GL065269.
- Xu, S., M. W. Liemohn, C. Dong, D. L. Mitchell, S. W. Bougher, and Y. Ma (2016), Pressure and ion composition boundaries at Mars, *J. Geophys. Res.(Space Physics)*, 121, 6417–6429, doi:10.1002/2016JA022644.
- Zhang, T. L., J. G. Luhmann, C. T. Russell (1991), The magnetic barrier at Venus, *J. Geophys. Res.*, 96(A7), 11145–11153, doi:10.1029/91JA00088.
- Zhang, T. L., J. Du, Y. J. Ma, H. Lammer, W. Baumjohann, C. Wang, and C. T. Russell (2009), Disappearing induced magnetosphere at Venus: Implications for close-in exoplanets, *Geophys. Res. Lett.*, 36, L20203, doi:10.1029/2009GL040515.



# Publications

- [1] Matsunaga, K., K. Seki, T. Hara, and D. A. Brain (2015), Asymmetric Penetration of Shocked Solar Wind Down to 400-km Altitudes at Mars, *J. Geophys. Res., Space Physics*, 120, 6874-6883, 2015, doi:10.1002/2014JA020757
- [2] Hara, T., K. Seki, H. Hasegawa, D. A. Brain, K. Matsunaga, and M. H. Saito (2014), The spatial structure of Martian magnetic flux ropes recovered by the Grad-Shafranov reconstruction technique, *J. Geophys. Res., Space Physics*, 119, 1262--1271, 2014, doi:10.1002/2013JA019414
- [3] Hara, T., K. Seki, H. Hasegawa, D. A. Brain, K. Matsunaga, M. H. Saito, and D. Shiota (2014), Formation processes of flux ropes downstream from Martian crustal magnetic fields inferred from Grad-Shafranov reconstruction, *J. Geophys. Res., Space Physics*, 119, 2014, doi:10.1002/2014JA019943

# Journal of Geophysical Research: Space Physics

## RESEARCH ARTICLE

10.1002/2014JA020757

**Key Points:**

- Magnetosheath often penetrates into Martian ionosphere under away IMF period
- Magnetosheath often penetrates into Martian ionosphere in northern hemisphere
- The magnetosheath penetrations mainly occur in upward electric field hemisphere

**Correspondence to:**K. Matsunaga,  
matsunagak@stelab.nagoya-u.ac.jp**Citation:**Matsunaga, K., K. Seki, T. Hara, and D. A. Brain (2015), Asymmetric penetration of shocked solar wind down to 400 km altitudes at Mars, *J. Geophys. Res. Space Physics*, 120, 6874–6883, doi:10.1002/2014JA020757.

Received 22 OCT 2014

Accepted 18 JUL 2015

Accepted article online 23 JUL 2015

Published online 13 AUG 2015

Corrected 29 OCT 2015

This article was corrected on 29 OCT 2015. See the end of the full text for details.

## Asymmetric penetration of shocked solar wind down to 400 km altitudes at Mars

Kazunari Matsunaga<sup>1</sup>, Kanako Seki<sup>1</sup>, Takuya Hara<sup>2</sup>, and David A. Brain<sup>3</sup>

<sup>1</sup>Solar-Terrestrial Environment Laboratory, Nagoya University, Nagoya, Japan, <sup>2</sup>Space Sciences Laboratory, University of California, Berkeley, California, USA, <sup>3</sup>Laboratory for Atmospheric and Space Physics, University of Colorado Boulder, Boulder, Colorado, USA

**Abstract** The penetration boundary of shocked solar wind (magnetosheath) into the Martian upper atmosphere is typically located at altitudes above 800 km. However, magnetosheath plasma occasionally penetrates into low altitudes below 400 km. Here we used Mars Global Surveyor magnetic field and electron observations from April 1999 to November 2006 to investigate the magnetosheath penetration events. We identified 1145 events and found that both solar wind dynamic pressure ( $P_{dyn}$ ) and the orientation of the interplanetary magnetic field (IMF) control the occurrence of the events. The magnetosheath penetration events during low  $P_{dyn}$  periods tend to be distributed in low latitudes of the northern hemisphere or where the crustal magnetic field is weak, while the event locations are widely distributed in terms of the latitude under high  $P_{dyn}$  conditions. During low  $P_{dyn}$  periods, a remarkable feature is that the observational probability is approximately 2.4 times larger during periods of the “away” IMF sector than during the “toward” sector. The northern hemisphere during the away sector corresponds to the upward electric field hemisphere due to the convection of draping solar wind origin magnetic flux tubes. These results thus indicate that the magnetosheath penetrations into Martian upper atmosphere more often occur in the upward electric field hemisphere than the downward hemisphere during low  $P_{dyn}$  periods. Large-amplitude undulation excited by the Kelvin-Helmholtz instability in the upward electric field hemisphere is a candidate process to cause the asymmetric penetration during low  $P_{dyn}$  periods. Another possibility might be the mirror-mode instability by the asymmetric distribution of planetary pickup ions.

### 1. Introduction

Mars has no intrinsic global magnetic field like Earth [Acuña *et al.*, 1998]. However, Mars Global Surveyor (MGS) observed the magnetic field from remnant crustal magnetizations mainly in the southern hemisphere [e.g., Acuña *et al.*, 1998, 1999]. Hence, Mars is not a simple unmagnetized planet, such as Venus. Interaction between the solar wind and the Martian ionosphere forms several varieties of plasma regime [e.g., Vignes *et al.*, 2000; Luhmann *et al.*, 2004]. The solar wind becomes subsonic at the bow shock before reaching Mars, and the downstream subsonic region is called the magnetosheath. The magnetosheath region has shock-heated plasma and turbulent magnetic field signatures. When the spacecraft passes through the magnetosheath region, fluctuations of the magnetic field and high-energy (from about 50 eV to  $\sim$ 1 keV) electron flux are known to increase [e.g., Nagy *et al.*, 2004; Crider *et al.*, 2005; Guicking *et al.*, 2010]. As a magnetosheath flux tube approaches Mars, it is decelerated by mass loading and draped around Mars. It thus forms the region of piled-up magnetic field. This region is referred to as the magnetic pileup region or induced magnetosphere, and its outer boundary is called the magnetic pileup boundary (MPB) or induced magnetosphere boundary [e.g., Vignes *et al.*, 2000; Luhmann *et al.*, 2004]. The lower boundary of the magnetic pileup region determines the upper boundary of ionosphere. MPB does not always have a clear structure. It sometimes has a complicated structure.

Ionospheric ions and electrons, accelerated by the electric field induced by the flowing solar wind, produce a current in the planetary ionosphere, which reduces the compressed interplanetary magnetic field (IMF) with decreasing altitude. The IMF draping can be described as produced by this electric field [e.g., Alfven, 1957; Cloutier and Daniell, 1973]. Hence, the flux tubes originated from the solar wind can directly interact with the Martian ionosphere. The situation is very different from the case of Earth, where the global intrinsic magnetic field deflects the shocked solar wind at much higher altitudes. Since the direct interaction with the solar wind causes energy and momentum exchange between the solar wind and the ionosphere

[e.g., *Lundin*, 2011], atmospheric escape processes induced by such interaction are important subjects of study in unmagnetized planets like Mars [e.g., *Jakosky and Phillips*, 2001]. The escape rate of planetary ions is related to the condition and/or location of the magnetosheath region. Therefore, it is important to know how often the magnetosheath plasma penetrates into altitudes lower than usual [e.g., *Brain et al.*, 2005; *Crider et al.*, 2005; *Nilsson et al.*, 2010] and to understand what is the physical mechanism to cause the penetration.

MGS observations showed that the MPB is typically located at about 800–1200 km altitudes from the surface on the dayside [e.g., *Vignes et al.*, 2000]. However, this boundary location can change significantly depending on solar wind conditions. Previous studies indicate that the magnetosheath can penetrate to altitudes lower than usual when the solar wind dynamic pressure ( $P_{dyn}$ ) is high [*Crider et al.*, 2005]. In addition, a number of investigators predicted that the MPB has an asymmetry in the shape [*Brech and Ferrante*, 1991; *Brech et al.*, 1993; *Harnett and Winglee*, 2003; *Brain et al.*, 2006a]. It has been also pointed out that the crustal magnetic fields can locally push the magnetosheath region upward and cause an asymmetric structure of MPB [e.g., *Brain et al.*, 2003, 2006a]. Moreover, *Brain et al.* [2005] shows that the detection of magnetosheath plasma at 400 km altitudes (hereafter referred to as “magnetosheath penetration events”) depends on  $P_{dyn}$ , IMF orientation, and season. However, the physical mechanisms causing the observed dependencies, especially effects of the IMF orientation, are not understood.

In this paper, we focus on the penetration of magnetosheath plasma down to 400 km altitudes on the dayside of Mars, based on MGS observations. In order to statistically investigate the properties of penetration events, we implemented a semiautomatic event selection and identified 1145 events from ~7.6 years of MGS data. We used solar wind proxy data derived from MGS observations [*Crider et al.*, 2003; *Brain et al.*, 2006a] and time-shifted solar wind data recorded at Earth by the Advanced Composition Explorer (ACE) satellite, to ensure the quality of the IMF polarity estimation at Mars. We also use a model of Martian crustal magnetic field (the Cain model) [*Cain et al.*, 2003]. Then, the dependence on the solar wind parameters and role of crustal magnetic field are investigated. In section 2, we introduce the MGS magnetometer (MAG) and electron reflectometer (ER) instrumentations. In section 3, we explain the methods to select magnetosheath penetration and of estimation of solar wind parameters at Mars. In section 4, we report on statistical properties of magnetosheath penetration events, especially focused on when the  $P_{dyn}$  is low. Finally, in section 5 we summarize the statistical results and discuss candidate physical mechanisms to cause the penetration of magnetosheath plasma to low altitudes.

## 2. Instrumentation

The Mars Global Surveyor (MGS) spacecraft was launched in 1996 and inserted into orbit around Mars in 1997. The MGS orbit was slowly circularized (through aerobraking) and formed into a quasi-polar orbit with an average altitude of about 400 km (mapping orbit) from April 1999 to November 2006 when contact with the spacecraft was lost. The mapping orbit used in this study was fixed in local time at 2 A.M./P.M., and the spacecraft orbital period is approximately 2 h. During the mapping orbit, MGS usually observed in the Martian ionosphere or magnetic pileup region when it was on the dayside.

MGS carried the magnetometer (MAG) and electron reflectometer (ER) in order to observe the plasma environment around Mars. MAG provided three-dimensional magnetic field data with a time resolution of 0.75–3 s over the range of ~1 to 65,536 nT with a digital resolution of 12 bits [*Acuña et al.*, 1992]. The ER instrument measured electrons in the range of ~10 eV to 20 keV with a time resolution of 12–48 s and an energy resolution of  $\Delta E/E \sim 25\%$  [*Mitchell et al.*, 2001; *Albee et al.*, 2001]. The lack of ion detectors on board MGS prevents the direct identification of magnetosheath from ion data. Previous studies during MGS premapping phase show the characteristics of electrons and magnetic field in the magnetosheath region [e.g., *Albee et al.*, 2001; *Crider et al.*, 2005]. Here we use these characteristics to identify the magnetosheath region.

We also use solar wind parameters obtained from ACE observations at ~1 AU, taking into account the radial distance and elongation between Earth and Mars [*Vennerstrom et al.*, 2003] in order to estimate the IMF polarity around Mars during the same time period.

## 3. Data Analysis

We use data from the MGS mapping orbits around 400 km altitudes from April 1999 to November 2006. We first introduce the selection criteria for magnetosheath penetration events. Previous measurements have shown

that the various plasma regions have different characteristic magnetic field fluctuations and electron energy spectra. We use these signatures to identify the periods when magnetosheath plasma penetrated down to the 400 km altitude. According to previous studies [e.g., Nagy *et al.*, 2004; Brain *et al.*, 2006b], when the spacecraft passed through the magnetosheath region, fluctuations of the magnetic field were enhanced [Brain *et al.*, 2003; Bertucci *et al.*, 2003; Espley *et al.*, 2004] and the electron energy spectrograms showed a characteristic change. Since the energy fluxes of high-energy electrons (over 100 eV) observed in the magnetosheath and magnetic pileup regions are higher than in the ionosphere [e.g., Mitchell *et al.*, 2001; Crider *et al.*, 2005], we can distinguish whether MGS is in or above the ionosphere. Since high-frequency fluctuations of the magnetic field in the magnetosheath are larger than in the magnetic pileup region [e.g., Nagy *et al.*, 2004], we can infer whether MGS is in the magnetosheath or the magnetic pileup region based on the wave power.

We first selected the time intervals when MGS is located on a dayside and the integrated differential electron flux above 400 eV was greater than  $5 \times 10^3 \text{ cm}^{-2} \text{ s}^{-1} \text{ sr}^{-1}$  in order to eliminate the data when MGS was in the Martian ionosphere. The MGS electron reflectometer often saturates between about 100 eV and 400 eV in high-electron flux regions [e.g., Crider *et al.*, 2005]. Therefore, we use the electron flux above 400 eV for our selection criteria. Next, we selected the time intervals when the power spectral density of the magnetic field fluctuation above 0.1 Hz was higher than  $1000 \text{ nT}^2/\text{Hz}$  in order to select the data when MGS was located in the Martian magnetosheath region by eliminating observations in the magnetic pileup region. Our threshold values are intentionally conservative to guard against false positives in our list of magnetosheath penetration events. We confirmed that our final conclusions are not sensitive to less stringent choices for these two threshold values. We discuss the impact of the choice of threshold value on conclusions in section 5. After automatically selecting events, we eliminated current sheet crossings or solar energetic particles (SEPs) events by inspection. Since we want to investigate the relation between the solar wind condition and the magnetosheath penetration to understand the physical mechanisms, we eliminate these inappropriate events. We eliminated the current sheet crossings events from the signature of inverting of magnetic field direction and SEPs events from the signature of suddenly enhanced high-energy (10–20 keV) electrons. Finally, we excluded the events with duration less than 1 min and crustal field magnitude larger than 15 nT. These events are most likely to be observed when MGS passed through Martian magnetic field cusps. Above cusp regions, magnetosheath plasma can more easily access low altitudes, regardless of solar wind conditions. This study focuses on magnetosheath penetration to ionospheric regions typically shielded by induced magnetic fields.

As a result, we identified 1145 events of the magnetosheath penetration. Figure 1 shows a typical event on 2 June 2003. Figure 1a shows the magnitude of magnetic field, and Figure 1e shows differential electron flux from MGS observation. We calculated the power of magnetic field fluctuations and integrated above 0.1 Hz (Figure 1b). Moreover, we integrated differential electron flux above 400 eV (Figure 1f). In this study, we only surveyed when the spacecraft was on dayside, colored as light blue in Figure 1c. During 14.2 min in Figure 1 (the period between two vertical red lines), MGS simultaneously observed highly fluctuating magnetic field and significant flux of high-energy electrons. The green color in Figure 1d indicates the time intervals satisfying the criteria. Since the wavelet power shows high fluctuations, we assume that the event is continuous when time gaps between green color (Figure 1d) intervals are shorter than 5 min and identified the time interval between two red vertical lines as one event.

The upstream solar wind seldom has an access to the 400 km altitude of the MGS mapping orbit. We thus cannot directly obtain the solar wind properties, such as  $P_{\text{dyn}}$  and the IMF polarity around Mars from MGS data. Therefore, we use proxies for  $P_{\text{dyn}}$  and the IMF orientation at Mars implemented by Brain *et al.* [2005, 2006a] and Crider *et al.* [2003].

The  $P_{\text{dyn}}$  proxy is derived from the measured intensity of the piled-up magnetic field on the Martian day-side [Crider *et al.*, 2003; Brain *et al.*, 2005]. As described in Brain *et al.* [2005], they exclude observations above crustal magnetic sources and with solar zenith angle (SZA) greater than 110°. Then, they fit the remaining field strengths to a  $\cos(\text{SZA})$  function to estimate the field strength at SZA = 0°.

The IMF draping direction proxy is derived from the azimuth direction of the draped magnetic field based on all dayside MAG data recorded in the latitude range between 50° and 60° in the northern hemisphere [Brain *et al.*, 2005, 2006a]. Azimuth direction is defined with 0° in the local eastward direction and 90° in the local northward direction [Brain *et al.*, 2006a]. However, the IMF draping direction proxy is known to have an asymmetry. Brain *et al.* [2006a] pointed out that the crustal magnetic fields locally push the MPB upward,

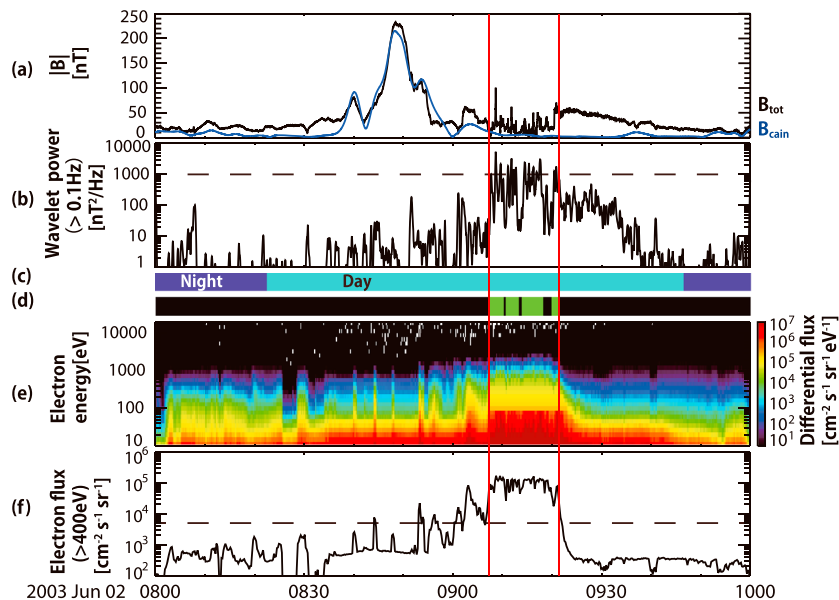


**Figure 1.** Overview of the time series plots of the solar wind (magnetosheath) penetration event observed by MGS on 2 June 2003: (a) the magnitude of magnetic field, (b) the power of magnetic field fluctuations above 0.1 Hz, (c) the day-night indices, (d) the indices of event time, (e) the differential electron flux, and (f) the integrated differential electron flux above 400 eV. The blue line in Figure 1a shows the crustal magnetic field model [Cain et al., 2003]. Missing data due to instrument saturation around 100 eV in the magnetosheath region are interpolated linearly. The time interval between two vertical red lines indicates the period of the magnetosheath penetration identified by the criteria described in the text. Black horizontal dashed lines in Figures 1b and 1f mean our thresholds used in this study, respectively.

which may play a role in creating the observed asymmetry. Since time resolution of these proxies is about 2 h due to the MGS orbit, we use the closest data in time available to represent solar wind conditions for an event.

Figure 2 shows the time series plots of the solar wind parameters estimated from ACE and MGS observations. The ACE solar wind data are time shifted to the location of Mars in order to infer the IMF sector polarity at Mars. The shifted time can be determined from a combination of propagation in the radial distance between Earth and Mars and rotation of the angular distance between Earth and Mars [Vernerstrom et al., 2003]. Green bars in Figure 2a correspond to the time of magnetosheath penetration events. The  $P_{\text{dyn}}$  (ACE) in Figure 2b is scaled to Mars heliocentric distances. In the scaling it was assumed that the density varies as  $1/r^2$  and that the solar wind speed is constant with heliocentric distance,  $r$ . Both the MGS and ACE pressure proxies could be used to sort the observations. Ideally, the two proxies would be highly correlated with each other, but this is not the case. The correlation coefficient for the two proxies is 0.25, and the mean absolute deviation is ~84%, suggesting that there are nonnegligible differences between the two. Some of the reasons for this are discussed in Vernerstrom et al. [2003]. In this study we have chosen to use the local proxy, derived from MGS data, to sort the observations. Figure 2c shows the magnitude of magnetic field from time-shifted ACE data to see the variation of upstream condition around Mars. Comparing the IMF polarity from the time-shifted ACE data with the IMF draping direction proxy from MGS data (Figures 2d and 2e), we determined the IMF polarity from only MGS IMF proxy data (Figure 2f). As pointed out by Brain et al. [2006a], the IMF draping direction proxy shows a clustering around  $210^\circ - 270^\circ$  regardless of the IMF sector polarity. Hence, it is sometimes difficult to determine the sector polarity only from individual proxy value taken in isolation. However, it is often possible to determine which solar wind sector polarities around Mars occupied for a given orbit based on the longer baseline time series of proxy values.

First, we compared the time-shifted ACE data with MGS data, when elongation between Mars and Earth is small (within  $90^\circ$ ), so as to investigate what characteristics of the IMF draping direction proxy from MGS correspond to the IMF sector polarity, i.e., “away” or “toward” sector of the Parker spiral structure in the solar wind. The azimuthal angle ( $\phi_B$ ) of the IMF observed by ACE is defined by the Geocentric Solar Ecliptic coordinate. As shown in Figure 2d, the time intervals when  $\phi_B$  are distributed around  $135^\circ$  correspond to away

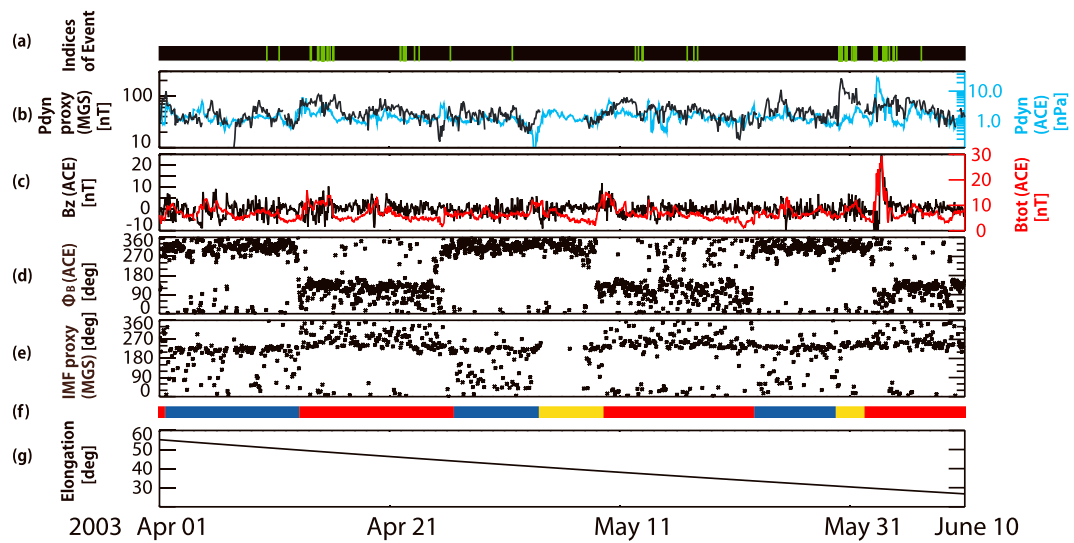


**Figure 2.** Time series plots of the solar wind parameters estimated from ACE and MGS observations. (a) The indices of event time, (b) the magnitude of solar wind dynamic pressure (black line shows the MGS data, and the blue corresponds to time-shifted ACE data), (c) the magnitude of magnetic field from time-shifted ACE data (black line shows  $B_z$  (north-south) component of  $B$ , and the red indicates the total  $B$ ), (d) the IMF polarity (GSE ( $\phi_B$ )) from time-shifted ACE data, (e) the IMF polarity proxy from MGS data, (f) the estimated IMF polarity (red, blue, and yellow correspond to the away polarity, toward polarity, and others, respectively), and (g) the elongation between Mars and Earth are shown. Note that the unit of the solar wind dynamic pressure derived from MGS is nT, and that of solar wind dynamic pressure derived from ACE is nPa in Figure 2b.

polarity and around  $315^\circ$  correspond to toward polarity. Therefore, we found that the time intervals when the MGS IMF draping direction proxy is clustered from about  $210^\circ$  to  $360^\circ$  correspond to away sector, and  $90^\circ$  to  $180^\circ$  correspond to toward sector. Next, based on this correspondence, we categorized the IMF sector polarity inferred from the MGS IMF draping direction proxy into three categories (away, toward, and other) for all MGS mapping phase data obtained during the surveyed 7 years and 7 month period regardless of elongation between Earth and Mars. This way to determine IMF polarity makes it less sensitive to the time resolution of IMF proxy. All events including those occurring near sector boundaries or not clustering as described above were classified as “other”. Other events include solar wind disturbances such as corotating interaction regions (CIRs) or coronal mass ejections (CMEs) and “unknown” events that we cannot categorize due to a lack of distinguishing clustering of the IMF proxy or sector boundary.

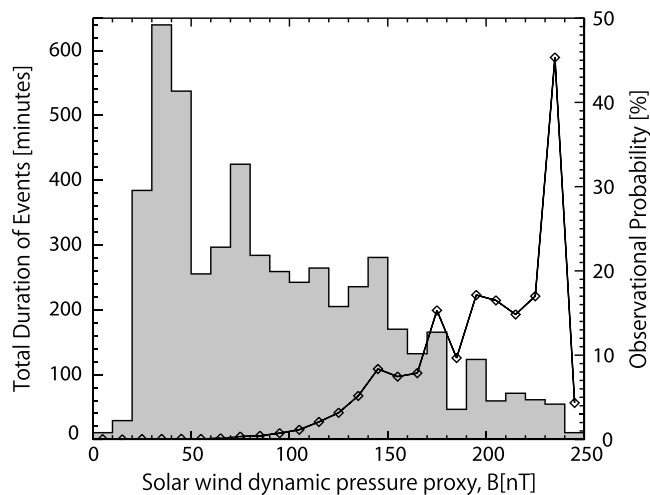


**Figure 3.** Histogram of the total duration and line plot of observational probability of the magnetosheath penetration events as a function of the solar wind dynamic pressure proxy obtained from the MGS/MAG observations.

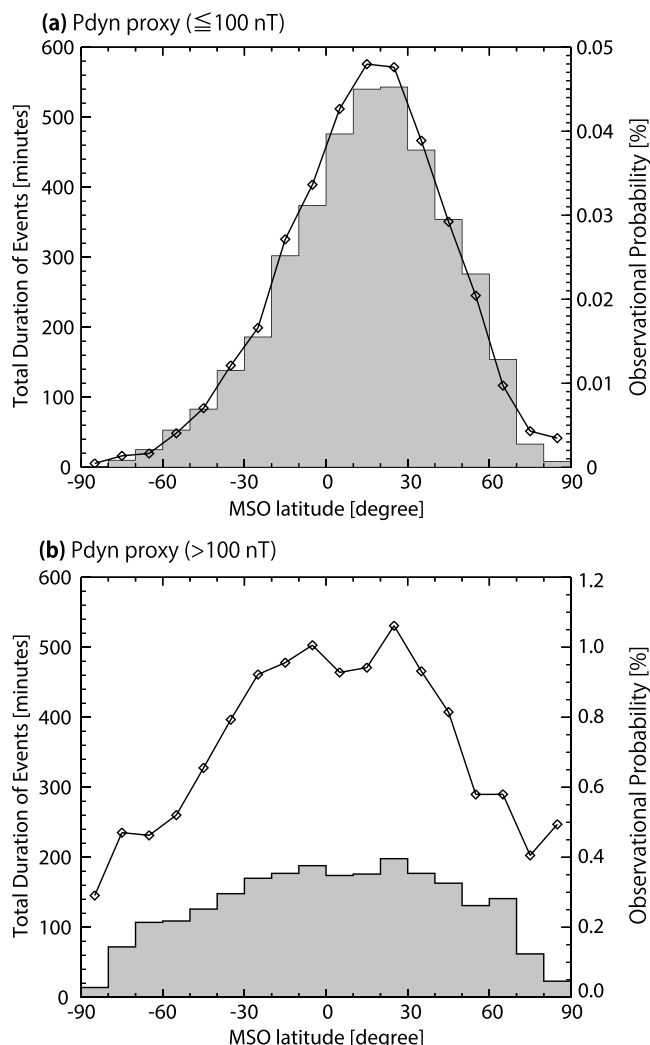


**Figure 4.** Histograms of the total duration and line plots of observational probability of the magnetosheath penetration events as a function of the MSO latitude, under (a) low and (b) high solar wind dynamic pressure ( $P_{\text{dyn}}$ ) conditions.

When we categorize the 1145 magnetosheath penetration events based on the inferred IMF conditions, it turned out that 442 events are identified as the away polarity events, 155 events as the toward polarity, and 548 events as other. Other events include 233 CMEs or CIRs events under low  $P_{\text{dyn}}$  conditions. We selected CMEs or CIRs events from the enhancement of  $P_{\text{dyn}}$  proxy data and rotation of IMF draping direction proxy.

#### 4. Statistical Properties

First, we investigate the dependence of the selected 1145 magnetosheath penetration events on the  $P_{\text{dyn}}$  proxy. Figure 3 shows the total duration (histogram) and the observational probability (line plot) of the magnetosheath penetration events as a function of the MGS  $P_{\text{dyn}}$  proxy. The observational probability means the duration of events under each  $P_{\text{dyn}}$  condition divided by the total observation time under each  $P_{\text{dyn}}$  condition during about 7.6 years. Figure 3 shows that the observational probability (line plot) increases when the  $P_{\text{dyn}}$  proxy exceeds about 100 nT. This tendency is consistent with that of Brain *et al.* [2005]. We thus henceforth define the relatively lower  $P_{\text{dyn}}$  condition of  $\leq 100$  nT as “low”  $P_{\text{dyn}}$  periods, while the higher  $P_{\text{dyn}}$  periods of  $> 100$  nT are referred to as “high”  $P_{\text{dyn}}$  periods. Assuming that upstream dynamic pressure is balanced to the magnetic pressure on the dayside magnetic pileup region, a dynamic pressure proxy of 100 nT can convert into a dynamic pressure of approximately 4 nPa. We can also see that there are a significant number of events even during the low  $P_{\text{dyn}}$  periods. Furthermore, the duration of the magnetosheath penetration events under the low and high  $P_{\text{dyn}}$  conditions accounts for 59.6% and 40.4% of the total duration, respectively. Therefore,

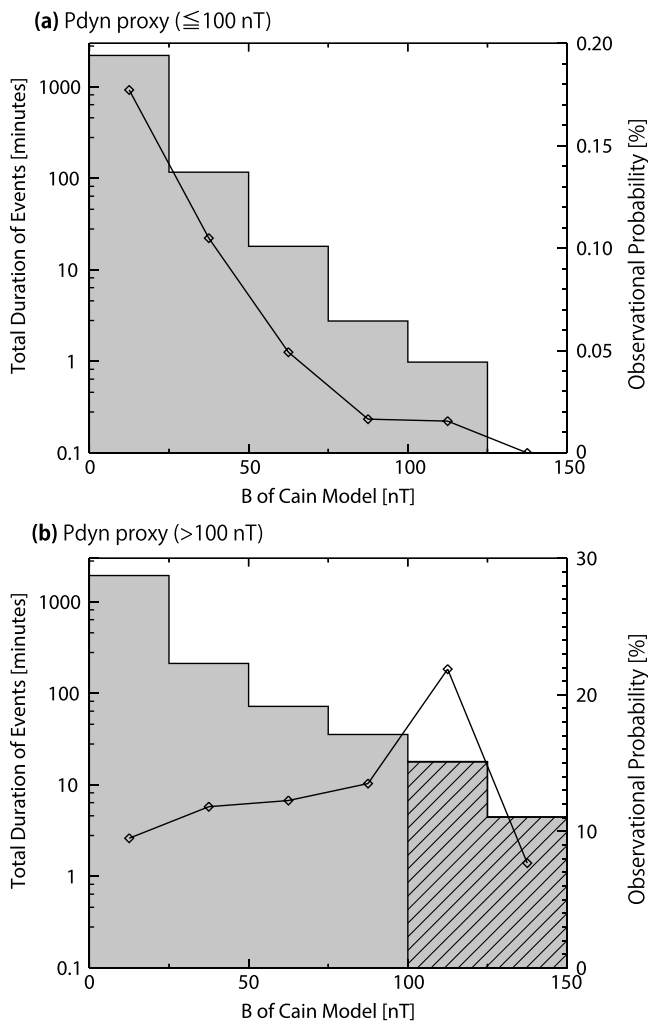


**Figure 5.** Histograms of the total duration and line plots of observational probability of the magnetosheath penetration events as a function of the estimated magnitude of crustal magnetic field from the Cain model [Cain et al., 2003], under (a) low and (b) high solar wind dynamic pressure ( $P_{\text{dyn}}$ ) conditions.

more than half of magnetosheath penetration events were observed under low  $P_{\text{dyn}}$  conditions. It should be noted that there is a rough tendency that short-duration events are often seen under low  $P_{\text{dyn}}$  conditions (not shown).

We next investigate the dependence on the observed event locations in terms of the Mars-centered Solar Orbital (MSO) latitude. MSO coordinate system is defined as follows: the X axis points from Mars to the Sun, the Y axis is opposite to the Mars orbital motion, and the Z axis completes the right-handed system. The MSO latitude is computed via  $\arctan(Z/\sqrt{X^2 + Y^2})$ . Figure 4 shows the total duration (histogram) and the observational probability (line plot) of the magnetosheath penetration events as a function of the MSO latitude separately for low (Figure 4a) and high (Figure 4b)  $P_{\text{dyn}}$  periods. In both the low and high  $P_{\text{dyn}}$  cases, the observational probability is higher near  $0^\circ$  of the MSO latitude where the  $P_{\text{dyn}}$  is highest. During the low  $P_{\text{dyn}}$  periods, the events tend to be observed in low latitudes of the northern hemisphere. On the other hand, during the high  $P_{\text{dyn}}$  periods, the events are distributed over a wide latitude range in both the southern and northern hemispheres. The magnetosheath penetration peaking in the northern hemisphere is consistent with that of a previous study by Brain et al. [2005]. It is considered that the strong magnetic pressure of the localized crustal fields in the southern hemisphere pushes MPB to higher altitudes, preventing magnetosheath penetration. As  $P_{\text{dyn}}$  increases, the shielding due to the crustal magnetic field becomes less effective at the 400 km altitude and the magnetosheath penetration more frequently occurs in a wide latitude range.

**Table 1.** Duration of Each Solar Wind Condition, Ratio of Each Solar Wind Condition, Number of Events, Ratio of Events' Duration, and Ratio of Observational Probability (Normalized by Toward)

Solar Wind	$P_{\text{dyn}}(>100 \text{ nT})$	Low $P_{\text{dyn}}(\leq 100 \text{ nT})$				Total
		Away	Toward	Other		
Duration of each solar wind condition (days)	38.8	1,172.1	768.6	622.7		2563.4
Ratio of each solar wind condition (%)	1.5	45.0	29.5	23.9		98.5
Low $P_{\text{dyn}}(\leq 100 \text{ nT})$						
Events	$P_{\text{dyn}}(>100 \text{ nT})$	High	Other			
		Away	Toward	CMEs or CIRs	Unknown	Total
Number of events (#)	248	416	150	233	98	897
Event total (h)	35.2	20.9	5.6	19.9	5.4	51.8
Ratio of events' duration (%)	40.4	24.1	6.5	22.8	6.2	59.6
Ratio of observational probability (normalized by toward)	124.3	2.4	1	4.4	1.2	

In order to investigate the effect of the crustal magnetic field, we further use the Cain model [Cain *et al.*, 2003]. Figure 5 shows the total duration (histograms) and the observational probability (line plot) of the magnetosheath penetration events as a function of the magnitude of the crustal magnetic field estimated from the Cain model. As shown in Figure 5a, the events during low  $P_{\text{dyn}}$  periods are mostly observed in the region where the crustal magnetic field is relatively weak ( $< 25 \text{ nT}$ ). This result is consistent with the concentration of magnetosheath penetration events in the northern hemisphere. On the other hand, the observation probability of the magnetosheath penetration during high  $P_{\text{dyn}}$  periods is relatively constant regardless of the strength of the crustal magnetic fields (Figure 5b). It may indicate that such a high  $P_{\text{dyn}}$  condition is enough to overcome the magnetic pressure due to the crustal magnetic fields. Or high  $P_{\text{dyn}}$  might make cusps due to the crustal magnetic fields wider than usual. Another possibility might be that the magnetic reconnection [e.g., Halekas *et al.*, 2009] plays an important role in eroding minimagnetospheres. However, the observation probability during high crustal magnetic field events (larger than 100 nT) is statistically less significant because of the small total duration of events (22.3 min or 1% of the histogram in Figure 5b). We shaded these less significant bins differently in Figure 5b. In section 3, we categorized 1145 events into three categories (away, toward, and other) in terms of the upstream IMF conditions. During the high  $P_{\text{dyn}}$  periods, it is natural to conclude that the  $P_{\text{dyn}}$  is strong enough to make the magnetosheath plasma penetrate down to 400 km altitude. Most of the high  $P_{\text{dyn}}$  events are categorized as other, since high  $P_{\text{dyn}}$  is often caused by solar wind disturbances such as CIRs or CMEs. On the other hand, during the low  $P_{\text{dyn}}$  periods, we need other mechanisms to cause the magnetosheath penetrations into 400 km altitude, especially when there are no CIRs or CMEs. We therefore focus on the 566 events (away and toward events) observed during the low  $P_{\text{dyn}}$  periods and further investigate their dependence on IMF polarity. Table 1 shows the summary of the magnetosheath penetration events with respect to the estimated solar wind conditions. The second row in Table 1 shows that the ratio of away to toward sector polarities during the low  $P_{\text{dyn}}$  periods was about 1.5 during the survey period. By contrast, the number of magnetosheath penetration events during the away polarity is significantly larger than that during the toward polarity. From Table 1, the observational probability of events during the away IMF sector periods is approximately 2.4 times higher than that of during the toward IMF sector periods.

## 5. Summary and Discussion

In this paper, we reported the result of a statistical investigation of the penetration of Martian magnetosheath plasma down to 400 km altitudes analyzing  $\sim 7.6$  years of MGS MAG and ER data (April 1999 to November 2006). We used semiautomatic event selection criteria based on these measurements in order to identify 1145 magnetosheath penetration events. We used a proxy for solar wind dynamic pressure ( $P_{\text{dyn}}$ ) and developed a method to determine the IMF sector polarities by comparing the IMF direction measured at Earth (time-shifted ACE data) with the IMF draping direction at Mars (MGS data).

We investigated the dependence of these 1145 events on the  $P_{\text{dyn}}$ , the MSO latitude, the local crustal magnetic field strength, and the IMF sector polarity. The events are frequently observed during high  $P_{\text{dyn}}$  periods ( $> 100 \text{ nT}$ ). However, the number of events is larger for low  $P_{\text{dyn}}$  periods ( $\leq 100 \text{ nT}$ ), which occur more often.

Moreover, the magnetosheath tends to penetrate mostly into regions where the crustal magnetic field is weak. The observation probability of the magnetosheath penetration is approximately 2.4 times higher under the away IMF sector polarity conditions than under the toward IMF sector polarity conditions during low  $P_{\text{dyn}}$  periods (Table 1).

We also investigated the threshold for electron flux used to select events. When using a more restrictive threshold (electron flux of  $5 \times 10^4 \text{ cm}^{-2} \text{ s}^{-1} \text{ sr}^{-1}$ , 1 order of magnitude higher than the previous threshold), the total duration of magnetosheath penetration events decreases by a factor of about 6. The number of events is 215. It also decreases. Nevertheless, the observation probability of the magnetosheath penetration is more than 7 times higher under the away IMF sector polarity conditions than under the toward IMF sector polarity conditions during low  $P_{\text{dyn}}$  periods. The qualitative trends with IMF sector polarity are not dependent upon the choice of threshold value, even though some of the quantitative results vary.

As mentioned in section 1, *Brain et al.* [2005] also investigated the dependence of magnetosheath plasma penetration at 400 km altitudes on  $P_{\text{dyn}}$ , IMF orientation, and season. The differences between this study and *Brain et al.* [2005] are the method and time range. *Brain et al.* [2005] used only the electron energy spectra to identify the magnetosheath region from mid-1999 to February 2005. In this study, we used the fluctuation of the magnetic field and the intensity of electron flux to identify whether MGS observed the magnetosheath region or not in all MGS mapping orbit phase (from April 1999 to November 2006). Using not only the magnetic field but also electron data, we detect the observation of magnetosheath plasma more conservatively. Moreover, we compared MGS data with time-shifted ACE solar wind data to estimate the IMF polarity. It thus allows us to more precisely investigate the solar wind dependence of the magnetosheath penetration at 400 km altitude.

Our results indicate that during the low  $P_{\text{dyn}}$  periods, both northern hemisphere events and “away” IMF polarity events are favored. Further investigation reveals that these two conditions are usually met at the same time—that is, the observed events often occur in the northern hemisphere during “away” IMF polarity. On the one hand, the frequent observation in the northern hemisphere compared to that in the southern hemisphere is consistent with a previous study by *Brain et al.* [2005]. The north-south asymmetry is most likely caused by the stronger crustal magnetic fields in the southern hemisphere than in the northern hemisphere. The northern hemisphere during the “away” IMF conditions corresponds to the upward electric field hemisphere, where the convective electric field is pointing away from Mars. It implies that the penetrations more often occur in the upward electric field hemisphere than in the downward electric field hemisphere. *Brain et al.* [2005] pointed out that the sheath observations peak locally eastward, i.e., the IMF draping direction is around  $0^\circ$ . From our results, the magnetosheath penetration events tend to be observed during IMF away sector polarity which corresponds to IMF draping direction clustering from  $210^\circ$  to  $0^\circ$ . Therefore, this tendency is consistent with *Brain et al.* [2005].

We suggest that one of possible physical mechanisms is Kelvin-Helmholtz (K-H) instability. Previous two-dimensional global hybrid simulation to investigate the solar wind interaction with an unmagnetized planet pointed out that the upward electric field hemisphere enhances K-H instability [Terada et al., 2002]. In the hemispheres of the upward electric field, the wavy structures generated by the K-H instability in the boundary of the simulation domain, which has shear of velocity and density, tend to be enhanced. This enhancement may make the magnetosheath plasma penetrate to lower altitudes than usual.

Another possibility might be the asymmetry in the magnetosheath caused by the solar wind electric field expected by the asymmetric distribution of planetary pickup ions [e.g., *Kallio et al.*, 2010]. If the pickup ions raise the temperature anisotropy, the resultant mirror-mode instability might cause the density fluctuations around the Martian ionopause [*Gurnett et al.*, 2010]. The enhanced density fluctuation is another candidate mechanism to explain the magnetosheath penetration. The latest Mars Atmosphere and Volatile Evolution (MAVEN) Mission comprehensive plasma and field measurements will provide clues to investigate these mechanisms further.

## References

- Acuña, M. H., J. E. P. Connerney, P. Wasilewski, R. P. Lin, K. A. Anderson, C. W. Carlson, J. McFadden, D. W. Curtis, H. Reme, and A. Cros (1992), Mars Observer magnetic fields investigation, *J. Geophys. Res.*, 97(E5), 7799–7814, doi:10.1029/92JE00344.  
Acuña, M. H., et al. (1998), Magnetic field and plasma observations at Mars: Initial results of the Mars Global Surveyor mission, *Science*, 279, 1676–1680, doi:10.1126/science.279.5357.1676.

## Acknowledgments

This work was supported by grant-in-aid for Scientific Research (B) 15H03731 as well as by the Program for Advancing Strategic International Networks to Accelerate the Circulation of Talented Researchers G2602 from JSPS and MEXT of Japan. Kazunari Matsunaga is supported by a research fellowship of Nagoya University Program for Leading Graduate Schools of “Leadership Development Program for Space Exploration and Research” from JSPS. The data used in this paper are publicly available in NASA’s Planetary Data System. The MGS solar wind proxy data are available at <http://sprg.ssl.berkeley.edu/~brain/proxies/subsofield.html>. The ACE solar wind data were obtained from the GSFC/SPDF OMNIWeb interface at <http://omniweb.gsfc.nasa.gov>. We are grateful to all Mars Global Surveyor science members. We also thank the ACE MAG and SWEPPAM instrument teams for providing the ACE data.

Michael Liemohn thanks Matthew Fillingim and two anonymous reviewers for their assistance in evaluating this paper.

- Acuña, M. H., et al. (1999), Global distribution of crustal magnetization discovered by the Mars Global Surveyor MAG/ER Experiment, *Science*, 284, 790–793, doi:10.1126/science.284.5415.790.
- Albee, A. L., R. E. Arvidson, F. Palluconi, and T. Thorpe (2001), Overview of the Mars Global Surveyor mission, *J. Geophys. Res.*, 106(E12), 23,291–23,316, doi:10.1029/2000JE001306.
- Alfvén, H. (1957), On the theory of comet tails, *Tellus*, 9, 92–96.
- Bertucci, C., et al. (2003), Magnetic field draping enhancement at the Martian magnetic pileup boundary from Mars global surveyor observations, *Geophys. Res. Lett.*, 30(2), 1099, doi:10.1029/2002GL015713.
- Brain, D. A., F. Bagenal, M. H. Acuña, and J. E. P. Connerney (2003), Martian magnetic morphology: Contributions from the solar wind and crust, *J. Geophys. Res.*, 108(A12), 1424, doi:10.1029/2002JA009482.
- Brain, D. A., J. S. Halekas, R. Lillis, D. L. Mitchell, R. P. Lin, and D. H. Crider (2005), Variability of the altitude of the Martian sheath, *Geophys. Res. Lett.*, 32, L18203, doi:10.1029/2005GL023126.
- Brain, D. A., D. L. Mitchell, and J. S. Halekas (2006a), The magnetic field draping direction at Mars from April 1999 through August 2004, *Icarus*, 182, 464–473, doi:10.1016/j.icarus.2005.09.023.
- Brain, D. A., J. S. Halekas, L. M. Petricolas, R. P. Lin, J. G. Luhmann, D. L. Mitchell, G. T. Delory, S. W. Bougher, M. H. Acuña, and H. Rème (2006b), On the origin of aurorae on Mars, *Geophys. Res. Lett.*, 33, L01201, doi:10.1029/2005GL024782.
- Brech, S. H., and J. R. Ferrante (1991), Global hybrid simulation of unmagnetized planets—Comparison of Venus and Mars, *J. Geophys. Res.*, 96, 11,209–11,220, doi:10.1029/91JA00671.
- Brech, S. H., J. R. Ferrante, and J. G. Luhmann (1993), Three-dimensional simulations of the solar wind interaction with Mars, *J. Geophys. Res.*, 98, 1345–1357, doi:10.1029/92JA02198.
- Cain, J. C., B. B. Ferguson, and D. Mozzoni (2003), An  $n = 90$  internal potential function of the Martian crustal magnetic field, *J. Geophys. Res.*, 108(E2), 5008, doi:10.1029/2000JE001487.
- Cloutier, P. A., and R. E. Daniell (1973), Ionospheric currents induced by solar wind interaction with planetary atmospheres, *Planet. Space Sci.*, 21, 463–474, doi:10.1016/0032-0633(73)90043-3.
- Crider, D. H., D. Vignes, A. M. Krymskii, T. K. Breus, N. F. Ness, D. L. Mitchell, J. A. Slavin, and M. H. Acuña (2003), A proxy for determining solar wind dynamic pressure at Mars using Mars Global Surveyor data, *J. Geophys. Res.*, 108(A12), 1461, doi:10.1029/2003JA009875.
- Crider, D. H., J. Espley, D. A. Brain, D. L. Mitchell, J. E. P. Connerney, and M. H. Acuña (2005), Mars Global Surveyor observations of the Halloween 2003 solar superstorm's encounter with Mars, *J. Geophys. Res.*, 110, A09S21, doi:10.1029/2004JA010881.
- Espley, J. R., P. A. Cloutier, D. A. Brain, D. H. Crider, and M. H. Acuña (2004), Observations of low-frequency magnetic oscillations in the Martian magnetosheath, magnetic pileup region, and tail, *J. Geophys. Res.*, 109, A07213, doi:10.1029/2003JA010193.
- Guicking, L., K.-H. Glassmeier, H.-U. Auster, M. Delva, U. Motschmann, Y. Narita, and T. L. Zhang (2010), Low-frequency magnetic field fluctuations in Venus' solar wind interaction region: Venus Express observations, *Ann. Geophys.*, 28, 951–967, doi:10.5194/angeo-28-951-2010.
- Gurnett, D. A., D. D. Morgan, F. Duru, F. Akalin, J. D. Winningham, R. A. Frahm, E. Dubinin, and S. Barabash (2010), Large density fluctuations in the Martian ionosphere as observed by the Mars Express radar sounder, *Icarus*, 206, 83–94, doi:10.1016/j.icarus.2009.02.019.
- Halekas, J. S., J. P. Eastwood, D. A. Brain, T. D. Phan, M. Øieroset, and R. P. Lin (2009), In situ observations of reconnection Hall magnetic fields at Mars: Evidence for ion diffusion region encounters, *J. Geophys. Res.*, 114, A11204, doi:10.1029/2009JA014544.
- Harnett, E. M., and R. M. Winglee (2003), The influence of a mini-magnetopause on the magnetic pileup boundary at Mars, *Geophys. Res. Lett.*, 30(20), 2074, doi:10.1029/2003GL017852.
- Jakosky, B. M., and R. J. Phillips (2001), Mars' volatile and climate history, *Nature*, 412, 237–244.
- Kallio, E., K. Liu, R. Jarvinen, V. Pohjola, and P. Janhunen (2010), Oxygen ion escape at Mars in a hybrid model: High energy and low energy ions, *Icarus*, 206, 152–163, doi:10.1016/j.icarus.2009.05.015.
- Luhmann, J. G., S. A. Ledvina, and C. T. Russell (2004), Induced magnetospheres, *Adv. Space Res.*, 33, 1905–1912, doi:10.1016/j.asr.2003.03.031.
- Lundin, R. (2011), Ion acceleration and outflow from Mars and Venus: An overview, *Space Sci. Rev.*, 162, 309–334, doi:10.1007/s11214-011-9811-y.
- Mitchell, D. L., R. P. Lin, C. Mazelle, H. Rème, P. A. Cloutier, J. E. P. Connerney, M. H. Acuña, and N. F. Ness (2001), Probing Mars' crustal magnetic field and ionosphere with the MGS electron reflectometer, *J. Geophys. Res.*, 106(E10), 23,419–23,428, doi:10.1029/2000JE001435.
- Nagy, A. F., et al. (2004), The plasma environment of Mars, *Space Sci. Rev.*, 111, 33–114, doi:10.1023/B:SPAC.0000032718.47512.92.
- Nilsson, H., E. Carlsson, D. A. Brain, M. Yamauchi, M. Holmström, S. Barabash, R. Lundin, and Y. Futaana (2010), Ion escape from Mars as a function of solar wind conditions: A statistical study, *Icarus*, 206, 40–49, doi:10.1016/j.icarus.2009.03.006.
- Terada, N., S. Machida, and H. Shinagawa (2002), Global hybrid simulation of the Kelvin-Helmholtz instability at the Venus ionopause, *J. Geophys. Res.*, 107(A12), 1471, doi:10.1029/2001JA009224.
- Vannerstrom, S., N. Olsen, M. Purucker, M. H. Acuña, and J. C. Cain (2003), The magnetic field in the pile-up region at Mars, and its variation with the solar wind, *Geophys. Res. Lett.*, 30(7), 1369, doi:10.1029/2003GL016883.
- Vignes, D., C. Mazelle, H. Rème, M. H. Acuña, J. E. P. Connerney, R. P. Lin, D. L. Mitchell, P. Cloutier, D. H. Crider, and N. F. Ness (2000), The solar wind interaction with Mars: Locations and shapes of the Bow Shock and the magnetic pile-up boundary from the observations of the MAG/ER experiment onboard Mars Global Surveyor, *Geophys. Res. Lett.*, 27(1), 49–52, doi:10.1029/1999GL010703.

## Erratum

In the originally published version of this article, Figure 1 contained an error. The following error has since been corrected, and this version may be considered the authoritative version of record. In Figure 1e, the unit of "Differential flux" has been changed from " $\text{cm}^{-2} \text{s}^{-1} \text{sr}^{-1}$ " to " $\text{cm}^{-2} \text{s}^{-1} \text{sr}^{-1} \text{eV}^{-1}$ ".

# Journal of Geophysical Research: Space Physics

## RESEARCH ARTICLE

10.1002/2013JA019414

**Key Points:**

- Structure of Mars flux ropes is recovered via the Grad-Shafranov (GS) equation
- Flux ropes observed downstream from crustal fields have larger scale
- GS reconstruction is used to estimate ion escape rates via flux ropes

**Correspondence to:**

T. Hara,  
hara@stelab.nagoya-u.ac.jp

**Citation:**

Hara, T., K. Seki, H. Hasegawa, D. A. Brain, K. Matsunaga, and M. H. Saito (2014), The spatial structure of Martian magnetic flux ropes recovered by the Grad-Shafranov reconstruction technique, *J. Geophys. Res. Space Physics*, 119, 1262–1271, doi:10.1002/2013JA019414.

Received 5 SEP 2013

Accepted 17 JAN 2014

Accepted article online 20 JAN 2014

Published online 12 FEB 2014

## The spatial structure of Martian magnetic flux ropes recovered by the Grad-Shafranov reconstruction technique

Takuya Hara<sup>1</sup>, Kanako Seki<sup>1</sup>, Hiroshi Hasegawa<sup>2</sup>, David A. Brain<sup>3</sup>, Kazunari Matsunaga<sup>1</sup>, and Miho H. Saito<sup>4</sup>

<sup>1</sup>Solar-Terrestrial Environment Laboratory, Nagoya University, Nagoya, Japan, <sup>2</sup>Institute of Space and Astronautical Science, Japan Aerospace Exploration Agency, Sagamihara, Japan, <sup>3</sup>Laboratory for Atmospheric and Space Physics, University of Colorado Boulder, Boulder, Colorado, USA, <sup>4</sup>Earth and Planetary Sciences, Tokyo Institute of Technology, Tokyo, Japan

**Abstract** We applied the Grad-Shafranov (GS) reconstruction technique to Martian magnetic flux ropes observed by Mars Global Surveyor in order to estimate their spatial structures. This technique can provide a magnetic field map of their cross section from single spacecraft data, under the assumption that the structure is two-dimensional, magnetohydrostatic, and time independent. We succeeded in recovering the spatial structure for 70 events observed between April 1999 and November 2006. The reconstruction results indicate that the flux rope axes were mostly oriented horizontal to the Martian surface and were randomly distributed with respect to the typical plasma streamline. A subset of events with duration longer than 240 s was observed at solar zenith angles larger than 75°. These events all occur downstream from strong crustal magnetic field in the southern hemisphere, indicating an association between the crustal fields and the detected flux ropes. Using the shape and size of the flux ropes obtained from the GS reconstruction, we estimate lower limits on their volume that span 2–3 orders of magnitude, with larger flux ropes observed downstream from strong crustal magnetic fields. Estimated ion escape rates associated with flux ropes are of the order of  $10^{22}$ – $10^{23}$  ion/s, being approximately 10% of previously estimated escape rates during solar minimum.

### 1. Introduction

Although Mars lacks a global intrinsic magnetic field, it possesses strong localized crustal magnetic fields [e.g., Acuña *et al.*, 1998, 1999]. Because the interplanetary magnetic field (IMF) embedded in the shocked solar wind interacts with the Martian crustal magnetic fields, the electromagnetic environment around Mars is known to be highly complicated and dynamic. Spacecraft measurements show that Martian upper atmosphere particles are escaping to interplanetary space in response to the interaction of Mars with the solar wind [e.g., Lundin *et al.*, 1989; Barabash *et al.*, 2007]. The role of the crustal magnetic fields in atmospheric escape from Mars is not yet well understood.

It is thought that Martian crustal magnetic fields may influence atmospheric escape in a few different ways, based on spacecraft measurements and numerical simulations. For example, ionospheric plasma can be removed via aurora-like plasma acceleration in the vicinity of the open field line areas above the crustal magnetic fields, analogous to the cusp regions of Earth's magnetosphere [e.g., Brain *et al.*, 2006; Lundin *et al.*, 2006; Nilsson *et al.*, 2006]. Current sheet structures observed near Mars are also apparently affected by crustal magnetic fields [e.g., Halekas *et al.*, 2006, 2008; Halekas and Brain, 2010]. The magnetic tension force associated with current sheets is capable of accelerating ionospheric plasma away from Mars [Dubinin *et al.*, 1993]. Magnetic reconnection between crustal magnetic fields and the IMF draped around the conducting Martian ionosphere may also be responsible for ripping Martian ionospheric plasma away to space. Mars Global Surveyor (MGS) measurements found Hall magnetic field signatures associated with magnetic reconnection [Eastwood *et al.*, 2008; Halekas *et al.*, 2009]. Magnetic flux ropes and plasma clouds strongly correlated with magnetic reconnection are key phenomena, because these magnetic structures may confine large amounts of ionospheric plasma, which is then removed from the planet [e.g., Vignes *et al.*, 2004; Brain *et al.*, 2010; Briggs *et al.*, 2011]. However, crustal magnetic fields may also prevent ionospheric plasma from escaping to space due to the formation of "minimagnetospheres" [e.g., Mitchell *et al.*, 2001; Lundin *et al.*, 2011]. Therefore, it is not well understood whether the crustal magnetic fields increase or decrease atmospheric escape rates relative to an "unmagnetized" Mars.

Flux ropes are characteristic twisted magnetic field structures. The magnetic field near the center of the flux rope is strong and aligned axially, and it becomes gradually weaker and more azimuthal with distance from the center. These flux ropes have been observed throughout the solar system, e.g., at the Sun [e.g., Okamoto *et al.*, 2008], in interplanetary space [e.g., Hu *et al.*, 2004; Qiu *et al.*, 2007], and at the terrestrial magnetosphere [e.g., Hasegawa *et al.*, 2006]. Flux ropes have been also detected at planets, such as at Venus and Mars [e.g., Russell and Elphic, 1979; Vignes *et al.*, 2004], which do not possess a global intrinsic magnetic field. Brain *et al.* [2010] reported large-scale isolated flux ropes filled with Martian ionospheric plasma located downstream from strong crustal magnetic fields, based on vector magnetic field and suprathermal electron measurements from MGS. Morgan *et al.* [2011] reported on the longevity of similar events based on a combination of MGS data and field magnitudes derived from the ionospheric radar sounding experiment (Mars Advanced Radar for Subsurface and Ionosphere Sounding (MARSIS)) onboard Mars Express (MEX). These flux ropes could intermittently carry significant large amounts of atmosphere away from Mars via a bulk removal process such as magnetic reconnection between the IMF and crustal magnetic fields. Brain *et al.* [2010] proposed that this process might account for as much as 10% of the total present-day ion escape from Mars. However, it is difficult to evaluate an atmospheric escape rate due to the Martian flux ropes from single spacecraft data, because there is ambiguity in estimation of the shape and size of the observed flux ropes.

There have been attempts to estimate the shape and size of flux ropes detected using from single spacecraft data by solving the Grad-Shafranov (GS) equation. This technique enables the reconstruction of the magnetohydrostatic spatial structure from the particle and field data, under the assumption that the structure is two-dimensional and time independent [e.g., Sturrock, 1994; Sonnerup and Guo, 1996]. The method has been used to reconstruct various magnetohydrostatic structures, such as the Earth's magnetopause [e.g., Hau and Sonnerup, 1999; Hasegawa *et al.*, 2004, 2005], flux ropes observed in interplanetary space [e.g., Hau and Sonnerup, 1999; Hau and Sonnerup, 2002], and flux ropes observed in Earth's magnetosphere [e.g., Sonnerup *et al.*, 2004; Hasegawa *et al.*, 2006].

In this study, we apply the GS reconstruction technique to Martian flux ropes observed by MGS in order to estimate their shape and size. Using their reconstructed spatial structures, we then impose constraints on their shape and size to assess the escape rate associated with removal of ions via magnetic flux ropes propagating away from the planet. The MGS instrumentation used in this study is described in section 2. The assumptions used in applying the GS reconstruction technique are shown in section 3. Results for a typical flux rope event are presented in section 4. A statistical analysis of 135 Martian magnetic flux ropes is shown in section 5. In section 6, we estimate the ionospheric plasma content inside the reconstructed flux rope structures. Finally, in section 7, we summarize the results and discuss the potential effects of the flux ropes on the atmospheric escape from Mars.

## 2. Instrumentation

We utilize data obtained from the magnetometer and electron reflectometer (MAG/ER) onboard Mars Global Surveyor (MGS) during the mapping phase. The mapping phase of the MGS mission began in March 1999 and lasted until the end of the mission (November 2006). MGS was in quasi-circular orbit at an altitude of approximately 400 km, and the spacecraft orbit had fixed local time of  $\sim 2$  A.M./2 P.M. during the mapping phase [e.g., Albee *et al.*, 2001].

MAG consists of two identical triaxial fluxgate magnetometers. MAG provides vector magnetic fields every 0.75–3.0 s [Acuña *et al.*, 1992]. ER is a cylindrically symmetric top-hat electrostatic analyzer used to detect suprathermal electrons. ER determines energy and angular distribution of electrons in the energy range from 10 eV to 20 keV with an energy resolution of 25%. ER measures electron fluxes in 16 sectors within the total field of view (FOV) of  $14^\circ \times 360^\circ$ , in which each sector has FOV of  $14^\circ \times 22.5^\circ$ . Omnidirectional energy spectra can be sampled every 12–48 s depending on the telemetry rate between Earth and Mars [Mitchell *et al.*, 2001]. By combining the two data sets described above, electron pitch angle distributions can be constructed. However, the coverage in pitch angle space varies as a function of time and location because this coverage depends on the orientation of the two-dimensional FOV of the ER experiment with respect to the observed magnetic field direction.

### 3. Grad-Shafranov Reconstruction

#### 3.1. Assumptions

Grad-Shafranov (GS) reconstruction can be applied under the following conditions: (i) the structure is approximately in magnetohydrostatic equilibrium, i.e., inertial effects are negligible; (ii) the structure is two-dimensional, i.e., there is a so-called invariant axis  $z$ , along which spatial gradient of the structure is much smaller than in the other directions,  $x$  and  $y$ , perpendicular to the  $z$  direction. This assumption is equivalent to  $\partial/\partial z \ll \partial/\partial x, \partial/\partial y$ ; (iii) and the structure is approximately time independent.

Plasma moment (e.g., density, velocity vector, and temperature) and magnetic field data are necessary to recover the two-dimensional magnetohydrostatic spatial configuration of the observed flux ropes. Because MGS lacked ion measurements, a few additional assumptions must therefore be provided. A typical plasma density and temperature of the Martian ionosphere at the spacecraft altitude ( $\sim 400$  km) [Fox, 2009] are assumed in order to calculate the input thermal pressure for the model. It is also assumed that the observed flux ropes are approximately stationary, which means that the spacecraft velocity,  $\mathbf{V}_{sc}$ , is the dominant component causing apparent movement of the flux rope relative to the MGS spacecraft. This assumption is supported by results of Morgan *et al.* [2011] and of Beharrell and Wild [2012]. Considering a typical duration of the flux ropes and  $\mathbf{V}_{sc}$ , the curvature of the spacecraft trajectory is small and is ignored in this study.

We tested the sensitivity assumptions described above and found no significant influence of the plasma density and temperature on the results, within ordinary conditions. If the flux ropes are moving antisunward with velocity of 5–15 km/s, as assumed by Brain *et al.* [2010], their estimated volumes will depend on the angle that the spacecraft trajectory makes with the flux rope axis. Our results presented in the following sections are not significantly influenced by this assumption as long as we only discuss an order estimation, because their volumes do not vary by as much as an order of magnitude.

#### 3.2. Application Procedures

In the GS reconstruction, we assume the following force balance in the MHD framework:

$$\mathbf{j} \times \mathbf{B} = \nabla p, \quad (1)$$

where  $\mathbf{j}$  is the current density,  $\mathbf{B}$  is the magnetic field, and  $p$  is the plasma thermal pressure. This equation describes the condition that the magnetic tension is balanced with the force from the total pressure gradient. The GS equation in the Cartesian coordinate system ( $x, y, z$ ) can be described as follows [see, e.g., Sturrock, 1994; Hau and Sonnerup, 1999]:

$$\frac{\partial^2 A}{\partial x^2} + \frac{\partial^2 A}{\partial y^2} = -\mu_0 \frac{dP_t}{dA}, \quad (2)$$

where the vector  $A$  is the magnetic vector potential, such that  $A(x, y)$ , and  $P_t$  is the transverse pressure defined as  $P_t = (p + B_z^2/2\mu_0)$ , which is the sum of the plasma thermal and axial field pressures. The magnetic field vector can be expressed by using the magnetic vector potential  $A$ ,

$$\mathbf{B} = \left[ \frac{\partial A}{\partial y}, -\frac{\partial A}{\partial x}, B_z(A) \right]. \quad (3)$$

The axial magnetic field  $B_z$  as well as the plasma pressure  $p$  are functions of  $A$  alone. Therefore, the transverse pressure  $P_t$  and the axial current density, which is given by  $j_z = dP_t(A)/dA$ , are also uniquely determined as a function of  $A$ . The values of  $A$  along the  $x$  axis, which is the projection of the spacecraft trajectory onto the  $x$ - $y$  plane, can be calculated from the observed magnetic field component,  $B_y$ , via the spatial integration,

$$A(x, 0) = \int_0^x \frac{\partial A}{\partial \xi} d\xi = - \int_0^x B_y(\xi, 0) d\xi. \quad (4)$$

Since we assume the observed flux ropes are stationary in this study, the spatial integration  $d\xi$  can be transformed into the time integration via the following relation,  $d\xi = \mathbf{V}_{sc} \cdot \hat{\mathbf{x}} dt$ , where  $\hat{\mathbf{x}}$  is the unit vector along the projection of  $\mathbf{V}_{sc}$  onto the plane perpendicular to the invariant axis  $\hat{\mathbf{z}}$ .

The invariant axis direction  $\hat{\mathbf{z}}$  is determined by trial and error on the basis of the requirements that  $P_t(A)$  and  $B_z(A)$  should be single-valued functions of  $A$ . Once we can calculate the values of  $A(x, 0)$  from equation (4), the transverse pressures along the spacecraft trajectory,  $P_t(x, 0)$ , can also be obtained. A residue as defined by Hu and Sonnerup [2002] evaluates the deviation of  $P_t(x, 0)$  versus  $A(x, 0)$  from a single-valued function.

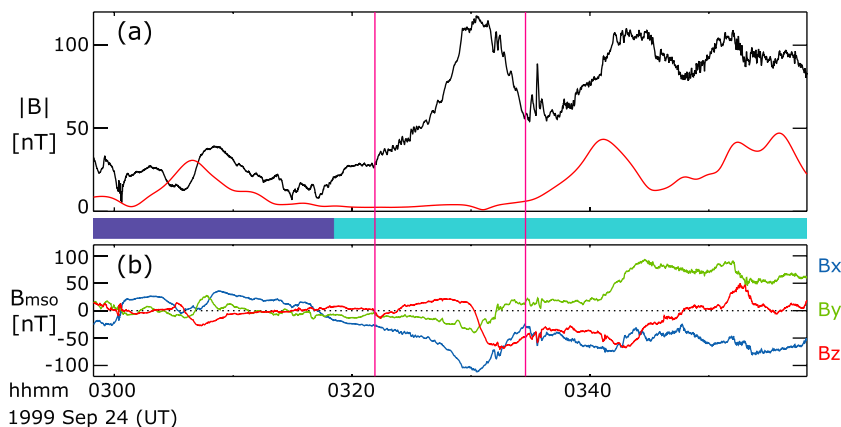


**Figure 1.** Time series plots of (a) magnetic field magnitude and (b) vector magnetic field, in the Mars-centered Solar Orbital (MSO) coordinate system, as observed by MGS on 24 September 1999. Expected crustal magnetic field magnitude is shown by the red solid line in Figure 1a. Color bar between Figures 1a and 1b indicates whether MGS was illuminated (light blue) or in eclipse (dark blue). MGS observed a magnetic flux rope during the time interval between two magenta vertical lines.

As a result, the  $z$  axis is singled out as the direction for which the residue is minimum among all calculated values associated with all possible trial directions. We calculate the right-hand side of the GS equation (2) using the single-valued function in all regions of the  $x$ - $y$  plane threaded by field lines crossing the trajectory. In terms of other parts of the  $x$ - $y$  plane, the field should be recovered via suitable extrapolations of the function  $P_r(A)$ .

Once the function  $P_r(A)$  has been determined, the integration of the GS equation (2) is conducted as follows: observed magnetic field components,  $B_x$  and  $B_y$ , at each point along the spacecraft trajectory are used as initial values. New  $A$  and  $B_x$  values at grid points away from the  $x$  axis by small steps,  $\pm\Delta y$ , are calculated via the GS equation (2). The integration is performed to complete a two-dimensional magnetic vector potential map of  $A(x, y)$ . The details of the integration procedures are extensively described in previous studies [e.g., Hau and Sonnerup, 1999; Hau and Sonnerup, 2002].

## 4. Application to Martian Flux Ropes

### 4.1. Identification of Magnetic Flux Ropes in MGS Data

We selected large magnetic flux ropes from MGS MAG data during the mapping phase between 1999 and 2006 to apply the Grad-Shafranov (GS) reconstruction. We chose candidate events in which the observed magnetic field strength exceeded the value expected from a crustal magnetic field model [Cain et al., 2003] by 70 nT or more. We then selected as flux ropes the events for which hodograms obtained from minimum variance analysis (MVA) of the observations show a partial rotation in the plane perpendicular to the minimum variance axis for which the eigenvalue ratio between the intermediate and minimum variance directions exceeded 5. We identified 135 clear magnetic flux rope events from the MGS data, similar to the result of the event search mentioned in Brain et al. [2010].

### 4.2. Event of 24 September 1999

Figure 1 shows an overview of magnetic field observations recorded by MGS on 24 September 1999. An enhancement of the magnetic field strength was observed during 03:21:55–03:34:55 UT (between two magenta vertical lines in Figure 1a). The magnetic field strength reached a peak of approximately 120 nT at 03:30:25 UT. The crustal magnetic field model [Cain et al., 2003] is shown by the red solid line in Figure 1a. It indicates that the expected crustal field strength is much smaller (less than 10 nT) than the observed field strength. The hodograms for this event (not shown here) in the MVA coordinate system clearly show that the vector magnetic field rotates in a circular manner in the plane perpendicular to the minimum variance axis during the enhancement of observed field strength. This vector magnetic field rotation is a feature of the magnetic flux rope. The intermediate to minimum eigenvalue ratio is 26.05, which is much larger than our event selection criterion. We thus infer that this magnetic field enhancement is due to a magnetic flux rope.

The spatial structure of the magnetic flux rope is estimated by the GS reconstruction described in section 3, using the observed vector magnetic field during the event. An optimal invariant  $z$  axis is determined to

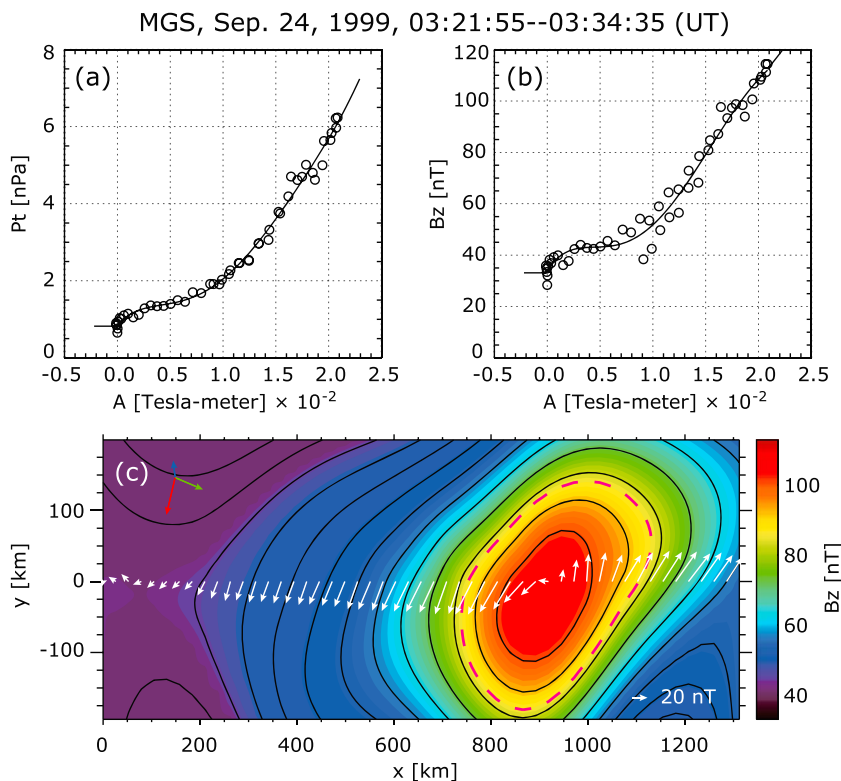


**Figure 2.** Results from the Grad-Shafranov reconstruction using MGS data. (a) Transverse pressure ( $P_t = p + B_z^2/2\mu_0$ ) and (b) axial magnetic field  $B_z$ , plotted as a function of the partial magnetic vector potential  $A$ . Open circles are the MGS observations, and thick solid curves denote the fitted polynomials. (c) The reconstructed transverse field lines with  $B_z$  in color. The MGS spacecraft was traveling (time progressed) from left to right along the line  $y = 0$ . White arrows represent the transverse magnetic field components measured by MGS. The blue, green, and red arrows are the projections of the MSO axes, respectively.

be  $[-0.94, -0.15, -0.30]$  in the Mars-centered Solar Orbital (MSO) coordinate system. The MSO coordinate system is defined with the  $X_{\text{mso}}$  axis toward the Sun, the  $Z_{\text{mso}}$  axis perpendicular to the ecliptic pointing to the northern hemisphere, and the  $Y_{\text{mso}}$  axis completing the right-hand system. Figures 2a and 2b show the transverse pressure  $P_t$  and axial magnetic field  $B_z$  as a function of magnetic vector potential  $A$ . The observed structure turns out to be approximately two-dimensional, because the observed data points (solid circles) are well fit by single curves (solid curves) as described in section 3.2. The right parts of the Figures 2a and 2b, where the fitted curves have only one branch and the vector potential is large, correspond to the core part of the magnetic flux rope. In contrast, the left parts correspond to the regions away from the core part of the magnetic flux rope. The slope of the fitted curves,  $dP_t(A)/dA$ , characterizes the spatial structure of the reconstructed magnetic flux rope, because it reflects the axial current,  $j_z(A)$ . The line on the left side of the panel is simply taken to be horizontal, which means that there is no axial current; this assumption has no significant influence on the reconstructed structure [Hasegawa et al., 2006]. Figure 2c shows the optimal magnetic field map in which magnetic field lines in the  $x$ - $y$  plane are shown by black curves and the axial ( $z$ ) magnetic field component is colored. The MGS spacecraft was traveling along the  $x$  direction from left to right at  $y = 0$ . The reconstructed spatial structure is not circular, but somewhat elliptic elongated to the direction roughly perpendicular to the MGS spacecraft trajectory. The overlaid magenta dashed curve on Figure 2c is our determined boundary to estimate the volume of the magnetic flux rope. The definition of the magnetic flux rope boundary in this study is described later in section 6.

## 5. Statistical Properties of Magnetic Flux Ropes

We applied the Grad-Shafranov (GS) reconstruction technique to the 135 magnetic flux rope events selected in section 4. Among the 135 events, we could uniquely and clearly determine the invariant axis for 70 events, and reconstruct the spatial structure of the magnetic flux ropes.

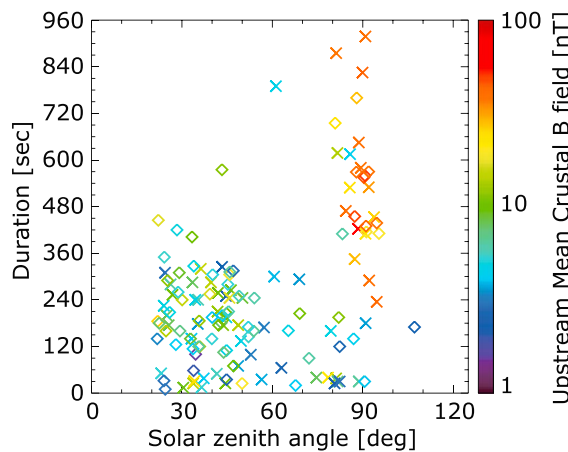


**Figure 3.** Scatterplot of the duration versus solar zenith angle of the observed magnetic flux ropes for all the 135 selected events. Symbols are colored by the averaged upstream crustal magnetic field strengths calculated based on the results of Connerney et al. [2001]. The symbol of diamonds (crosses) indicates the events in which their spatial structures could (could not) be estimated from the Grad-Shafranov reconstruction.

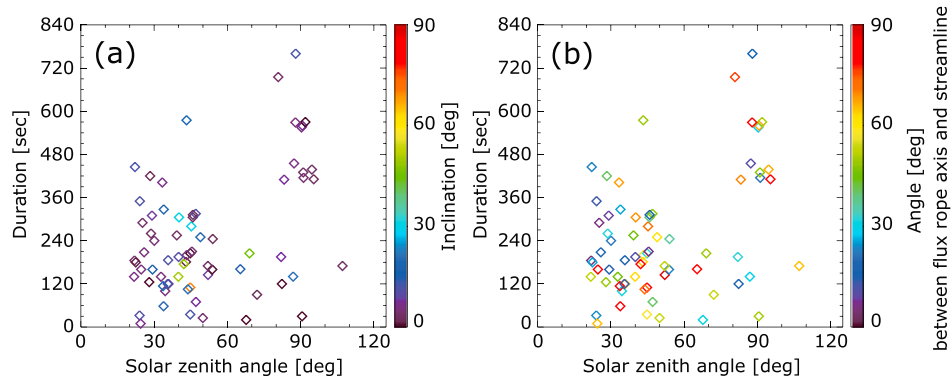
Figure 3 represents relations between the duration of the magnetic flux ropes and the solar zenith angle (SZA) for all the 135 events. The color shows the averaged upstream crustal magnetic field strength derived from Connerney et al. [2001]. The upstream crustal magnetic field strength is calculated as the averaged value of the crustal magnetic field model from the observed location to the subsolar point along the typical plasma streamline. Because MGS made no ion measurements, the typical plasma streamline is defined as the shortest route flowing from the subsolar point to the nightside. The flow direction is obtained as follows: If the MGS spacecraft position is given by  $\mathbf{R}$  in the MSO coordinate system, the unit vector of flow direction  $\hat{\mathbf{f}}$  is given by

$$\hat{\mathbf{f}} \equiv \left( \frac{\hat{\mathbf{X}}_{\text{mso}} \times \mathbf{R}}{|\hat{\mathbf{X}}_{\text{mso}} \times \mathbf{R}|} \right) \times \left( \frac{\mathbf{R}}{|\mathbf{R}|} \right), \quad (5)$$

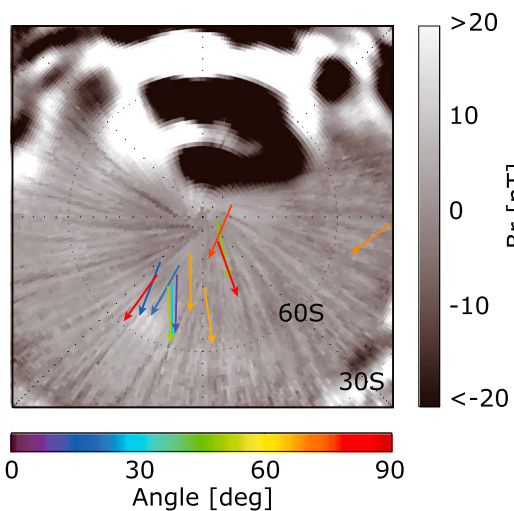
where  $\hat{\mathbf{X}}_{\text{mso}}$  is the unit vector along the  $X_{\text{mso}}$  axis, that is, along the Mars-Sun direction. The flow direction  $\hat{\mathbf{f}}$  is assumed to be symmetrical with respect to the subsolar point and has no radial component except at the subsolar point. This assumption of the flow direction  $\hat{\mathbf{f}}$  is also employed by Strangeway and Russell [1996]. It is clearly shown in Figure 3 that the expected upstream crustal magnetic field strength is relatively large for the events in which the SZA is high ( $> 75^\circ$ ), and the duration is long ( $> 240$  s).

Figure 4 is a scatterplot similar to Figure 3; however, it represents the GS reconstruction results for the 70 events in which we could recover their spatial structures. Figure 4a shows that the axes of magnetic flux ropes are mostly horizontal to the Martian surface. Figure 4b shows that the angle of the magnetic flux rope axes with respect to the typical plasma streamline is rather randomly distributed.

The spatial structure could be recovered for 12 events which are observed at SZA larger than  $75^\circ$  with duration longer than 240 s. These 12 events are mostly observed in the region where the upstream crustal magnetic field strength is relatively large (Figure 3). The geographic distribution for those 12 events is shown in Figure 5. These large magnetic flux ropes are mostly observed downstream from the strong crustal magnetic field in the southern hemisphere, similar to the previous reported large-scale isolated magnetic flux ropes [Brain et al., 2010; Morgan et al., 2011; Beharrell and Wild, 2012]. One exception is the event in which the averaged upstream crustal magnetic field strength is the weakest among these 12 events. We hereafter



**Figure 4.** Scatterplots of the magnetic flux rope events in which their spatial structures could be recovered by the Grad-Shafranov reconstruction technique. The format is the same as in Figure 3. Symbols are colored by the values of (a) the inclination of the magnetic flux rope axis relative to the Martian surface:  $0^\circ$  ( $90^\circ$ ) is horizontal (vertical) to the Martian surface at the foot point of MGS and (b) the angle between the flux rope axis and the typical plasma convection streamline. The definition of the direction of the typical plasma convection streamline is given in the text.



**Figure 5.** The geographic location, viewed from above the south pole in the geographic coordinate system of the long-duration and high solar zenith angle events for which the spatial structure of the magnetic flux ropes was successfully recovered. Gray scale background indicates the radial component  $B_r$  of crustal magnetic fields expected at the altitude of about 400 km from the Martian surface [Connerney et al., 2001]. Arrows show the direction of the typical plasma convection streamline derived from equation (5). The arrow colors represent the angle of the recovered magnetic flux rope axes relative to the direction of the typical plasma convection streamline.

the axial magnetic field strength of the data bin furthest from the center of the magnetic flux rope is zero, i.e., the magnetic field strength at the center of the reconstructed magnetic flux rope is shifted to be strongest.

1. The axial magnetic field strength at the center of the magnetic flux rope is generally strongest. Hence, the reconstructed two-dimensional axial ( $B_z$ ) magnetic field data of Figure 2c is uniformly shifted so that
2. Normalization is performed for the shifted two-dimensional axial ( $B_z$ ) magnetic field so that the magnetic field strength at the center of the magnetic flux rope is one.
3. The boundary of the recovered magnetic flux rope is defined as a flux surface where the shifted two-dimensional axial ( $B_z$ ) magnetic field strength normalized at the center of the magnetic flux rope is 66%.

An example of the boundary determination is shown with the magenta dashed curve in Figures 2c and 6. This boundary definition might underestimate the flux rope size. However, our defined boundary is completely within the reconstructed two-dimensional axial magnetic field map for 48 events among the 70 events in which their spatial structures can be estimated from the GS reconstruction. Therefore,

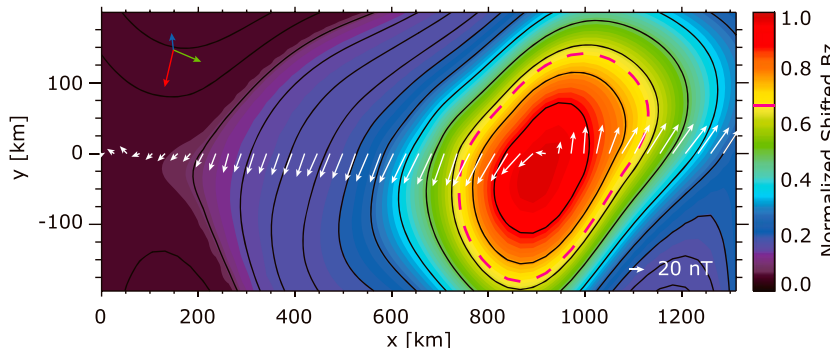


**Figure 6.** The map of the reconstructed axial magnetic field  $B_z$ , shifted and normalized in the following way. The format is mostly same as in Figure 2c. Here two-dimensional axial magnetic field data are shifted so that the axial magnetic field value is zero on a field line furthest from the center of flux rope, and then the shifted values are normalized by the shifted axial field value at the center of magnetic flux rope. The dashed magenta line is the boundary of the flux rope, defined as a surface where the shifted axial magnetic field strength is 66% of the core field value.

categorize the remaining 11 events in which the observed locations are clustered downstream from the strong crustal magnetic field into “Event category A” throughout in this paper. On the other hand, the rest of events whose spatial structures could be recovered from the GS reconstruction technique, regardless of their location or duration, are referred to as “Event category B”.

## 6. Magnetic Flux Rope Size Estimation

In this section, we estimate the shape and size of the magnetic flux rope, based on their spatial structures estimated from the Grad-Shafranov (GS) reconstruction. In this study, we defined a flux rope boundary via transforming the two-dimensional axial ( $B_z$ ) magnetic field data of Figure 2c into Figure 6 in the following steps:

1. The axial magnetic field strength at the center of the magnetic flux rope is generally strongest. Hence, the reconstructed two-dimensional axial ( $B_z$ ) magnetic field data of Figure 2c is uniformly shifted so that

**Table 1.** A Summary of an Equivalent Radius and a Stretched Length of the Reconstructed Magnetic Flux Ropes and Photoelectron Observation Probability for Event Categories A and B

Event Category	A	B
Photoelectron observation probability (%)	$90.9 \pm 17.5$	$58.0 \pm 44.4$
Equivalent radius (km)	$149.2 \pm 115.0$	$134.0 \pm 115.3$
Stretched length (km)	$212.4 \pm 145.7$	$110.6 \pm 94.0$

we could at least assess lower limits of the volume of the observed magnetic flux ropes based on this boundary determination.

We also investigated the probability of observing photoelectrons when MGS traversed the interior of the reconstructed magnetic flux ropes. Photoelectrons are a good proxy for whether the observed magnetic flux ropes contain Martian ionospheric plasma. Photoelectrons have been detected by the ER experiment onboard MGS with energies of about 20 eV [e.g., *Mitchell et al.*, 2001] and  $\sim 500$  eV (oxygen auger electrons) [*Mitchell et al.*, 2000]. In this study, we only surveyed the 53 events (including 11 Event category A and 42 Event category B) in which MGS stayed inside our defined boundary for a time interval long enough to sample at least one electron energy spectrum. The resulting photoelectron observation probability is 90.9% and 58.0% for Event categories A and B, respectively. This result indicates that photoelectrons are more frequently observed for Event category A than for Event category B, even though Event category A is observed at relatively larger SZA regions than Event category B, as seen in Figures 3 and 4. High solar zenith angles could correspond to lower photoelectron production, and therefore lower rates of observation. We infer that Event category A consists of flux ropes filled with ionospheric plasma.

We then estimate the cross section of the recovered magnetic flux ropes for the 53 recovered events mentioned above. The equivalent radius is derived from the estimated cross section, under the assumption that the shape of each flux rope is strictly circular. It ranges from  $\sim 30$  to 341 km and  $\sim 19$  to 670 km in Event categories A and B. The estimated equivalent radii vary by a factor of 10 among the 53 recovered events. The length along the flux rope axis is estimated from the MGS flight distance. We assume that the reconstructed spatial structure is maintained at least over the time interval when MGS was inside the magnetic flux rope. The axial length is in the range  $\sim 31$ –575 km for Event category A and  $\sim 3$ –456 km for Event category B, respectively.

The averaged values for flux rope shape and photoelectron observation probability for Event categories A and B are summarized in Table 1. We note again that our defined boundary for a recovered magnetic flux rope might be partially beyond the reconstructed two-dimensional frame. Hence, the estimated values of the equivalent radius and axial strength are underestimated in some of the events.

Once lower limits of their volume are calculated, we can estimate lower limits on the ionospheric plasma content contained inside the flux ropes. The radar sounder MARSIS onboard the Mars Express (MEX) space-craft provides us with the local electron density profile in the Martian ionosphere [e.g., *Gurnett et al.*, 2005]. The electron density derived from the MARSIS instrument around the MGS altitude ( $\sim 400$  km from the surface) is expected to be typically between  $10^2$  and  $10^4$  cm $^{-3}$  depending on the observed SZA between 30° and 120° [e.g., *Gurnett et al.*, 2008; *Morgan et al.*, 2008]. In this study, we adopt the typical ionospheric plasma density to be 10 $^3$  cm $^{-3}$ . The resultant lower limits on the ionospheric plasma content inside the magnetic flux ropes range between  $1.7 \times 10^{23}$  and  $4.8 \times 10^{25}$  ( $6.7 \times 10^{24}$  on average) ions and between  $1.9 \times 10^{22}$  and  $4.5 \times 10^{25}$  ( $2.9 \times 10^{24}$  on average) ions in Event categories A and B, respectively.

## 7. Summary and Discussions

In this study, we investigated the spatial structure of Martian magnetic flux ropes observed by MGS by applying the Grad-Shafranov (GS) reconstruction technique. We succeeded in recovering their spatial structures for 70 obvious magnetic flux rope events. The results indicated that the magnetic flux rope axes are mostly oriented horizontal to the Martian surface (Figure 4a) and are rather randomly distributed with respect to the typical plasma streamline (Figure 4b). We found that the events observed at SZA larger than 75° with duration longer than 240 s are mostly seen in the region where the upstream crustal magnetic field strength is large (Figure 3). This is because the observed geographic location corresponds to the region downstream from the strong crustal magnetic field in the southern hemisphere, as shown in Figure 5. In this study, we defined these characteristic events as Event category A. We calculated lower limits on the

volume of the recovered flux ropes, based on the shape and size obtained from the GS reconstruction. The estimated volumes vary by 2–3 orders of magnitude among the recovered events.

If we assume that the ionospheric plasma inside the flux ropes is completely removed from the Martian upper atmosphere within the duration that MGS samples each structure, ion escape rates can be estimated by dividing the ionospheric plasma content inside the flux rope by the duration of the events. The estimated escape rates are on the order of  $10^{22}$ – $10^{23}$  ions/s for Event category A, because the observed durations are typically a few minutes. This escape rate is approximately 10% of the global average ion escape rate (integrating all escape processes) during solar minimum [e.g., Barabash *et al.*, 2007; Lundin *et al.*, 2008]. Our estimates are approximately comparable to the results of Brain *et al.* [2010], even though our estimation of the flux rope length is shorter than that of Brain *et al.* [2010]. However, Brain *et al.* [2010] assumed that the magnetic flux rope is moving with the 5–15 km/s plasma flow velocity relative to the MGS spacecraft.

As mentioned in section 5, we could reconstruct the spatial structure of 70 magnetic flux ropes among the identified 135 events, i.e., we could not reliably determine the invariant axis for 65 events. It might indicate that some of the assumptions used in the GS reconstruction are invalid for these 65 events. Possible candidates include spatial structures that are not two-dimensional but three-dimensional, or structures that were evolving in time. Interestingly, we could not uniquely determine the invariant axis in the event reported by Brain *et al.* [2010], and this situation can be consistent with the possible time-dependent formation scenario proposed in Brain *et al.* [2010, Figure 3].

In this study, the typical plasma streamline derived via equation (5) is simply assumed to be the shortest route flowing from the subsolar point to the nightside, because MGS lacks ion measurements. However, Lundin *et al.* [2011] reported that flow directions of planetary oxygen ions ( $O^+$ ) in the vicinity of the Martian ionosphere around the south pole show complicated patterns, based on their statistical study of the MEX ion observations. Hence, simultaneous spacecraft observations of vector magnetic field as well as ionospheric ion flow directions are important to investigate the actual relationship between the flux rope axis obtained from the GS reconstruction and the local plasma streamline.

The association of large-scale magnetic flux ropes with the region downstream from strong crustal magnetic fields indicates that crustal magnetic fields play a role in their formation. Brain *et al.* [2010] inferred from the observed time variations of the electron pitch angle distribution that the upstream crustal magnetic field had been stretched tailward from the dayside via interaction with the solar wind and had been detached [Brain *et al.*, 2010, Figure 3]. In the meanwhile, Beharrell and Wild [2012] reported that MGS frequently detected magnetic field enhancements associated with magnetic flux ropes in the terminator region in the Martian southern hemisphere, when the strong crustal magnetic fields are distributed upstream. They pointed out that the flux rope can be formed by internal reconnections between neighboring crustal magnetic field lines, whereby field lines are stretched and overlay neighboring crustal magnetic field lines [Beharrell and Wild, 2012, Figure 6]. The resultant flux rope remains attached to the crust [Beharrell and Wild, 2012]. In both Brain *et al.* [2010] and Beharrell and Wild [2012], the flux rope axes should be approximately either parallel or antiparallel to the polarity inversion line between crustal magnetic fields. This tendency is partially consistent with our GS reconstruction results (warm colored arrows for Event category A in Figure 5). However, our GS reconstruction results have some exceptions, suggesting that there may be multiple flux rope formation mechanisms associated with the crustal magnetic fields. Another factor potentially responsible for flux rope formation is magnetic reconnection between the interplanetary magnetic field (IMF) draping around Mars and the crustal magnetic field as suggested by Brain *et al.* [2010]. Investigation of IMF effects on the flux rope formation thus remains as an open issue for future missions such as Mars Atmosphere and Volatile Evolution (MAVEN), which was launched in November 2013.

#### Acknowledgments

This work was supported by a research fellowship of Japan Society for the Promotion of Science (JSPS) and the Global COE Program of Nagoya University "Quest for Fundamental Principles in the Universe (QFPU)".

Robert Lysak thanks Rickard Lundin and an anonymous reviewer for their assistance in evaluating this paper.

#### References

- Acuña, M. H., et al. (1992), Mars Observer magnetic fields investigation, *J. Geophys. Res.*, 97(E5), 7799–7814, doi:10.1029/92JE00344.
- Acuña, M. H., et al. (1998), Magnetic field and plasma observations at Mars: Initial results of the Mars Global Surveyor mission, *Science*, 279, 1676–1680, doi:10.1126/science.279.5357.1676.
- Acuña, M. H., et al. (1999), Global distribution of crustal magnetization discovered by the Mars Global Surveyor MAG/ER experiment, *Science*, 284, 790–793, doi:10.1126/science.284.5415.790.
- Albee, A. L., R. E. Arvidson, F. Palluconi, and T. Thorpe (2001), Overview of the Mars Global Surveyor mission, *J. Geophys. Res.*, 316(E12), 23,291–23,316, doi:10.1029/2000JE001306.
- Barabash, S., A. Fedorov, R. Lundin, and J.-A. Sauvage (2007), Martian atmospheric erosion rates, *Science*, 315, 501–503, doi:10.1126/science.1134358.

- Beharrell, M. J., and J. A. Wild (2012), Stationary flux ropes at the southern terminator of Mars, *J. Geophys. Res.*, **117**, A12212, doi:10.1029/2012JA017738.
- Brain, D. A., et al. (2006), On the origin of aurorae on Mars, *Geophys. Res. Lett.*, **33**, L01201, doi:10.1029/2005GL024782.
- Brain, D. A., A. H. Baker, J. Briggs, J. P. Eastwood, J. S. Halekas, and T.-D. Phan (2010), Episodic detachment of Martian crustal magnetic fields leading to bulk atmospheric plasma escape, *Geophys. Res. Lett.*, **37**, L14108, doi:10.1029/2010GL043916.
- Briggs, J. A., D. A. Brain, M. L. Cartwright, J. P. Eastwood, and J. S. Halekas (2011), A statistical study of flux ropes in the Martian magnetosphere, *Planet. Space Sci.*, **59**, 1498–1505, doi:10.1016/j.pss.2011.06.010.
- Cain, J. C., B. B. Ferguson, and D. Mozzoni (2003), An  $n = 90$  internal potential function of the Martian crustal magnetic field, *J. Geophys. Res.*, **108**, 5008, doi:10.1029/2000JE001487.
- Connerney, J. E. P., M. H. Acuña, P. J. Wasilewski, G. Kletetschka, N. F. Ness, H. Rème, R. P. Lin, and D. L. Mitchell (2001), The global magnetic field of Mars and implications for crustal evolution, *Geophys. Res. Lett.*, **28**, 4015–4018, doi:10.1029/2001GL013619.
- Dubinin, E., R. Lundin, O. Norberg, and N. Pisarenko (1993), Ion acceleration in the Martian tail: Phobos observations, *J. Geophys. Res.*, **98**, 3991–3997, doi:10.1029/92JA02233.
- Eastwood, J. P., D. A. Brain, J. S. Halekas, J. F. Drake, T. D. Phan, M. Øieroset, D. L. Mitchell, R. P. Lin, and M. Acuña (2008), Evidence for collisionless magnetic reconnection at Mars, *Geophys. Res. Lett.*, **35**, L02106, doi:10.1029/2007GL032289.
- Fox, J. L. (2009), Morphology of the dayside ionosphere of Mars: Implications for ion outflows, *J. Geophys. Res.*, **114**, E12005, doi:10.1029/2009JE003432.
- Gurnett, D. A., et al. (2005), Radar soundings of the ionosphere of Mars, *Science*, **310**, 1929–1933, doi:10.1126/science.1121868.
- Gurnett, D. A., et al. (2008), An overview of radar soundings of the Martian ionosphere from the Mars Express spacecraft, *Adv. Space Res.*, **41**, 1335–1346, doi:10.1016/j.asr.2007.01.062.
- Halekas, J. S., and D. A. Brain (2010), Global distribution, structure, and solar wind control of low altitude current sheets at Mars, *Icarus*, **206**, 64–73, doi:10.1016/j.icarus.2008.12.032.
- Halekas, J. S., D. A. Brain, R. J. Lillis, M. O. Fillingim, D. L. Mitchell, and R. P. Lin (2006), Current sheets at low altitudes in the Martian magnetotail, *Geophys. Res. Lett.*, **33**, L13101, doi:10.1029/2006GL026229.
- Halekas, J. S., D. A. Brain, R. P. Lin, J. G. Luhmann, and D. L. Mitchell (2008), Distribution and variability of accelerated electrons at Mars, *Adv. Space Res.*, **41**(9), 1347–1352, doi:10.1016/j.asr.2007.01.034.
- Halekas, J. S., J. P. Eastwood, D. A. Brain, T. D. Phan, M. Øieroset, and R. P. Lin (2009), In situ observations of reconnection Hall magnetic fields at Mars: Evidence for ion diffusion region encounters, *J. Geophys. Res.*, **114**(A13), A11204, doi:10.1029/2009JA014544.
- Hasegawa, H., et al. (2004), Reconstruction of two-dimensional magnetopause structures from Cluster observations: Verification of method, *Ann. Geophys.*, **22**, 1251–1266, doi:10.5194/angeo-22-1251-2004.
- Hasegawa, H., B. U. Ö. Sonnerup, B. Klecker, G. Paschmann, M. W. Dunlop, and H. Rème (2005), Optimal reconstruction of magnetopause structures from Cluster data, *Ann. Geophys.*, **23**, 973–982, doi:10.5194/angeo-23-973-2005.
- Hasegawa, H., B. U. Ö. Sonnerup, C. J. Owen, B. Klecker, G. Paschmann, A. Balogh, and H. Rème (2006), The structure of flux transfer events recovered from Cluster data, *Ann. Geophys.*, **24**, 603–618, doi:10.5194/angeo-24-603-2006.
- Hau, L.-N., and B. U. Ö. Sonnerup (1999), Two-dimensional coherent structures in the magnetopause: Recovery of static equilibria from single-spacecraft data, *J. Geophys. Res.*, **104**, 6899–6918, doi:10.1029/1999JA900002.
- Hu, Q., and B. U. Ö. Sonnerup (2002), Reconstruction of magnetic clouds in the solar wind: Orientations and configurations, *J. Geophys. Res.*, **107**(A7), 1142, doi:10.1029/2001JA000293.
- Hu, Q., C. W. Smith, N. F. Ness, and R. M. Skoug (2004), Multiple flux rope magnetic ejecta in the solar wind, *J. Geophys. Res.*, **109**, A03102, doi:10.1029/2003JA010101.
- Lundin, R., H. Borg, B. Hultqvist, A. Zakharov, and R. Pellinen (1989), First measurements of the ionospheric plasma escape from Mars, *Nature*, **341**, 609–612, doi:10.1038/341609a0.
- Lundin, R., et al. (2006), Plasma acceleration above Martian magnetic anomalies, *Science*, **311**, 980–983, doi:10.1126/science.1122071.
- Lundin, R., S. Barabash, M. Holmström, H. Nilsson, M. Yamauchi, M. Fränz, and E. M. Dubinin (2008), A comet-like escape of ionospheric plasma from Mars, *Geophys. Res. Lett.*, **35**, L18203, doi:10.1029/2008GL034811.
- Lundin, R., S. Barabash, M. Yamauchi, H. Nilsson, and D. Brain (2011), On the relation between plasma escape and the Martian crustal magnetic field, *Geophys. Res. Lett.*, **38**, L02102, doi:10.1029/2010GL046019.
- Mitchell, D. L., R. P. Lin, H. Rème, D. H. Crider, P. A. Cloutier, J. E. P. Connerney, M. H. Acuña, and N. F. Ness (2000), Oxygen Auger electrons observed in Mars' ionosphere, *Geophys. Res. Lett.*, **27**(13), 1871–1874, doi:10.1029/1999GL010754.
- Mitchell, D. L., R. P. Lin, C. Mazelle, H. Rème, P. A. Cloutier, J. E. P. Connerney, M. H. Acuña, and N. F. Ness (2001), Probing Mars' crustal magnetic field and ionosphere with the MGS Electron Reflectometer, *J. Geophys. Res.*, **106**(E10), 23,419–23,428, doi:10.1029/2000JE001435.
- Morgan, D. D., D. A. Gurnett, D. L. Kirchner, J. L. Fox, E. Nielsen, and J. J. Plaut (2008), Variation of the Martian ionospheric electron density from Mars Express radar soundings, *J. Geophys. Res.*, **113**, A09303, doi:10.1029/2008JA013313.
- Morgan, D. D., D. A. Gurnett, F. Akalin, D. A. Brain, J. S. Leisner, F. Duru, R. A. Frahm, and J. D. Winningham (2011), Dual-spacecraft observation of large-scale magnetic flux ropes in the Martian ionosphere, *J. Geophys. Res.*, **116**, A02319, doi:10.1029/2010JA016134.
- Nilsson, H., et al. (2006), Investigation of the influence of magnetic anomalies on ion distributions at Mars, *Space Sci. Rev.*, **126**, 355–372, doi:10.1007/s11214-006-9030-0.
- Okamoto, T. J., et al. (2008), Emergence of a helical flux rope under an active region prominence, *Astrophys. J. Lett.*, **673**, L215–L218, doi:10.1088/0004-8289.
- Qiu, J., Q. Hu, T. A. Howard, and V. B. Yurchyshyn (2007), On the magnetic flux budget in low-corona magnetic reconnection and interplanetary coronal mass ejections, *Astrophys. J.*, **659**, 758–772, doi:10.1086/512060.
- Russell, C. T., and R. C. Elphic (1979), Observation of magnetic flux ropes in the Venus ionosphere, *Nature*, **279**, 616–618, doi:10.1038/279616a0.
- Sonnerup, B. U. Ö., and M. Guo (1996), Magnetopause transects, *Geophys. Res. Lett.*, **23**, 3679–3682, doi:10.1029/96GL03573.
- Sonnerup, B. U. Ö., H. Hasegawa, and G. Paschmann (2004), Anatomy of a flux transfer event seen by Cluster, *Geophys. Res. Lett.*, **31**, L11803, doi:10.1029/2004GL020134.
- Strangeway, R. J., and C. T. Russell (1996), Plasma waves and field-aligned currents in the Venus plasma mantle, *J. Geophys. Res.*, **101**(A8), 17,313–17,324, doi:10.1029/96JA00927.
- Sturrock, P. A. (1994), *Plasma Physics: An Introduction to the Theory of Astrophysical, Geophysical and Laboratory Plasmas*, Stanford-Cambridge Program, Cambridge Univ. Press, Cambridge, U. K., and New York.
- Vignes, D., M. H. Acuña, J. E. P. Connerney, D. H. Crider, H. Rème, and C. Mazelle (2004), Magnetic flux ropes in the Martian atmosphere: Global characteristics, *Space Sci. Rev.*, **111**, 223–231, doi:10.1023/B:SPAC.0000032716.21619.f2.

# Journal of Geophysical Research: Space Physics

## RESEARCH ARTICLE

10.1002/2014JA019943

**Key Points:**

- Mars flux rope structures are recovered via the Grad-Shafranov (GS) equation
- One third of flux ropes may be formed via merging of crustal and draped fields
- Ion escape rates via flux ropes are estimated to be at least  $10^{22}$ – $10^{23}$  ions/s

**Correspondence to:**T. Hara,  
hara@ssl.berkeley.edu**Citation:**

Hara, T., K. Seki, H. Hasegawa, D. A. Brain, K. Matsunaga, M. H. Saito, and D. Shiota (2014), Formation processes of flux ropes downstream from Martian crustal magnetic fields inferred from Grad-Shafranov reconstruction, *J. Geophys. Res. Space Physics*, 119, 7947–7962, doi:10.1002/2014JA019943.

Received 12 MAR 2014

Accepted 9 SEP 2014

Accepted article online 11 SEP 2014

Published online 30 SEP 2014

## Formation processes of flux ropes downstream from Martian crustal magnetic fields inferred from Grad-Shafranov reconstruction

Takuya Hara<sup>1,2</sup>, Kanako Seki<sup>2</sup>, Hiroshi Hasegawa<sup>3</sup>, David A. Brain<sup>4</sup>, Kazunari Matsunaga<sup>2</sup>, Miho H. Saito<sup>5</sup>, and Daikou Shiota<sup>2</sup>

<sup>1</sup>Space Sciences Laboratory, University of California, Berkeley, California, USA, <sup>2</sup>Solar-Terrestrial Environment Laboratory, Nagoya University, Nagoya, Japan, <sup>3</sup>Institute of Space and Astronautical Science, Japan Aerospace Exploration Agency, Sagamihara, Japan, <sup>4</sup>Laboratory for Atmospheric and Space Physics, University of Colorado Boulder, Boulder, Colorado, USA, <sup>5</sup>Earth and Planetary Sciences, Tokyo Institute of Technology, Tokyo, Japan

**Abstract** We applied the Grad-Shafranov reconstruction (GSR) technique to Martian magnetic flux ropes observed downstream from strong crustal magnetic fields in the southern hemisphere. The GSR technique can provide a two-dimensional axial magnetic field map as well as the axial orientation of flux ropes from single-spacecraft data under assumptions that the structure is magnetohydrostatic and time independent. The reconstructed structures, including their orientation, allowed us to evaluate possible formation processes for the flux ropes. We reconstructed 297 magnetic flux ropes observed by Mars Global Surveyor between April 1999 and November 2006. Based on characteristics of their geometrical axial orientation and transverse magnetic field topology, we found that they can be mainly distinguished according to whether draped interplanetary magnetic fields overlaying the crustal magnetic fields are involved or not. Approximately two thirds of the flux ropes can be formed by magnetic reconnection between neighboring crustal magnetic fields attached to the surface. The remaining events seem to require magnetic reconnection between crustal and overlaid draped magnetic fields. The latter scenario should allow planetary ions to be transferred from closed magnetic flux tube to flux tubes connected to interplanetary space, allowing atmospheric ions to escape from Mars. We quantitatively evaluate lower limits on potential ion escape rates from Mars owing to magnetic flux ropes.

### 1. Introduction

Magnetic flux ropes are characteristic twisted helical magnetic field structures. The magnetic field close to the center of a flux rope is strong and aligned axially and becomes gradually weaker and more azimuthal far from the center [Russell and Elphic, 1979]. Flux ropes have been observed throughout the solar system, including at the Earth's magnetosphere [e.g., Sonnerup *et al.*, 2004; Hasegawa *et al.*, 2006], in interplanetary space [e.g., Hu *et al.*, 2004; Qiu *et al.*, 2007], and at the Sun [e.g., Okamoto *et al.*, 2008; Shiota *et al.*, 2010]. In addition, flux ropes have been detected at other planets, such as at Venus [e.g., Russell and Elphic, 1979; Zhang *et al.*, 2012], Mars [e.g., Cloutier *et al.*, 1999; Vignes *et al.*, 2004], Mercury [Slavin *et al.*, 2009], and the Jovian planets [e.g., Russell *et al.*, 1998; Jackman *et al.*, 2007].

Venus and Mars lack a global intrinsic magnetic field. The properties of the plasma environment around these unmagnetized planets are controlled in part by conditions of the solar wind such as the interplanetary magnetic field (IMF) strength and direction. As the solar wind passes Venus and Mars, the IMF drapes around their highly conducting ionospheres, and an induced magnetosphere (or often called magnetic pileup region) is formed around the unmagnetized planets. Planetary ions are energized through the direct interaction of the solar wind with the upper atmosphere, resulting in ion escape into interplanetary space. Planetary escaping ions have been observed using in situ spacecraft measurements, such as Pioneer Venus Orbiter (PVO) [e.g., Brace *et al.*, 1987] and Venus Express for Venus [e.g., Barabash *et al.*, 2007a] and Phobos 2 [e.g., Lundin *et al.*, 1989] and Mars Express (MEX) for Mars [e.g., Barabash *et al.*, 2007b].

Statistical properties of flux ropes detected at unmagnetized planets have been extensively investigated based on the PVO measurements for Venus [e.g., Luhmann and Cravens, 1991, and references therein]. A large number of flux ropes were observed in the dayside Venus ionosphere during 70% of the PVO orbits

[e.g., *Russell and Elphic*, 1979; *Elphic and Russell*, 1983a, 1983b]. Interpretation of the PVO measurements suggested several possible formation processes. For example, *Wolff et al.* [1980] proposed that viscous-type plasma instabilities (such as the Kelvin-Helmholtz instability) originating at the interface between the solar wind flow and ionosphere at moderate and/or high solar zenith angles, allow draped magnetic field lines to sink from the magnetosheath, and become twisted in the ionosphere, forming flux ropes. *Elphic and Russell* [1983c] pointed out that a helical kink instability could coil magnetic flux tubes into rope structures and be responsible for their observed random axial orientations [*Elphic and Russell*, 1983b]. *Luhmann and Elphic* [1985] suggested that flux ropes are the result of a kinematic dynamo process acting on weak seed fields in the Venus ionosphere. However, there is no direct evidence to demonstrate any of the proposed formation scenarios. No matter which processes form the observed flux ropes, the IMF and an associated draped magnetic field lines play a role.

The IMF and associated draped magnetic field lines may not be the only origin of magnetic flux ropes at Mars, because Mars possesses strong localized crustal magnetic fields [e.g., *Acuña et al.*, 1998]. The electromagnetic environment around Mars is thus expected to be more complicated than Venus. Flux ropes similar in spatial scale to those observed at Venus are reported in the Martian ionosphere [e.g., *Cloutier et al.*, 1999; *Vignes et al.*, 2004; *Briggs et al.*, 2011], though they are less frequently observed than at Venus [*Vignes et al.*, 2004]. *Eastwood et al.* [2012] also presented observation of Mars Global Surveyor (MGS) of a chain of flux ropes in the nightside current sheet of the Martian deep tail region. They discussed an implication in the interaction between upstream crustal and draped magnetic fields for their formation [*Eastwood et al.*, 2012].

Furthermore, *Brain et al.* [2010] found large-scale isolated flux ropes downstream from strong crustal magnetic fields. *Morgan et al.* [2011] reported on the longevity of similar events based on a combination of MGS data and field magnitudes derived from the ionospheric radar sounding experiment referred to as MARSIS (Mars Advanced Radar for Subsurface and Ionosphere Sounding) onboard MEX. *Beharrell and Wild* [2012] statistically investigated their spatial distribution based on an automated detection method. They found that the enhancements of magnetic field amplitude mostly associated with flux rope signatures were concentrated at solar zenith angles between 90° and 100° in the southern hemisphere. Moreover, such events are repeatedly detected, when the strong crustal magnetic fields are located on the dayside, upstream of the southern pole region [*Beharrell and Wild*, 2012]. Large-scale magnetic flux ropes near the Martian terminator are also predicted by three-dimensional multifluid simulation that include crustal magnetic fields [*Harnett*, 2009].

Possible formation processes of large-scale flux ropes associated with strong crustal magnetic fields have been proposed by several authors. Based on the observed time variations of the electron pitch angle distribution, *Brain et al.* [2010] proposed that the upstream crustal magnetic field is stretched tailward from the dayside via interaction with the solar wind and may detach, similar to plasmoids in Earth's magnetotail. *Beharrell and Wild* [2012] pointed out that the flux rope can be formed by internal reconnections between neighboring crustal magnetic field lines, whereby field lines are stretched and overlay neighboring crustal magnetic field lines.

If the flux ropes detach, they could intermittently carry significant large amounts of atmosphere away from Mars. *Brain et al.* [2010] proposed that this process might account for as much as 10% of the total present-day ion escape from Mars. Recently, *Hara et al.* [2014] estimated lower limits on the potential ion escape rate due to these large-scale magnetic flux ropes by using the Grad-Shafranov reconstruction (GSR) technique, which is capable of reconstructing the two-dimensional magnetohydrostatic structure from single-spacecraft data [e.g., *Hu and Sonnerup*, 2002; *Hasegawa et al.*, 2006]. The GSR results also provide us with various spatial characteristics, including their shape (lower limits of their radii and lengths), axial orientation, and chirality (handedness) of the flux rope magnetic fields. The estimated lower limits on potential ion escape rates turned out to be on the order of  $10^{22}$ – $10^{23}$  ions/s. It is corresponding to approximately 10% of the global average ion escape rate during solar minimum [*Hara et al.*, 2014].

Based on spatial and geometrical characteristics acquired from the GSR technique [*Hara et al.*, 2014], we investigate possible formation scenarios of these large-scale magnetic flux ropes observed downstream from the strong crustal magnetic fields in the Martian southern hemisphere. In section 2, we show the method for identifying large flux rope events between April 1999 and November 2006. In section 3, the GSR technique is applied to the events from section 2. In section 4, we conduct a statistical study, categorizing the flux ropes into four types according to the characteristics of their estimated axial orientation. We

also investigate dependencies on external conditions such as solar wind dynamic pressure and the local external draped magnetic field direction. In section 5, we discuss possible formation scenarios for each type categorized in section 4. Finally, in section 6, we summarize our results and interpretation and discuss the contribution of magnetic flux ropes to the ion escape rate from Mars.

## 2. Identification of Magnetic Flux Rope Candidates From MGS Data

We utilize data obtained from the magnetometer (MAG) and electron reflectometer onboard Mars Global Surveyor (MGS) during its mapping phase in order to identify Martian magnetic flux ropes. The mapping phase of the MGS mission began in March 1999 and lasted until the end of the mission (November 2006). During this time, MGS was in a quasi-circular orbit at an altitude of approximately 400 km. The MGS orbital configuration during the mapping phase had fixed local time of  $\sim 2$  A.M./2 P.M. [e.g., Albee *et al.*, 2001]. Since the orbital periods were approximately 2 h, MGS orbited Mars  $\sim 34,200$  times in total during the mapping phase. In this study, we surveyed magnetic flux ropes identified in MGS magnetic field data between April 1999 and November 2006.

Several authors reported that MGS repeatedly detected the enhancements of magnetic field strength mostly associated with flux rope signatures around the south pole downstream from the strong crustal magnetic fields, based on their automated method [Brain *et al.*, 2010; Beharrell and Wild, 2012]. Hara *et al.* [2014] also found that the spatial scale of flux rope events observed downstream from the strong crustal magnetic fields in the southern hemisphere is larger than the other events observed regardless of the crustal magnetic fields, based on the GSR results. Here we defined criteria to select candidate MGS orbits in terms of the geographic locations and the solar zenith angle to systematically search for magnetic flux ropes downstream from crustal magnetic fields: When MGS was near the terminator at solar zenith angles between  $85^\circ$  and  $95^\circ$ , we selected for the following conditions: (i) MGS was located between  $-120^\circ$  and  $60^\circ$  east longitude, and  $70^\circ$ – $90^\circ$  south latitude. (ii) Upstream average crustal magnetic field along the typical plasma streamline is larger than 15 nT. (iii) Magnetic field data were available.

The typical plasma streamline is assumed to be the shortest route flowing from the subsolar point to the nightside, as defined by several previous authors [Hara *et al.*, 2014; Strangeway and Russell, 1996]. The upstream crustal magnetic field strength is calculated as the averaged value derived from Connerney *et al.* [2001] from the observed location to the subsolar point along the typical plasma streamline, which is also identical to the method of Hara *et al.* [2014].

We first systematically determined the time intervals when the selection criterion (i) is satisfied orbit by orbit. Through the selection criteria (ii) and (iii), we next selected 3007 candidate orbits to survey magnetic flux ropes. Figure 1 shows the average direction of the typical plasma streamline for each orbit, binned and averaged as seen from the Martian southern pole. Figure 1 indicates that our criteria single out the appropriate orbits to investigate magnetic flux ropes downstream from crustal magnetic fields. Through our selection criteria, the candidate orbits tend to be systematically selected, when the subsolar point is located around  $180^\circ$  east longitude. Because the calculated typical plasma streamline is basically defined to flow from the dayside to nightside, the most correspondent local time with the geographic east longitude is described around the perimeter in Figure 1.

We then surveyed whether large magnetic flux ropes were recorded in MGS MAG data among the selected orbits. We extended the time interval surveyed by 10 min from when the orbit selection criterion (i) were fulfilled to ensure that we could isolate the event. We first chose by eye inspection candidate events in which the observed magnetic field strength was enhanced by 20 nT over the value expected from a crustal magnetic field model [Cain *et al.*, 2003]. It should be noted that Hara *et al.* [2014] already analyzed events for which the observed magnetic field strength exceeded the crustal field model by 70 nT. This large value was chosen to ensure that the GSR technique could be safely applied. Here we have made sure that the GSR technique can safely reconstruct the spatial structure for the weaker field strength events utilized in this study. From our candidate events, we selected flux rope events for which magnetic field hodograms obtained from minimum variance analysis (MVA) show a partial rotation in the plane perpendicular to the minimum variance axis and for which the intermediate to minimum eigenvalue ratio obtained from MVA is at least 5. By this selection method, we identified 682 magnetic flux ropes from the MGS data in the selected 3007 orbits.

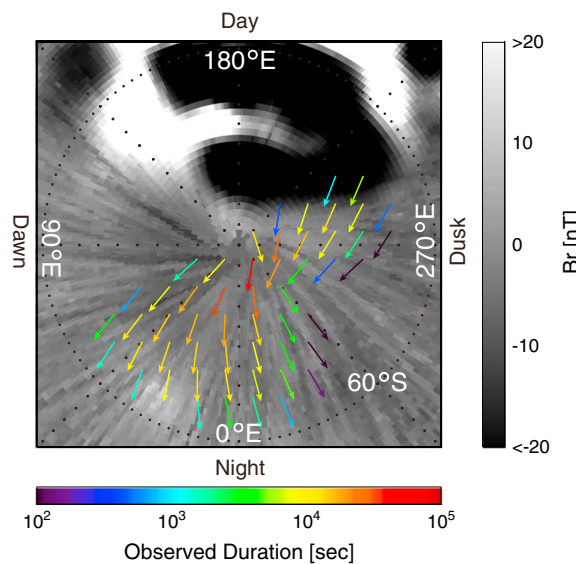


**Figure 1.** The average direction of the plasma streamline of the 3007 orbits utilized so as to conduct our statistical study of magnetic flux ropes, viewed from above the south pole in the geographic coordinate system. Gray scale background indicates the radial component  $B_r$  of crustal magnetic fields expected at the altitude of about 400 km from the Martian surface [Connerney et al., 2001]. East longitude (latitude) grid lines are spaced every 45(30) $^{\circ}$ . The arrow colors represent the total duration of observation accumulated over the 3007 orbits. The definition of the direction of the typical plasma streamline is given in the text.

We defined the invariant axis as the z axis of the GSR coordinate system. The direction of the invariant (GSR z) axis is defined so that transverse magnetic field rotation (in GSR x-y plane) perpendicular to the flux rope axis (z) obeys the right-handed screw rule in this study. The GSR x axis is defined to be parallel to the projection of the spacecraft velocity,  $\mathbf{V}_{sc}$ , onto the plane perpendicular to the z axis. The GSR y axis completes the right-handed orthogonal system. Hence, the GSR x axis (at  $y = 0$ ) represents the projection of the spacecraft trajectory onto the GSR x-y plane.

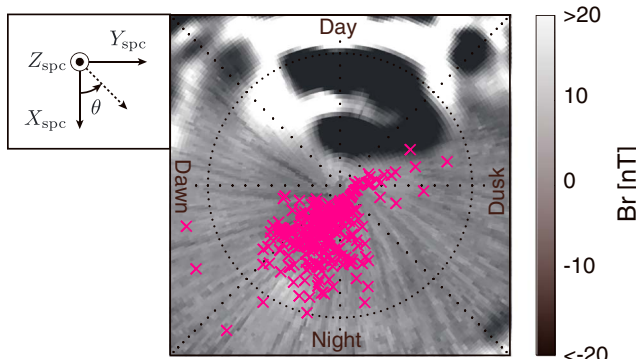


**Figure 2.** Geographic distribution of the 297 identified magnetic flux ropes events, viewed from above the south pole. Magenta crosses are their observed locations. The format of the background crustal magnetic field map is mostly the same as that of Figure 1; however, the displayed background field is more extensive than Figure 1. The definition of the south pole directed planetocentric (SPC) coordinate system and  $\theta$  as shown in the upper left side corner are given in the text.

### 3. Grad-Shafranov Reconstruction of MGS Flux Ropes

We applied the Grad-Shafranov reconstruction (GSR) technique to estimate the flux rope axial orientation and spatial structure of the 682 magnetic flux ropes identified in MGS data, assuming that their structures were two-dimensional and magnetohydrostatic. Owing to the absence of ion measurements by MGS, we were unable to determine the plasma velocity for each event. Therefore, we assumed that the observed magnetic flux ropes are approximately stationary, which means that the spacecraft velocity is dominant over the speed of the structure, namely, movement of the flux rope is only determined by the relative velocity to the MGS spacecraft. Since GSR assumes two-dimensional structures, we determine the axis along which the spatial gradient of the observed magnetic field structure is minimized. This axis is referred to as the invariant axis and is taken to be parallel to the flux rope axis [e.g., Hau and Sonnerup, 1999; Hau and Sonnerup, 2002]. (See Hara et al., [2014], for the detailed methodology to determine the invariant axis and to apply the GSR technique to Martian magnetic flux ropes observed by MGS).

Among the selected 682 magnetic flux ropes in the previous section, we were able to uniquely and clearly determine the invariant axis for 297 events and reconstruct their spatial structure. The remaining events have several candidates for the invariant axis, indicating that some of assumptions used in the GSR technique may be invalid; e.g., the structure might be three-dimensional and/or evolving in time [Hara et al., 2014]. Hereafter, we utilize these 297 events in order to further investigate their possible formation processes. Note that the hodograms for these 297 events rotate by  $282.4 \pm 22.1^{\circ}$  in average in the plane perpendicular to the minimum variance direction. Figure 2

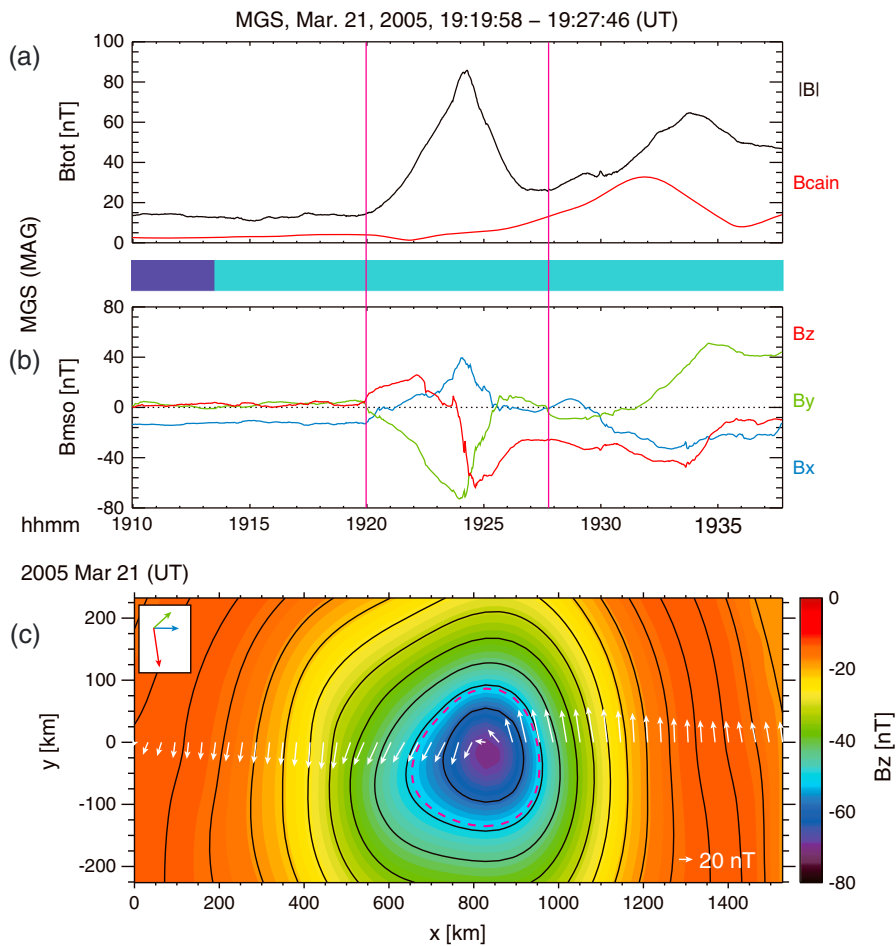


**Figure 3.** Time series plots of (a) magnetic field magnitude and (b) vector magnetic field in the Mars-centered Solar Orbital (MSO) coordinate system observed by MGS on 21 March 2005. Expected crustal magnetic field magnitude (labeled as  $B_{\text{cain}}$ ) is shown by the red solid line in 3a. Color bar between Figures 3a and 3b indicates whether MGS was illuminated (light blue) or in eclipse (dark blue). MGS observed a magnetic flux rope during the time interval between two magenta vertical lines. (c) The reconstructed two-dimensional axial magnetic field  $B_z$  map obtained from the Grad-Shafranov reconstruction using MGS magnetic field data. The MGS spacecraft was traveling (time progressed) from left to right along the line  $y = 0$ . Overlaid white arrows represent the transverse magnetic field components measured by MGS. The blue, green, and red arrows shown just above the reconstructed map are the projections of the MSO axes, respectively.

represents the geographic distribution of our 297 events, viewed from above the Martian south pole. The observed magnetic flux ropes are concentrated between  $0^\circ$  and  $45^\circ$  east longitude.

Here is defined another coordinate system used in this paper hereafter. This is referred as the south pole directed planetocentric (SPC) coordinate system. The SPC coordinate system is Mars centered and fixed with respect to the planet, and the  $Z_{\text{spc}}$  axis points vertically upward from the south pole. The  $X_{\text{spc}}$  axis points toward  $0^\circ$  longitude, and the  $Y_{\text{spc}}$  axis completes the right-handed system (i.e., points toward  $270^\circ$  east longitude). The SPC coordinate system is shown in the upper left side of Figure 2.

Figure 3 shows an example of a result obtained from the GSR technique for a flux rope event on 21 March 2005. The magnetic field strength is enhanced during 19:19:58–19:27:46 UT (between the two magenta vertical lines in Figures 3a and 3b), compared with the field given by the crustal magnetic field model [Cain *et al.*, 2003] shown by the red solid line in Figure 3a. Hodograms for this event (not shown here) in the MVA coordinate system clearly show that the vector magnetic field rotates by approximately  $295.2^\circ$  in a circular manner, which is an expected feature of magnetic flux ropes. Figure 3c represents the invariant axial ( $B_z$ ) magnetic field map in which magnetic field lines in the  $x$ - $y$  plane are the black curves and the axial magnetic field component (out of the plane of the figure) is color coded. The MGS spacecraft traveled in the

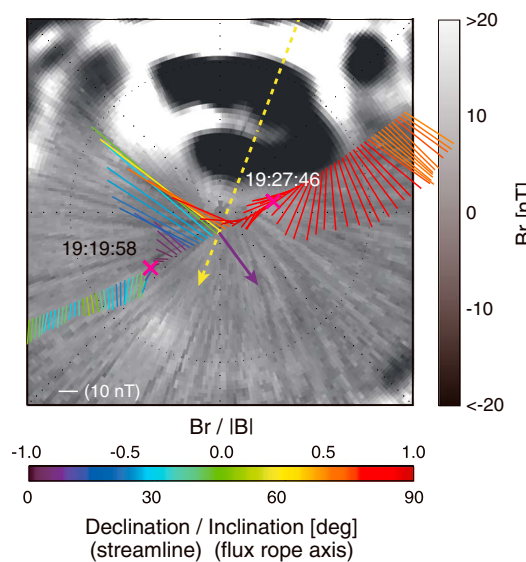


**Figure 4.** External draped magnetic field vectors viewed from above the south pole, with tangential components represented by whisker length and direction originating from orbital track, and the ratio of radial component to the field amplitude indicated by whisker color, as shown by color bar in the bottom. Bold solid (dashed) arrows at the location of the flux rope center are the directions of the flux rope axis (typical plasma streamline), with the axial inclination and declination relative to the typical plasma streamline represented by arrow color, respectively. The axial orientation is defined so that the reconstructed transverse magnetic field rotation (Figure 3c) obeys the right-handed screw rule. The locations of two magenta crosses correspond to the times of two magenta vertical lines in Figures 3a and 3b.

two methods. Since our GSR technique is assumed that the structure is two-dimensional, the angular difference of the estimated flux rope axial orientation between one-dimensional model [Rong *et al.*, 2013] and our GSR technique indicates that the two-dimensional GSR results is more adequate method to infer the flux rope spatial properties rather than such a one-dimensional model.

Figure 4 represents an overview of the event viewed from above the south pole. External fields, which should be dominated by draped IMF, are shown as whisker length in Figure 4. The external field is deduced by subtracting a crustal magnetic field model [Cain *et al.*, 2003] from the observations. The external field is mostly stable and oriented from day to night, along the typical plasma streamline shown as a dashed arrow in Figure 4. The magnetic field vectors rotate through the flux rope, which corresponds to the segment between two magenta crosses in Figure 4.

The estimated flux rope axis of this event in SPC coordinates system is [0.80, 0.59, 0.07]. We define an axial orientation,  $\theta$ , as the angle between the flux rope axis and the  $X_{\text{spc}}$  axis in the  $X$ - $Y$  plane of the SPC coordinate system shown in Figure 2. The  $X_{\text{spc}}$  axis is roughly parallel to the antisunward direction for these events. For this event  $\theta$  is approximately 36.4°, and the flux rope axis is quasi-perpendicular to the spacecraft trajectory, shown as the solid arrow in Figure 4.

#### 4. Properties of Reconstructed Magnetic Flux Ropes

##### 4.1. Axial Orientation

Figure 5 shows the measured distribution of axial orientation  $\theta$  for the 297 flux rope events. As mentioned in section 3, the flux rope axes are defined so that field rotation perpendicular to the estimated rope axis is right-handed screw rule, namely, they are aligned with the direction of the axial core current density. MGS frequently detected flux ropes with axes directed duskward, perpendicular to the  $+X_{\text{spc}}$  axis. Flux ropes with downward-directed axes are, by contrast, rare. In order to better understand the possible different formation

$x$  direction from left to right at  $y = 0$  in the figure. The transverse magnetic field components at  $y = 0$  are overplotted as white arrows, which satisfy the right-handed screw rule as mentioned above. The overlaid magenta dashed curve on Figure 3c is the boundary used to estimate the volume of the magnetic flux rope. The concrete definition of the flux rope boundary is given in section 4.3.

The flux rope axis for this event is estimated to be  $[-0.59, 0.75, 0.28]$  in the Mars-centered Solar Orbital (MSO) coordinate system. The MSO coordinate system is defined with the  $X_{\text{mso}}$  axis toward the Sun, the  $Z_{\text{mso}}$  axis perpendicular to the ecliptic pointing to the northern hemisphere, and the  $Y_{\text{mso}}$  axis completing the right-hand system. Since the flux rope axis is identical with the invariant (GSR  $z$ ) axis, it is also determined so that magnetic field rotation perpendicular to the estimated rope axis obeys the right-handed screw rule. To assess the validity of the derived flux rope orientation, we compare our GSR result with the one-dimensional cylindrical geometric structure analysis method recently presented by Rong *et al.* [2013]. This method utilizes the single-point magnetic field data and infers a flux rope's axial orientation with high accuracy and stability [Rong *et al.*, 2013]. The axial orientation inferred from this method is  $[-0.45, 0.79, 0.42]$ , with an angular difference of approximately 11.4° between the

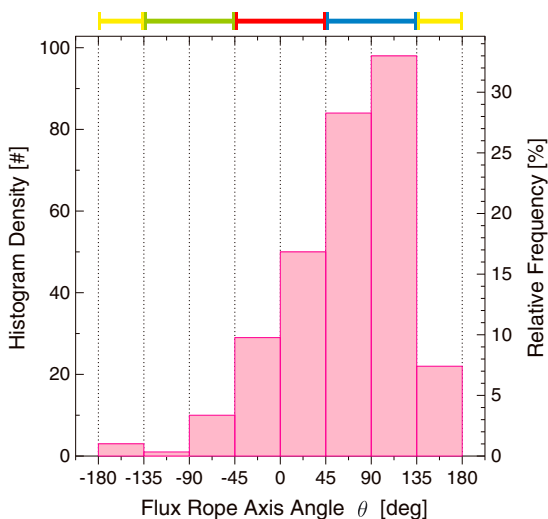


**Figure 5.** Histogram of the 297 identified magnetic flux rope events as a function of the rope axis orientation  $\theta$  in the south pole directed planetocentric (SPC) coordinate system. These flux rope axes are determined so that magnetic field rotation perpendicular to the estimated rope axes obeys the right-handed screw rule based on the Grad-Shafranov reconstruction results. Horizontal left (right) side axis is the event numbers (relative frequencies) of these events, respectively. The blue, yellow, green, and red bars correspond to the four event types categorized according to the estimated flux rope axial orientation  $\theta$ .

In this subsection we statistically investigate the dependence of observed flux ropes on solar wind conditions. Because MGS observed at  $\sim 400$  km altitude, the solar wind properties cannot be directly obtained from MGS observations. However, solar wind proxies such as dynamic pressure ( $P_{sw}$ ) and IMF draping direction can be inferred once per orbit from the magnetic field data [Brain et al., 2005, 2006].

The solar wind dynamic pressure  $P_{sw}$  proxy is calculated on each 2 h orbit as the subsolar magnetic field strength at about 400 km altitude, under the assumption that magnetic pressure is the dominant pressure term inside the induced magnetosphere of Mars and is approximately balanced with the solar wind dynamic pressure [Crider et al., 2003; Brain et al., 2005]. In this study, we adopted the value of the  $P_{sw}$  proxy nearest in time to each observed flux rope, assuming that the  $P_{sw}$  proxy is nearly constant over a spacecraft orbit. Figure 8 represents the distribution of the  $P_{sw}$  proxy for the 297 identified events and their observational probability relative to the 3007 orbits for the statistical study. Observation probability is calculated by dividing the histogram of the 297 flux rope events by that of all 3007 orbits we surveyed. The event numbers are large when the  $P_{sw}$  proxy is about 30–40 nT. However, the probability of observing flux ropes increases up to  $\sim 100$  nT. Events are seldom observed during very high solar wind dynamic pressure periods (larger than  $\sim 100$  nT), although the statistics are poor. There is no clear difference for each of the four event types discussed above (not shown).

We also surveyed the observation probability as a function of time (year). We found that the observation probability was the highest in 2004 and the lowest in 2001. It is likely that this trend can reflect the solar activity. However, this trend does not reflect the solar cycle dependence on the overall Martian magnetic flux ropes, because the events in this study are localized, which is observed downstream from the crustal magnetic fields (around the southern polar region). Moreover, MGS orbited the constrained altitude ( $\sim 400$  km) and the local time (2 A.M./2 P.M.). Hence, we need more measurements to understand the solar cycle dependence on the Martian magnetic flux ropes.

The draped IMF field lines in an induced magnetosphere tend to be aligned along the plasma streamline at high magnetic latitudes because of the velocity shear across the ionopause, as suggested by spacecraft observations [e.g., Law and Cloutier, 1995; Strangeway and Russell, 1996; Brain et al., 2006], as well as numerical simulations [e.g., Ma et al., 2013]. We here investigated the dependence of flux ropes on the local external

scenarios of flux ropes detected in this region downstream from strong crustal fields, we categorized the events according to their axial orientation: duskward, sunward, downward, and antisunward.

Figure 6 shows the observed geographic distribution for each of the four event types.

Duskward flux ropes (Figure 6a) are the most frequently observed ( $\sim 61\%$ ) among the four types and are widely distributed in longitude. In contrast, sunward flux ropes (Figure 6b) are mostly observed within  $30^\circ$  of  $0^\circ$  east. The antisunward flux ropes in Figure 6d are concentrated at longitudes larger than  $0^\circ$ . Figure 7 illustrates three-dimensional crustal magnetic field topologies, viewed from above the south pole in the geographic coordinate system, based on a Martian crustal magnetic field model [Cain et al., 2003]. The upstream crustal field region labeled “B” has field lines oriented roughly perpendicular to the major region labeled “A”. These magnetic flux ropes are thus observed downstream from such a characteristic crustal magnetic field configuration.

#### 4.2. Dependence on External Conditions

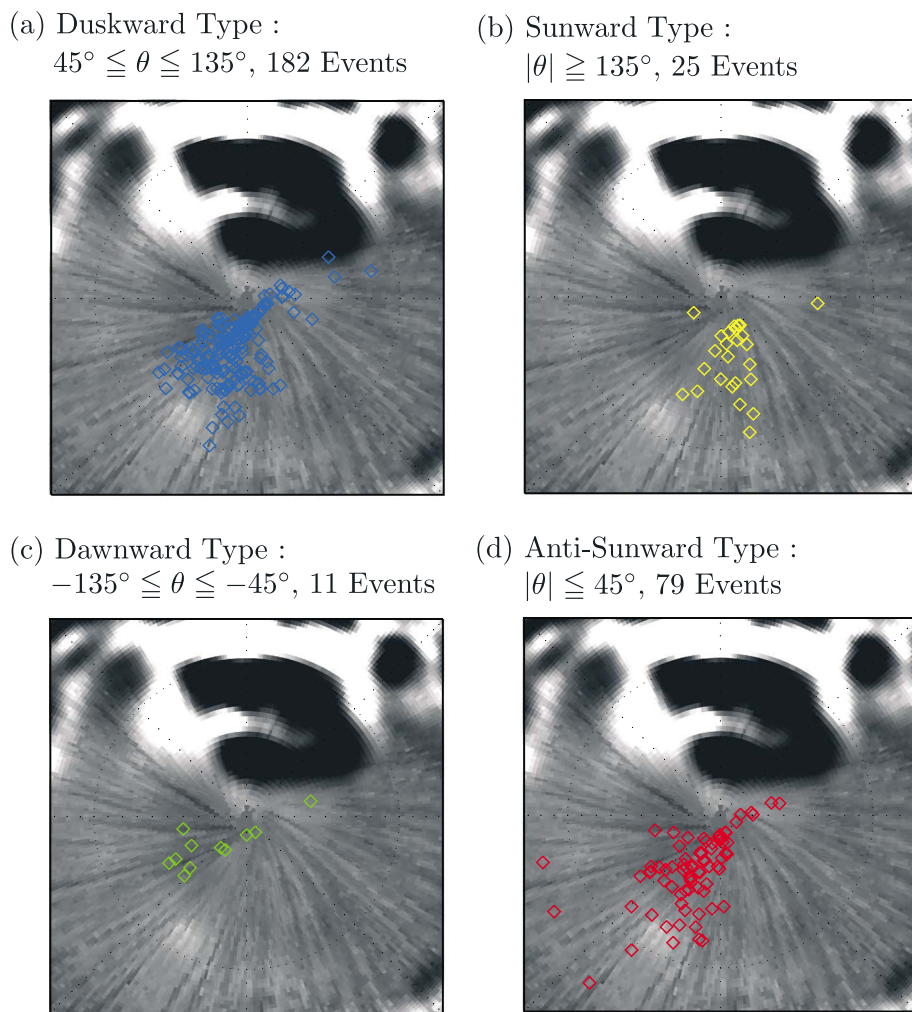


**Figure 6.** The observed geographic location of the 297 magnetic flux rope events divided into four categories: (a) duskward, (b) sunward, (c) downward, and (d) antisunward types based on the GSR-estimated flux rope axial orientation  $\theta$  relative to the  $X_{\text{SPC}}$  axis. The format of background crustal magnetic field map is the same as that of Figure 2. All the plasma streamlines at the observed location are approximately flowing from top (dayside) to bottom (nightside) on each panel.

draped field direction derived from the method as mentioned in section 3 (displayed in Figure 4). Figure 9 illustrates the observation frequency as a function of the external draped magnetic field direction  $\theta$  in the SPC coordinate system for the four magnetic flux rope types categorized in section 4.1. The histogram for each type of event is normalized in Figure 9. We used the MGS vector magnetic field data from the time interval 5–10 min before the start time in which the GSR technique is applied for each event, to avoid distortion from the crustal magnetic field. This local external draped magnetic field orientation (the abscissa of Figure 9) is defined by  $\theta$  in the SPC coordinates system. Figure 9 indicates that there is no significant difference in the distributions of duskward (Figure 9a) and antisunward (Figure 9d) flux ropes. However, the sunward type in Figure 9b shows a relatively different pattern. The external draped magnetic field including all types tends to be draped between  $-60^\circ$  and  $0^\circ$  ( $-32.1^\circ$  in average) in the SPC coordinate system, roughly corresponding to a direction between downward and antisunward.

#### 4.3. Flux Rope Size

As shown by the magenta dashed line in Figure 3c, we define the flux rope boundary to be a surface where the shifted normalized axial magnetic field strength is 66% of the core field value in this study. The shifted normalized axial magnetic field strength is obtained in the following way: we shifted Figure 3c so that the axial magnetic field value is zero on a field line farthest from the center of the flux rope because the reconstructed map sometimes has both signs, and then the shifted values are normalized by the shifted axial field

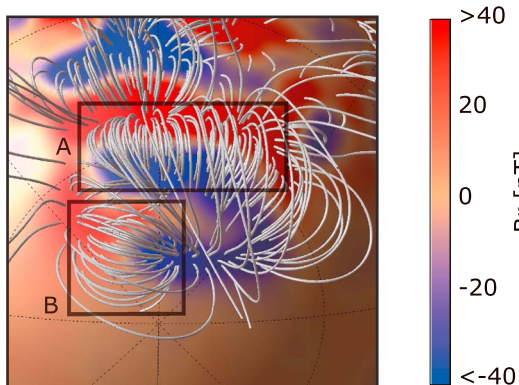


**Figure 7.** Three-dimensional visualization of the Martian crustal magnetic field lines, viewed from above the south pole in the geographic coordinate system, based on the Martian crustal magnetic field model [Cain et al., 2003]. Magnetic field lines are only traced from strong crustal magnetic field region with the altitude of  $\sim 400$  km from the Martian surface by using fourth-order Runge-Kutta integrator. The density of magnetic field lines is roughly proportional to the crustal magnetic field strength. Red- (blue-) colored crustal magnetic field regions have positive (negative) magnetic field polarities. The crustal magnetic field regions labeled A and B are utilized to discuss the formation processes of magnetic flux ropes associated with the strong crustal magnetic fields in section 5.

$10^{21}$  and  $10^{22}$  cm $^3$ . Assuming the local ionospheric plasma number density  $N_i = 10^3$  ions/cm $^3$ , which is the typical for an altitude of about 400 km based on the MEX/MARSIS observations [e.g., Gurnett et al., 2008; Morgan et al., 2008], the estimated flux rope plasma content therefore ranges between  $10^{24}$  and  $10^{25}$  ions.

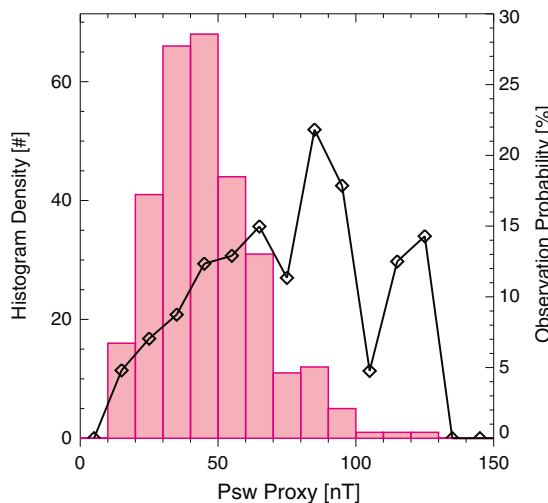


**Figure 8.** Histogram of the 297 identified magnetic flux rope events as a function of solar wind dynamic pressure  $P_{sw}$  proxy. Magenta bar chart shows the event numbers being subject to the left side vertical axis. Black diamonds with a black solid line represent the observation probability (being subject to the right side vertical axis) of the 297 magnetic flux rope events normalized to the 3007 orbits, systematically selected for the statistical survey to search magnetic flux ropes as mentioned in section 2.

value at the center. The detailed methodology to determine this boundary is identical to that in Hara et al. [2014]. The methodology for deriving flux rope radius ( $r$ ) and length ( $L$ ) is also the same as that of Hara et al. [2014]. Because there are events for which the boundary of a recovered magnetic flux rope may not be strictly defined but is partly beyond the two-dimensional reconstruction domain, the derived flux rope volume (radius and length) might be an underestimate. Hence, it should be emphasized that the flux rope size estimation utilized in this study provides lower limits.

Table 1 summarizes the averaged results. In this study, the events in which MGS traveled inside our defined boundary at least are utilized for their volume calculation. Flux rope volume is calculated by multiplying cross section ( $\pi r^2$ ) and length ( $L$ ). The estimated lower limits of the volume of duskward and sunward magnetic flux ropes are larger by a factor of approximately 3–5 than those of the downward and antisunward ones.

Overall, the flux rope volumes are between

$10^{21}$  and  $10^{22}$  cm $^3$ , which is the typical for an altitude of about 400 km based on the MEX/MARSIS observations [e.g., Gurnett et al., 2008; Morgan et al., 2008], the estimated flux rope plasma content therefore ranges between  $10^{24}$  and  $10^{25}$  ions.

## 5. Discussion

### 5.1. Formation Scenarios

Brain et al. [2010] proposed that large-scale magnetic flux ropes at Mars can be formed by magnetic reconnection between upstream crustal magnetic fields that had been stretched tailward, analogous to plasmoids in Earth's magnetotail [Brain et al., 2010, Figure 3]. They suggested that the resultant flux rope may detach from the planet and be transported downstream. If flux ropes form via this scenario at the region labeled A in Figure 7, the resultant flux rope axis should be quasi-perpendicular to the typical plasma streamline. Moreover, transverse magnetic field lines perpendicular to the flux rope axis on the side closest to the planet should be directed toward  $-X_{spc}$ , which is approximately opposite to typical crustal magnetic field lines in region A. Beharrell and Wild [2012] suggested that flux ropes can be formed by internal reconnection whereby crustal field lines are stretched and overlay neighboring crustal magnetic field lines [Beharrell and Wild, 2012, Figure 6]. Hence, the

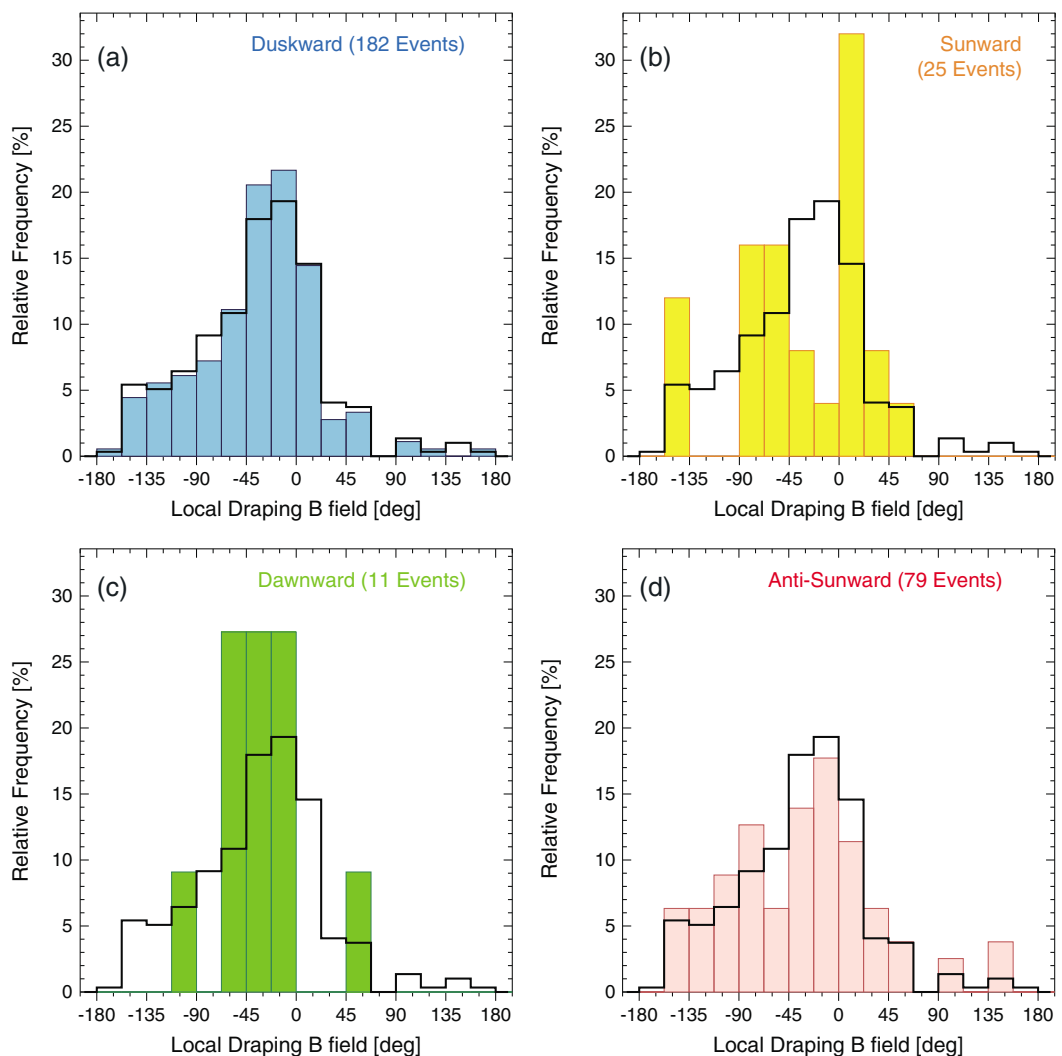


**Figure 9.** Histogram of the 297 identified magnetic flux rope events as a function of the local external draped magnetic field orientation in the south pole directed planetocentric (SPC) coordinate system divided into four categories: (a) duskward, (b) sunward, (c) downward, and (d) antisunward types relative to the  $X_{\text{spc}}$  axis direction. Black solid lines represent the histogram for all the 297 magnetic flux rope events.

flux rope tends to remain attached to the surface. However, if the magnetic flux ropes are formed in the region A through *Beharrell and Wild's* [2012] scenario, the axial orientation and transverse magnetic field lines should be qualitatively similar to those formed via the mechanism proposed by *Brain et al.* [2010].

The formation process proposed by *Brain et al.* [2010] consequently appears to be different from that of *Beharrell and Wild* [2012]. However, crustal magnetic field lines should be initially closed, i.e., attached to the Martian surface. Therefore, detached flux ropes formed via the mechanism that *Brain et al.* [2010]

**Table 1.** A Summary of Lower Limits on the Averaged Magnetic Flux Rope Spatial Properties for the Four Types Categorized According to Axial Orientation Based on the Grad-Shafranov Reconstruction (GSR) Technique

Category	Duskward	Sunward	Downward	Antisunward	All
Events (ratio %)	182 (61.3)	25 (8.4)	11 (3.7)	79 (26.6)	297
Events for volume calculation	164	23	11	59	257
Equivalent radius (km)	$104.1 \pm 67.2$	$88.1 \pm 78.4$	$43.9 \pm 38.3$	$78.0 \pm 39.4$	$94.1 \pm 63.7$
Rope length (km)	$187.1 \pm 149.0$	$252.5 \pm 164.2$	$255.9 \pm 107.4$	$127.3 \pm 113.1$	$182.1 \pm 145.5$
Rope volume ( $\text{cm}^3$ )	$1.12 \times 10^{22}$	$1.29 \times 10^{22}$	$2.31 \times 10^{21}$	$3.42 \times 10^{21}$	$9.16 \times 10^{21}$
$P_{\text{sw}}$ proxy (nT)	45.2	52.2	58.7	44.2	46.0

proposed can be established only if there is no guide field, or a significant ionospheric tailward flow sufficient to overcome the magnetic tension force. The resultant magnetic flux ropes in this study have significant guide field, implying that if they formed via the *Brain et al.* [2010] mechanism they should not detach unless there is a significant ionospheric tailward flow sufficient to overcome the magnetic tension force. Thus, the *Brain et al.*'s [2010] scenario requires subsequent detachment of the flux ropes from the crustal field lines, once formed. Hence, we do not distinguish between the proposed formation scenarios [*Brain et al.*, 2010; *Beharrell and Wild*, 2012] in this study, and hereafter refer to a single "internal reconnection" scenario whereby flux ropes form via reconnection between neighboring crustal field lines. The multifluid simulation presented by *Harnett* [2009] predicted that the interaction between the solar wind and crustal magnetic fields can be highly dynamic and that large flux ropes dissipate a few minutes after their formation. However, in this subsection, we assume that the observed flux ropes can maintain their structure during the MGS measurements at least and examine whether the magnetic flux ropes used in this statistical study can be explained by internal reconnection based on two aspects of the GSR results: (i) the flux rope axial orientation and (ii) transverse field direction in the magnetic flux rope on the side closest to the planet in the SPC coordinate system.

### 5.1.1. Duskward Type

Duskward magnetic flux ropes are the most common of the four types. They are widely distributed in longitude as shown in Figure 6a. They have no significant dependence on the solar wind dynamic pressure or the external draped magnetic field direction (Figure 9a), compared with other flux rope types. Their axes are approximately oriented toward the  $+Y_{\text{spc}}$  axis, duskward and perpendicular to the typical plasma streamline.

It should be noted again that the transverse magnetic field rotation perpendicular to the flux rope axis must be right handed. Hence, the transverse magnetic field direction on the side closest to the planet should be approximately parallel to the  $-X_{\text{spc}}$  axis. If duskward magnetic flux ropes are formed at crustal magnetic field region A, the transverse field lines on the side closest to the planet are thus opposite to the local crustal magnetic field lines in region A. Therefore, the characteristics of the magnetic field configuration, namely, both the flux rope axial orientation and transverse field direction, are consistent with the internal reconnection scenario.

### 5.1.2. Sunward Type

Sunward flux ropes have axes that point approximately antiparallel to the typical plasma streamline. They are only detected when the solar wind dynamic pressure is relatively larger than usual by about 10 nT, and the distribution of the external draped direction differs significantly from the average distribution over all events (Figure 9b). The direction of their transverse magnetic field on the side closest to the planet, derived from the right-hand rule, is approximately oriented toward the  $-Y_{\text{spc}}$  axis.

If magnetic flux ropes are assumed to be formed around region B via internal reconnection, their axes should be oriented approximately parallel to the  $-X_{\text{spc}}$  axis, and the  $-Y_{\text{spc}}$  axis should be their transverse magnetic field direction on the side closest to the planet, as we observe. Therefore, sunward magnetic flux ropes can be explained by the internal reconnection driven at the crustal magnetic field region B.

### 5.1.3. Downward Type

Downward magnetic flux ropes are the rarest ( $\sim 3.7\%$ ) among the identified 297 events. The axial orientation  $\theta$  is directed between  $-135^\circ$  and  $-45^\circ$  in the x-y plane of the SPC coordinate system (Figure 5), which is roughly along the  $-Y_{\text{spc}}$  axis. Their transverse magnetic field direction on the side closest to the planet should be approximately along the  $+X_{\text{spc}}$  axis. This orientation is aligned with the typical plasma streamline as well as the local crustal magnetic field direction at region A and is roughly perpendicular to the local crustal magnetic field direction at region B. Therefore, downward magnetic flux ropes cannot be explained by internal reconnection.

Figure 10a illustrates a possible formation process. We assume that flux ropes are formed by crustal magnetic fields at region A, because it is the largest upstream crustal field complex. The downward magnetic flux ropes can be formed via the following scenario shown in Figure 10a:

1. There are crustal magnetic field lines at the region as labeled A in Figure 7.
2. The local external magnetic field (black dashed arrows) overlays the crustal magnetic fields lines in region A, consistent with the observations of the external magnetic field as shown in Figure 9.

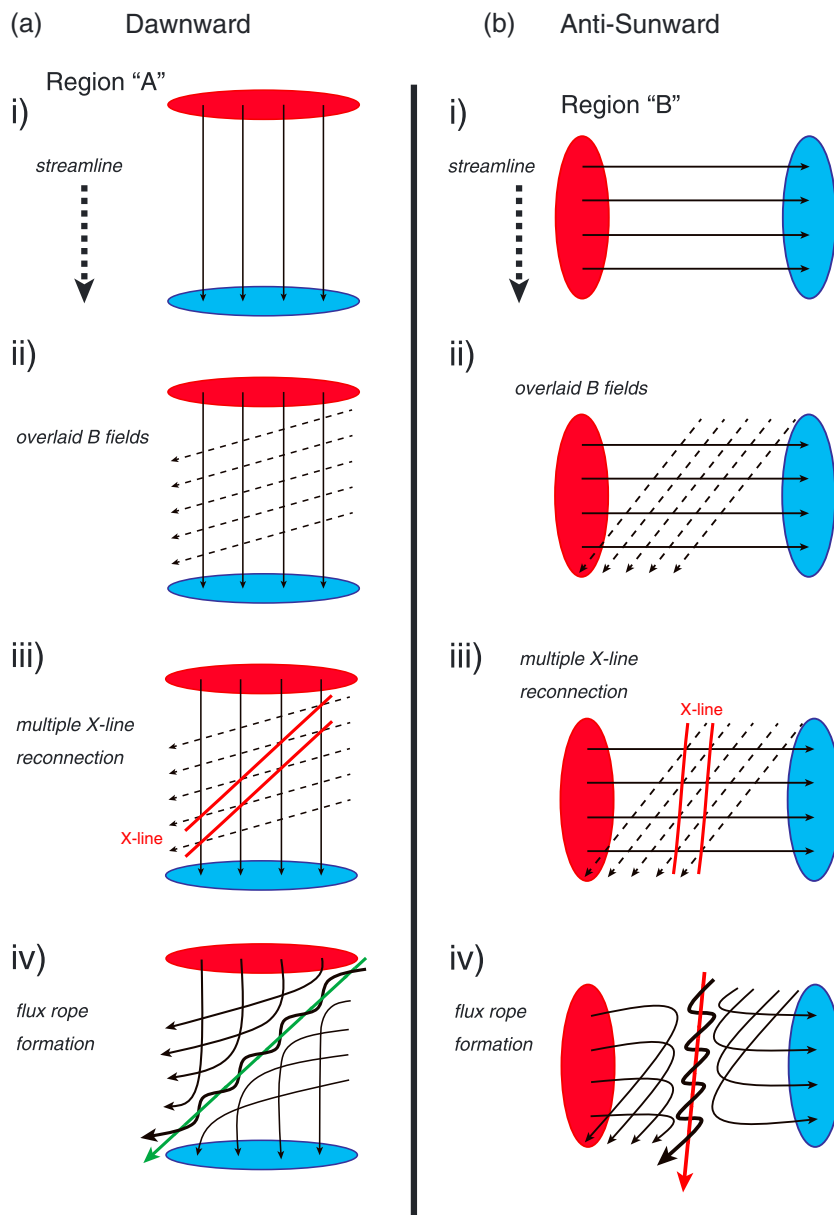


**Figure 10.** Schematic illustration of new possible scenarios for (a) downward and (b) antisunward types to form large-scale magnetic flux ropes observed downstream from the strong crustal magnetic fields. Scenes are evolved from (i) to (iv) to form the magnetic flux ropes. These schematic illustrations are viewed from above the south pole in the x-y plane in the SPC coordinate system, similar to Figures 1, 2, 4, 6, and 7. Red- and blue-colored regions are depicted to be positive and negative polarity crustal magnetic field regions, respectively, similar to Figure 7. Black solid arrows are described magnetic field lines. Black dashed arrows shown in scenes (ii) and (iii) are overlaid magnetic field lines, assumed to be the local external draped magnetic fields. Multiple X line reconnections can be caused on the two parallel red solid lines in scene (iii). Helical black bold arrows are resultant magnetic flux ropes. Green and red bold arrows are resultant magnetic flux rope axis.

3. Multiple X line reconnection events are simultaneously driven between the original crustal magnetic fields (black solid arrows) and the overlaid local external draped magnetic fields (black dashed arrows) on the two parallel red solid lines.
4. A magnetic flux rope forms (helical black bold arrow). The axial orientation of the resultant magnetic flux ropes (green bold arrow) is directed downward and perpendicular to the typical plasma streamline.

We hereafter refer to magnetic flux ropes formed via the mechanism described above as formed in an “external reconnection” scenario. Panel (iv) of Figure 10a indicates that the orientation of the internal core

magnetic field should be directed parallel to the flux rope axis. The GSR results show that the geometrical configuration of internal core magnetic field is consistent with Figure 10a for all the downward magnetic flux rope events. One consideration for the external reconnection case is the shear angle between crustal and overlaid draping magnetic field lines. Downward magnetic flux ropes are often under low shear angle conditions: crustal magnetic field lines in region A are approximately  $\theta = 0^\circ$  ( $+X_{\text{spc}}$ ), and the local external draped direction is mostly approximately  $-60^\circ < \theta < 0^\circ$  in Figure 9c. Swisdak *et al.* [2003, 2010] suggested that the magnetic reconnection occurrence depends on  $\Delta\beta$  (the difference of plasma  $\beta$  on two sides of the current sheet) as well as magnetic shear angle. In other words, magnetic reconnection can occur even under low shear angle during low  $\Delta\beta$  ( $\approx 1-2$ ) conditions [Swisdak *et al.*, 2010; Phan *et al.*, 2013]. This is why the downward magnetic flux ropes might be the most rare events among the four types, because the low  $\Delta\beta$  condition must be fulfilled to drive magnetic reconnection between crustal and overlaid draping magnetic field lines under the low shear angle.

#### 5.1.4. Antisunward Type

Antisunward magnetic flux ropes are the second most common ( $\approx 26.6\%$ ) type. The axial orientation  $\theta$  is directed less than  $45^\circ$  in the  $x$ - $y$  plane of the SPC coordinate system (Figure 5), which is approximately parallel to the typical plasma streamline ( $+X_{\text{spc}}$  axis). Their event distribution with respect to external conditions is similar to the average. Their transverse magnetic field direction on the side closest to the planet is along approximately the  $+Y_{\text{spc}}$  axis. This orientation is quasi-perpendicular to the local crustal magnetic field direction in region A, however, aligned to that in region B. Therefore, the antisunward magnetic flux ropes cannot be explained by internal reconnection. Figure 6d indicates the typical plasma streamline for antisunward magnetic flux ropes is often along the crustal magnetic field region labeled B in Figure 7. Hence, we propose a possible scenario to form antisunward flux ropes originating from region B, similar to that of the downward type illustrated in Figure 10b.

The axial orientation of the resultant magnetic flux rope (red bold arrow in Figure 10b) is directed to the  $+X_{\text{spc}}$ , which is quasi-parallel to the typical plasma streamline. The transverse magnetic field direction in the resultant magnetic flux ropes (helical black bold arrow in Figure 10b) on the side closest to the planet is aligned with the local crustal magnetic field direction at region B, which is along approximately the  $+Y_{\text{spc}}$  axis. Therefore, we suggest that antisunward magnetic flux ropes can be explained by external reconnection at region B. That is, they might be formed via multiple X line reconnections between crustal magnetic fields at region B and the overlaid local external draped magnetic fields (black dashed arrows in Figure 10b).

As mentioned above, magnetic reconnection rates can depend on the shear angle between crustal and overlaid magnetic field lines [Swisdak *et al.*, 2010; Phan *et al.*, 2013]. Antisunward magnetic flux ropes are often observed under relatively larger shear angles than the downward ones, because crustal magnetic field lines in region B are directed approximately  $\theta = 90^\circ$  ( $+Y_{\text{spc}}$ ), and the local external draped direction is mostly in the range  $-90^\circ < \theta < 0^\circ$  in the  $x$ - $y$  plane in the SPC coordinate system (Figure 9d). Hence, the difference in the shear angle might explain the difference in the numbers of antisunward and downward events.

The orientation of the internal core magnetic field in scene (iv) of Figure 10b implies that it is also directed parallel to the flux rope axis. However, a part of the recovered antisunward magnetic flux ropes have a different orientation of the internal core field. That is, it is antiparallel to the flux rope axis. We interpret that such events can be produced when the local external draped magnetic field is  $\theta < -90^\circ$  (Figure 9d).

One of the considerations seen in the GSR statistical results is the observation probabilities between the internal and external magnetic flux rope cases. The GSR statistical results show that internal reconnection (duskward + sunward: 207 events) cases are observed more than twice as often as external reconnection (dawnward + antisunward: 90 events) cases. One possible interpretation is that the altitude at which flux ropes form via external reconnection is higher than for internal reconnection event, because overlaid draping magnetic fields are necessary for their formation. This interpretation leads to another possibility that magnetic flux ropes resulting from external reconnection might be formed more frequently than MGS can observe at an altitude of 400 km.

#### 5.2. Contribution to Ion Escape From Mars

As described in section 4.3, Table 1 shows that duskward and sunward magnetic flux ropes (internal reconnection cases) are larger by a factor of approximately 3–5 than downward and antisunward ones (external reconnection cases), with the caveat that the derived sizes are lower limits. The GSR statistical results suggest that internal reconnection cases can be formed via magnetic reconnections between neighboring

crustal magnetic field lines and should remain attached to the crust unless there is a significant ionospheric tailward flow to overcome the magnetic tension force of the flux ropes. Hence, internal reconnection cases should not contribute much to the ion escape from Mars unless additional reconnection detaches the flux ropes from the crust. On the other hand, the external reconnection cases can be easily detached from the surface, because they are formed via multiple X line reconnections between crustal and overlaid draping magnetic field lines connected to the IMF.

We estimate the ion escape rates assuming that ionospheric plasma inside the flux ropes is completely removed from the Martian upper atmosphere within the interval of MGS sampling each structure. The potential ion escape rates via transport away from the planet by downward and antisunward magnetic flux ropes (external reconnection cases) are estimated to be approximately  $10^{22}$  ions/s, because the durations of the recovered magnetic flux ropes are typically a few minutes or less. MEX observations confirm that global average ion escape rates during solar minimum are approximately  $10^{24}$  ions/s [e.g., Barabash *et al.*, 2007b; Lundin *et al.*, 2008]. These results indicate that ion escape due to detached magnetic flux ropes downstream from strong crustal magnetic fields can instantaneously contribute approximately 1% of the global average ion escape rate during the solar minimum. Therefore, ion escape rates due to magnetic flux ropes do not significantly contribute to atmospheric ion escape from Mars.

## 6. Summary

In this paper, we investigated possible formation scenarios of Martian magnetic flux ropes observed in the vicinity of the Martian south pole and downstream from strong crustal magnetic fields, based on the Grad-Shafranov reconstruction (GSR) technique. We performed a statistical study on 682 magnetic flux rope candidates observed by Mars Global Surveyor (MGS) between April 1999 and November 2006. We were able to uniquely estimate their axial orientation and spatial structures by the GSR technique for 297 magnetic flux rope events (Figure 2). The statistical results are summarized as follows:

1. The observed frequency of magnetic flux ropes increases with the solar wind dynamic pressure  $P_{sw}$  proxy [Brain *et al.*, 2005] up to a pressure proxy value of  $\sim 100$  nT (Figure 8). Local external draped magnetic fields are typically oriented between  $-60^\circ$  and  $0^\circ$  in the south pole directed planetocentric (SPC) coordinate system as the precondition during the large-scale magnetic flux rope events (Figure 9).
2. The 297 magnetic flux rope events can be categorized into four types according to axial orientation  $\theta$  in the  $x$ - $y$  plane of the SPC coordinate system: duskward, sunward, duskward, and antisunward magnetic flux rope orientations, respectively (Figure 5).
3. Based on their axial orientation and transverse magnetic field direction on the side closest to the planet, we inferred possible formation scenarios for each event type.
4. Duskward and sunward magnetic flux ropes (Figures 6a and 6b) can be explained by an internal reconnection scenario, in which they are formed via magnetic reconnections between neighboring crustal magnetic field lines. Such formation scenarios were previously proposed by Brain *et al.* [2010] and Beharrell and Wild [2012].
5. Downward and antisunward magnetic flux ropes (Figures 6c and 6d) cannot be explained by magnetic reconnections between only neighboring crustal magnetic field lines. Overlaid magnetic field lines (i.e., external draped magnetic field lines) above the ambient crustal magnetic field lines could enable multiple X line reconnection as summarized in Figure 10.
6. Flux ropes formed via internal reconnection should remain attached to the crust and hence do not make a large contribution to ion escape from Mars unless an additional reconnection occurs that can detach them from the crust. On the other hand, external reconnection cases should be detached from the surface and may contribute to ion escape rates.
7. The estimated lower limits of the volume of duskward and sunward magnetic flux ropes (internal reconnection cases) are larger by a factor of approximately 3–5 than those of downward and antisunward ones (external reconnection cases) as summarized in Table 1. The potential ion escape rates via transport away from the planet by downward and antisunward magnetic flux ropes (external reconnection cases) are estimated to be approximately  $10^{22}$  ions/s. This results indicate that ion escape rates due to detached magnetic flux ropes downstream from strong crustal magnetic fields can instantaneously contribute approximately 1% of the global average ion escape rate during the solar minimum [e.g., Barabash *et al.*, 2007b; Lundin *et al.*, 2008].

We had to impose additional assumptions for an application of the GSR technique to our data sets, due to the lack of ion observation by MGS [Hara *et al.*, 2014]. If Martian ionospheric plasma properties, such as number density, bulk velocity vector, and temperature, are simultaneously available during magnetic flux rope observations, we could estimate their spatial structure more accurately. Moreover, we could better evaluate possible ion escape rates owing to the magnetic flux ropes, if the ionospheric ion density inside the magnetic flux rope were available. Therefore, comprehensive in situ plasma and magnetic field observations are essential in order to understand ion escape rates and formation scenarios of Martian magnetic flux ropes. The MAVEN (Mars Atmosphere and Volatile Evolution) spacecraft was successfully launched on 18 November 2013 and entered orbit around Mars on 22 September 2014. MAVEN carries a suite of atmospheric and plasma instruments which are capable of investigating the role of the magnetic flux ropes in atmospheric escape from Mars. Hence, MAVEN will provide us with numerous helpful data to better understand possible formation scenarios of magnetic flux ropes observed over a wide range of local time, latitude, and altitude.

### Acknowledgments

The data used in this paper are publicly available in NASA's Planetary Data System. This work was supported by a research fellowship of Japan Society for the Promotion of Science (JSPS) and the Global COE Program of Nagoya University "Quest for Fundamental Principles in the Universe (QFPU)" from JSPS and MEXT of Japan. T.H. is also supported by NASA Award 1000013136 for the Mars Atmosphere and Volatile Evolution (MAVEN) mission.

Michael Liemohn thanks Yong Wei and one anonymous reviewer for their assistance in evaluating this paper.

### References

- Acuña, M. H., et al. (1998), Magnetic field and plasma observations at Mars: Initial results of the Mars Global Surveyor mission, *Science*, 279, 1676–1680, doi:10.1126/science.279.5357.1676.
- Albee, A. L., R. E. Arvidson, F. Palluconi, and T. Thorpe (2001), Overview of the Mars Global Surveyor mission, *J. Geophys. Res.*, 106(E12), 23,291–23,316, doi:10.1029/2000JE001306.
- Barabash, S., et al. (2007a), The loss of ions from Venus through the plasma wake, *Nature*, 450, 650–653, doi:10.1038/nature06434.
- Barabash, S., A. Fedorov, R. Lundin, and J.-A. Sauvad (2007b), Martian atmospheric erosion rates, *Science*, 315, 501–503, doi:10.1126/science.1134358.
- Beharrell, M. J., and J. A. Wild (2012), Stationary flux ropes at the southern terminator of Mars, *J. Geophys. Res.*, 117, A12212, doi:10.1029/2012JA017738.
- Brace, L. H., W. T. Kasperzak, H. A. Taylor, R. F. Theis, C. T. Russell, A. Barnes, J. D. Mihalov, and D. M. Hunten (1987), The ionotail of Venus: Its configuration and evidence for ion escape, *J. Geophys. Res.*, 92(A1), 15–26, doi:10.1029/JA092iA01p00015.
- Brain, D. A., J. S. Halekas, R. Lillis, D. L. Mitchell, R. P. Lin, and D. H. Crider (2005), Variability of the altitude of the Martian sheath, *Geophys. Res. Lett.*, 32, L18203, doi:10.1029/2005GL023126.
- Brain, D. A., D. L. Mitchell, and J. S. Halekas (2006), The magnetic field draping direction at Mars from April 1999 through August 2004, *Icarus*, 182, 464–473, doi:10.1016/j.icarus.2005.09.023.
- Brain, D. A., A. H. Baker, J. Briggs, J. P. Eastwood, J. S. Halekas, and T.-D. Phan (2010), Episodic detachment of Martian crustal magnetic fields leading to bulk atmospheric plasma escape, *Geophys. Res. Lett.*, 37, L14108, doi:10.1029/2010GL043916.
- Briggs, J. A., D. A. Brain, M. L. Cartwright, J. P. Eastwood, and J. S. Halekas (2011), A statistical study of flux ropes in the Martian magnetosphere, *Planet. Space Sci.*, 59, 1498–1505, doi:10.1016/j.pss.2011.06.010.
- Cain, J. C., B. F. Ferguson, and D. Mozzoni (2003), An  $n = 90$  internal potential function of the Martian crustal magnetic field, *J. Geophys. Res.*, 108, 5008, doi:10.1029/2000JE001487.
- Cloutier, P. A., et al. (1999), Venus-like interaction of the solar wind with Mars, *Geophys. Res. Lett.*, 26(17), 2685–2688, doi:10.1029/1999GL900591.
- Connerney, J. E. P., M. H. Acuña, P. J. Wasilewski, G. Kletetschka, N. F. Ness, H. Rème, R. P. Lin, and D. L. Mitchell (2001), The global magnetic field of Mars and implications for crustal evolution, *Geophys. Res. Lett.*, 28, 4015–4018, doi:10.1029/2001GL013619.
- Crider, D. H., D. Vignes, A. M. Krymskii, T. K. Breus, N. F. Ness, D. L. Mitchell, J. A. Slavin, and M. H. Acuña (2003), A proxy for determining solar wind dynamic pressure at Mars using Mars Global Surveyor data, *J. Geophys. Res.*, 108(A12), 1461, doi:10.1029/2003JA009875.
- Eastwood, J. P., J. J. H. Videira, D. A. Brain, and J. S. Halekas (2012), A chain of magnetic flux ropes in the magnetotail of Mars, *Geophys. Res. Lett.*, 39, L03104, doi:10.1029/2011GL050444.
- Elphic, R. C., and C. T. Russell (1983a), Magnetic flux ropes in the Venus ionosphere—Observations and models, *J. Geophys. Res.*, 88, 58–72, doi:10.1029/JA088iA01p00058.
- Elphic, R. C., and C. T. Russell (1983b), Global characteristics of magnetic flux ropes in the Venus ionosphere, *J. Geophys. Res.*, 88, 2993–3003, doi:10.1029/JA088iA04p02993.
- Elphic, R. C., and C. T. Russell (1983c), Evidence for helical kink instability in the Venus magnetic flux ropes, *Geophys. Res. Lett.*, 10, 459–462, doi:10.1029/GL010i006p00459.
- Gurnett, D. A., et al. (2008), An overview of radar soundings of the Martian ionosphere from the Mars Express spacecraft, *Adv. Space Res.*, 41, 1335–1346, doi:10.1016/j.asr.2007.01.062.
- Hara, T., K. Seki, H. Hasegawa, D. A. Brain, K. Matsunaga, and M. H. Saito (2014), The spatial structure of Martian magnetic flux ropes recovered by the Grad-Shafranov reconstruction technique, *J. Geophys. Res. Space Physics*, 119, 1262–1271, doi:10.1002/2013JA019414.
- Harnett, E. M. (2009), High-resolution multifluid simulations of flux ropes in the Martian magnetosphere, *J. Geophys. Res.*, 114, A01208, doi:10.1029/2008JA013648.
- Hasegawa, H., B. U. Ö. Sonnerup, C. J. Owen, B. Klecker, G. Paschmann, A. Balogh, and H. Rème (2006), The structure of flux transfer events recovered from Cluster data, *Ann. Geophys.*, 24, 603–618, doi:10.5194/angeo-24-603-2006.
- Hau, L.-N., and B. U. Ö. Sonnerup (1999), Two-dimensional coherent structures in the magnetopause: Recovery of static equilibria from single-spacecraft data, *J. Geophys. Res.*, 104, 6899–6918, doi:10.1029/1999JA900002.
- Hu, Q., and B. U. Ö. Sonnerup (2002), Reconstruction of magnetic clouds in the solar wind: Orientations and configurations, *J. Geophys. Res.*, 107, 1142, doi:10.1029/2001JA000293.
- Hu, Q., C. W. Smith, N. F. Ness, and R. M. Skoug (2004), Multiple flux rope magnetic ejecta in the solar wind, *J. Geophys. Res.*, 109, A03102, doi:10.1029/2003JA010101.
- Jackman, C. M., C. T. Russell, D. J. Southwood, C. S. Arridge, N. Achilleos, and M. K. Dougherty (2007), Strong rapid dipolarizations in Saturn's magnetotail: In situ evidence of reconnection, *Geophys. Res. Lett.*, 34, L11203, doi:10.1029/2007GL029764.
- Law, C. C., and P. A. Cloutier (1995), Observations of magnetic structure at the dayside ionopause of Venus, *J. Geophys. Res.*, 100, 23,973–23,982, doi:10.1029/95JA02756.

- Luhmann, J. G., and T. E. Cravens (1991), Magnetic fields in the ionosphere of Venus, *Space Sci. Rev.*, **55**, 201–274, doi:10.1007/BF00177138.
- Luhmann, J. G., and R. C. Elphic (1985), On the dynamo generation of flux ropes in the Venus ionosphere, *J. Geophys. Res.*, **90**, 12,047–12,056, doi:10.1029/JA090iA12p12047.
- Lundin, R., H. Borg, B. Hultqvist, A. Zakharov, and R. Pellinen (1989), First measurements of the ionospheric plasma escape from Mars, *Nature*, **341**, 609–612, doi:10.1038/341609a0.
- Lundin, R., S. Barabash, M. Holmström, H. Nilsson, M. Yamauchi, M. Fränz, and E. M. Dubinin (2008), A comet-like escape of ionospheric plasma from Mars, *Geophys. Res. Lett.*, **35**, L18203, doi:10.1029/2008GL034811.
- Ma, Y. J., A. F. Nagy, C. T. Russell, R. J. Strangeway, H. Y. Wei, and G. Toth (2013), A global multispecies single-fluid MHD study of the plasma interaction around Venus, *J. Geophys. Res. Space Physics*, **118**, 321–330, doi:10.1029/2012JA018265.
- Morgan, D. D., D. A. Gurnett, D. L. Kirchner, J. L. Fox, E. Nielsen, and J. J. Plaut (2008), Variation of the Martian ionospheric electron density from Mars Express radar soundings, *J. Geophys. Res.*, **113**, A09303, doi:10.1029/2008JA013313.
- Morgan, D. D., D. A. Gurnett, F. Akalin, D. A. Brain, J. S. Leisner, F. Duru, R. A. Fahrm, and J. D. Wingham (2011), Dual-spacecraft observation of large-scale magnetic flux ropes in the Martian ionosphere, *J. Geophys. Res.*, **116**, A02319, doi:10.1029/2010JA016134.
- Okamoto, T. J., et al. (2008), Emergence of a helical flux rope under an active region prominence, *Astrophys. J. Lett.*, **673**, L215–L218, doi:10.1086/528792.
- Phan, T. D., G. Paschmann, J. T. Gosling, M. Oieroset, M. Fujimoto, J. F. Drake, and V. Angelopoulos (2013), The dependence of magnetic reconnection on plasma  $\beta$  and magnetic shear: Evidence from magnetopause observations, *Geophys. Res. Lett.*, **40**, 11–16, doi:10.1029/2012GL054528.
- Qiu, J., Q. Hu, T. A. Howard, and V. B. Yurchyshyn (2007), On the magnetic flux budget in low-corona magnetic reconnection and interplanetary coronal mass ejections, *Astrophys. J.*, **659**, 758–772, doi:10.1086/512060.
- Rong, Z. J., W. X. Wan, C. Shen, T. L. Zhang, A. T. Y. Lui, Y. Wang, M. W. Dunlop, Y. C. Zhang, and Q.-G. Zong (2013), Method for inferring the axis orientation of cylindrical magnetic flux rope based on single-point measurement, *J. Geophys. Res. Space Physics*, **118**, 271–283, doi:10.1029/2012JA018079.
- Russell, C. T., and R. C. Elphic (1979), Observation of magnetic flux ropes in the Venus ionosphere, *Nature*, **279**, 616–618, doi:10.1038/279616a0.
- Russell, C. T., K. K. Khurana, D. E. Huddleston, and M. G. Kivelson (1998), Localized reconnection in the near jovian magnetotail, *Science*, **280**, 1061–1064, doi:10.1126/science.280.5366.1061.
- Shiota, D., K. Kusano, T. Miyoshi, and K. Shibata (2010), Magnetohydrodynamic modeling for a formation process of coronal mass ejections: Interaction between an ejecting flux rope and an ambient field, *Astrophys. J.*, **718**, 1305–1314, doi:10.1088/0004-637X/718/2/1305.
- Slavin, J. A., et al. (2009), MESSENGER observations of magnetic reconnection in Mercury's magnetosphere, *Science*, **324**(5927), 606–610, doi:10.1126/science.1172011.
- Sonnerup, B. U. Ö., H. Hasegawa, and G. Paschmann (2004), Anatomy of a flux transfer event seen by Cluster, *Geophys. Res. Lett.*, **31**, L11803, doi:10.1029/2004GL020134.
- Strangeway, R. J., and C. T. Russell (1996), Plasma waves and field-aligned currents in the Venus plasma mantle, *J. Geophys. Res.*, **101**(A8), 17,313–17,324, doi:10.1029/96JA00927.
- Swisdak, M., B. N. Rogers, J. F. Drake, and M. A. Shay (2003), Diamagnetic suppression of component magnetic reconnection at the magnetopause, *J. Geophys. Res.*, **108**, 1218, doi:10.1029/2002JA009726.
- Swisdak, M., M. Opher, J. F. Drake, and F. Alouani Bibi (2010), The Vector direction of the interstellar magnetic field outside the heliosphere, *Astrophys. J.*, **710**, 1769–1775, doi:10.1088/0004-637X/710/2/1769.
- Vignes, D., M. H. Acuña, J. E. P. Connerney, D. H. Crider, H. Rème, and C. Mazelle (2004), Magnetic flux ropes in the Martian atmosphere: Global characteristics, *Space Sci. Rev.*, **111**, 223–231, doi:10.1023/B:SPAC.0000032716.21619.f2.
- Wolff, R. S., B. E. Goldstein, and C. M. Yeates (1980), The onset and development of Kelvin-Helmholtz instability at the Venus ionopause, *J. Geophys. Res.*, **85**(A13), 7697–7707, doi:10.1029/JA085iA13p07697.
- Zhang, T. L., et al. (2012), Giant flux ropes observed in the magnetized ionosphere at Venus, *Geophys. Res. Lett.*, **39**, L23103, doi:10.1029/2012GL054236.